Ph. D Thesis

Analysis and Experiments on Coupling Enhancement of Rectangular Waveguide fed Dielectric Resonator Antennas

by

Jasmine P. M.

Under the guidance of

Prof. Abdulla P.

School of Engineering

Cochin University of Science and Technology, Kochi – 22, India.

May 2016

Analysis and Experiments on Coupling Enhancement of Rectangular Waveguide fed Dielectric Resonator Antennas

A thesis submitted to Cochin University of Science and Technology
in partial fulfillment of the requirements
for the award of the degree of

Doctor of Philosophy
(Faculty of Engineering)

by

Jasmine P. M.
(Reg. No. 3976)

Under the guidance of

Prof. Abdulla P.

School of Engineering
Cochin University of Science and Technology
Kochi, Kerala

May 2016

Analysis and Experiments on Coupling Enhancement of Rectangular Waveguide fed Dielectric Resonator Antennas

Ph.D. Thesis under the Faculty of Engineering

Author

Jasmine P. M.
Research Scholar
Electronics and Communication Engineering Division
School of Engineering
Cochin University of Science and Technology
Kochi-22
email: jasmine.maiyn@gmail.com

Supervising Guide

Prof. Abdulla P.
Electronics and Communication Engineering Division
School of Engineering
Cochin University of Science and Technology
Kochi-22
email: abdulla@cusat.ac.in

Electronics and Communication Engineering Division
School of Engineering
Cochin University of Science and Technology
Kochi - 682022

May 2016

School of Engineering
Cochin University of Science and Technology
Kochi, Kerala

Prof. Abdulla P.

Ph: 9496445235
email: abdulla@cusat.ac.in

Certificate

This is to certify that the thesis entitled **Analysis and Experiments on Coupling Enhancement of Rectangular Waveguide fed Dielectric Resonator Antennas** is a bonafide work carried out by Ms. Jasmine P. M. under my supervision and guidance at Electronics and Communication Engineering Division, School of Engineering, Cochin University of Science and Technology, Kochi-22. The results embodied in this thesis or parts of it have not been presented for the award of any other degree.

I further certify that the corrections and modifications suggested by the audience during the pre-synopsis seminar and recommended by the Doctoral Committee of Ms. Jasmine P. M. are incorporated in the thesis.

Kochi
May 2016

Prof. Abdulla P.
(Supervising Guide)

Declaration

I hereby declare that the thesis entitled "**Analysis and experiments on coupling enhancement of rectangular waveguide fed dielectric resonator antennas**" is a bonafide record of the research work carried out by me, under the supervision of Prof. Abdulla P., Electronics and Communication Engineering Division, School of Engineering, Cochin University of Science and Technology, Kochi-22. I further declare that this work has not formed the basis for the award of any other degree, diploma, associateship, fellowship or any other title for recognition.

Kochi — Jasmine P. M.

May 2016

Acknowledgements

It is my pleasure and privilege to thank the many persons who made this thesis possible. First and foremost I offer my sincere gratitude towards my supervisor, Prof. P. Abdulla, who has guided me through this work with his patience and constant encouragement. His sincerity, devotion to work and tremendous support has been a steady source of inspiration for me. A gentleman personified, in true form and spirit, I consider it to be my good fortune to have been associated with him.

I would like to express my sincere gratitude towards Dr. S. Mridula, Doctoral Committee member and Prof. G. Madhu, Principal, School of Engineering for their encouragement and support offered.

I take this opportunity to thank Dr. A. Biju, Principal, M. E. S. College, Maramapally for his constant encouragement and timely support. I also thank Dr. P. A. Fathima, former Principal, M. E. S. College, Marampally, who encouraged and helped me to apply for the Ph.D course and Faculty Development Programme of the UGC for doing the Ph.D work. Gratitude is also extended to the management committee members of M. E. S. College, Marampally especially to Dr. Zakkariya K, A. for his whole hearted support.

I thank from the bottom of my heart Smt. Raphika P. M., who had been my work associate at the Department for the entire period of my research. We have been complimentary to each other in many ways and this enabled us to work together productively.

I would like to thank Prof. C. K, Aanandan, Department of Electronics, Cochin University of Science and Technology for giving me the opportunity to take measurements in his lab. Sincere thanks are also extended to Dr. Nishamol M. S., Dr. Nijas C. M., Dr. Dinesh, Mr. Deepak, Ms. Libi and Mr. Jayakrishnan of the CREMA Lab for their timely help.

I would like to thank my friends Ms. Rekha T. K, Ms. Anu A. R., Ms. Jesna Anwer, Ms. Ami Iqubal, Mr. Ajimsha Maidheen, Ms. Sheeba Varghese and Ms. Sindhu

Radhakrishnan for their support and suggestions. Thanks are also extended to my neighbor, Mr. Jayaprakash for his helps while drafting research papers.

Special thanks are also extended to all the staff members of Section A, School of Engineering especially Mr. Ajas, Mr. Nazer, Ms. Anjana and Ms. Indira T. C. for their kind support. I also thank all my colleagues at M. E. S. College, Marampally.

I am grateful to the University Grants Commission for giving me the opportunity to do the research by availing the faculty development programme of UGC.

My deepest gratitude goes to my parents and sister for their unflagging love and support throughout my life. I am really proud of my family for their prayers and encouragement which gave me the courage to persevere. Above all, I thank my husband Maiyn Aboobacker for his love, support, care and patience especially during the hard times. I also thank my children Althaf, Nabeel and Namiya for their love, sacrifice and support.

Finally, I would like to thank everybody who was important to the successful realization of the thesis, as well as expressing my apology that I could not mention personally one by one.

Above all there is the god almighty whose blessings and kindness helped a lot to tide over.

Jasmine P. M.

ABSTRACT

The main objective of the thesis is the rigorous method of moments (MoM) analysis and experiments on the coupling enhancement of waveguide fed dielectric resonator antenna (DRA). The MoM analysis of waveguide shorted end slot coupled hemispherical DRA is carried out initially. The problem is formulated using Green's function approach and the unknown currents are solved using MoM. The hemispherical DRA is modeled using exact magnetic field Green's function due to equivalent magnetic currents in the slot. The field inside the waveguide is expressed in terms of modal vectors and modal functions. The rectangular slot is considered as a rectangular cavity and cavity Green's function is used for the analysis of the slot. The waveguide shorted end slot coupled hemispherical DRA gives only poor coupling. Therefore different coupling enhancement techniques are to be developed, which is the subject matter of the thesis. The poor coupling of waveguide shorted end slot coupled DRA is due to the inductive susceptance offered by the DRA loaded slot. Coupling can be improved by neutralizing the inductive susceptance of the DRA loaded slot by using its capacitive counterpart. The capacitive susceptance can be introduced by reducing the narrow wall dimension of the waveguide. Three different methods for reducing the narrow wall dimension of the waveguide are discussed in this work. Theoretical analysis of one of the coupling enhancement techniques, the double step junction coupled waveguide fed hemispherical DRA is carried out using method of moments. The proposed coupling enhancement techniques ensure very good coupling and is applicable for DRAs of different shapes.

CONTENTS

List of Figures

Chapter 1

Introduction

The main objective of the thesis is the analysis and experiments on coupling enhancement of rectangular waveguide fed dielectric resonator antenna. A broad literature review regarding the development of dielectric resonator antenna and the different methods for exciting the DRA are discussed in this chapter. Since the thesis concentrates on coupling enhancement of rectangular waveguide fed DRAs, a thorough literature review on the coupling enhancement techniques of rectangular waveguide fed DRA especially at the shorted end of the waveguide is described in chapter 1. The motivation behind the present work, regarding the coupling enhancement technique of waveguide shorted end slot coupled DRA persistent towards the current technological developments is explained in detail in this chapter.

1.1 Dielectric Resonator Antenna

In the early days of microwaves, guided electromagnetic wave propagation in dielectric media received wide spread attention. The term 'dielectric resonator' was coined by Robert D. Richtmyer of Stanford University in 1939 [1]. He showed that nonmetallic dielectric objects (toroid) can function as microwave resonators. Richtmyer also demonstrated that, the dielectric resonator when exposed to free space must radiate because of the boundary conditions at the dielectric-to-air interface. His theoretical work failed to generate any significant interest, and practically nothing happened in this field for more than 25 years. However, these results were later used in the development of dielectric resonator antenna (DRA). Dielectric resonators gained significance in 1960s, as high-frequency electronics and modern communications industry started to take off. They offered a size-reducing design alternative to bulky waveguide filters and lower-cost alternatives for electronic oscillator, frequency selective limiter and slow-wave circuits [2, 3]. In addition to the cost and size, other advantages of dielectric resonators over conventional metallic cavity resonators are lower weight, material availability, and ease of manufacturing. In 1967, Gastine et al. studied the radiation Q factors of isolated spherical dielectric resonators [4].

The possibility of constructing very small antennas using dielectric resonators was described in [5]. In 1975, Van Bladel reported a rigorous asymptotic theory for evaluating the modes of dielectric resonators of arbitrary shape [6], [7]. A small experimental array of rectangular dielectric resonators excited by a dielectric guide was reported in [8]. However, in spite of the high Q and small size, dielectric resonators were not considered for use in microwave devices, due to their poor temperature stability. The development of the first temperature stable, low loss, barium tetratitanate ceramics in the early 1970's was a real breakthrough in ceramic technology. The first theoretical and experimental study on a specific dielectric resonator antenna (DRA) configuration was reported by Long et al. in 1983 [9]. Theoretical and experimental investigations have been reported by many investigators on DRAs of various shapes such as spherical, cylindrical, cylindrical ring, and rectangular. The open dielectric resonators are potentially useful antenna elements [10]. They offer several attractive

features such as small size, high radiation efficiency, compatibility with monolithic integrated circuits, intrinsic mechanical simplicity and the ability to obtain different radiation patterns using different modes. When the frequency range of interest for many systems has progressed upwards to millimeter and near millimeter range the conductor loss of metallic antennas becomes severe and the efficiency of microstrip patch antennas reduces significantly. As the only loss of a DRA is due to the imperfect dielectric material, which is very small in practice, it can be used as a suitable alternative at millimeter range of frequencies. In addition, DRAs exhibit a relatively large bandwidth, approximately 10% for a dielectric constant of $\varepsilon_r = 10$, whereas patch antennas have a typical bandwidth of only 1% – 3% in their basic form.

Antenna miniaturization is very important, especially in wireless and low frequency applications. Wireless devices like cell phones, laptops, tablets, game pad controllers, GPS receivers, security sensors etc. require very small antennas with good performance in terms of connectivity, stability and data rate. As the frequency of operation is lowered, miniaturization techniques must be developed to make the antenna size practical. Two primary techniques are used for antenna miniaturization. One of them uses a novel topology to reduce the overall area consumed by the antenna and the second one uses material with permittivity, permeability, or both greater than one [11]. Since wavelength inside such materials reduces, size of the antenna decreases.

As the demand for bandwidth is growing, we have to opt for higher frequencies. Millimeter waves that occupy the frequency spectrum from 30 GHz to 300 GHz open up new spectrum and permit high data rates. Telecommunication systems are increasingly being used in the millimeter wave range due to the large bandwidth available [12]. Radar is another important use of millimeter waves, which takes advantage of another important property of millimeter wave propagation called beamwidth. In radar, it is desirable to have a beam that stays narrow, rather than fanning out. For a given antenna size, the beamwidth can be made smaller by increasing the frequency, and so the antenna can be made smaller as well. The 60 GHz signal can be used for short range communication and satellite communications. Two-three decades back, the commonly used antenna for high frequency applications was

the printed or patch antenna. However, conductor loss of the patch antenna becomes significant at high frequencies that degrade the performance of the system. On the other hand, DRAs that are made up of only dielectric material show great potential for high frequency applications. Conductor loss is absent for DRAs, and the only loss is due to the dielectric, which is very small in practice. For high gain applications DRA arrays are a good choice [13, 14, 15].

One of the main parameters that affect the performance of the antenna is the coupling technique used. Different planar techniques like direct microstrip line, aperture coupled microstrip, coplanar waveguide, conformal strip, coaxial probe etc. can be used for feeding the DRA. But all these coupling mechanisms suffer from feed line losses at high frequencies, especially at millimeter wave frequencies. The waveguide will not suffer from radiation loss and interference effects due to the metallic walls [16]. Therefore waveguide fed DRA is an excellent candidate for low loss millimeter wave communication systems.

1.2 Survey of Literature

Dielectric resonators have been used as high Q elements in microwave circuit applications since the development of low loss ceramics in late 1960s [17]. Dielectric resonators are more compact compared to waveguide cavity resonators. Dielectric resonators are often enclosed in metallic cavities to prevent radiation and to maintain high Q factor. Cylindrical resonators with relatively high dielectric constant are used for these applications. By removing the shielding and with proper excitation, some of the resonators could become efficient radiators. The radiation could be maintained over a relatively wide range of frequencies by reducing the dielectric constant [18]. A systematic study of the dielectric resonator as a radiating element was first carried out by Long et al. [9]. Their research demonstrated that DRAs could be considered as an attractive alternative to traditional low gain antennas like microstrip patches, monopoles and dipoles.

At high frequencies, mechanical tolerances and electrical losses are the two factors that dominate antenna designs. The dimensions of the dielectric resonator

antenna are of the order of $\lambda_0 \varepsilon_r^{-0.5}$, where λ_0 is the free space wavelength and ε_r is the dielectric constant of the resonator material [18]. Since radiation efficiency is not significantly affected by dielectric constant, a wide range of values can be used. However, bandwidth of the DRA is inversely related to dielectric constant; low values of dielectric constants are preferred for increased bandwidth [19]. Dielectric resonator antenna does not suffer from conductor loss and surface wave loss. DRAs have better radiation efficiency and high bandwidth than the corresponding microstrip antenna [20]. Apart from these advantages, DRAs have additional advantages like small size, low cost, light weight, ease of excitation and integration with active circuitry [21]. The use of micro-machining techniques can endure fine fabrication accuracy that allows the upper frequency limit of DRA to extend beyond 100 GHz. The aspect ratio of most shapes of DRAs can be altered, while maintaining the same resonant frequency for a given dielectric constant [22]. This allows a certain degree of flexibility in shaping the DRA to suit specific requirements.

A substantial amount of research work has been carried out since 1980s for the study of DRAs. Different shapes of DRAs like cylindrical [23], hemispherical [24], rectangular [25], triangular [26], conical [27], spherical cap [28], elliptical [29], hexagonal [30], cross [31], cylindrical ring [32] and split hemispherical [33] can be designed to radiate efficiently. Cylindrical DRAs are easy to fabricate, but they have edge shaped boundaries that make analytical solution difficult to obtain. The perfect magnetic wall approximation results in unsatisfactory discrepancies of about 20% between the measured and simulated results [34]. Theoretical models like body-of-revolution (BOR) based on the integral equation formulation for the equivalent electric and magnetic surface current densities, finite difference time domain method (FDTD) and surface integral equation technique are extensively applied [35-38]. However, extensive memory and computational time are required for these methods. A rectangular DRA gives better flexibility to design in terms of frequency and bandwidth [39], [40]. Also rectangular DRAs are easy to fabricate, but they have more edge shaped boundaries that make analysis even more difficult. The conical DRA is difficult

to fabricate and difficult to analyze. For triangular and cross DRAs, only experimental studies are carried out so far.

Hemispherical dielectric resonator antenna (HDRA) is mainly used in this thesis due to its simple interface with free space, which makes the analysis easier. The simple structure requires no magnetic wall assumption in the problem formulation and hence accurate solution can be obtained. Moreover, its closed form Green's function is available. In earlier days, analysis of DRAs was concentrated only on the far field radiation patterns. The magnetic wall model cannot be used to calculate the input impedance of the DRA [9]. The first theoretical analysis of the input impedance of hemispherical DRA was computed by Leung et al. [41]. The input impedance and radiation pattern of HDRA are investigated in [24]. HDRA residing above the ground plane can be viewed as a spherical DR by using image theory. In spherical coordinate system, variables of the wave functions are separable, which greatly simplifies the analysis. For spherical geometry, exact closed form expressions for the Green's function of point currents in the dielectric body can be derived using modal expansion technique. The unknown feed current and hence the input impedance and reflection coefficient can be found out by using method of moments (MoM) [42].

Feeding techniques play an important role in the performance of the antenna. Various methods like coaxial probe [24, 43], direct microstrip [44-47], aperture coupled microstrip [48-52], conformal strip [53-55], coplanar waveguide [56-59] and metallic waveguide [60], [61] are used for feeding the DRA. In coaxial probe coupling, a hole is to be drilled into the DRA to accommodate the probe. Normally the probe does not perfectly fit into the hole; an air gap exists between the probe and DRA [62]. The air gap causes the measured results to deviate from the predicted value. To avoid these problems, the probe can also be placed outside the DRA [63]. However, this is applicable to DRAs with a vertical side wall, such as rectangular and cylindrical DRAs. For DRAs with a curved side wall, coupling between the probe and DRA is rather inefficient. Moreover it generates ohmic loss and large probe self reactance at millimeter wave frequencies. A common method of coupling to dielectric resonators makes use of microstrip lines. DRA is placed either above the strip or near the strip.

Microstrip coupling will excite magnetic fields in the DRA to produce short horizontal magnetic dipole mode. Though the design topology of microstrip feeding is simple, analysis of the structure is very complicated since the conductive strip and dielectric substrate are close together.

The aperture coupled antenna was first suggested by D. M. Pozar [64]. In aperture coupling, DRA is placed above the slot on the ground plane and fed by a microstrip line beneath the ground plane. The aperture behaves like a magnetic current running parallel to the length of the slot and excites magnetic fields in the DRA. Since feed network is located below the ground plane, spurious radiation is not present and analysis is easy. Conformal strip is another type of feeding mechanism, in which a conducting strip is mounted on the DRA surface without creating air gaps. Since electric current can flow on the DRA surface, energy coupling is more efficient than coaxial probe placed on the walls of the DRA. This method can be easily implemented by cutting a strip from an adhesive conducting tape. Furthermore, it admits very convenient post manufacturing trimmings, since the length of the conformal strip can be adjusted very easily [65]. However, in this method also, a hole is to be drilled into the substrate for probe penetration.

Co-planar waveguide feed is preferred when the antennas are required to be integrated with active devices. CPW offers several advantages over conventional microstrip line like simplified fabrication, easy shunt as well as series surface mounting of active and passive devices, avoidance of wrap-around and via holes [57]. It also reduces radiation loss. But all these excitation techniques suffer from feed line losses at high frequencies. On the other hand, rectangular waveguide is an attractive feed to the DRA at high frequencies. Since rectangular waveguide is surrounded by metallic walls, excellent shielding between the interior and exterior region is achieved, avoiding radiation loss even in the millimeter wave band. Waveguide and waveguide based components are used as antenna elements since World War II. Waveguide based elements have got wide applications in ground based, air borne and ship borne radars as well as in onboard satellite applications in various frequency bands ranging from 1 GHz to 1000 GHz. These are due to the high power handling capability, ability to

sustain high environmental variations, ruggedness and the possibility of achieving high accuracy in fabrication.

Studies on waveguide and waveguide cavities date back well before World War II. During post world war II, extensive studies have been performed on waveguide [67-69]. Waveguide is the basic component of many microwave/millimeter wave components such as magic Tees, directional couplers, filters and phase shifters. Due to the very low losses of waveguide and DRA, they form an excellent combination for millimeter wave applications.

In the literature, very little data or studies have been reported on rectangular waveguide fed DRA, either at the waveguide shorted end or at the broad wall. Though a high permittivity DRA can be efficiently excited by an empty waveguide [70], coupling is very poor with DRAs of low dielectric constants. A low loss excitation of rectangular waveguide fed cylindrical DRA was reported in [35]. However the coupling achieved was only 28% and DRA is analyzed using body of revolution, which is applicable only for rotationally symmetric structures. Insufficient coupling was also noticed for a hemispherical DRA of dielectric constant, ε_r = 10 coupled to the shorted end of a rectangular waveguide [71]. Poor coupling of waveguide shorted end slot coupled DRA is due to the inductive susceptance offered by the DRA loaded slot. Therefore different coupling enhancement techniques are to be developed for waveguide fed DRAs. Coupling can be improved by a coax probe fed DRA/stacked DRA coupled to the waveguide through an aperture in the waveguide wall, which involves drilling a hole into the DRA to accommodate the probe [72]. Drilling a hole into the DRA for inserting the probe creates undesirable air gaps. Embedded DRA placed inside the standard X-band waveguide, which is excited by an off-centred coaxial probe provides good coupling [61]. However, embedded DRA configuration increases the complexity and cost of the system.

Coupling enhancement using another dielectric resonator inside the waveguide was reported in [73]. This technique requires a second dielectric resonator, which is to be placed inside the waveguide close to the slot to increase coupling. The additional DRA increases the overall cost of the system, and keeping the dielectric resonator

inside the waveguide seems to be very difficult. Moreover, bandwidth of the antenna is very low. The bandwidth is improved by using an 'I' slot; still the bandwidth is only 5.38%. Coupling enhancement can also be achieved by inserting a capacitive waveguide junction between the rectangular waveguide and the ground plane [74]. But the narrow wall dimension of the capacitive waveguide junction is very small that makes fabrication difficult at millimeter wave frequencies. Another technique for coupling enhancement using multilayer DRA was proposed in [75]. Though this technique does not require extra matching elements, fabrication of multilayer DRA is very difficult and costly. This thesis explores the analysis and experiments of different coupling enhancement techniques of waveguide shorted end slot coupled DRA.

The waveguide shorted end slot coupled HDRA consists of waveguide, rectangular cavity and HDRA. Waveguide and waveguide based cavities are well studied even before World War II. Green's function of the waveguide was presented in [76]. Green's function of the rectangular cavity using vector wave functions was discussed in [77]. Rahmat Samii presented the Green's function of the electric field for rectangular waveguide and cavities using eigen function expansion [78]. A hybrid-ray representation of the Green's function in a rectangular cavity was developed using the finite Poisson summation formula [79]. In order to obtain a numerically efficient scheme for computing the field generated by a point source in a large rectangular cavity, the conventional modal representation of Green's function was modified in such a way that all the modes near resonance are retained, while the truncated reminder of the mode series is expressed in terms of the weighted contribution of rays. For an electrically large cavity, contribution of rays from distant images becomes small; therefore the ray sum was approximated by one or two dominant terms without losing numerical accuracy. Balanis [80] and Collin [67] studied the generalized Green's function, which is utilized for deriving the Green's function of rectangular cavity in the present work.

Many wireless and radar applications operate over wide frequency bands and thus broadband antennas are required. Since bandwidth of the DRA is inversely related to its dielectric constant, wideband performance is achieved with DRAs of low

dielectric constant. The compact size and wideband performance achieved by DRAs give them an advantage over many other resonant antennas, which typically exhibits narrower bands. Broader impedance bandwidths can be achieved by adopting various enhancement techniques. Stacked DRAs or embedded DRA configuration can be used to obtain impedance bandwidths ranging from 25% to nearly 80% [81-86]. The technique of using stacked DRAs increases the cost of the system due to the additional DRA required. Increased bandwidths can also be achieved by modifying the shape of the DRA, using multiple layers, or by adopting new feeding structures [87-94]. However, these methods increase the complexity of the system. Hybrid designs, where dielectric resonator antennas are combined with other antenna elements such as microstrip patches, or monopoles have led to wideband designs [95], [96]. This method will also increase the complexity of the system. The technique of merging the resonance of feed mechanism with the radiating structure is used in this thesis to improve the bandwidth.

Apart from wideband, dual or multiple frequency band operation is highly desirable in modern wireless communication systems. Dual frequency operation can be achieved by using multiple DRAs [97]. Requirement of additional DRA increases the cost of the system. If a single DRA can support multiple frequency bands, need for multiple single frequency antennas can be avoided. Dual frequency operation can also be obtained by using strip fed method and DRAs of special shapes [98, 99]. Resonant frequency of the feeding structure and DRA can be adjusted to obtain dual frequency operation. [100], [101].

1.3 Areas to be investigated

From the survey of the literature, it is strongly felt that the coupling problems of waveguide fed DRA need to be addressed. Dielectric resonator antenna offers a number of advantages like small size, light weight, high power handling capability, increased bandwidth, low losses and ease of integration with active circuitry. The low losses of DRA, especially the absence of conductor loss makes DRA a suitable candidate for millimetre wave communication systems. Various techniques like coaxial probe, direct

microstrip, aperture coupled microstrip, coplanar waveguide, conformal strip, and metallic waveguide can be used for feeding the DRA. But all the coupling mechanisms except metallic waveguide suffer from feed line losses at millimetre wave frequencies. Due to metallic walls, waveguide has excellent shielding between the interior and exterior regions avoiding radiation loss even in the millimetre wave band. DRAs can be placed either at the shorted end of the waveguide or at the broad wall and narrow wall of the waveguide. A rectangular waveguide broad wall slot fed DRA was reported in [35], in which the cylindrical DRA is analysed using body of revolution. However, the power coupling achieved was only 28%. In [70] a high permittivity DRA excited by a slot at the shorted end of the waveguide was reported. However, the case with DRAs of low dielectric constant is different. The reason for poor coupling of waveguide shorted end slot coupled DRA with low dielectric constant is the inductive susceptance offered by the DRA loaded slot. Therefore coupling enhancement techniques are to be developed, for waveguide fed DRAs, with low dielectric constant values, which is the major objective of the thesis.

Due to various reasons, experimentation in gigahertz frequencies to generate the measured data on aperture and slot antennas with metallic waveguide is extremely time consuming and expensive. It is worthwhile to substitute this costly experimentation with theoretical modeling which would very closely repeat the practical results. A small number of experimental validations are sufficient to test the utility of those algorithms, which would be useful for the electromagnetic community at a much lower cost. In this thesis method of moments (MoM) is used for the theoretical analysis and the theoretical study is implemented using MATLAB [102]. The code developed using theoretical study is computationally more efficient than the codes available with commercial softwares. This is due to the fact that commercially available codes are generic problem solvers due to their versatility, while codes developed using MoM are problem specific.

1.4 Methodology

The main objective of this thesis is the development of different coupling enhancement techniques for waveguide shorted end slot coupled DRA. The poor

coupling of waveguide shorted end slot coupled DRA is due to the inductive susceptance of the DRA loaded slot [74]. Coupling enhancement can be achieved by introducing the capacitive susceptance required to neutralize the inductive susceptance of waveguide shorted end slot coupled DRA. The capacitive susceptance can be introduced by reducing the narrow wall dimension of the waveguide. Different methods used for reducing the narrow wall dimension are discussed in this thesis. Due to various reasons experimentation in giga hertz frequencies to generate measured data is costly and time consuming. This costly experimentation can be substituted with theoretical analysis, which will closely repeat the experimental results. A small number of experimental validations are sufficient to test the utility of these programs. The techniques, which cannot be solved theoretically, are optimized using the simulation softwares: Ansoft HFSS [103] and CST Design Studio [104].

In order to perform theoretical analysis, method of moments (MoM) is used. The problem can be formulated by writing integral equations. The unknown quantities in the equations are represented using known basis functions with unknown constants. The integral equations are expressed using matrix format. After evaluating the known elements of the matrix, the unknown constants can be computed using matrix inversion technique. Reflection coefficient can be computed using the unknown constants of the currents evaluated using MoM. After optimizing the different parameters of the proposed structure using simulations, prototype of the structure can be fabricated. Due to fabrication difficulties in the millimetre wave band, feasibility of the proposed structures is implemented in X band. The reflection and radiation characteristics of the antenna can be measured using network analyser.

1.5 Organization of the thesis

The thesis describes different coupling enhancement techniques of waveguide shorted end slot coupled DRA. Though the application of the proposed technique is in millimeter wave frequencies, due to the limited fabrication facility available in our laboratory, experimental study has been performed in the X-band. WR90 waveguide with cross section 22.86 mm x 10.16 mm is used for exciting the DRA in X band.

Theoretical analysis of one of the coupling enhancement techniques is studied using MoM. Hemispherical DRA is mainly used in this thesis due to its simple interface with free space. HDRA residing above the ground plane can be viewed as a spherical DRA by using image theory. For the spherical geometry, exact closed form expression for the Green's function is available. The input impedance, reflection coefficient, radiation pattern and gain of the proposed techniques are investigated. The proposed coupling enhancement techniques are applicable for DRAs of any shape. Experimental verification of the coupling enhancement techniques for cylindrical DRA is also performed.

Chapter 2

The main objective of the thesis is the analysis and experiments of various coupling enhancement techniques of rectangular waveguide fed DRA. Initially the drawbacks of the waveguide shorted end slot coupled DRA is found out. Chapter 2 deals with the analysis of waveguide shorted end slot coupled HDRA. The different components of waveguide shorted end slot coupled HDRA are: waveguide, slot and hemispherical DRA. In order to carry out MoM analysis of waveguide shorted end slot coupled hemispherical DRA, the problem is represented using a set of integral equations. The equations are developed by applying magnetic field boundary conditions at various apertures. The scattered magnetic fields inside the waveguide, slot and HDRA are required to solve the integral equations. Expressions for the scattered fields inside the waveguide, rectangular cavity, and HDRA are derived in this chapter using Green's function. Though these derivations are not original, they are presented using uniform notation as they are referred repeatedly in the rest of the thesis. A general MATLAB code has been written to perform the theoretical analysis.

Chapter 3

In this chapter, a novel technique for the coupling enhancement of waveguide shorted end slot coupled hemispherical DRA is presented. Double step junction with reduced narrow wall dimension is inserted between the rectangular waveguide and the

ground plane to provide increased coupling. The double step junction provides the capacitive susceptance required to neutralize the inductive susceptance of waveguide shorted end slot coupled HDRA. The broad wall dimension of the steps is same as that of the rectangular waveguide, which makes fabrication easier. The proposed technique for coupling enhancement is analyzed rigorously using MoM. The scattered fields derived in chapter 2 are used for solving the equations corresponding to double step junction coupled waveguide fed HDRA. An in house MATLAB code is developed to implement the theory of the proposed work. Parametric study has been carried out using the developed code. In addition to single resonance operation, dual and wide band operations are implemented using the developed MATLAB code. Measurements were carried out to verify the theory.

Chapter 4

The poor performance of direct coupled waveguide fed DRA is due to the abrupt transition from the large width of the rectangular waveguide to the very small width of the slot. If the abrupt termination is replaced by gradual termination, coupling could be enhanced. This is achieved by inserting a tapered section of the waveguide between the rectangular waveguide and the ground plane. The tapered section reduces only the narrow wall dimension of the waveguide, which also acts as a capacitive susceptance. Parametric study has been conducted using Ansoft HFSS to find out the optimum value of various parameters. Prototype of the tapered section coupled waveguide fed HDRA has been fabricated and measured the reflection and radiation characteristics.

Chapter 5

Coupling enhancement technique described in chapter 3 uses two steps symmetrical to the centre of the narrow wall. Symmetrical steps produce the capacitive susceptance required to obtain impedance matching. The capacitive susceptance can also be realized by using non-symmetric steps. The non-symmetric steps give the waveguide a stair shaped appearance. The total number of steps in the stair shaped waveguide fed HDRA is only two; while the total number of steps in double step

junction coupled waveguide fed HDRA is four. The reduced number of steps in the stair shaped waveguide fed HDRA makes fabrication easier Simulation and measurement results of stair shaped waveguide fed hemispherical DRA are discussed in chapter 5. The proposed stair shaped waveguide fed HDRA gives very good coupling.

Chapter 6

The coupling enhancement techniques developed for hemispherical DRA, which are discussed in the previous chapters can be extended to DRAs of other shapes. Chapter 6 discusses the measured and simulated results of double step junction and tapered section coupled waveguide fed cylindrical DRA. Very good matching is obtained for the coupling enhancement techniques applied to cylindrical DRA. Symmetrical broadside radiation patterns with low cross-polarization levels are obtained for both the structures.

Chapter 7

The major achievements of the thesis based on the analysis and results presented in the previous chapters are summed up in this chapter. It also examines the areas that are not studied in the present work, and outlines the areas where efforts need to put in to further the state of knowledge in this area.

Chapter 2

MoM Analysis of Waveguide Shorted End Slot Coupled Hemispherical Dielectric Resonator Antenna

Theoretical analysis of waveguide shorted end slot coupled hemispherical dielectric resonator antenna (HDRA) using method of moments (MoM) is carried out in this chapter. The problem is formulated using Green's function; the unknown magnetic currents at the slot are solved using MoM. Dyadic Green's function and the fields due to unit magnetic current excitation of HDRA are derived in this chapter. HDRA is modeled using exact magnetic field Green's function due to equivalent magnetic currents in the slot. The modal series is represented as the sum of particular and homogeneous solutions to enhance the efficiency of computation. Initially the fields are computed in spherical coordinates due to spherical components of unit current. The spherical components of the fields are transformed into rectangular coordinates due to magnetic currents in rectangular coordinates. Field inside the waveguide is expressed in terms of modal vectors and modal functions. The thick slot can be considered as a rectangular cavity, which can be analyzed using cavity Green's function. Magnetic field inside the waveguide, slot, and HDRA is used for the analysis of waveguide shorted end slot coupled hemispherical DRA.

2.1 Introduction

Dielectric Resonator Antenna (DRA) is very much suitable for high frequency applications due to the absence of conductor loss. Though DRAs can be excited with direct microstrip, aperture coupled microstrip, coaxial probe, coplanar waveguide and conformal strip; they suffer from feed line losses that become significant at high frequencies. Instead, metallic waveguide used for exciting the DRA, avoids feed line losses. The metallic walls of the waveguide offer excellent shielding between the interior and exterior regions, avoiding radiation loss even in the millimeter wave band. DRAs can be excited by slots kept at the broad wall, narrow wall or at the shorted end of the waveguide. This work concentrates only on waveguide shorted end slot coupled DRAs.

Experimentation in gigahertz frequencies to generate measured data for waveguide fed DRA is very costly and time consuming. If the costly experimentation can be substituted with theory, only a few experiments are needed to validate the theory. In the field of electromagetics, solutions of many problems are obtained using second order uncoupled partial differential equations, derived from Maxwell's equation and appropriate boundary conditions. The form of most of these types of solutions is an infinite series, provided the partial differential equations and the boundary conditions representing the problems are separable in the coordinate system chosen. However, these solutions are usually slowly convergent, especially at regions where rapid changes occur. Closed form solutions would be desirable for some problems and even solutions in the form of integrals would be acceptable. The technique known as Green's function accomplishes this goal [80]. With Green's function, solutions to the partial differential equations are obtained using a unit source (impulse, Dirac delta) as the driving function. Solutions to the actual driving function are computed by the superposition of Green's function with Dirac delta source at different locations, which in the limit reduces to an integral. In engineering terminology, Green's function is the impulse response of a system and in system theory it is called transfer function. Just as *h(t)* gives the response in time to a temporally impulsive source, $G(\bar{r})$, gives the response in space to a spatially impulsive (electric or magnetic current) source.

For a given problem, Green's function can take various forms. In one form, the solution can be expressed in terms of finite explicit functions. This method can be used only if the solution to the homogeneous differential equation is known. Another form of the Green's function is to construct its solution by an infinite series of suitably chosen orthonormal functions. The boundary conditions determine the eigen values of the eigen functions and the strength of the sources influences the coefficients of eigen functions. Integral forms can also be used to represent the Green's function, especially when the eigen value spectrum is continuous. All solutions, though different in form, give the same results. The form of Green's function that is most appropriate will depend on the problem to be solved.

2.2 Waveguide Shorted End Slot Coupled HDRA

Configuration of the waveguide shorted end slot coupled HDRA is shown in Fig 2.1. The longitudinal cross section and top view are shown in Fig. 2.2. We assume that the ground plane of thickness *2t* on which the HDRA placed is extended to infinity in the $\hat{x}$ and $\hat{y}$ directions for theoretical analysis. The HDRA is excited by a slot kept at the thick ground plane; width of the slot is narrow to eliminate any possible cross-polarization. Therefore variation of the slot magnetic current only along the *x* direction is to be considered for the magnetic field, i.e., the electric field E_y in the aperture varies only in the x-direction and is non-varying in the y- direction.

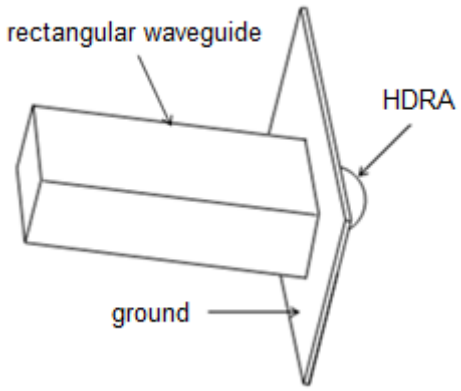

Fig. 2.1 Configuration of waveguide shorted end slot coupled HDRA.

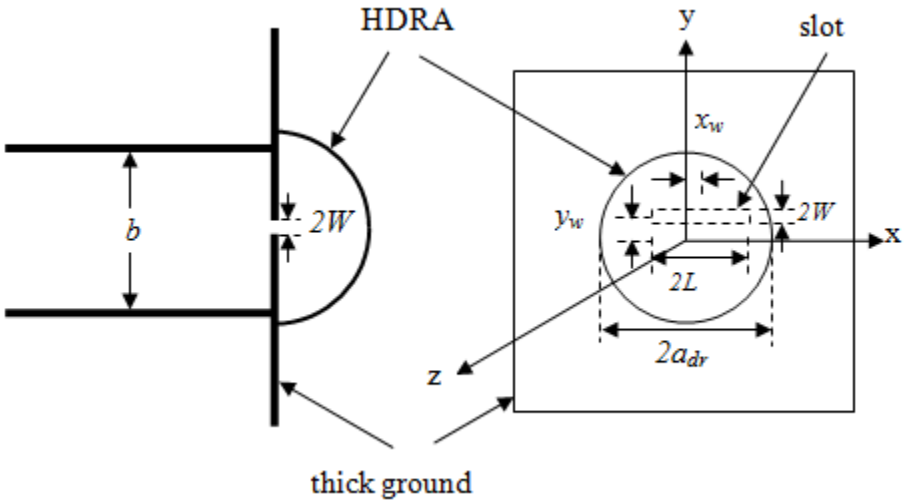

Fig. 2.2 Longitudinal cross section and top view of waveguide shorted end slot coupled HDRA.

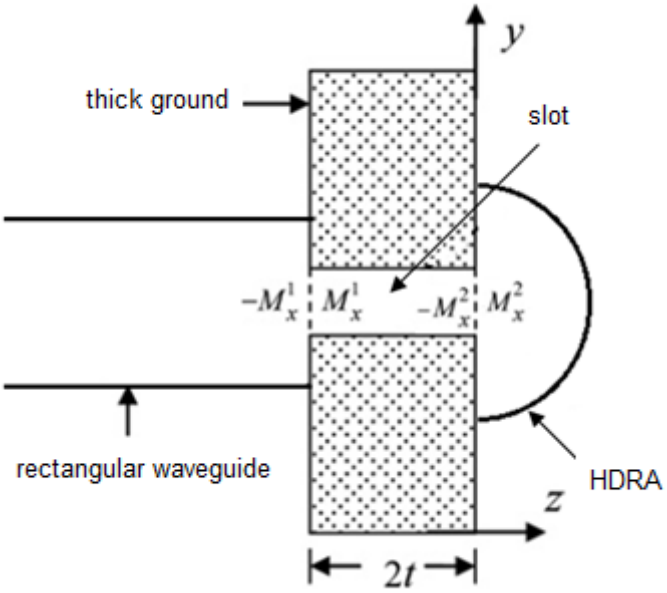

Fig. 2.3 Longitudinal cross section of waveguide shorted end slot coupled HDRA with enlarged thick ground plane.

Invoking equivalence principle [66], the aperture can be closed off and can be replaced by magnetic surface currents just above and below the ground plane. Continuity of the tangential components of the magnetic field through the aperture is ensured by making the magnetic current above the ground plane, which is equal to the

negative of that below the ground plane. This separates the problem into two equivalent problems: the slotted waveguide part and the DRA placed above the infinite ground plane. The longitudinal cross section of the structure with enlarged ground plane along with aperture currents is shown in Fig, 2.3. In the following formulations, the fields are assumed to vary as $e^{j\omega t}$ which is suppressed throughout. Applying magnetic field boundary conditions at the apertures equations (2.1) and (2.2) are obtained.

At aperture 1 (between the waveguide and the ground plane)

$$2H_x^{inc} - H_x^{WG}(\vec{M}_x^1) - H_x^{SL}(\vec{M}_x^1) + H_x^{SL}(\vec{M}_x^2) = 0 \tag{2.1}$$

At aperture 2 (between the ground plane and the DRA)

$$H_x^{SL}(\vec{M}_x^1) - H_x^{SL}(\vec{M}_x^2) - H_x^{DRA}(\vec{M}_x^2) = 0 \tag{2.2}$$

where $H_x^{\alpha}\left(\vec{M}_x^{i}\right)(i = 1, 2 \text{ and } \alpha = WG, SL, DRA)$ is the x component of the magnetic field due to x component of the magnetic current at aperture i. The unknown magnetic current can be expressed in terms of the electric field, which is also unknown. The relationship between the magnetic current and electric field is given by

$$\vec{M} = \vec{E} \times \hat{n} \tag{2.3}$$

If E_p^i is the unknown coefficient of the electric field $\vec{E}$ that exists at aperture i, the electric field is assumed to be of the form:

$$\vec{E}_y^i(x') = \hat{u}_y \sum_{p=1}^{M} E_{yp}^i e_p^i(x') \tag{2.4}$$

where $e_p^i(x')(p = 1, 2, 3, \ldots, M)$ is defined by

$$e_p^i(x') = \begin{cases} \sin\left[\dfrac{p\pi}{2L_i}(x' - x_{wi} + L_i)\right], & x_{wi} - L_i \le x' \le x_{wi} + L_i \\ & y_{wi} - W_i \le y' \le y_{wi} + W_i \\ 0, & \text{elsewhere} \end{cases} \tag{2.5}$$

where L_i, W_i, denote the length, width of the slot respectively and x_{wi}, y_{wi} represent the offset given to the slot along x and y direction respectively. As each of the field is described by M number of basis functions, 2M unknowns are to be determined for finding out the unknowns, $\vec{M}_x^1$ and $\vec{M}_x^2$ from the boundary conditions given by equations (2.1) and (2.2). Galerkin's specialization of MoM is used to obtain 2M different equations from the boundary conditions to enable the determination of 2M unknowns. For Galerkin's procedure of MoM [42], the weighting function is same as the testing function and is given by:

$$e_q^i(x) = \begin{cases} \sin\left[\dfrac{q\pi}{2L_i}(x - x_{wi} + L_i)\right], & x_{wi}\text{- L}_\text{i} \le x \le x_{wi} + L_i \\ 0, & \text{elsewhere} \end{cases} \quad y_{wi}\text{-W}_\text{i} \le y \le y_{wi} + W_i \tag{2.6}$$

where the primed coordinates represent the source location and non primed coordinates represent the observation location. Multiplying (2.1) and (2.2) with testing function same as the basis function,

$$-\left\langle\left[H_x^{WG}\left(M_x^1\right) + H_x^{SL}\left(M_x^1\right)\right], e_q^1(x)\right\rangle + \left\langle\left[H_x^{SL}\left(M_x^2\right)\right], e_q^1(x)\right\rangle = -2\left\langle H_x^{inc}, e_q^1(x)\right\rangle \tag{2.7}$$

$$\left\langle\left[H_x^{SL}\left(M_x^1\right)\right], e_q^2(x)\right\rangle - \left\langle\left[H_x^{SL}\left(M_x^2\right) + H_x^{DRA}\left(M_x^2\right)\right], e_q^2(x)\right\rangle = 0 \tag{2.8}$$

where the inner product is defined as:

$$\left\langle H(x), e_q(x)\right\rangle = \iint_{Aperture} H.e_q\,dxdy \tag{2.9}$$

Rearranging (2.7) and (2.8) in matrix form as

$$\Rightarrow \begin{pmatrix} Y_{11} & Y_{12} \\ Y_{21} & Y_{22} \end{pmatrix} \begin{pmatrix} E_{yp}^1 \\ E_{yp}^2 \end{pmatrix} = \begin{pmatrix} -2H_x^{inc} \\ 0 \end{pmatrix} \tag{2.10}$$

Elements of the moment matrix are:

$$Y_{11} = -\left\langle \left[H_x^{WG}(\bar{M}_x^1) + H_x^{SL}(\bar{M}_x^1) \right], e_q^1(x) \right\rangle \tag{2.11}$$

$$Y_{12} = \left\langle \left[H_x^{SL}(\bar{M}_x^2) \right], e_q^1(x) \right\rangle \tag{2.12}$$

$$Y_{21} = \left\langle \left[H_x^{SL}(\bar{M}_x^1) \right], e_q^2(x) \right\rangle \tag{2.13}$$

$$Y_{22} = -\left\langle \left[H_x^{SL}(\bar{M}_x^2) + H_x^{DRA}(\bar{M}_x^2) \right], e_q^2(x) \right\rangle \tag{2.14}$$

In order to solve the boundary condition equations, scattered magnetic fields inside the waveguide, slot and HDRA are to be determined. Also the expression for the incident magnetic field is to be found out. The *x* component of incident magnetic field at aperture 1 for transmitting mode, the dominant TE_{10} mode is given by [66].

$$H_x^{inc} = -Y_0 \cos\left(\frac{\pi x}{2a}\right) e^{-j\beta z} \tag{2.15}$$

The thick slot can be considered as a rectangular cavity and the scattered magnetic field inside the rectangular cavity can be determined by deriving the cavity Green's function of the electric vector potential. The cavity Green's function can be derived by solving the Helmholtz equation for the electric vector potential. Scattered magnetic field inside the waveguide can be determined using modal analysis. The field coupled to the DRA is determined using Green's function.

2.3 Scattered Magnetic Field inside the HDRA

Consider a rectangular slot with length *2L* and width *2W* located on the ground plane with an offset, x_w along *x* direction and y_w along *y* direction and DRA is placed at the center of the ground plane as shown in Fig. 2.4. The Green's function, $G_{M_x}^{H_x}$ (*x* directed magnetic field due to *x* directed magnetic current), $G_{M_x}^{Hy}$ (*y* directed magnetic field due to *x* directed magnetic current), $G_{M_y}^{H_x}$ (*x* directed magnetic field due to *y*

directed magnetic current), $G_{M_y}^{H_y}$ (y directed magnetic field due to y directed magnetic current) are to be found out.

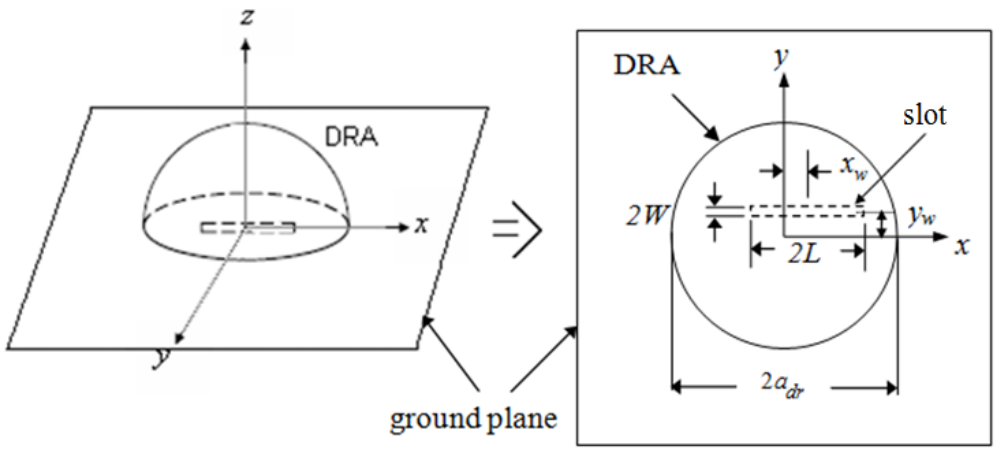

Fig. 2.4 Hemispherical DRA placed above the slotted ground plane.

Since the DRA is hemispherical in shape, it is easy to find out the Green's function in spherical coordinates due to spherical components of magnetic currents. Also in spherical coordinate system, variables of the wave function are separable that simplifies the analysis. Even though the slot is assumed to be narrow in this problem, we are deriving the magnetic field inside the HDRA for a wide slot. The magnetic currents $\vec{M}_x$ and $\vec{M}_y$ in the ground plane ($z'=0$ or $\theta'=\pi/2$) can be expressed in terms of spherical components as:

$$\vec{M}_x = \vec{M}_r \sin\theta' \cos\phi' - \vec{M}_\varphi \sin\phi' \tag{2.16a}$$

$$\vec{M}_y = \vec{M}_r \sin\theta' \sin\phi' + \vec{M}_\varphi \cos\phi' \tag{2.16b}$$

Since $\vec{M}_r$ can excite only transverse electric (TE to r) modes, electric potential function, $G_{M_r}^{Fr}$ alone is sufficient to represent the solution. On the other hand, $\vec{M}_\phi$ can excite both transverse electric and transverse magnetic (TE and TM to r) modes, both

the electric potential function $G_{M_\phi}^{Fr}$ and magnetic potential function, $G_{M_\phi}^{Ar}$ are required, to find all possible fields.

2.3.1 Derivation of Potential Green's Function of HDRA

To enhance the efficiency of computation, each of the potential Green's function is expressed as the sum of particular and homogeneous solutions. The particular solution represents the source radiating in the unbounded dielectric medium (field radiated into space), whereas the homogeneous solution accounts for the dielectric discontinuity. Therefore each potential Green's function can be expressed as:

$$G_{M_r}^{Fr} = G_{M_r}^{Frp} + G_{M_r}^{Frh} \tag{2.17}$$

$$G_{M_\phi}^{Fr} = G_{M_\phi}^{Frp} + G_{M_\phi}^{Frh} \tag{2.18}$$

$$G_{M_\phi}^{Ar} = G_{M_\phi}^{Arp} + G_{M_\phi}^{Arh} \tag{2.19}$$

where the superscripts *h and p* represents the homogeneous and particular solution respectively.

2.3.1.1 Determination of $G_{M_r}^{Fr}$ (Electric potential Green's function due to *r*-directed current)

The electric potential Green's function, $G_{M_r}^{Fr}$ consists of two parts: $G_{M_r}^{Frp}$, the particular solution and $G_{M_r}^{Frh}$, the homogeneous solution. To represent an arbitrary electromagnetic field in spherical coordinates, consider the field as a superposition of two parts: TE to r and TM to r. The electric and magnetic potential functions are represented by,

$$\vec{F} = F_r \hat{a}_r \tag{2.20}$$

and

$$\vec{A} = A_r \hat{a}_r \tag{2.21}$$

The electric and magnetic fields are represented by

$$\vec{E} = -\nabla\times\vec{F} + \frac{1}{\hat{y}}\nabla\times\nabla\times\vec{A} \tag{2.22}$$

$$\vec{H} = \nabla\times\vec{A} + \frac{1}{\hat{z}}\nabla\times\nabla\times\vec{F} \tag{2.23}$$

where $\hat{y} = j\omega\varepsilon$, and $\hat{z} = j\omega\mu$. F_r and A_r are not the solutions of the Helmholtz equation, since $\nabla^2 A_r \neq \left(\nabla^2 A\right)_r$. To determine the equations which A_r and F_r must satisfy, consider the general equations for vector potentials as:

$$\nabla\times\nabla\times\vec{A} - k^2\vec{A} = \vec{J} - \hat{y}\nabla\Phi^a \tag{2.24}$$

$$\nabla\times\nabla\times\vec{F} - k^2\vec{F} = \vec{M} - \hat{z}\nabla\Phi^f \tag{2.25}$$

where Φ^a, Φ^f are arbitrary scalars and $\vec{J}$, $\vec{M}$ are the electric and magnetic currents respectively. There is a great deal of arbitrariness in the choice of vector potentials. For instance, choosing the arbitrary 'Φ' according to:

$$\nabla.\vec{A} = -\hat{y}\Phi^a \tag{2.26}$$

$$\nabla.\vec{F} = -\hat{z}\Phi^f \tag{2.27}$$

Substituting (2.20) into (2.25)

$$\nabla\times\nabla\times\left(F_r\,\hat{a}_r\right) - k^2\left(F_r\,\hat{a}_r\right) = M_r\,\hat{a}_r - \hat{z}\nabla\Phi^f \tag{2.28}$$

where $k = \omega\sqrt{\mu\varepsilon}$, and $\nabla\Phi^f$ in spherical coordinates is represented by,

$$\nabla\Phi^f = \frac{\partial\Phi^f}{\partial r}\hat{a}_r + \frac{1}{r}\frac{\partial\Phi^f}{\partial\theta}\hat{a}_\theta + \frac{1}{r\sin\theta}\frac{\partial\Phi^f}{\partial\phi}\hat{a}_\phi \tag{2.29}$$

Substituting (2.29) into (2.28) and expanding,

$$\frac{\hat{a}_r}{r\sin\theta}\left[\frac{\partial}{\partial\theta}\left(-\frac{1}{r}\frac{\partial F_r\sin\theta}{\partial\theta}\right)-\frac{\partial}{\partial\phi}\left(\frac{1}{r\sin\theta}\frac{\partial F_r}{\partial\varphi}\right)\right]+\frac{\hat{a}_\theta}{r}\left[\frac{\partial}{\partial r}\left(\frac{\partial F_r}{\partial\theta}\right)\right]+\frac{\hat{a}_\phi}{r}\left[\frac{\partial}{\partial r}\left(\frac{1}{r\sin\theta}\frac{\partial F_r}{\partial\phi}\right)\right]$$
$$-k^2F_r\hat{a}_r=M_r\hat{a}_r-\hat{z}\left[\frac{\partial\Phi^f}{\partial r}\hat{a}_r+\frac{1}{r}\frac{\partial\Phi^f}{\partial\theta}\hat{a}_\theta+\frac{1}{r\sin\theta}\frac{\partial\Phi^f}{\partial\phi}\hat{a}_\phi\right] \quad (2.30)$$

Comparing $\hat{a}_\theta$ and $\hat{a}_\phi$ components on both sides of (2.30)

$$\frac{1}{r}\frac{\partial^2F_r}{\partial r\partial\theta}=-\frac{\hat{z}}{r}\frac{\partial\Phi^f}{\partial\theta} \quad (2.31)$$

$$\frac{1}{r\sin\theta}\frac{\partial^2F_r}{\partial r\partial\phi}=-\frac{\hat{z}}{r\sin\theta}\frac{\partial\Phi^f}{\partial\phi} \quad (2.32)$$

From (2.31) and (2.32)

$$\frac{\partial^2F_r}{\partial r\partial\theta}=-\hat{z}\frac{\partial\Phi^f}{\partial\theta} \quad (2.33)$$

$$\frac{\partial^2F_r}{\partial r\partial\phi}=-\hat{z}\frac{\partial\Phi^f}{\partial\phi} \quad (2.34)$$

Equations (2.33) and (2.34) can be satisfied only if

$$-\hat{z}\Phi^f=\frac{\partial F_r}{\partial r} \quad (2.35)$$

For $\hat{a}_r$ component, (2.28) can be written as

$$F_r''-k^2F_r=M_r-\hat{z}\frac{\partial\Phi^f}{\partial r} \quad (2.36)$$

where $$F_r''=-\frac{1}{r^2\sin\theta}\left[\frac{\partial}{\partial\theta}\left(\sin\theta\frac{\partial F_r}{\partial\theta}\right)+\frac{1}{\sin\theta}\frac{\partial^2F_r}{\partial\phi^2}\right] \quad (2.37)$$

Substituting (2.37) into (2.36)

$$\frac{-1}{r^2\sin\theta}\left[\frac{\partial}{\partial\theta}\left(\sin\theta\frac{\partial F_r}{\partial\theta}\right)+\frac{1}{\sin\theta}\frac{\partial^2 F_r}{\partial\phi^2}\right]-k^2F_r=M_r-\hat{z}\frac{\partial\Phi^f}{\partial r} \tag{2.38}$$

Substituting (2.35) into (2.38)

$$\frac{-1}{r^2\sin\theta}\frac{\partial}{\partial\theta}\left(\sin\theta\frac{\partial F_r}{\partial\theta}\right)-\frac{1}{r^2\sin^2\theta}\frac{\partial^2 F_r}{\partial\phi^2}-k^2F_r=M_r+\frac{\partial^2 F_r}{\partial r^2} \tag{2.39}$$

Rearranging (2.39)

$$\frac{\partial^2 F_r}{\partial r^2}+\frac{1}{r^2\sin\theta}\frac{\partial}{\partial\theta}\left(\sin\theta\frac{\partial F_r}{\partial\theta}\right)+\frac{1}{r^2\sin^2\theta}\frac{\partial^2 F_r}{\partial\phi^2}+k^2F_r=-M_r \tag{2.40}$$

Dividing both sides of (2.40) by r gives

$$\frac{1}{r}\frac{\partial^2 F_r}{\partial r^2}+\frac{1}{r^3\sin\theta}\frac{\partial}{\partial\theta}\left(\sin\theta\frac{\partial F_r}{\partial\theta}\right)+\frac{1}{r^3\sin^2\theta}\frac{\partial^2 F_r}{\partial\phi^2}+\frac{k^2}{r}F_r=-\frac{M_r}{r} \tag{2.41}$$

For the general Laplacian operator

$$\nabla^2 t=\frac{1}{fgh}\left[\frac{\partial}{\partial u}\left(\frac{gh}{f}\frac{\partial t}{\partial u}\right)+\frac{\partial}{\partial v}\left(\frac{fh}{g}\frac{\partial t}{\partial v}\right)+\frac{\partial}{\partial w}\left(\frac{fg}{h}\frac{\partial t}{\partial w}\right)\right] \tag{2.42}$$

Therefore

$$\nabla^2\left(\frac{F_r}{r}\right)=\frac{1}{r^2\sin\theta}\left[\sin\theta\frac{\partial}{\partial r}\left(r^2\frac{\partial\left(F_r/r\right)}{\partial r}\right)\right]+\frac{1}{r^3\sin\theta}\frac{\partial}{\partial\theta}\left[\sin\theta\frac{\partial F_r}{\partial\theta}\right]+\frac{1}{r^3\sin^2\theta}\frac{\partial^2 F_r}{\partial\phi^2} \tag{2.43}$$

where,
$$\frac{1}{r^2\sin\theta}\left[\sin\theta\frac{\partial}{\partial r}\left(r^2\frac{\partial\left(F_r/r\right)}{\partial r}\right)\right]=\frac{1}{r}\frac{\partial^2 F_r}{\partial r^2} \tag{2.44}$$

Substituting (2.44) into (2.43)

$$\nabla^2\left(\frac{F_r}{r}\right)=\frac{1}{r}\frac{\partial^2 F_r}{\partial r^2}+\frac{1}{r^3\sin\theta}\frac{\partial}{\partial\theta}\left[\sin\theta\frac{\partial F_r}{\partial\theta}\right]+\frac{1}{r^3\sin^2\theta}\frac{\partial^2 F_r}{\partial\phi^2} \tag{2.45}$$

Substituting (2.45) into (2.41)

$$\nabla^2\left(\frac{F_r}{r}\right)+k^2\left(\frac{F_r}{r}\right)=-\frac{M_r}{r} \tag{2.46}$$

$$\Rightarrow\ \left(\nabla^2+k^2\right)\frac{F_r}{r}=-\frac{M_r}{r} \tag{2.47}$$

Equation (2.47) represents the Helmholtz equation. Corresponding Green's function equation for the delta source will be:

$$\left(\nabla^2+k^2\right)\frac{G_{M_r}^{Frp}}{r}=-\frac{\varepsilon}{r}\frac{\delta\left(r-r'\right)\delta\left(\theta-\theta'\right)\delta\left(\phi-\phi'\right)}{r'^2\sin\theta'} \tag{2.48}$$

where (r',θ',ϕ') represents the source coordinates and (r,θ,ϕ) represents observation coordinates. The general solutions to the Helmholtz equation can be constructed by forming linear combinations of elementary wave functions [66]. The most general form of the solutions is

$$G_{M_r}^{Frp}=\sum_{n=0}^{\infty}\sum_{m=-n}^{n}A_{nm1}P_n^m\left(\cos\theta\right)e^{jm\phi}\begin{cases}\hat{J}_n\left(kr'\right)\hat{H}_n^{(2)}\left(kr\right), & r>r'\\ \hat{H}_n^{(2)}\left(kr'\right)\hat{J}_n\left(kr\right), & r<r'\end{cases} \tag{2.49}$$

$$G_{M_r}^{Frh}=\sum_{n=0}^{\infty}\sum_{m=-n}^{n}P_n^m\left(\cos\theta\right)e^{jm\phi}\begin{cases}h_{nm1}\hat{J}_n(kr), & r\le a_{dr}\\ h_{nm2}\hat{H}_n^{(2)}(kr), & r\ge a_{dr}\end{cases} \tag{2.50}$$

where, A_{nm1}, h_{nm1} and h_{nm2} are the unknown constants. $P_n^m\left(\cos\theta\right)$ represents the associated Legendre function of first kind, $e^{jm\phi}$ represents harmonic function, $\hat{J}_n(kr)$ represents Bessel function and $\hat{H}_n^{(2)}(kr)$ represents outward travelling waves. Equation (2.49), (2.50) represent the particular and homogeneous solution respectively. First we determine the unknown constant A_{nm1} of the particular solution and homogenous part will be discussed later in this section.

2.3.1.1.1 Determination of $G_{M_r}^{F_{rp}}$

The general solution of Helmholtz equation consists of homogeneous and particular parts. In order to determine the particular solution corresponding to the problem, the unknown constant is to be determined. Substituting the general solution of the particular solution in the first term of (2.45) yields

$$\frac{1}{r}\frac{\partial^2 G_{M_r}^{F_{rp}}}{\partial r^2}=\frac{1}{r}\sum_{n=0}^{\infty}\sum_{m=-n}^{n}A_{nm1}P_n^m(\cos\theta)e^{jm\phi}\begin{cases}\hat{J}_n(kr')k^2\hat{H}_n^{(2)\prime\prime}(kr), & r>r'\\ \hat{H}_n^{(2)}(kr')k^2\hat{J}_n''(kr), & r<r'\end{cases} \tag{2.51}$$

The second term of (2.45) can be written as:

$$\frac{\partial}{\partial\theta}\left(\sin\theta\frac{\partial G_{M_r}^{F_{rp}}}{\partial\theta}\right)=\cos\theta\frac{dG_{M_r}^{F_{rp}}}{d\theta}+\sin\theta\frac{d^2G_{M_r}^{F_{rp}}}{d\theta^2} \tag{2.52}$$

where

$$\frac{d^2G_{M_r}^{F_{rp}}}{d\theta^2}=\sum_{n=0}^{\infty}\sum_{m=-n}^{n}A_{nm1}\frac{d^2P_n^m(\cos\theta)}{d\theta^2}e^{jm\phi}\begin{cases}\hat{J}_n(kr')\hat{H}_n^{(2)}(kr), & r>r'\\ \hat{H}_n^{(2)}(kr')\hat{J}_n(kr), & r<r'\end{cases} \tag{2.53}$$

where

$$\frac{d^2P_n^m(\cos\theta)}{d\theta^2}=\frac{dP_n^{m+1}(\cos\theta)}{d\theta}+\frac{m\cos\theta}{\sin\theta}\frac{dP_n^m(\cos\theta)}{d\theta}-\frac{m}{\sin^2\theta}P_n^m(\cos\theta) \tag{2.54}$$

Combining the second and third terms of (2.45) and substituting for the particular solution and simplifying

$$\begin{aligned}&\frac{1}{r^3\sin\theta}\frac{\partial}{\partial\theta}\left[\sin\theta\frac{\partial F_r}{\partial\theta}\right]+\frac{1}{r^3\sin^2\theta}\frac{\partial^2F_r}{\partial\phi^2}\\&=\sum_{n=0}^{\infty}\sum_{m=-n}^{n}A_{nm1}\frac{e^{jm\phi}}{r^3}\left[2(m+1)\frac{\cos\theta}{\sin\theta}P_n^{m+1}(\cos\theta)-m(m+1)P_n^m(\cos\theta)+P_n^{m+2}(\cos\theta)\right]\\&\qquad\cdot\begin{cases}\hat{J}_n(kr')\hat{H}_n^{(2)}(kr), & r>r'\\ \hat{H}_n^{(2)}(kr')\hat{J}_n(kr), & r<r'\end{cases}\end{aligned} \tag{2.55}$$

The first term of the RHS of (2.45) after simplification gives

$$\frac{1}{r}\frac{\partial^2 G_{M_r}^{F_{rp}}}{\partial r^2} = \frac{1}{r}\sum_{n=0}^{\infty}\sum_{m=-n}^{n} A_{nm1} P_n^m(\cos\theta)\cdot e^{jm\phi} \cdot\left[\hat{B}_{n-2}(kr) - \frac{2n-1}{kr}\hat{B}_{n-1}(kr) + \frac{n}{kr}\hat{B}_n(kr)\left(n+\frac{1}{kr}\right)\right] \tag{2.56}$$

where

$$\hat{B}_n(kr) = \begin{cases} \hat{J}_n(kr')\hat{H}_n^{(2)}(kr), & r > r' \\ \hat{H}_n^{(2)}(kr')\hat{J}_n(kr), & r < r' \end{cases} \tag{2.57}$$

Multiplying (2.48) by $P_n^m(\cos\theta)\cdot e^{-jm\phi} r\sin\theta$ and performing the volume integral

$$\int_{r'}\int_{\theta=0}^{\pi}\int_{\phi=0}^{2\pi}\left(\nabla^2+k^2\right)G_{M_r}^{Frp}P_n^m(\cos\theta)\cdot e^{-jm\phi}\sin\theta dr d\theta d\phi = \int_{r'}\int_{\theta=0}^{\pi}\int_{\phi=0}^{2\pi} -\varepsilon\frac{\delta(r-r')\delta(\theta-\theta')\delta(\phi-\phi')}{r'^2\sin\theta'}P_n^m(\cos\theta)\cdot e^{-jm\phi}\sin\theta dr d\theta d\phi \tag{2.58}$$

$$\Rightarrow \int_{r'}\int_{\theta=0}^{\pi}\int_{\phi=0}^{2\pi}\left(\nabla^2+k^2\right)G_{M_r}^{Frp}P_n^m(\cos\theta)\cdot e^{-jm\phi}\sin\theta dr d\theta d\phi = -\frac{\varepsilon}{r'^2}P_n^m\left(\cos\theta'\right)\cdot e^{-jm\phi'} \tag{2.59}$$

L.H.S. of (2.59) can be written as

$$\int_{r'}\int_{\theta=0}^{\pi}\int_{\phi=0}^{2\pi}\left(\nabla^2+k^2\right)G_{M_r}^{Frp}P_n^m(\cos\theta)\cdot e^{-jm\phi}\sin\theta dr d\theta d\phi = I_1 + I_2 \tag{2.60}$$

where

$$I_1 = \int_{r=r^-}^{r^+}\int_{\theta=0}^{\pi}\int_{\phi=0}^{2\pi} k\left[\frac{\partial^2 G_{M_r}^{Frp}}{\partial(kr)^2} + G_{M_r}^{Frp}\right]P_n^m(\cos\theta)\cdot e^{-jm\phi}\sin\theta dk r d\theta d\phi \tag{2.61}$$

and

$$I_2 = \int_{r=r^-}^{r^+}\int_{\theta=0}^{\pi}\int_{\phi=0}^{2\pi}\left[\frac{1}{r^2}\frac{\partial}{\partial\theta}\left(\sin\theta\frac{\partial G_{M_r}^{Frp}}{\partial\theta}\right) + \frac{1}{\sin\theta}\frac{\partial^2 G_{M_r}^{Frp}}{\partial\phi^2}\right]P_n^m(\cos\theta)\cdot e^{-jm\phi} dr d\theta d\phi \tag{2.62}$$

(2.61) and (2.62) can be simplified using the orthogonal relationships for the associated Legendre function [66]

$$\int_0^{\pi} P_n^m(\cos\theta) P_r^m(\cos\theta) \cdot \sin\theta \, d\theta = \frac{2}{(2n+1)} \frac{(n+m)!}{(n-m)!} \delta_{nr} \tag{2.63}$$

$$\int_0^{\pi} \frac{P_n^m(\cos\theta) P_n^r(\cos\theta)}{\sin\theta} \, d\theta = \begin{cases} \frac{1}{m} \frac{(n+m)!}{(n-m)!} \delta_{mr} \\ \infty \qquad \text{if } m = r = 0 \end{cases} \tag{2.64}$$

where, δ_{nr} is the Kronekar delta function and it is defined by,

$$\delta_{nr} = \begin{cases} 1 & n = r \\ 0 & \text{Otherwise} \end{cases} \tag{2.65}$$

Using (2.63) and (2.64)

$$I_1 = A_{nm1} \frac{4\pi k}{(2n+1)} \frac{(n+m)!}{(n-m)!} \int_{x=x^-}^{x^+} \left[\frac{d^2 \hat{B}_n(x)}{dx^2} + \hat{B}_n(x) \right] dx \tag{2.66}$$

$$I_1 = A_{nm1} \frac{4\pi k}{(2n+1)} \frac{(n+m)!}{(n-m)!} \left[\int_{x=x^-}^{x^+} \frac{d^2 \hat{B}_n(x)}{dx^2} + \int_{x=x^-}^{x^+} \hat{B}_n(x) \right] dx \tag{2.67}$$

Second integral in (2.67) vanishes over the given limits, since it is a continuous function of x. Hence (2.67) reduces to

$$I_1 = A_{nm1} \frac{4\pi k}{(2n+1)} \frac{(n+m)!}{(n-m)!} \left[\hat{B}_n'(x) \right]_{x=x^-}^{x^+} \tag{2.68}$$

$$I_1 = A_{nm1} \frac{4\pi k}{(2n+1)} \frac{(n+m)!}{(n-m)!} \left[\hat{J}_n(kr') \hat{H}_n^{(2)\prime}(kr') - \hat{J}_n'(kr') \hat{H}_n^{(2)}(kr') \right] \tag{2.69}$$

Using the Wronskian of spherical Bessel's function

$$\hat{J}_n\left(kr'\right)\hat{H}_n^{(2)\prime}\left(kr'\right)-\hat{J}_n'\left(kr'\right)\hat{H}_n^{(2)}\left(kr'\right)=-j \tag{2.70}$$

Equation (2.69) becomes

$$I_1=-j\cdot A_{nm1}\frac{4\pi k}{(2n+1)}\frac{(n+m)!}{(n-m)!} \tag{2.71}$$

Employing the orthogonal relationship for the trigonometric function and simplifying, equation (2.62) reduces to

$$I_2=2\pi\sum_{n=0}^{\infty}A_{nm1}\int_{r=r^{-'}}^{r^{+'}}\frac{\hat{B}_n(kr)}{r^2}dr\int_{\theta=0}^{\pi}\left[\frac{d}{d\theta}\left(\sin\theta\frac{dP_n^m(\cos\theta)}{d\theta}\right)-\frac{m^2}{\sin\theta}P_n^m(\cos\theta)\right]d\theta \tag{2.72}$$

Since $\frac{\hat{B}_n(kr)}{r^2}$ is a discontinuous function at $r=r'$, its integral will be continuous at $r=r'$ and the integral when evaluated over the limits $r^{-'}$ to $r^{+'}$ will be zero and I_2 will become zero.

$$I_2=0 \tag{2.73}$$

Substituting (2.71) and (2.73) into (2.60)

$$-j\cdot A_{nm1}\frac{4\pi k}{(2n+1)}\frac{(n+m)!}{(n-m)!}=-\frac{\varepsilon}{r'^2}P_n^m\left(\cos\theta'\right)\cdot e^{-jm\phi'} \tag{2.74}$$

$$\Rightarrow A_{nm1}=-j\frac{(2n+1)(n-m)!}{4\pi k(n+m)!}\frac{\varepsilon}{r'^2}P_n^m\left(\cos\theta'\right)\cdot e^{-jm\phi'} \tag{2.75}$$

Substituting (2.75) into (2.49) and simplifying,

$$G_{M_r}^{F_{rp}}=\frac{1}{r'^2}\sum_{n=0}^{\infty}\sum_{m=0}^{n}g_{nm}P_n^m(\cos\theta)P_n^m\left(\cos\theta'\right)\cdot\cos m\left(\phi-\phi'\right)\begin{cases}\hat{J}_n\left(kr'\right)\hat{H}_n^{(2)}(kr), & r>r'\\ \hat{H}_n^{(2)}\left(kr'\right)\hat{J}_n(kr), & r<r'\end{cases} \tag{2.76}$$

where $$g_{nm} = \frac{-j\varepsilon}{2\pi k}\frac{(2n+1)(n-m)!}{\Delta_m (n+m)!} \tag{2.77}$$

and $$\Delta_m = \begin{cases} 1 & \text{if } m \geq 1 \\ 2 & \text{if } m = 0 \end{cases} \tag{2.78}$$

2.3.1.1.2 Determination of $G_{M_r}^{F_{rh}}$

Considering the homogeneous solution, the unknowns h_{nm1} and h_{nm2} of (2.50) can be determined using the continuity of electric and magnetic fields at the spherical surface of the DRA. The boundary conditions of the tangential components of the electric and magnetic fields at the surface of the DRA can be written as:

$$E_{\theta 1i} + E_{\theta 1s} = E_{\theta 2s} \tag{2.79}$$

$$E_{\phi 1i} + E_{\phi 1s} = E_{\phi 2s} \tag{2.80}$$

$$H_{\theta 1i} + H_{\theta 1s} = H_{\theta 2s} \tag{2.81}$$

$$H_{\phi 1i} + H_{\phi 1s} = H_{\phi 2s} \tag{2.82}$$

where the subscript '1' represents inside the DRA and '2' represents outside the DRA. The subscripts *i*, *s* represents the incident and scattered fields respectively. Various field components can be evaluated from potential Green's functions using equations (2.83) to (2.88) [66].

$$E_r = \frac{1}{\hat{y}}\left(\frac{\partial^2}{\partial r^2} + k^2\right) A_r \tag{2.83}$$

$$E_\theta = \frac{-1}{r\sin\theta}\frac{\partial F_r}{\partial \phi} + \frac{1}{\hat{y} r}\frac{\partial^2 A_r}{\partial r \partial \theta} \tag{2.84}$$

$$E_\phi = \frac{1}{r}\frac{\partial F_r}{\partial \theta} + \frac{1}{\hat{y} r \sin\theta}\frac{\partial^2 A_r}{\partial r \partial \phi} \tag{2.85}$$

$$H_r = \frac{1}{\hat{z}}\left(\frac{\partial^2}{\partial r^2} + k^2\right)F_r \tag{2.86}$$

$$H_\theta = \frac{1}{r\sin\theta}\frac{\partial A_r}{\partial \phi} + \frac{1}{\hat{z}r}\frac{\partial^2 F_r}{\partial r \partial \theta} \tag{2.87}$$

$$H_\phi = -\frac{1}{r}\frac{\partial A_r}{\partial \theta} + \frac{1}{\hat{z}r\sin\theta}\frac{\partial^2 F_r}{\partial r \partial \phi} \tag{2.88}$$

When $A_r = 0$, and only F_r exists, the field is transverse electric, TE to r. When $F_r = 0$ and only A_r exists, the field is transverse magnetic, TM to r. Using (2.84) in (2.79)

$$-\frac{1}{a_{dr}\sin\theta}\frac{\partial\left(G_{M_r}^{Frp}\right)}{\partial\phi}\Big|(r > r') - \frac{1}{a_{dr}\sin\theta}\frac{\partial\left(G_{M_r}^{Frh}\right)}{\partial\phi}\Big|(r \le a_{dr}) = \frac{1}{a_{dr}\sin\theta}\frac{\partial\left(G_{M_r}^{Frh}\right)}{\partial\phi}\Big|(r > a_{dr}) \tag{2.89}$$

Substituting for $G_{M_r}^{Frp}$ *and* $G_{M_r}^{Frh}$ from (2.76) and (2.50), the boundary condition becomes

$$\text{L.H.S.} = \frac{1}{r'^2}\sum_{n=0}^{\infty}\sum_{m=0}^{n} g_{nm} P_n^m(\cos\theta) P_n^m(\cos\theta') \cdot \frac{\partial}{\partial\phi}\cos m(\phi - \phi')\hat{J}_n(kr')\hat{H}_n^{(2)}(ka_{dr}) + \sum_{n=0}^{\infty}\sum_{m=-n}^{n} P_n^m(\cos\theta)\frac{\partial}{\partial\phi}e^{jm\phi} h_{nm1}\,\hat{J}_n(ka_{dr}) \tag{2.90}$$

$$\text{R.H.S.} = \sum_{n=0}^{\infty}\sum_{m=-n}^{n} P_n^m(\cos\theta)\frac{\partial}{\partial\phi}e^{jm\phi} h_{nm2}\,\hat{H}_n^{(2)}(k_0 a_{dr}) \tag{2.91}$$

Using (2.90) and (2.91) in (2.89)

$$\sum_{n=0}^{\infty}\left[\frac{1}{2r'^2}\; g_{nm} P_n^m(\cos\theta) P_n^m(\cos\theta')\, e^{-jm\phi'}\, jm\,\hat{J}_n(kr')\hat{H}_n^{(2)}(ka_{dr}) + P_n^m(\cos\theta)\, jm\, h_{nm1}\,\hat{J}_n(ka_{dr})\right] = \sum_{n=0}^{\infty}\left[P_n^m(\cos\theta)\, jm\; h_{nm2}\,\hat{H}_n^{(2)}(k_0 a_{dr})\right] \tag{2.92}$$

In the boundary condition (2.80), substituting for the electric field using (2.85)

$$\sum_{n=0}^{\infty}\left[\frac{1}{2r'^2}\ \mathrm{g}_{nm}\frac{\partial}{\partial\theta}P_n^m(\cos\theta)P_n^m(\cos\theta')\ e^{-jm\phi'}\ \hat{J}_n(kr')\hat{H}_n^{(2)}(ka_{dr})\right.$$
$$\left.+\frac{\partial}{\partial\theta}P_n^m(\cos\theta)\ h_{nm1}\hat{J}_n(ka_{dr})\right]=\sum_{n=0}^{\infty}\left[\frac{\partial}{\partial\theta}P_n^m(\cos\theta)h_{nm2}\hat{H}_n^{(2)}(k_0a_{dr})\right] \tag{2.93}$$

Substituting for the θ component of the magnetic field using (2.87) in the boundary condition equation, (2.81)

$$\frac{1}{\hat{z}}\sum_{n=0}^{\infty}\left[\frac{1}{2r'^2}\ \mathrm{g}_{nm}\frac{\partial}{\partial\theta}P_n^m(\cos\theta)P_n^m(\cos\theta')\ e^{-jm\phi'}\ \hat{J}_n(kr')\hat{H}_n^{(2)}(ka_{dr})\right.$$
$$\left.+\frac{\partial}{\partial\theta}P_n^m(\cos\theta)\ kh_{nm1}\hat{J}_n'(ka_{dr})\right]=\frac{1}{\hat{z}_0}\sum_{n=0}^{\infty}\left[\frac{\partial}{\partial\theta}P_n^m(\cos\theta)h_{nm2}\,k_0\hat{H}_n^{(2)\prime}(k_0a_{dr})\right] \tag{2.94}$$

Substituting (2.88) in (2.82)

$$\frac{1}{\hat{z}\sin\theta}\sum_{n=0}^{\infty}\left[\frac{1}{2r'^2}\ \mathrm{g}_{nm}P_n^m(\cos\theta)P_n^m(\cos\theta')\,jm\ e^{-jm\phi'}k\ \hat{J}_n(kr')\hat{H}_n^{(2)}(ka_{dr})\right.$$
$$\left.+P_n^m(\cos\theta)\,jmkh_{nm1}\hat{J}_n'(ka_{dr})\right]=\frac{1}{\hat{z}_0\sin\theta}\sum_{n=0}^{\infty}\left[\frac{\partial}{\partial\theta}P_n^m(\cos\theta)jmh_{nm2}\,k_0\hat{H}_n^{(2)\prime}(k_0a_{dr})\right] \tag{2.95}$$

To determine the unknowns, h_{nm1} and h_{nm2}, (2.92) to (2.95) are to be simplified. Simplification can be done by employing the properties of associated Legendre function and trigonometric functions, given by (2.96) and (2.97).

$$\int_0^{\pi}\left[\frac{d\left(P_l^m(\cos\theta)\right)}{d\theta}.P_n^m(\cos\theta)+\frac{d\left(P_n^m(\cos\theta)\right)}{d\theta}.\left(P_l^m(\cos\theta)\right)\right]d\theta=0 \tag{2.96}$$

$$\int_0^{\pi}\left[\frac{d\left(P_n^m(\cos\theta)\right)}{d\theta}\frac{d\left(P_l^m(\cos\theta)\right)}{d\theta}+\frac{m^2}{\sin^2\theta}P_n^m(\cos\theta)P_l^m(\cos\theta)\right]\sin\theta d\theta$$
$$=\begin{cases}\dfrac{2}{(2n+1)}\dfrac{(n-m)}{(n+m)}n(n+1)\ , & \text{for } n=l\\ 0\ , & \text{for } n\neq l\end{cases} \tag{2.97}$$

$$\frac{(2n+1)}{2n(n+1)}\frac{(n-m)!}{(n+m)!}\int_0^{\pi}\left[\frac{\partial}{\partial\theta}P_r^m(\cos\theta)\times equation(2.92)+equation(2.93)\times\frac{m^2}{\sin^2\theta}\right]\sin\theta\,d\theta$$

$$\Rightarrow\frac{1}{2r'^2}g_{nm}P_n^m(\cos\theta')e^{-jm\phi'}\hat{J}_n(kr')\hat{H}_n^{(2)}(ka_{dr})+h_{nm1}\hat{J}_n'(ka)=h_{nm2}\hat{H}_n^{(2)}(k_0a_{dr}) \qquad (2.98)$$

Similarly

$$\frac{(2n+1)}{2n(n+1)}\frac{(n-m)!}{(n+m)!}\int_0^{\pi}\left[\frac{\partial}{\partial\theta}P_r^m(\cos\theta)\times equation(2.94)+equation(2.95)\times\frac{m^2}{\sin^2\theta}\right]\sin\theta\,d\theta$$

$$\Rightarrow\ \frac{1}{\hat{z}}\frac{1}{2r'^2}g_{nm}P_n^m(\cos\theta')e^{-jm\phi'}\hat{J}_n(kr')k\hat{H}_n^{(2)\prime}(ka_{dr})+h_{nm1}k\hat{J}_n'(ka_{dr})$$

$$=\frac{1}{\hat{z}_0}h_{nm2}k_0\hat{H}_n^{(2)\prime}(k_0a_{dr}) \qquad (2.99)$$

h_{nm1} can be extracted from (2.98) and (2.99). Since we are interested in the computation of reflection coefficient only, homogeneous part of the Green's function for $r\le a_{dr}$ is only needed. Homogeneous part of the Green's function for $r\le a_{dr}$ is:

$$G_{M_r}^{F_{rh}}=\frac{1}{r'^2}\sum_{n=0}^{\infty}\sum_{m=0}^{n}h_{nm}P_n^m(\cos\theta')P_n^m(\cos\theta)\cos m(\phi-\phi')\hat{J}_n(kr')\hat{J}_n(kr) \qquad (2.100)$$

where

$$h_{nm}=\frac{-g_{nm}}{\Delta_n^{TE}}\left[\hat{H}_n^{(2)}(ka_{dr})\hat{H}_n^{(2)\prime}(k_0a_{dr})-\frac{k}{k_0}\hat{H}_n^{(2)\prime}(ka_{dr})\hat{H}_n^{(2)}(k_0a_{dr})\right] \qquad (2.101)$$

and

$$\Delta_n^{TE}=\hat{J}_n(ka_{dr})\hat{H}_n^{(2)\prime}(k_0a_{dr})-\frac{k}{k_0}\hat{J}_n'(ka_{dr})\hat{H}_n^{(2)}(k_0a_{dr}) \qquad (2.102)$$

$\Delta_n^{TE}=0$ represents the characteristic equation of the transverse electric mode. Resonant frequency of the DRA can be obtained by solving the characteristic equation.

2.3.1.2 Determination of $G_{M_\phi}^{F_{rp}}$ and $G_{M_\phi}^{A_{rp}}$

The particular solutions due to ϕ directed current (first parts of (2.18) and (2.19)) are solved in this section. The homogenous parts will be solved in the next section. As in the previous case, particular solutions are assumed as:

$$G_{M_\phi}^{F_{rp}} = \sum_{n=0}^{\infty}\sum_{m=-n}^{n} A_{nm} P_n^m(\cos\theta) e^{jm\phi} \begin{cases} \hat{J}_n(kr')\hat{H}_n^{(2)}(kr), & r > r' \\ \hat{H}_n^{(2)}(kr')\hat{J}_n(kr), & r < r' \end{cases} \tag{2.103}$$

$$G_{M_\phi}^{A_{rp}} = \sum_{n=0}^{\infty}\sum_{m=-n}^{n} D_{nm} P_n^m(\cos\theta) e^{jm\phi} \begin{cases} \hat{J}_n(kr')\hat{H}_n^{(2)'}(kr), & r > r' \\ \hat{H}_n^{(2)}(kr')\hat{J}_n'(kr), & r < r' \end{cases} \tag{2.104}$$

The coefficients A_{nm} and D_{nm} can be solved by matching the boundary conditions at the source point. H_θ, H_ϕ and E_ϕ are continuous at $r=r'$, while, E_θ is discontinuous by the surface magnetic current $M_{\phi s}$. The boundary conditions at the source point can be written as:

$$H_{\theta 1} = H_{\theta 2} \tag{2.105}$$

$$H_{\phi 1} = H_{\phi 2} \tag{2.106}$$

$$E_{\phi 1} = E_{\phi 2} \tag{2.107}$$

$$E_{\theta 1} - E_{\theta 2} = M_{\phi s} \tag{2.108}$$

Using (2.103) and (2.104) in (2.85) and substituting in (2.107) at $r=r'$ gives:

$$\frac{1}{r'}\sum_{n=0}^{\infty}\sum_{m=-n}^{n}A_{nm}\frac{\partial}{\partial\theta}P_n^m(\cos\theta)e^{jm\phi}\hat{H}_n^{(2)\prime}(kr')\hat{J}_n(kr')$$
$$+\frac{1}{\hat{y}r'\sin\theta}\sum_{n=0}^{\infty}\sum_{m=-n}^{n}D_{nm}P_n^m(\cos\theta)\,jme^{jm\phi}\hat{H}_n^{(2)}(kr')k\hat{J}_n'(kr')$$
$$=\frac{1}{r'}\sum_{n=0}^{\infty}\sum_{m=-n}^{n}A_{nm}\frac{\partial}{\partial\theta}P_n^m(\cos\theta)e^{jm\phi}\hat{J}_n'(kr')\hat{H}_n^{(2)}(kr')$$
$$+\frac{1}{\hat{y}r'\sin\theta}\sum_{n=0}^{\infty}\sum_{m=-n}^{n}D_{nm}P_n^m(\cos\theta)\,jme^{jm\phi}\hat{J}_n(kr')k\hat{H}_n^{(2)\prime}(kr') \qquad (2.109)$$

To eliminate ϕ and one of the summations in (2.109), orthogonal property of the trigonometric function $e^{jm\phi}$ is used.

$$\frac{1}{r'}\sum_{n=0}^{\infty}A_{nm}\frac{\partial}{\partial\theta}P_n^m(\cos\theta)\hat{H}_n^{(2)\prime}(kr')\hat{J}_n(kr')$$
$$+\frac{1}{\hat{y}r'\sin\theta}\sum_{n=0}^{\infty}D_{nm}P_n^m(\cos\theta)\,jm\hat{H}_n^{(2)}(kr')k\hat{J}_n'(kr')$$
$$=\frac{1}{r'}\sum_{n=0}^{\infty}A_{nm}\frac{\partial}{\partial\theta}P_n^m(\cos\theta)\hat{J}_n'(kr')\hat{H}_n^{(2)}(kr')$$
$$+\frac{1}{\hat{y}r'\sin\theta}\sum_{n=0}^{\infty}D_{nm}P_n^m(\cos\theta)\,jm\hat{J}_n(kr')k\hat{H}_n^{(2)\prime}(kr') \qquad (2.110)$$

Using (2.103) and (2.104) in (2.84) and substituting in (2.108)

$$\frac{1}{r'\sin\theta}\sum_{n=0}^{\infty}A_{nm}P_n^m(\cos\theta)\,jm\hat{H}_n^{(2)\prime}(kr')\hat{J}_n(kr')+\frac{1}{\hat{y}r'}\sum_{n=0}^{\infty}D_{nm}\frac{\partial}{\partial\theta}P_n^m(\cos\theta)\hat{H}_n^{(2)}(kr')k\hat{J}_n'(kr')$$
$$=\frac{-1}{r'\sin\theta}\sum_{n=0}^{\infty}A_{nm}jmP_n^m(\cos\theta)\hat{J}_n'(kr')\hat{H}_n^{(2)}(kr')$$
$$+\frac{1}{\hat{y}r'}\sum_{n=0}^{\infty}D_{nm}\frac{\partial}{\partial\theta}P_n^m(\cos\theta)\,jme^{jm\phi}\hat{J}_n(kr')k\hat{H}_n^{(2)\prime}(kr')+\frac{1}{2\pi}\int_0^{2\pi}M_{\phi s}e^{-jm\phi}d\phi \qquad (2.111)$$

Equations (2.110) and (2.111) can be simplified to obtain D_{nm} using the properties of associated Legendre functions and trigonometric functions given by (2.96) and (2.97).

$$\int_0^{\pi}\left[\frac{d}{d\theta}\left[P_r^m(\cos\theta)\right]\times j.(2.111)+\frac{m}{\sin\theta}P_r^m(\cos\theta)\times(2.110)\right]$$

$$=\frac{m}{r'\sin\theta}\sum_{n=0}^{\infty}A_{nm}\left(P_n^m(\cos\theta)\frac{d\left[P_l^m(\cos\theta)\right]}{d\theta}+P_l^m(\cos\theta)\frac{d\left[P_n^m(\cos\theta)\right]}{d\theta}\right)\hat{H}_n^{(2)\prime}(kr')\hat{J}_n(kr')$$

$$-\frac{m}{r'\sin\theta}\sum_{n=0}^{\infty}A_{nm}\left(P_n^m(\cos\theta)\frac{d\left[P_l^m(\cos\theta)\right]}{d\theta}+P_l^m(\cos\theta)\frac{d\left[P_n^m(\cos\theta)\right]}{d\theta}\right)\hat{H}_n^{(2)}(kr')\hat{J}'_n(kr')$$

$$+\frac{jk}{\hat{y}r'}\sum_{n=0}^{\infty}D_{nm}\left(\frac{d\left[P_n^m(\cos\theta)\right]}{d\theta}\frac{d\left[P_l^m(\cos\theta)\right]}{d\theta}+\frac{m^2}{\sin^2\theta}P_n^m(\cos\theta)P_l^m(\cos\theta)\right)\hat{H}_n^{(2)}(kr')\hat{J}'_n(kr')$$

$$-\frac{jk}{\hat{y}r'}\sum_{n=0}^{\infty}D_{nm}\left(\frac{d\left[P_n^m(\cos\theta)\right]}{d\theta}\frac{d\left[P_l^m(\cos\theta)\right]}{d\theta}+\frac{m^2}{\sin^2\theta}P_n^m(\cos\theta)P_l^m(\cos\theta)\right)\hat{H}_n^{(2)\prime}(kr')\hat{J}_n(kr')$$

$$=\frac{j}{2\pi}\int_0^{2\pi}\frac{d\left[P_l^m(\cos\theta)\right]}{d\theta}M_{\phi s}e^{-jm\phi}d\phi \tag{2.112}$$

$$\Rightarrow\quad\frac{k}{\hat{y}r'}D_{nm}\frac{2}{2n+1}\frac{(n+m)!}{(n-m)!}n(n+1)\left[\hat{H}_n^{(2)}(kr')\hat{J}'_n(kr')-\hat{H}_n^{(2)\prime}(kr')\hat{J}_n(kr')\right]$$

$$=\frac{1}{2\pi}\int_0^{\pi}\int_0^{2\pi}M_{\phi s}\frac{d\left[P_l^m(\cos\theta)\right]}{d\theta}\sin\theta e^{-jm\phi}d\theta d\phi \tag{2.113}$$

Using (2.70) in (2.113) gives

$$\frac{k}{\omega\varepsilon r'}D_{nm}\frac{2}{(2n+1)}\frac{(n+m)!}{(n-m)!}n(n+1)=\frac{1}{2\pi}\int_0^{\pi}\int_0^{2\pi}M_{\phi s}\frac{d\left[P_l^m(\cos\theta)\right]}{d\theta}\sin\theta e^{-jm\phi}d\theta d\phi \tag{2.114}$$

where $M_{\phi s}$ is the point sheet of magnetic current located at (r',θ',ϕ') and is given by

$$M_{\phi s}=\frac{\delta(\phi-\phi')\delta(\theta-\theta')}{r'^2\sin\theta'} \tag{2.115}$$

Substituting (2.115) in (2.114) and simplifying

$$D_{nm}=\frac{k}{r'4\pi\omega}\frac{(2n+1)}{n(n+1)}\frac{(n-m)!}{(n+m)!}\frac{d\left[P_n^m(\cos\theta')\right]}{d\theta'}e^{-jm\phi'} \tag{2.116}$$

Similarly A_{nm} can be obtained by performing the following operation

$$\int_0^{\pi}\left[\frac{d}{d\theta}\left[P_r^m(\cos\theta)\right]\times j.(2.110)-\frac{m}{\sin\theta}P_r^m(\cos\theta)\times(2.111)\right]$$

$$=\frac{j}{r'}\sum_{n=0}^{\infty}A_{nm}\left(\frac{d\left[P_n^m(\cos\theta)\right]}{d\theta}\frac{d\left[P_l^m(\cos\theta)\right]}{d\theta}+\frac{m^2}{\sin^2\theta}P_n^m(\cos\theta)P_l^m(\cos\theta)\right)\hat{H}_n^{(2)\prime}(kr')\hat{J}_n(kr')$$

$$-\frac{j}{r'}\sum_{n=0}^{\infty}A_{nm}\left(\frac{d\left[P_n^m(\cos\theta)\right]}{d\theta}\frac{d\left[P_l^m(\cos\theta)\right]}{d\theta}+\frac{m^2}{\sin^2\theta}P_n^m(\cos\theta)P_l^m(\cos\theta)\right)\hat{H}_n^{(2)}(kr')\hat{J}_n'(kr')$$

$$-\frac{mk}{r'\sin\theta}\sum_{n=0}^{\infty}D_{nm}\left(P_n^m(\cos\theta)\frac{d\left[P_l^m(\cos\theta)\right]}{d\theta}+P_l^m(\cos\theta)\frac{d\left[P_n^m(\cos\theta)\right]}{d\theta}\right)\hat{H}_n^{(2)}(kr')\hat{J}_n'(kr')$$

$$+\frac{mk}{r'\sin\theta}\sum_{n=0}^{\infty}D_{nm}\left(P_n^m(\cos\theta)\frac{d\left[P_l^m(\cos\theta)\right]}{d\theta}+P_l^m(\cos\theta)\frac{d\left[P_n^m(\cos\theta)\right]}{d\theta}\right)\hat{H}_n^{(2)\prime}(kr')\hat{J}_n(kr')$$

$$=\frac{1}{2\pi}\int_{\phi=0}^{2\pi}M_{\phi s}P_l^m(\cos\theta)\frac{m}{\sin\theta}e^{-jm\phi}d\phi \qquad (2.117)$$

$$\Rightarrow\quad \frac{j}{r'}A_{nm}\frac{2}{2n+1}\frac{(n+m)!}{(n-m)!}n(n+1)\left[\hat{H}_n^{(2)\prime}(kr')\hat{J}_n(kr')-\hat{H}_n^{(2)}(kr')\hat{J}_n'(kr')\right]$$

$$=\frac{m}{2\pi}\int_0^{\pi}\int_0^{2\pi}M_{\phi s}P_l^m(\cos\theta)e^{-jm\phi}d\theta d\phi \qquad (2.118)$$

Using (2.70) in (2.118) gives

$$\frac{1}{r'}A_{nm}\frac{2}{(2n+1)}\frac{(n+m)!}{(n-m)!}n(n+1)=\frac{m}{2\pi}\int_0^{\pi}\int_0^{2\pi}M_{\phi s}P_l^m(\cos\theta)e^{-jm\phi}d\theta d\phi \qquad (2.119)$$

Substituting (2.115) in (2.119) and simplifying,

$$A_{nm}=\frac{\varepsilon}{r'\sin\theta' 4\pi}\frac{2n+1}{n(n+1)}\frac{(n-m)!}{(n+m)!}mP_n^m(\cos\theta')e^{-jm\phi'} \qquad (2.120)$$

Substituting for A_{nm} and D_{nm} in (2.103) and (2.104)

$$G_{M_\phi}^{Frp} = \frac{1}{r' \sin\theta'} \sum_{n=1}^{\infty} \sum_{m=1}^{n} a_{nm} P_n^m(\cos\theta) P_n^m(\cos\theta') \sin m(\phi - \phi') \begin{cases} \hat{J}_n'(kr') \hat{H}_n^{(2)}(kr), & r > r' \\ \hat{H}_n^{(2)\prime}(kr') \hat{J}_n(kr), & r < r' \end{cases} \quad (2.121)$$

$$G_{M_\phi}^{Arp} = \frac{1}{r'} \sum_{n=1}^{\infty} \sum_{m=0}^{n} d_{nm} P_n^m(\cos\theta) \frac{d}{d\theta'} P_n^m(\cos\theta') \cos m(\phi - \phi') \begin{cases} \hat{J}_n(kr') \hat{H}_n^{(2)}(kr), & r > r' \\ \hat{H}_n^{(2)}(kr') \hat{J}_n(kr), & r < r' \end{cases} \quad (2.122)$$

where

$$a_{nm} = \frac{-j\varepsilon}{2\pi} \frac{2n+1}{n(n+1)} \frac{(n-m)!}{(n+m)!} m \quad (2.123)$$

$$d_{nm} = \frac{\omega \mu_0 \varepsilon}{\Delta_m 2\pi k} \frac{2n+1}{n(n+1)} \frac{(n-m)!}{(n+m)!} \quad (2.124)$$

2.3.1.3 Determination of $G_{M_\phi}^{Frh}$ and $G_{M_\phi}^{Arh}$

In this section homogenous solutions due to ϕ directed current (second parts of (2.18) and (2.19)) are to be determined. Homogenous solutions are assumed to be linear combinations of the elementary wave functions as described in the previous section. The most general form of the solutions commonly used over possible values of *m* and *n* are:

$$G_{M_\phi}^{Frh} = \sum_{n=0}^{\infty} \sum_{m=-n}^{n} P_n^m(\cos\theta) e^{jm\phi} \begin{cases} B_{nm} \hat{J}_n(kr), & r \le a_{dr} \\ C_{nm} \hat{H}_n^{(2)}(kr), & r \ge a_{dr} \end{cases} \quad (2.125)$$

$$G_{M_\phi}^{Arh} = \sum_{n=0}^{\infty} \sum_{m=-n}^{n} P_n^m(\cos\theta) e^{jm\phi} \begin{cases} E_{nm} \hat{J}_n(kr), & r \le a_{dr} \\ F_{nm} \hat{H}_n^{(2)}(kr), & r \ge a_{dr} \end{cases} \quad (2.126)$$

To determine the unknowns B_{nm}, C_{nm}, E_{nm} and F_{nm}, field matching equations (2.79) to (2.82) are used. Using (2.125) and (2.126) in (2.84) and substituting in (2.79) gives

$$\frac{-1}{\sin\theta}\frac{1}{r'\sin\theta}\sum_{n=0}^{\infty}a_{nm}P_n^m(\cos\theta)P_n^m(\cos\theta')\,jme^{-jm\phi'}\hat{H}_n^{(2)}(ka_{dr})\hat{J}_n'(kr')$$
$$+\frac{1}{\hat{y}r'}\sum_{n=0}^{\infty}d_{nm}\frac{d}{d\theta}\left[P_n^m(\cos\theta)\right]\frac{d}{d\theta'}\left[P_n^m(\cos\theta')\right]e^{-jm\phi'}\hat{J}_n(kr')k\hat{H}_n^{(2)\prime}(ka_{dr})$$
$$-\frac{-1}{\sin\theta}\sum_{n=0}^{\infty}B_{nm}P_n^m(\cos\theta)\,jm\,\hat{J}_n(ka_{dr})+\frac{1}{\hat{y}}\sum_{n=0}^{\infty}E_{nm}\frac{d}{d\theta}\left[P_n^m(\cos\theta)\right]k\hat{J}_n(ka_{dr})$$
$$=-\frac{-1}{\sin\theta}\sum_{n=0}^{\infty}C_{nm}P_n^m(\cos\theta)\,jm\,\hat{H}_n^{(2)}(ka_{dr})+\frac{1}{\hat{y}_0}\sum_{n=0}^{\infty}F_{nm}\frac{d}{d\theta}\left[P_n^m(\cos\theta)\right]k_0\hat{H}_n^{(2)\prime}(ka_{dr}) \qquad (2.127)$$

Using (2.125) and (2.126) in (2.85) and substituting in (2.80) gives

$$\frac{1}{r'\sin\theta}\sum_{n=0}^{\infty}a_{nm}\frac{d}{d\theta}P_n^m(\cos\theta)P_n^m(\cos\theta')e^{-jm\phi'}\hat{H}_n^{(2)}(ka_{dr})\hat{J}_n'(kr')$$
$$+\frac{1}{\hat{y}r'\sin\theta}\sum_{n=0}^{\infty}d_{nm}P_n^m(\cos\theta)\frac{d}{d\theta'}\left[P_n^m(\cos\theta')\right]jme^{-jm\phi'}\hat{J}_n(kr')\cdot k\hat{H}_n^{(2)\prime}(ka_{dr})$$
$$+\sum_{n=0}^{\infty}B_{nm}\frac{d}{d\theta}P_n^m(\cos\theta)\hat{J}_n(ka_{dr})+\frac{1}{\hat{y}\sin\theta}\sum_{n=0}^{\infty}E_{nm}\cdot jm\cdot P_n^m(\cos\theta)k\cdot\hat{J}_n'(ka_{dr})$$
$$=\sum_{n=0}^{\infty}C_{nm}\frac{d}{d\theta}P_n^m(\cos\theta)\,\hat{H}_n^{(2)}(ka_{dr})+\frac{1}{\hat{y}_0\sin\theta}\sum_{n=0}^{\infty}F_{nm}\cdot jm\cdot P_n^m(\cos\theta)k_0\hat{H}_n^{(2)\prime}(ka_{dr}) \qquad (2.128)$$

Using (2.125) and (2.126) in (2.87) and substituting in (2.81) gives

$$\frac{1}{r'\sin\theta}\sum_{n=0}^{\infty}d_{nm}\frac{d}{d\theta'}P_n^m(\cos\theta')P_n^m(\cos\theta)\cdot jm\cdot e^{-jm\phi'}\hat{H}_n^{(2)}(ka_{dr})\hat{J}_n(kr')$$
$$+\frac{1}{\hat{z}r'\sin\theta'}\sum_{n=0}^{\infty}a_{nm}P_n^m(\cos\theta')\frac{d}{d\theta}\left[P_n^m(\cos\theta)\right]e^{-jm\phi'}\hat{J}_n'(kr')\cdot k\hat{H}_n^{(2)\prime}(ka_{dr})$$
$$+\frac{1}{\sin\theta}\sum_{n=0}^{\infty}E_{nm}\cdot jm\cdot P_n^m(\cos\theta)\hat{J}_n(ka_{dr})+\frac{1}{\hat{z}}\sum_{n=0}^{\infty}B_{nm}\frac{d}{d\theta}P_n^m(\cos\theta)k\cdot\hat{J}_n'(ka_{dr})$$
$$=\frac{1}{\sin\theta}\sum_{n=0}^{\infty}F_{nm}\cdot jm\cdot P_n^m(\cos\theta)\,\hat{H}_n^{(2)}(ka_{dr})+\frac{1}{\hat{z}}\sum_{n=0}^{\infty}C_{nm}\frac{d}{d\theta}P_n^m(\cos\theta)k_0\hat{H}_n^{(2)\prime}(ka_{dr}) \qquad (2.129)$$

Using (2.125) and (2.126) in (2.88) and substituting in (2.82) gives

$$-\frac{1}{r'}\sum_{n=0}^{\infty}d_{nm}\frac{d}{d\theta'}P_n^m(\cos\theta')\frac{d}{d\theta}P_n^m(\cos\theta)\cdot e^{-jm\phi'}\hat{H}_n^{(2)}(ka_{dr})\hat{J}_n(kr')$$
$$+\frac{1}{\hat{z}r'\sin\theta'\sin\theta}\sum_{n=0}^{\infty}a_{nm}P_n^m(\cos\theta')P_n^m(\cos\theta)\cdot jm\cdot e^{-jm\phi'}\hat{J}_n'(kr')\cdot k\cdot\hat{H}_n^{(2)\prime}(ka_{dr})$$
$$-\sum_{n=0}^{\infty}E_{nm}\frac{d}{d\theta}P_n^m(\cos\theta)\hat{J}_n(ka_{dr})+\frac{1}{\hat{z}\sin\theta}\sum_{n=0}^{\infty}B_{nm}\cdot jm\cdot P_n^m(\cos\theta)k\cdot\hat{J}_n'(ka_{dr})$$
$$=-\sum_{n=0}^{\infty}F_{nm}\frac{d}{d\theta}P_n^m(\cos\theta)\,\hat{H}_n^{(2)}(ka_{dr})+\frac{1}{\hat{z}\sin\theta}\sum_{n=0}^{\infty}C_{nm}\cdot jm\cdot P_n^m(\cos\theta)k_0\hat{H}_n^{(2)\prime}(ka_{dr}) \qquad (2.130)$$

Since Green's function outside the DRA is not needed for computing the input impedance and reflection coefficient, the unknowns to be determined are B_{nm} and E_{nm}. The unknowns C_{nm} and F_{nm} are required for determining the radiation pattern. The unknowns B_{nm} and E_{nm} can be determined by solving (2.127) to (2.130) simultaneously.

$$B_{nm}=\frac{1}{\Delta_n^{TE}}\frac{-a_{nm}}{r'\sin\theta'}e^{-jm\phi'}P_n^m(\cos\theta')\hat{J}_n'(kr') \cdot\left[\hat{H}_n^{(2)}(ka_{dr})\hat{H}_n^{(2)'}(k_0a_{dr})-\frac{k}{k_0}\hat{H}_n^{(2)}(k_0a_{dr})\hat{H}_n^{(2)'}(ka_{dr})\right] \tag{2.131}$$

$$E_{nm}=\frac{1}{\Delta_n^{TM}}\frac{-d_{nm}}{r'}e^{-jm\phi'}\frac{d}{d\theta'}P_n^m(\cos\theta')\hat{J}_n(kr') \cdot\left[\hat{H}_n^{(2)}(k_0a_{dr})\hat{H}_n^{(2)'}(ka_{dr})-\frac{k}{k_0}\hat{H}_n^{(2)}(ka_{dr})\hat{H}_n^{(2)'}(k_0a_{dr})\right] \tag{2.132}$$

where Δ_n^{TE} is given in (2.102) and,

$$\Delta_n^{TM}=\hat{J}_n'(ka_{dr})\hat{H}_n^{(2)}(k_0a_{dr})-\frac{k}{k_0}\hat{J}_n(ka_{dr})\hat{H}_n^{(2)'}(k_0a_{dr}) \tag{2.133}$$

On substituting (2.131) and (2.132) in (2.125) and (2.126) respectively, the homogeneous solutions can be written as

$$G_{M\phi}^{Frh}=\frac{1}{r'\sin\theta}\sum_{n=1}^{\infty}\sum_{m=1}^{n}b_{nm}P_n^m(\cos\theta')P_n^m(\cos\theta)\sin m(\phi-\phi')\hat{J}_n'(kr')\hat{J}_n(kr) \tag{2.134}$$

$$G_{M\phi}^{Arh}=\frac{1}{r'}\sum_{n=1}^{\infty}\sum_{m=0}^{n}e_{nm}\frac{d}{d\theta}\left[P_n^m(\cos\theta')\right]P_n^m(\cos\theta)\cos m(\phi-\phi')\hat{J}_n(kr')\hat{J}_n(kr) \tag{2.135}$$

where

$$b_{nm}=\frac{-a_{nm}}{\Delta_n^{TE}}\left[\hat{H}_n^{(2)}(ka_{dr})\hat{H}_n^{(2)'}(k_0a_{dr})-\frac{k}{k_0}\hat{H}_n^{(2)}(k_0a_{dr})\hat{H}_n^{(2)'}(ka_{dr})\right] \tag{2.136}$$

$$e_{nm}=\frac{-d_{nm}}{\Delta_n^{TM}}\left[\hat{H}_n^{(2)}(k_0a_{dr})\hat{H}_n^{(2)\prime}(ka_{dr})-\frac{k}{k_0}\hat{H}_n^{(2)}(ka_{dr})\hat{H}_n^{(2)\prime}(k_0a_{dr})\right] \quad (2.137)$$

All the potential Green's functions of HDRA placed above the slotted ground plane are derived. The constants k_0, k, and ε denote the wave number in vacuum, wave number in dielectric and dielectric constant of DRA respectively. $P_n^m(\cos\theta)$ is the associated Legendre function of the first kind with order *m* and degree *n* that has finite solutions over the entire range $0 \le \theta \le \pi$. $\hat{J}_n(kr)$ is the spherical Bessel function of the first kind and $\hat{H}_n^{(2)}(kr)$ is the spherical Hankel function of the second kind, both of order *n* and of Schelkunoff type. For real values of k, $\hat{J}_n(kr)$ represents standing waves inside the DRA and $\hat{H}_n^{(2)}(kr)$ represents outward travelling wave. $\Delta_n^{TE}=0$, and $\Delta_n^{TM}=0$ are respectively, the characteristic equations for TE and TM modes, which can be solved to obtain the resonant frequency and Q of different modes.

2.3.2 Extraction of Green's Functions in Rectangular coordinate System

The potential Green's functions derived are for unit delta currents in spherical coordinate system. Since the original problem involves $\hat{x}$ and $\hat{y}$ directed currents, the derived potential Green's functions are to be modified in rectangular coordinate system. Modifications can be done by multiplying the potential Green's functions due to $\hat{r}$ directed current by $\cos\phi'$ and $\hat{\phi}$ directed current by $-\sin\phi'$. The transformed potential Green's functions represent various components of the fields at the observation location in spherical coordinates. The potential Green's functions in rectangular coordinate system at the observation location can be computed by performing spherical to rectangular coordinate transformation using observation coordinates.

For conversion, the Potential Green's functions can be written in compact form as:

$$G_{M_r}^{Frp}=\frac{1}{r'^2}\sum_{n=0}^{\infty}\sum_{m=0}^{n}g_{nm}P_n^m(\cos\theta)P_n^m(\cos\theta')\cdot\cos m(\phi-\phi')\Phi_n(kr')\Psi_n(kr) \quad (2.138)$$

$$G_{M\phi}^{Frp} = \frac{1}{r' \sin\theta'} \sum_{n=1}^{\infty} \sum_{m=1}^{n} a_{nm} P_n^m(\cos\theta) P_n^m(\cos\theta') \sin m(\phi - \phi') \Phi_n'(kr') \Psi_n(kr) \quad (2.139)$$

$$G_{M\phi}^{Arp} = \frac{1}{r'} \sum_{n=1}^{\infty} \sum_{m=0}^{n} d_{nm} P_n^m(\cos\theta) \frac{d}{d\theta'} P_n^m(\cos\theta') \cos m(\phi - \phi') \Phi_n(kr') \Psi_n(kr) \quad (2.140)$$

$$G_{Mr}^{Frh} = \frac{1}{r'^2} \sum_{n=0}^{\infty} \sum_{m=0}^{n} h_{nm} P_n^m(\cos\theta') P_n^m(\cos\theta) \cos m(\phi - \phi') \hat{J}_n(kr') \hat{J}_n(kr) \quad (2.141)$$

$$G_{M\phi}^{Frh} = \frac{1}{r' \sin\theta} \sum_{n=1}^{\infty} \sum_{m=1}^{n} b_{nm} P_n^m(\cos\theta') P_n^m(\cos\theta) \sin m(\phi - \phi') \hat{J}_n'(kr') \hat{J}_n(kr) \quad (2.142)$$

$$G_{M\phi}^{Arh} = \frac{1}{r'} \sum_{n=1}^{\infty} \sum_{m=0}^{n} e_{nm} \frac{d}{d\theta} \left[P_n^m(\cos\theta') \right] P_n^m(\cos\theta) \cos m(\phi - \phi') \hat{J}_n(kr') \hat{J}_n(kr) \quad (2.143)$$

where

$$\Phi_n(kr') = \begin{cases} \hat{J}_n(kr') & r > r' \\ \hat{H}_n^{(2)}(kr') & r < r' \end{cases} \quad (2.144)$$

$$\Psi_n(kr) = \begin{cases} \hat{H}_n^{(2)}(kr) & r > r' \\ \hat{J}_n(kr) & r < r' \end{cases} \quad (2.145)$$

2.3.2.1 Extraction of Particular Solution of Green's Function

Green's functions of the fields in spherical coordinates due to spherical components of the currents are derived in section 2.3.1. However, the original problem involves currents in rectangular coordinates and the Green's function in rectangular coordinates is to be found out. In order to perform the source transformation, (2.146) and (2.147) are used.

$$\vec{M}_x = \vec{M}_r \cos\phi' - \vec{M}_\varphi \sin\phi' \quad (2.146)$$

$$\vec{M}_y = \vec{M}_r \sin\phi' + \vec{M}_\varphi \cos\phi' \quad (2.147)$$

After performing source transformation, the resulting potential functions are substituted in (2.83) to (2.88) to obtain the spherical components of the fields. Simplification can be done by using the identities, (2.148) to (2.150).

$$\left(\frac{\partial}{\partial r^2}+k^2\right)\Phi_{\mathrm{n}}(kr')\Psi_n(kr) = \frac{\mathrm{n(n+1)}}{\mathrm{r}^2}\Phi_{\mathrm{n}}(kr')\Psi_n(kr) \tag{2.148}$$

$$P_n(\cos\xi)=\sum_{m=0}^{n}\varepsilon_m\frac{(n-m)!}{(n+m)!}P_n^m(\cos\theta)P_n^m(\cos\theta')\cos m(\phi-\phi') \tag{2.149}$$

$$\cos\xi=\cos\theta\cos\theta'+\sin\theta\sin\theta'\cos(\phi-\phi')=\cos(\phi-\phi') \tag{2.150}$$

Expressions for Green's function of the spherical components of the fields using rectangular components of the currents are:

$$\begin{aligned} G_{M_x}^{H_r} = & -\frac{1}{4\pi\omega\mu_0 k}\frac{\cos\phi'}{r^2r'^2}\sum_{n=1}^{\infty}(2n+1)n(n+1)P_n\left[\cos(\phi-\phi')\right]\Phi_n(kr')\Psi_n(kr) \\ & +\frac{1}{4\pi\omega\mu_0}\frac{\sin\phi'}{r^2r'}\sum_{n=1}^{\infty}(2n+1)\frac{\partial}{\partial\phi'}P_n\left[\cos(\phi-\phi')\right]\Phi_n'(kr')\Psi_n(kr) \end{aligned} \tag{2.151}$$

$$\begin{aligned} G_{M_y}^{H_r} = & -\frac{1}{4\pi\omega\mu_0 k}\frac{\sin\phi'}{r^2r'^2}\sum_{n=1}^{\infty}(2n+1)n(n+1)P_n\left[\cos(\phi-\phi')\right]\Phi_n(kr')\Psi_n(kr) \\ & -\frac{1}{4\pi\omega\mu_0}\frac{\cos\phi'}{r^2r'}\sum_{n=1}^{\infty}(2n+1)\frac{\partial}{\partial\phi'}P_n\left[\cos(\phi-\phi')\right]\Phi_n'(kr')\Psi_n(kr) \end{aligned} \tag{2.152}$$

$$\begin{aligned} G_{M_x}^{H_\phi} = & -\frac{\omega\varepsilon}{4\pi k}\frac{\sin\phi'}{r\cdot r'}\sum_{n=1}^{\infty}\frac{(2n+1)}{n(n+1)}\cdot P_n'\left[\cos(\phi-\phi')\right]\Phi_n(kr')\Psi_n(kr) \\ & +\frac{1}{4\pi\omega\mu_0}\frac{\cos\phi'}{rr'^2}\sum_{n=1}^{\infty}(2n+1)\frac{\partial}{\partial\phi}P_n\left[\cos(\phi-\phi')\right]\Phi_n(kr')\Psi_n'(kr) \\ & -\frac{k}{4\pi\omega\mu_0}\frac{\sin\phi'}{r\cdot r'}\sum_{n=1}^{\infty}\frac{(2n+1)}{n(n+1)}\cdot\frac{\partial^2}{\partial\phi\partial\phi'}P_n\left[\cos(\phi-\phi')\right]\Phi_n(kr')\Psi_n(kr) \end{aligned} \tag{2.153}$$

$$G_{My}^{H_\phi} = -\frac{\omega\varepsilon}{4\pi k}\frac{\cos\phi'}{r\cdot r'}\sum_{n=1}^{\infty}\frac{(2n+1)}{n(n+1)}\cdot P_n'\left[\cos(\phi-\phi')\right]\Phi_n(kr')\Psi_n(kr)$$
$$+\frac{1}{4\pi\omega\mu_0}\frac{\sin\phi'}{rr'^2}\sum_{n=1}^{\infty}(2n+1)\frac{\partial}{\partial\phi}P_n\left[\cos(\phi-\phi')\right]\Phi_n(kr')\Psi_n'(kr)$$
$$-\frac{k}{4\pi\omega\mu_0}\frac{\cos\phi'}{r\cdot r'}\sum_{n=1}^{\infty}\frac{(2n+1)}{n(n+1)}\cdot\frac{\partial^2}{\partial\phi\partial\phi'}P_n\left[\cos(\phi-\phi')\right]\Phi_n(kr')\Psi_n(kr) \quad (2.154)$$

Once all the field components in spherical coordinates are obtained, the fields can be transformed into rectangular coordinates at observation location. The particular part of the Green's function for *x* directed magnetic field due to *x* directed magnetic current is computed using:

$$G_p \text{ of } G_{M_x}^{H_x} = G_{M_x}^{H_r}\cos\phi - G_{M_x}^{H_\phi}\sin\phi \quad (2.155)$$

Substituting for $G_{M_x}^{H_r}$ and $G_{M_x}^{H_\phi}$ using (2.151) and (2.153), in (2.155) and simplifying

$$G_p \text{ of } G_{M_x}^{Hx} = -\frac{1}{4\pi\omega\mu_0 k}\frac{\cos\phi\cos\phi'}{r^2r'^2}\sum_{n=1}^{\infty}(2n+1)n(n+1)P_n\left[\cos(\phi-\phi')\right]\Phi_n(kr')\Psi_n(kr)$$
$$+\frac{1}{4\pi\omega\mu_0}\frac{\cos\phi\sin\phi'}{r^2r'}\sum_{n=1}^{\infty}(2n+1)\frac{\partial}{\partial\phi'}P_n\left[\cos(\phi-\phi')\right]\Phi_n'(kr')\Psi_n(kr)$$
$$-\frac{1}{4\pi\omega\mu_0}\frac{\sin\phi\cos\phi'}{rr'^2}\sum_{n=1}^{\infty}(2n+1)\frac{\partial}{\partial\phi}P_n\left[\cos(\phi-\phi')\right]\Phi_n(kr')\Psi_n'(kr)$$
$$+\frac{\omega\varepsilon}{4\pi k}\frac{\sin\phi\sin\phi'}{r\cdot r'}\sum_{n=1}^{\infty}\frac{(2n+1)}{n(n+1)}\cdot P_n'\left[\cos(\phi-\phi')\right]\Phi_n(kr')\Psi_n(kr)$$
$$+\frac{k}{4\pi\omega\mu_0}\frac{\sin\phi\sin\phi'}{r\cdot r'}\sum_{n=1}^{\infty}\frac{(2n+1)}{n(n+1)}\cdot\frac{\partial^2}{\partial\phi\partial\phi'}P_n\left[\cos(\phi-\phi')\right]\Phi_n(kr')\Psi_n(kr) \quad (2.156)$$

$$\mathrm{G}_p \text{ of } G_{M_y}^{H_y} = G_{M_y}^{H_r}\sin\phi + G_{M_y}^{H_\phi}\cos\phi \quad (2.157)$$

Substituting for $G_{M_y}^{H_r}$ and $G_{M_y}^{H_\phi}$ using (2.152) and (2.154), in (2.157) and simplifying

$$
\begin{aligned}
\mathrm{G}_p \text{ of } G_{M_y}^{H_y} = & -\frac{1}{4\pi\omega\mu_0 k}\frac{\sin\phi\sin\phi'}{r^2 r'^2}\sum_{n=1}^{\infty}(2n+1)n(n+1)P_n\left[\cos(\phi-\phi')\right]\Phi_n(kr')\Psi_n(kr) \\
& -\frac{1}{4\pi\omega\mu_0}\frac{\sin\phi\cos\phi'}{r^2 r'}\sum_{n=1}^{\infty}(2n+1)\frac{\partial}{\partial\phi'}P_n\left[\cos(\phi-\phi')\right]\Phi_n'(kr')\Psi_n(kr) \\
& -\frac{\omega\varepsilon}{4\pi k}\frac{\cos\phi\cos\phi'}{r\cdot r'}\sum_{n=1}^{\infty}\frac{(2n+1)}{n(n+1)}\cdot P_n'\left[\cos(\phi-\phi')\right]\Phi_n(kr')\Psi_n(kr) \\
& +\frac{1}{4\pi\omega\mu_0}\frac{\cos\phi\sin\phi'}{rr'^2}\sum_{n=1}^{\infty}(2n+1)\frac{\partial}{\partial\phi}P_n\left[\cos(\phi-\phi')\right]\Phi_n(kr')\Psi_n'(kr) \\
& -\frac{k}{4\pi\omega\mu_0}\frac{\cos\phi\cos\phi'}{r\cdot r'}\sum_{n=1}^{\infty}\frac{(2n+1)}{n(n+1)}\cdot\frac{\partial^2}{\partial\phi\partial\phi'}P_n\left[\cos(\phi-\phi')\right]\Phi_n(kr')\Psi_n(kr)
\end{aligned}
\tag{2.158}
$$

$$
\mathrm{G}_p \text{ of } G_{M_x}^{H_y} = G_{M_x}^{H_r}\sin\phi + G_{M_x}^{H_\phi}\cos\phi \tag{2.159}
$$

Substituting for $G_{M_x}^{H_r}$ and $G_{M_x}^{H_\phi}$ using (2.151) and (2.153), in (2.159) and simplifying

$$
\begin{aligned}
\mathrm{G}_p \text{ of } G_{M_x}^{H_y} = & -\frac{1}{4\pi\omega\mu_0 k}\frac{\sin\phi\cos\phi'}{r^2 r'^2}\sum_{n=1}^{\infty}(2n+1)n(n+1)P_n\left[\cos(\phi-\phi')\right]\Phi_n(kr')\Psi_n(kr) \\
& +\frac{1}{4\pi\omega\mu_0}\frac{\sin\phi\sin\phi'}{r^2 r'}\sum_{n=1}^{\infty}(2n+1)\frac{\partial}{\partial\phi'}P_n\left[\cos(\phi-\phi')\right]\Phi_n'(kr')\Psi_n(kr) \\
& -\frac{\omega\varepsilon}{4\pi k}\frac{\cos\phi\sin\phi'}{r\cdot r'}\sum_{n=1}^{\infty}\frac{(2n+1)}{n(n+1)}\cdot P_n'\left[\cos(\phi-\phi')\right]\Phi_n(kr')\Psi_n(kr) \\
& +\frac{1}{4\pi\omega\mu_0}\frac{\cos\phi\cos\phi'}{rr'^2}\sum_{n=1}^{\infty}(2n+1)\frac{\partial}{\partial\phi}P_n\left[\cos(\phi-\phi')\right]\Phi_n(kr')\Psi_n'(kr) \\
& -\frac{k}{4\pi\omega\mu_0}\frac{\cos\phi\sin\phi'}{r\cdot r'}\sum_{n=1}^{\infty}\frac{(2n+1)}{n(n+1)}\cdot\frac{\partial^2}{\partial\phi\partial\phi'}P_n\left[\cos(\phi-\phi')\right]\Phi_n(kr')\Psi_n(kr)
\end{aligned}
\tag{2.160}
$$

$$
\mathrm{G}_p \text{ of } G_{M_y}^{H_x} = G_{M_y}^{H_r}\cos\phi - G_{M_y}^{H_\phi}\sin\phi \tag{2.161}
$$

Substituting for $G_{M_y}^{H_r}$ and $G_{M_y}^{H_\phi}$ using (2.152) and (2.154), in (2.161) and simplifying

$$
\begin{aligned}
\mathrm{G}_p \text{ of } G_{My}^{Hx} = & -\frac{1}{4\pi\omega\mu_0 k}\frac{\cos\phi\sin\phi'}{r^2 r'^2}\sum_{n=1}^{\infty}(2n+1)n(n+1)P_n\left[\cos(\phi-\phi')\right]\Phi_n(kr')\Psi_n(kr) \\
& -\frac{1}{4\pi\omega\mu_0}\frac{\cos\phi\cos\phi'}{r^2 r'}\sum_{n=1}^{\infty}(2n+1)\frac{\partial}{\partial\phi'}P_n\left[\cos(\phi-\phi')\right]\Phi'_n(kr')\Psi_n(kr) \\
& -\frac{1}{4\pi\omega\mu_0}\frac{\sin\phi\sin\phi'}{rr'^2}\sum_{n=1}^{\infty}(2n+1)\frac{\partial}{\partial\phi}P_n\left[\cos(\phi-\phi')\right]\Phi_n(kr')\Psi'_n(kr) \\
& +\frac{\omega\varepsilon}{4\pi k}\frac{\sin\phi\cos\phi'}{r\cdot r'}\sum_{n=1}^{\infty}\frac{(2n+1)}{n(n+1)}\cdot P'_n\left[\cos(\phi-\phi')\right]\Phi_n(kr')\Psi_n(kr) \\
& +\frac{k}{4\pi\omega\mu_0}\frac{\sin\phi\cos\phi'}{r\cdot r'}\sum_{n=1}^{\infty}\frac{(2n+1)}{n(n+1)}\cdot\frac{\partial^2}{\partial\phi\partial\phi'}P_n\left[\cos(\phi-\phi')\right]\Phi_n(kr')\Psi_n(kr) \qquad (2.162)
\end{aligned}
$$

2.3.2.2 Extraction of Homogeneous Solution of Green's Function

The procedure explained in section 2.3.2.1 for extracting the particular solution in rectangular co-ordinates can also be used for the extraction of the homogeneous solution. The homogeneous solutions of the Green's function in rectangular coordinates are:

$$
G_h \text{ of } G_{M_x}^{H_x} = G_{M_x}^{H_r}\cos\phi - G_{M_x}^{H_\phi}\sin\phi \qquad (2.163)
$$

$$
\begin{aligned}
G_h \text{ of } G_{M_x}^{H_x} = & -\frac{1}{4\pi\omega\mu_0 k}\frac{\cos\phi\cos\phi'}{r^2 r'^2}\sum_{n=1}^{\infty}(2n+1)n(n+1)P_n\left[\cos(\phi-\phi')\right]\hat{J}_n(kr')\hat{J}_n(kr) \\
& -\frac{1}{4\pi\omega\mu_0}\frac{\cos\phi\sin\phi'}{r^2 r'}\sum_{n=1}^{\infty}(2n+1)\frac{\partial}{\partial\phi'}P_n\left[\cos(\phi-\phi')\right]\hat{J}'_n(kr')\hat{J}_n(kr) \\
& +\frac{1}{4\pi\omega\mu_0}\frac{\sin\phi\cos\phi'}{rr'^2}\sum_{n=1}^{\infty}(2n+1)\frac{\partial}{\partial\phi}P_n\left[\cos(\phi-\phi')\right]\hat{J}_n(kr')\hat{J}'_n(kr) \\
& -\frac{\omega\varepsilon}{4\pi k}\frac{\sin\phi\sin\phi'}{r\cdot r'}\sum_{n=1}^{\infty}\frac{(2n+1)}{n(n+1)}\cdot P'_n\left[\cos(\phi-\phi')\right]\hat{J}_n(kr')\hat{J}_n(kr) \\
& -\frac{k}{4\pi\omega\mu_0}\frac{\sin\phi\sin\phi'}{r\cdot r'}\sum_{n=1}^{\infty}\frac{(2n+1)}{n(n+1)}\cdot\frac{\partial^2}{\partial\phi\partial\phi'}P_n\left[\cos(\phi-\phi')\right]\hat{J}'_n(kr')\hat{J}'_n(kr) \qquad (2.164)
\end{aligned}
$$

$$
G_h \text{ of } G_{M_y}^{H_y} = G_{M_y}^{H_r}\sin\phi + G_{M_y}^{H_y}\cos\phi \qquad (2.165)
$$

$$
\begin{aligned}
G_h \text{ of } G_{M_y}^{H_y} = & -\frac{1}{4\pi\omega\mu_0 k}\frac{\sin\phi\sin\phi'}{r^2 r'^2}\sum_{n=1}^{\infty}(2n+1)n(n+1)P_n\left[\cos(\phi-\phi')\right]\hat{J}_n(kr')\hat{J}_n(kr) \\
& -\frac{1}{4\pi\omega\mu_0}\frac{\sin\phi\cos\phi'}{r^2 r'}\sum_{n=1}^{\infty}(2n+1)\frac{\partial}{\partial\phi'}P_n\left[\cos(\phi-\phi')\right]\hat{J}_n'(kr')\hat{J}_n(kr) \\
& -\frac{1}{4\pi\omega\mu_0}\frac{\cos\phi\sin\phi'}{rr'^2}\sum_{n=1}^{\infty}(2n+1)\frac{\partial}{\partial\phi}P_n\left[\cos(\phi-\phi')\right]\hat{J}_n(kr')\hat{J}_n'(kr) \\
& -\frac{\omega\varepsilon}{4\pi k}\frac{\cos\phi\cos\phi'}{r\cdot r'}\sum_{n=1}^{\infty}\frac{(2n+1)}{n(n+1)}\cdot P_n'\left[\cos(\phi-\phi')\right]\hat{J}_n(kr')\hat{J}_n(kr) \\
& -\frac{k}{4\pi\omega\mu_0}\frac{\cos\phi\cos\phi'}{r\cdot r'}\sum_{n=1}^{\infty}\frac{(2n+1)}{n(n+1)}\cdot\frac{\partial^2}{\partial\phi\partial\phi'}P_n\left[\cos(\phi-\phi')\right]\hat{J}_n'(kr')\hat{J}_n'(kr) \qquad (2.166)
\end{aligned}
$$

$$
G_h \text{ of } G_{M_x}^{H_y} = G_{M_x}^{H_r}\sin\phi + G_{M_x}^{H_\phi}\cos\phi \qquad (2.167)
$$

$$
\begin{aligned}
G_h \text{ of } G_{M_x}^{H_y} = & -\frac{1}{4\pi\omega\mu_0 k}\frac{\sin\phi\cos\phi'}{r^2 r'^2}\sum_{n=1}^{\infty}(2n+1)n(n+1)P_n\left[\cos(\phi-\phi')\right]\hat{J}_n(kr')\hat{J}_n(kr) \\
& +\frac{1}{4\pi\omega\mu_0}\frac{\sin\phi\sin\phi'}{r^2 r'}\sum_{n=1}^{\infty}(2n+1)\frac{\partial}{\partial\phi'}P_n\left[\cos(\phi-\phi')\right]\hat{J}_n'(kr')\hat{J}_n(kr) \\
& +\frac{1}{4\pi\omega\mu_0}\frac{\cos\phi\cos\phi'}{rr'^2}\sum_{n=1}^{\infty}(2n+1)\frac{\partial}{\partial\phi}P_n\left[\cos(\phi-\phi')\right]\hat{J}_n(kr')\hat{J}_n'(kr) \\
& -\frac{\omega\varepsilon}{4\pi k}\frac{\cos\phi\sin\phi'}{r\cdot r'}\sum_{n=1}^{\infty}\frac{(2n+1)}{n(n+1)}\cdot P_n'\left[\cos(\phi-\phi')\right]\hat{J}_n(kr')\hat{J}_n(kr) \\
& -\frac{k}{4\pi\omega\mu_0}\frac{\cos\phi\sin\phi'}{r\cdot r'}\sum_{n=1}^{\infty}\frac{(2n+1)}{n(n+1)}\cdot\frac{\partial^2}{\partial\phi\partial\phi'}P_n\left[\cos(\phi-\phi')\right]\hat{J}_n'(kr')\hat{J}_n'(kr) \qquad (2.168)
\end{aligned}
$$

$$
G_h \text{ of } G_{M_y}^{H_x} = G_{M_y}^{H_r}\cos\phi - G_{M_y}^{H_\phi}\sin\phi \qquad (2.169)
$$

$$
\begin{aligned}
G_h \text{ of } G_{M_y}^{H_x} = & -\frac{1}{4\pi\omega\mu_0 k}\frac{\cos\phi\sin\phi'}{r^2 r'^2}\sum_{n=1}^{\infty}(2n+1)n(n+1)P_n\left[\cos(\phi-\phi')\right]\hat{J}_n(kr')\hat{J}_n(kr) \\
& -\frac{1}{4\pi\omega\mu_0}\frac{\cos\phi\cos\phi'}{r^2 r'}\sum_{n=1}^{\infty}(2n+1)\frac{\partial}{\partial\phi'}P_n\left[\cos(\phi-\phi')\right]\hat{J}_n'(kr')\hat{J}_n(kr) \\
& +\frac{1}{4\pi\omega\mu_0}\frac{\sin\phi\sin\phi'}{rr'^2}\sum_{n=1}^{\infty}(2n+1)\frac{\partial}{\partial\phi}P_n\left[\cos(\phi-\phi')\right]\hat{J}_n(kr')\hat{J}_n'(kr) \\
& -\frac{\omega\varepsilon}{4\pi k}\frac{\sin\phi\cos\phi'}{r\cdot r'}\sum_{n=1}^{\infty}\frac{(2n+1)}{n(n+1)}\cdot P_n'\left[\cos(\phi-\phi')\right]\hat{J}_n(kr')\hat{J}_n(kr) \\
& -\frac{k}{4\pi\omega\mu_0}\frac{\sin\phi\cos\phi'}{r\cdot r'}\sum_{n=1}^{\infty}\frac{(2n+1)}{n(n+1)}\cdot\frac{\partial^2}{\partial\phi\partial\phi'}P_n\left[\cos(\phi-\phi')\right]\hat{J}_n'(kr')\hat{J}_n'(kr)
\end{aligned}
\tag{2.170}
$$

where

$$
b_n = \frac{-1}{\Delta_n^{TE}}\left[\hat{H}_n^{(2)}(ka_{dr})\hat{H}_n^{(2)'}(k_0 a_{dr}) - \frac{k}{k_0}\hat{H}_n^{(2)}(k_0 a_{dr})\hat{H}_n^{(2)'}(ka_{dr})\right] \tag{2.171}
$$

$$
e_n = \frac{-1}{\Delta_n^{TM}}\left[\hat{H}_n^{(2)}(k_0 a_{dr})\hat{H}_n^{(2)'}(ka_{dr}) - \frac{k}{k_0}\hat{H}_n^{(2)}(ka_{dr})\hat{H}_n^{(2)'}(k_0 a_{dr})\right] \tag{2.172}
$$

Once the particular and homogeneous solutions are determined, the Green's function can be found out by adding the particular and homogeneous solutions. However, the particular part of the Green's function is a slowly convergent series and takes a lot of computation time. The values of the Hankel function become very large, when its argument reduces. Therefore the particular solution is found out by using spectral domain approach, which is discussed in the following section.

2.4 Field Radiated into Free Space by an Aperture in the Transverse Plane of a Rectangular Waveguide

The particular solution of the DRA is a slowly convergent series and it takes a lot of computation time. Therefore, the particular solution, which represents the source radiating in the unbounded dielectric medium is derived using spectral domain approach**.** This representation is more general and hence can be used with narrow as well as wide slots. From the field existing at the aperture of the waveguide shorted end,

the radiated field can be evaluated using the plane wave spectrum approach [105]. The radiated field can be obtained by expanding the spherical waves in terms of plane wave spectrum in the vector potential formulation. Figure 2.5 shows schematic of the waveguide with an aperture at the shorted end. The length and width of the aperture are denoted by *2L* and *2W* respectively.

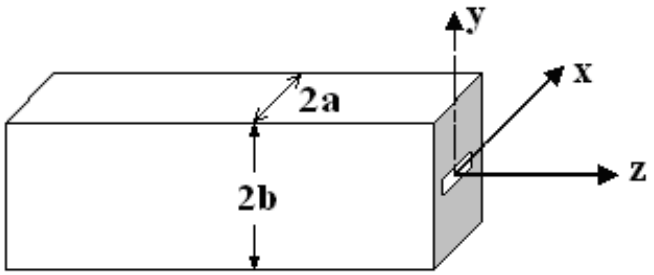

Fig. 2.5 Waveguide with an aperture at the shorted end

If a tangential electric field $\vec{E}_s$ is excited at the aperture, the equivalent magnetic current at the aperture, $\vec{M}_s$ can be expressed as:

$$\vec{M}_s = \vec{E}_s \times \hat{u}_z \tag{2.173}$$

where $\hat{u}_z$ is the unit vector perpendicular to the plane containing the aperture.

Since the aperture is surrounded by an infinite ground plane, which is assumed to be perfectly conducting, the magnetic current exists only at the aperture. The boundary conditions at a perfect electric conductor are vanishing tangential components of $\vec{E}$. An element of source, plus its image element, radiating into free space, produces zero tangential components of $\vec{E}$ over the plane bisecting the line joining the two elements. Therefore, while evaluating the magnetic field $\vec{H}$, the magnetic field due to both the magnetic currents $\vec{M}_s$ at the slot, and its image $\vec{M}_i$ are to be considered. The total magnetic field $\vec{H}$ is due to the total magnetic current $\vec{M}$ which is the sum of $\vec{M}_s$ and $\vec{M}_i$.

$$\vec{M} = \vec{M}_s + \vec{M}_i = 2\vec{M}_s \tag{2.174}$$

The electric vector potential $\vec{F}$ at any point in the space is given by

$$\vec{F} = \frac{1}{4\pi} \iint_{Aperture} \frac{\vec{M}(r')\, e^{-jk|r-r'|}}{|r-r'|} ds' \tag{2.175}$$

The electric and magnetic fields at any point in space are given by

$$\vec{E} = -\nabla \times \vec{F} \tag{2.176}$$

$$\vec{H} = -\frac{1}{j\omega\mu} \nabla \times \vec{E} = \frac{1}{jk\eta} \nabla \times \nabla \times \vec{F} \tag{2.177}$$

Substituting (2.175) in (2.177)

$$\vec{H} = \frac{1}{j4\pi k\eta} \nabla \times \nabla \times \iint_{Aperture} \frac{\left(2\vec{E}_s \times \hat{u}_z\right) e^{-jk|r-r'|}}{|r-r'|} ds' \tag{2.178}$$

Using the following identity from [66]

$$\frac{e^{-jkr}}{r} = \frac{1}{j2\pi} \int_{-\infty}^{\infty} \int_{-\infty}^{\infty} \frac{e^{j\left(k_x x + k_y y + k_z z\right)}}{k_z} dk_x dk_y \tag{2.179}$$

and substituting for $|r-r'|$ results in

$$\frac{e^{-jk|r-r'|}}{|r-r'|} = \frac{1}{j2\pi} \int_{-\infty}^{\infty} \int_{-\infty}^{\infty} \frac{e^{j\left\{k_x(x-x')+k_y(y-y')+k_z(z-z')\right\}}}{k_z} dk_x dk_y \tag{2.180}$$

Where x', y', z' refers to any point of the source, and x, y, z refers to any point of observation in space, where the radiated field is to be determined. In the present problem, the source magnetic current is on the $z' = 0$ plane. The radiated magnetic

field at the $z=0$ plane is to be determined. Substituting equation (2.180) in (2.178) and simplifying

$$\vec{H} = -\frac{1}{2\pi k\eta}\nabla\times\nabla\times\int_{-\infty}^{\infty}\int_{-\infty}^{\infty}\frac{1}{2\pi}\iint_{Aperture}\vec{E}_s e^{-j\left(k_x x'+k_y y'\right)}dx'dy'\times\frac{\hat{u}_z}{k_z}e^{j\left(k_x x+k_y y\right)}dk_x dk_y \qquad (2.181)$$

Since $\vec{E}_s$ is zero everywhere on the ground plane, except at the aperture, the inner integral can be written as

$$\frac{1}{2\pi}\int_{-\infty}^{\infty}\int_{-\infty}^{\infty}\vec{E}_s e^{-j\left(k_x x'+k_y y'\right)}dx'dy' = \vec{\varepsilon}_s\left(k_x,k_y,k_z\right) \qquad (2.182)$$

Where the inner integral is the Fourier Transform of the aperture electric field, which is represented by $\vec{\varepsilon}_s$. Carrying out the necessary substitution in (2.181)

$$\vec{H} = -\frac{1}{2\pi k\eta}\nabla\times\nabla\times\int_{-\infty}^{\infty}\int_{-\infty}^{\infty}\vec{\varepsilon}_s\left(k_x,k_y,k_z\right)\times\frac{\hat{u}_z}{k_z}e^{j\left(k_x x+k_y y\right)}dk_x dk_y \qquad (2.183)$$

which is in the form of inverse Fourier Transform. The del operator is replaced by $-j\vec{k}$, when taken inside the transform integral:

$$\vec{H} = \frac{1}{2\pi k\eta}\int_{-\infty}^{\infty}\int_{-\infty}^{\infty}\vec{k}\times\vec{k}\times\vec{\varepsilon}_s\left(k_x,k_y,k_z\right)\times\frac{\hat{u}_z}{k_z}e^{j\left(k_x x+k_y y\right)}dk_x dk_y \qquad (2.184)$$

The free space wave number k and the separation parameters k_x, k_y and k_z must satisfy the separation equation (2.186). Since the aperture field has been assumed to be tangential to the plane (assuming *xy* plane) containing it, it can be represented as:

$$\vec{E}_s = \hat{u}_x E_x + \hat{u}_y E_y \qquad (2.185)$$

$$k_x^2 + k_y^2 + k_z^2 = k^2 \qquad (2.186)$$

The transform of the field, $\vec{\varepsilon}_s$ is then given by:

$$\vec{\varepsilon}_s = \hat{u}_x \varepsilon_x + \hat{u}_y \varepsilon_y \tag{2.187}$$

On carrying out the integration in (2.184) and simplifying, the components of the magnetic field at the aperture plane are:

$$H_x = -\frac{1}{2\pi k\eta} \int_{-\infty}^{\infty} \int_{-\infty}^{\infty} \frac{k_x k_y \varepsilon_x + \left(k^2 - k_x^2\right)\varepsilon_y}{k_z} e^{j\left(k_x x + k_y y\right)} dk_x dk_y \tag{2.188}$$

$$H_y = \frac{1}{2\pi k\eta} \int_{-\infty}^{\infty} \int_{-\infty}^{\infty} \frac{k_x k_y \varepsilon_y + \left(k^2 - k_y^2\right)\varepsilon_x}{k_z} e^{j\left(k_x x + k_y y\right)} dk_x dk_y \tag{2.189}$$

$$H_z = \frac{1}{2\pi k\eta} \int_{-\infty}^{\infty} \int_{-\infty}^{\infty} \frac{k_x k_z \varepsilon_y - k_y k_z \varepsilon_x}{k_z} e^{j\left(k_x x + k_y y\right)} dk_x dk_y \tag{2.190}$$

For any aperture electric field distribution, the magnetic field at any point in space can be found out using the approach outlined so far. Since electric field at the aperture is assumed to have only y component, there is no ε_x term in (2.188).

$$G_{spec} = H_x^{ext} = -\frac{1}{2\pi k\eta} \int_{-\infty}^{\infty} \int_{-\infty}^{\infty} \frac{\left(k^2 - k_x^2\right)\varepsilon_y}{k_z} e^{j\left(k_x x + k_y y\right)} dk_x dk_y \tag{2.191}$$

The Fourier transform of the electric field at the aperture is given by

$$\varepsilon_y = \frac{1}{2\pi} \iint_{aperture} E_y\left(x', y', 0\right) e^{-j\left(k_x x' + k_y y'\right)} dx' dy' \tag{2.192}$$

Writing out this transform integral for ε_y at the z = 0 plane,

$$\varepsilon_y = \frac{1}{2\pi}\sum_{p=1}^{M} E_p \iint_{Aperture} \sin\left[\frac{p\pi}{2L}\left(x' - x_{w2} + L_2\right)\right] e^{-j\left(k_x x' + k_y y'\right)} dx'dy' \tag{2.193}$$

Carrying out the necessary integration and simplifying

$$\varepsilon_y = \frac{2W}{\pi}\sum_{p=1}^{M} E_p \mathrm{sinc}\left(k_y W\right) \frac{\left\{\begin{matrix} j\sin\left(k_x L\right) & \text{for p even} \\ \cos\left(k_x L\right) & \text{for p odd} \end{matrix}\right\}}{\frac{\mathrm{p}\pi}{2\mathrm{L}}\left\{1-\left(\frac{2Lk_x}{p\pi}\right)^2\right\}} \tag{2.194}$$

$$G_{spec} = H_x^{ext} = -\frac{WL}{\pi^2 k\eta}\sum_{p=1}^{M} E_p \int_{-\infty}^{\infty}\int_{-\infty}^{\infty} \frac{k^2 - k_x^2}{\left(k^2 - k_x^2 - k_y^2\right)^{1/2}} \mathrm{sinc}\left(k_y W\right) \frac{\left\{\begin{matrix} j\sin\left(k_x L\right) & \text{for p even} \\ \cos\left(k_x L\right) & \text{for p odd} \end{matrix}\right\}}{\frac{\mathrm{p}\pi}{2}\left\{1-\left(\frac{2Lk_x}{p\pi}\right)^2\right\}} e^{j\left\{k_x x + k_y y\right\}} dk_x dk_y \tag{2.195}$$

After obtaining the homogeneous and particular solution, the magnetic field coupled to the DRA can be computed using:

$$H_x^{DRA}(\bar{M}_x^2) = G_{spec} + \iint_{slot} G_{HS} e_p^2\left(x'\right) ds' \tag{2.196}$$

where, G_{spec} is given in (2.195) and G_{HS} is given in (2.164). Field due to G_{HS} is computed spatially and field due to G_{PS} is computed using spectral domain approach.

2.5 Scattered Magnetic Field inside the Waveguide

To analyze waveguide shorted end slot coupled HDRA, *x* component of the scattered magnetic field inside the waveguide due to *x* component of the magnetic current is to be determined. Scattered magnetic field inside the waveguide due to a wide aperture in the transverse plane of the waveguide is derived in this section. In

order to completely characterize waveguide circuits and radiators, field scattered by the discontinuities represented by slot/aperture into either a bounded (such as inside the waveguide or cavity) or an unbounded medium (such as free space) is to be evaluated. The aperture can be a transverse or longitudinal slot, an aperture in the transverse plane of the waveguide radiating into free space, or a diaphragm. Transverse electric fields exist in the slots and apertures due to which fields are scattered both inside and outside the waveguide. The electromagnetic field for the case of a magnetic current source is given by Maxwell's equation [66]:

$$\nabla \times \vec{E} = -j\omega\mu\vec{H} - \vec{M} \tag{2.197}$$

$$\nabla \times \vec{H} = j\omega\varepsilon\vec{E} \tag{2.198}$$

For a static charge free region

$$\nabla \cdot \vec{E} = 0 \tag{2.199}$$

The vector field $\vec{E}$ has only circulation. Therefore it is often called a solenoidal field, and can be represented by the curl of some other vector function as follows:

$$\vec{E} = -\nabla \times \vec{F} \tag{2.200}$$

where $\vec{F}$ is the electric vector potential. Substituting (2.200) into (2.198) gives

$$\nabla \times \vec{H} = -j\omega\varepsilon\nabla \times \vec{F}$$

or $$\nabla \times \left(\vec{H} + j\omega\varepsilon\vec{F}\right) = 0 \tag{2.201}$$

Using the vector identity:

$$\nabla \times \nabla\omega = 0 \tag{2.202}$$

where ω is a scalar function. The argument of equation (2.201) can be written as

$$\vec{H} + j\omega\varepsilon\vec{F} = -\nabla\phi \tag{2.203}$$

Where ϕ is the scalar potential function. Substituting (2.200) in (2.197) results in:

$$\nabla \times \vec{E} = -\nabla \times \nabla \times \vec{F} = -j\omega\mu\vec{H} - \vec{M} \tag{2.204}$$

$$\nabla \times \nabla \times \vec{F} = j\omega\mu\left(-\nabla\phi - j\omega\varepsilon\vec{F}\right) + \vec{M} \tag{2.205}$$

$$\nabla \times \nabla \times \vec{F} = \omega^2\mu\varepsilon\vec{F} - j\omega\mu\nabla\phi + \vec{M} \tag{2.206}$$

Using the vector notation,

$$\nabla \times \nabla \times \vec{F} = \nabla\left(\nabla.\vec{F}\right) - \nabla^2\vec{F} \tag{2.207}$$

equation (2.206) can be written as

$$\nabla\left(\nabla.\vec{F}\right) - \nabla^2\vec{F} - k^2\vec{F} = -j\omega\mu\nabla\phi + \vec{M} \tag{2.208}$$

Since ϕ is arbitrary, using the Laurentz gauge,

$$\nabla.\vec{F} = -j\omega\mu\phi \tag{2.209}$$

Substituting (2.209) in (2.208)

$$\nabla^2\vec{F} + k^2\vec{F} = -\vec{M} \tag{2.210}$$

Corresponding Green's function equation is

$$\nabla^2\overline{\overline{G}} + k^2\overline{\overline{G}} = -\overline{\overline{\mathrm{I}}} \cdot \delta(r - r') \tag{2.211}$$

The above equation is known as inhomogeneous vector Helmholtz equation. Solution of the Helmholtz equation can be obtained by deriving the Green's function, satisfying the boundary conditions. In the case of rectangular waveguides/cavities, the boundary conditions are zero tangential electric fields at the walls. Many

methodologies are possible to solve the Helmholtz equation. One method is deriving the Green's function by using the boundary conditions. So, the Green's function $G(r|r')$ for a given boundary condition, where r refers to observation coordinates and r' refers to the source coordinates, should satisfy,

$$\nabla^2\bar{\bar{G}}(r|r')+k^2\bar{\bar{G}}(r|r')=-\bar{\bar{\mathbf{I}}}\,\delta(\bar{r}-\bar{r}') \tag{2.212}$$

$$\text{where}\quad \bar{\bar{\mathbf{I}}}=\hat{x}\hat{x}+\hat{y}\hat{y}+\hat{z}\hat{z} \tag{2.213}$$

This equality should be satisfied at the boundary points as well as in the neighborhood of the source and field region in general. The boundary conditions to be satisfied by the Green's function $G(r|r')$ are same as that of the vector potential. This method has an analogy in circuit theory, where the response of a linear time invariant network to an arbitrary input function can be determined by convolution based on the impulse response. Similarly the Green's function for a spatial domain electromagnetic problem plays the same role as the impulse function in time domain. Hence the electric vector potential $\vec{F}$ in terms of Green's function is given by,

$$\vec{F}=\int_{r'}\bar{\bar{G}}(r|r')\,\bar{M}(r')dr' \tag{2.214}$$

The integral may be a single integral if $\bar{M}(r')$ corresponds to a line source, a double integral if $\bar{M}(r')$ corresponds to a surface and triple integral if $\bar{M}(r')$ corresponds to a volume. The two bars over G indicate that Green's function G is dyadic. Since the source can be conceptualized as the integration of delta functions over the entire region, the vector potential is obtained from integration of the Helmholtz equation corresponding to the Green's function. Hence this method of solution is referred to as integral equation method. Inside the waveguide, the homogeneous scalar Helmholtz equation is given by,

$$\nabla^2\psi+k^2\psi=0 \tag{2.215}$$

where, ψ is the scalar potential and Helmholtz equation can be solved as a discrete set of modes. Thus, any arbitrary transverse field inside a section of the waveguide can be expressed as the sum of all possible waveguide modes, as given below [66]:

$$\vec{E}_t^{wg} = \sum_m \sum_n \left(V_{mn}^e \vec{e}_{mn}^e + V_{mn}^m \vec{e}_{mn}^m \right) \tag{2.216}$$

$$\vec{H}_t^{wg} = \sum_m \sum_n \left(I_{mn}^e \vec{h}_{mn}^e + I_{mn}^m \vec{h}_{mn}^m \right) \tag{2.217}$$

where $\vec{E}_t^{wg}$ and $\vec{H}_t^{wg}$ are respectively the scattered transverse electric and magnetic fields inside the waveguide. $\vec{e}_{mn}^{\,e}$, $\vec{h}_{mn}^e$ are the electric and magnetic modal vectors for the TE_{mn} modes and $\vec{e}_{mn}^{\,m}$, $\vec{h}_{mn}^m$ are the modal vectors corresponding to the TM_{mn} modes. Similarly V_{mn}^e , V_{mn}^m are the modal voltages, and I_{mn}^e , I_{mn}^m are the modal currents for the TE_{mn} and TM_{mn} modes respectively.

The modal vectors are normalized to obey the following condition:

$$\iint \left(\vec{e}^{\,e} \right)^2 .ds = \iint \left(\vec{h}^{\,e} \right)^2 .ds = 1 \tag{2.218a}$$

$$\iint \left(\vec{e}^{\,m} \right)^2 .ds = \iint \left(\vec{h}^{\,m} \right)^2 .ds = 1 \tag{2.218b}$$

where the integration extends over the cross section of the waveguide. The modal vectors are defined by [66]:

$$\vec{e}_{mn}^e = \hat{u}_z \times \nabla_t \psi_{mn}^e = \vec{h}_{mn}^e \times \hat{u}_z \tag{2.219}$$

$$\vec{e}_{mn}^m = -\nabla_t \psi_{mn}^m = \vec{h}_{mn}^m \times \hat{u}_z \tag{2.220}$$

$$\vec{h}_{mn}^e = -\nabla_t \psi_{mn}^e = \hat{u}_z \times \vec{e}_{mn}^e \tag{2.221}$$

$$\vec{h}_{mn}^m = -\hat{u}_z \times \nabla_t \psi_{mn}^m = \hat{u}_z \times \vec{e}_{mn}^m \tag{2.222}$$

where ∇_t is the two dimensional del operator, which is defined by

$$\nabla_t = \hat{u}_x \frac{\partial}{\partial x} + \hat{u}_y \frac{\partial}{\partial y} \tag{2.223}$$

For a rectangular waveguide of cross section 2*a* x 2*b,* the scalar potential function ψ can be written for the TE_{mn} and TM_{mn} modes as follows:

$$\Psi^e_{mn} = \frac{1}{\pi}\sqrt{\frac{ab\varepsilon_m\varepsilon_n}{(mb)^2+(na)^2}}\cos\left\{\frac{m\pi}{2a}(x+a)\right\}\cos\left\{\frac{n\pi}{2b}(y+b)\right\} \tag{2.224}$$

$$\Psi^m_{mn} = \frac{2}{\pi}\sqrt{\frac{ab}{(mb)^2+(na)^2}}\sin\left\{\frac{m\pi}{2a}(x+a)\right\}\sin\left\{\frac{n\pi}{2b}(y+b)\right\} \tag{2.225}$$

where ε_m, ε_n are the Neumann's numbers

$$\varepsilon_m, \varepsilon_n = \begin{cases} 1 & \text{for } m,n = 0 \\ 2 & \text{otherwise} \end{cases} \tag{2.226}$$

The electric modal vectors for the TE_{mn} and TM_{mn} mode, $\vec{e}^{\,e}_{mn}$ and $\vec{e}^{\,m}_{mn}$ can be derived using equations (2.219) and (2.220).

$$\vec{e}^{\,e}_{mn} = \frac{1}{\pi}\sqrt{\frac{ab\varepsilon_m\varepsilon_n}{(mb)^2+(na)^2}}\left[\frac{n\pi}{2b}\cos\left\{\frac{m\pi}{2a}(x+a)\right\}\right.$$
$$\left.\times\sin\left\{\frac{n\pi}{2b}(y+b)\right\}\hat{u}_x - \frac{m\pi}{2a}\sin\left\{\frac{m\pi}{2a}(x+a)\right\}\cos\left\{\frac{n\pi}{2b}(y+b)\right\}\hat{u}_y\right] \tag{2.227}$$

$$\vec{e}^{\,m}_{mn} = -\frac{2}{\pi}\sqrt{\frac{ab}{(mb)^2+(na)^2}}\left[\frac{m\pi}{2a}\cos\left\{\frac{m\pi}{2a}(x+a)\right\}\right.$$
$$\left.\times\sin\left\{\frac{n\pi}{2b}(y+b)\right\}\hat{u}_x + \frac{n\pi}{2b}\sin\left\{\frac{m\pi}{2a}(x+a)\right\}\cos\left\{\frac{n\pi}{2b}(y+b)\right\}\hat{u}_y\right] \tag{2.228}$$

The same derivations can be carried out for the magnetic mode functions. The scattered magnetic field can be written in terms of the scattered electric field and wave admittance as follows:

$$\vec{H}^{wg} = \sum_m \sum_n \left\{ Y^e_{mn} V^e_{mn} \left(\hat{u}_z \times \vec{e}^{\,e}_{mn} \right) + Y^m_{mn} V^m_{mn} \left(\hat{u}_z \times \vec{e}^{\,m}_{mn} \right) \right\} \tag{2.229}$$

where, the wave admittances Y^e_{mn} and Y^m_{mn} for the TE_{mn} and TM_{mn} modes are given by,

$$Y^e_{mn} = \frac{k_z}{\omega\mu} = \frac{k_z}{k\eta} \tag{2.230}$$

and

$$Y^m_{mn} = \frac{\omega\varepsilon}{k_z} = \frac{k}{k_z\eta} \tag{2.231}$$

In these expressions k_z is the z-directed wave number in the waveguide, k is the free space wave number, and η is the intrinsic impedance of free space:

$$\eta = \sqrt{\mu_0 / \varepsilon_0} \tag{2.232}$$

Where, μ_0 is the permeability of free space, and ε_0 is the permittivity of free space. Further k_x, k_y and k_z should satisfy the separation equation,

$$k_x^2 + k_y^2 + k_z^2 = k^2 \tag{2.233}$$

In rectangular waveguides with dimension *2a x 2b*, the eigen values or characteristic values for the separation parameter k_x and k_y, obtained by imposing the boundary conditions are given by,

$$k_x = \frac{m\pi}{2a} \tag{2.234}$$

$$k_y = \frac{n\pi}{2b} \tag{2.235}$$

When the waveguide is filled with some dielectric material with relative permittivity ε_r, the intrinsic impedance η_d and the wave number k_d in the dielectric medium, are given by,

$$\eta_d = \eta / \sqrt{\varepsilon_r} \tag{2.236}$$

$$k_d = k\sqrt{\varepsilon_r} \tag{2.237}$$

If $\vec{E}_{slot}$ represents the electric field at the slot/aperture, the expression for modal voltages, using the orthogonal properties of $\vec{e}^{\,e}_{mn}$ and $\vec{e}^{\,m}_{mn}$ are obtained as:

$$V^e_{mn} = \iint\limits_{Aperture} \vec{E}_{slot/aperture}.\vec{e}^{\,e}_{mn} ds \tag{2.238}$$

$$V^m_{mn} = \iint\limits_{Aperture} \vec{E}_{slot/aperture}.\vec{e}^{\,m}_{mn} ds \tag{2.239}$$

To determine the scattered magnetic field inside the waveguide, the modal voltages for the transverse electric and transverse magnetic modes are to be determined.

$$V^e_{nm} = \iint\limits_{slot} \vec{E}(x', y', 0)\ \vec{e}^{\,e}_{mn} dx'dy' \tag{2.240}$$

$$V^m_{nm} = \iint\limits_{slot} \vec{E}(x', y', 0)\ \vec{e}^{\,m}_{mn} dx'dy' \tag{2.241}$$

In general the electric field $\vec{E}$ for a wide slot at the aperture, *i* is described in terms of known basis function with unknown coefficients and is given by

$$\vec{E}^i(x', y', o) = \hat{u}_x \sum_{p=1}^{M} E^i_{xp} e^i_p(x') + \hat{u}_y \sum_{p=1}^{M} E^i_{yp} e^i_p(y') \tag{2.242}$$

where

$$e_p^i(x') = \begin{cases} \sin\left[\dfrac{p\pi}{2L_i}\left(x' - x_{wi} + L_i\right)\right], & \begin{matrix} x_{wi} - L_i \le x' \le x_{wi} + L_i \\ y_{wi} - W_i \le y' \le y_{wi} + W_i \end{matrix} \\ 0, & \text{elsewhere} \end{cases} \tag{2.243}$$

$$e_p^i(y') = \begin{cases} \sin\left[\dfrac{p\pi}{2W_i}\left(y' - y_{wi} + W_i\right)\right], & \begin{matrix} x_{wi} - L_i \le x' \le x_{wi} + L_i \\ y_{wi} - W_i \le y' \le y_{wi} + W_i \end{matrix} \\ 0, & \text{elsewhere} \end{cases} \tag{2.244}$$

where E_{xp}^i and E_{yp}^i are the unknown coefficients for the magnetic current expansion at aperture, i in x and y direction respectively. L_i, W_i represent respectively the length and width of the aperture i and x_{wi}, y_{wi} represent the offset along x and y direction respectively. On substituting (2.243), and (2.244) in (2.242), simplified expression for the electric field at aperture i is obtained, which is substituted in (2.240) and (2.241) to obtain the modal voltages.

$$\begin{aligned} V_{mn}^e = \frac{1}{\pi}\sqrt{\frac{ab\varepsilon_m\varepsilon_n}{(mb)^2+(na)^2}}\Bigg[& \frac{n\pi}{2b}\int_{x_{wi}-L_i}^{x_{wi}+L_i}\cos\left\{\frac{m\pi}{2a}(x+a)\right\}dx\int_{y_{wi}-W_i}^{y_{wi}+W_i}\sin\left\{\frac{n\pi}{2b}(y+b)\right\} \\ & \times\sum_{p=1}^{M}E_{xp}^i\ \sin\left\{\frac{p\pi}{2W_i}\left(y'-y_{wi}+W_i\right)\right\}dydy' - \frac{m\pi}{2a}\int_{x_{wi}-L_i}^{x_{wi}+L_i}\sin\left\{\frac{m\pi}{2a}(x+a)\right\} \\ & \times\sin\left\{\frac{p\pi}{2L_i}\left(x'-x_{wi}+L_i\right)\right\}dxdx'\sum_{p=1}^{M}E_{yp}^i\int_{y_{wi}-W_i}^{y_{wi}+W_i}\cos\left\{\frac{n\pi}{2b}(y+b)\right\}dy\Bigg] \end{aligned} \tag{2.245}$$

$$\begin{aligned} V_{mn}^e = \frac{2L_iW_i}{\pi}\sqrt{\frac{ab\varepsilon_m\varepsilon_n}{(mb)^2+(na)^2}}\sum_{p=1}^{M}E_{xp}^i\Bigg[& \frac{n\pi}{2b}\cos\left\{\frac{m\pi}{2a}\left(x_{w_i}+a\right)\right\}\mathrm{sinc}\left\{\frac{m\pi}{2a}L_i\right\}\cdot F_y(p) \\ & -\sum_{p=1}^{M}E_{yp}^i\frac{m\pi}{2a}\cos\left\{\frac{n\pi}{2b}\left(y_{wi}+b\right)\right\}\mathrm{sinc}\left\{\frac{n\pi}{2b}W_i\right\}\cdot F_x(p)\Bigg] \end{aligned} \tag{2.246}$$

$$V_{nm}^{m}=-\frac{2}{\pi}\sqrt{\frac{ab}{(mb)^2+(na)^2}}\left[\frac{m\pi}{2a}\int_{x_{wi}-L_i}^{x_{wi}+L_i}\cos\left\{\frac{m\pi}{2a}(x+a)\right\}dx\int_{y_{wi}-W_i}^{y_{wi}+W_i}\sin\left\{\frac{n\pi}{2b}(y+b)\right\}\right.$$
$$\times\sum_{p=1}^{M}E_{xp}^{i}\ \sin\left\{\frac{p\pi}{2W_i}(y'-y_{wi}+W_i)\right\}dydy'+\frac{n\pi}{2b}\int_{x_{wi}-L_i}^{x_{wi}+L_i}\sin\left\{\frac{m\pi}{2a}(x+a)\right\}$$
$$\left.\times\sin\left\{\frac{p\pi}{2L_i}(x'-x_{wi}+L_i)\right\}dxdx'\sum_{p=1}^{M}E_{yp}^{i}\int_{y_w-W}^{y_w+W}\cos\left\{\frac{n\pi}{2b}(y+b)\right\}dy\right] \tag{2.247}$$

$$V_{nm}^{m}=-\frac{4L_iW_i}{\pi}\sqrt{\frac{ab}{(mb)^2+(na)^2}}\left[\sum_{p=1}^{M}E_{xp}^{i}\frac{m\pi}{2a}\cos\left\{\frac{m\pi}{2a}(x_{wi}+a)\right\}\mathrm{sinc}\left\{\frac{m\pi}{2a}L_i\right\}F_y(p)\right.$$
$$\left.+\sum_{p=1}^{M}E_{yp}^{i}\frac{n\pi}{2b}\cos\left\{\frac{n\pi}{2b}(y_{wi}+b)\right\}\mathrm{sinc}\left\{\frac{n\pi}{2b}W_i\right\}F_x(p)\right] \tag{2.248}$$

where

$$F_x(p)=\left[\cos\left\{\frac{\pi}{2}\left(-\frac{mx_{wi}}{a}+p-m\right)\right\}\mathrm{sinc}\left\{\frac{\pi L_i}{2}\left(\frac{p}{L_i}-\frac{m}{a}\right)\right\}\right.$$
$$\left.-\cos\left\{\frac{\pi}{2}\left(\frac{mx_{wi}}{a}+p+m\right)\right\}\mathrm{sinc}\left\{\frac{\pi L_i}{2}\left(\frac{p}{L_i}+\frac{m}{a}\right)\right\}\right] \tag{2.249}$$

and

$$F_y(p)=\left[\cos\left\{\frac{\pi}{2}\left(-\frac{ny_{wi}}{b}+p-n\right)\right\}\mathrm{sinc}\left\{\frac{\pi W_i}{2}\left(\frac{p}{W_i}-\frac{n}{b}\right)\right\}\right.$$
$$\left.-\cos\left\{\frac{\pi}{2}\left(\frac{ny_{wi}}{b}+p+n\right)\right\}\mathrm{sinc}\left\{\frac{\pi W_i}{2}\left(\frac{p}{W_i}+\frac{n}{b}\right)\right\}\right] \tag{2.250}$$

The transverse components of the internally scattered magnetic fields are obtained using

$$H_x^{\ e}=Y_{mn}^{e}\sum_m\sum_n V_{mn}^{e}\left(\hat{u}_z\times\vec{e}_{mn}^{\,e}\right) \tag{2.251}$$

$$H_x^{\ m}=Y_{mn}^{m}\sum_m\sum_n V_{mn}^{m}\left(\hat{u}_z\times\vec{e}_{mn}^{\,m}\right) \tag{2.252}$$

where the wave admittances Y_{mn}^{e} and Y_{mn}^{m} are defined by (2.230) and (2.231) respectively. The x and y components of the internally scattered magnetic fields are obtained by substituting for modal voltage and modal vector in (2.251) and (2.252).

$$H_x^{WG}\left(E_x^i\right) = -H_x^{WG}\left(M_y^i\right) = 2L_iW_i\sum_{p=1}^{M}E_{xp}^i\sum_{m}^{\infty}\sum_{n}^{\infty}\left\{Y_{mn}^e\left(C_{mn}^e\right)^2 - Y_{mn}^m\left(C_{mn}^m\right)^2\right\}\frac{m\pi}{2a}\frac{n\pi}{2b}$$
$$\times\sin\left\{\frac{m\pi}{2a}(x+a)\right\}\cos\left\{\frac{n\pi}{2b}(y+b)\right\}\cos\left\{\frac{m\pi}{2a}(x_{wi}+a)\right\}\operatorname{sinc}\left\{\frac{m\pi}{2a}L_i\right\}F_y(p) \quad (2.253)$$

$$H_x^{WG}\left(E_y^i\right) = H_x^{WG}\left(M_x^i\right) = -2L_iW_i\sum_{p=1}^{M}E_{yp}^i\sum_{m}^{\infty}\sum_{n}^{\infty}\left\{Y_{mn}^e\left(C_{mn}^e\frac{m\pi}{2a}\right)^2 + Y_{mn}^m\left(C_{mn}^m\frac{n\pi}{2b}\right)^2\right\}$$
$$\times\sin\left\{\frac{m\pi}{2a}(x+a)\right\}\cos\left\{\frac{n\pi}{2b}(y+b)\right\}\cos\left\{\frac{n\pi}{2b}(y_{wi}+b)\right\}\operatorname{sinc}\left\{\frac{n\pi}{2b}W\right\}F_x(p) \quad (2.254)$$

$$H_y^{WG}\left(E_y^i\right) = H_y^{WG}\left(M_x^i\right) = -2L_iW_i\sum_{p=1}^{M}E_{yp}^i\sum_{m}^{\infty}\sum_{n}^{\infty}\left\{Y_{mn}^e\left(C_{mn}^e\right)^2 - Y_{mn}^m\left(C_{mn}^m\right)^2\right\}\frac{m\pi}{2a}\frac{n\pi}{2b}$$
$$\times\cos\left\{\frac{m\pi}{2a}(x+a)\right\}\sin\left\{\frac{n\pi}{2b}(y+b)\right\}\cos\left\{\frac{n\pi}{2b}(y_{wi}+b)\right\}\operatorname{sinc}\left\{\frac{n\pi}{2b}W_i\right\}F_x(p) \quad (2.255)$$

$$H_y^{WG}\left(E_x^i\right) = -H_y^{WG}\left(M_y^i\right) = 2L_iW_i\sum_{p=1}^{M}E_{xp}^i\sum_{m}^{\infty}\sum_{n}^{\infty}\left\{Y_{mn}^e\left(C_{mn}^e\frac{n\pi}{2b}\right)^2 + Y_{mn}^m\left(C_{mn}^m\frac{m\pi}{2a}\right)^2\right\}$$
$$\times\cos\left\{\frac{m\pi}{2a}(x+a)\right\}\sin\left\{\frac{n\pi}{2b}(y+b)\right\}\cos\left\{\frac{m\pi}{2a}(x_{wi}+a)\right\}\operatorname{sinc}\left\{\frac{m\pi}{2a}L_i\right\}F_y(p) \quad (2.256)$$

where

$$C_{mn}^e = \frac{1}{\pi}\sqrt{\frac{ab\varepsilon_m\varepsilon_n}{(mb)^2+(na)^2}} \quad (2.257)$$

and

$$C_{mn}^m = \frac{2}{\pi}\sqrt{\frac{ab}{(mb)^2+(na)^2}} \quad (2.258)$$

Equations (2.253) to (2.256) represent the internally scattered magnetic fields inside the waveguide due to the magnetic currents, M_x and M_y at the transverse aperture *i*.

2.6 Scattered Magnetic Field inside the Rectangular Cavity

In the analysis of waveguide shorted end slot coupled HDRA, the slot can be considered as a rectangular cavity. The dimensions of the cavity are 2*l*, *2w* and 2*t* in the *x, y* and *z* direction respectively as shown in Fig. 2.6. The origin is located at the center and the limits are *–l* to *+l, -w* to *+w* and *-t* to *+t.* In this case the propagation is along *z* direction, hence only TE_z components are present. With this, the Green's function for the rectangular cavity $\tilde{G}^{cty}$ is

$$\nabla^2 \tilde{G}^{cty} + k^2 \tilde{G}^{cty} = -\bar{\bar{\mathbf{I}}} \cdot \delta(x-x')\delta(y-y')\delta(z-z') \tag{2.259}$$

where the source coordinate is given by (x', y', z'). Being a dyadic, $\tilde{G}_{cty}$ can be expressed as:

$$\tilde{G}^{cty} = \hat{x}\hat{x}G_{xx} + \hat{y}\hat{y}G_{yy} + \hat{z}\hat{z}G_{zz} \tag{2.260}$$

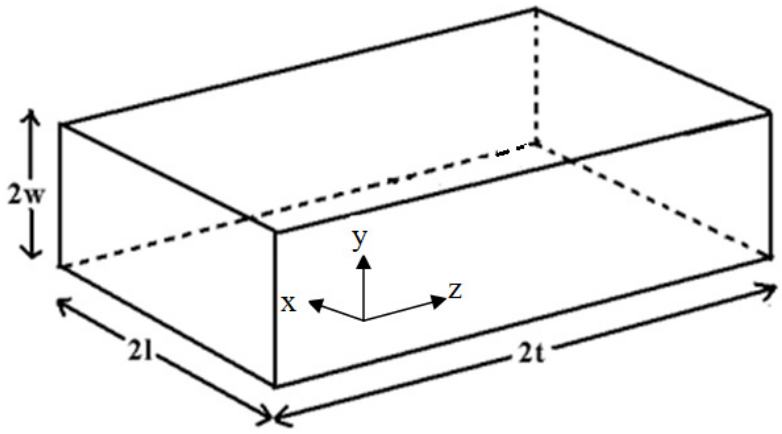

Fig. 2.6 Schematic diagram of a rectangular cavity with its dimension.

Applying the boundary condition that the tangential component of the electric field $\vec{E}_{\tan}$ vanishes at the walls of the cavity,

$$\hat{n}\times\vec{E}=0 \quad \Rightarrow \quad \hat{n}\times(\nabla\times\vec{F})=0 \tag{2.261}$$

$$\hat{n}\times\left(\nabla\times\bar{\bar{G}}\right)=0 \tag{2.262}$$

where $\vec{F}$ is the electric vector potential for magnetic current $\vec{M}$ and $\bar{\bar{G}}$ is electric dyadic potential for δ current.

$$\nabla\times\bar{\bar{G}}=\left(\hat{x}\frac{\partial}{\partial x}+\hat{y}\frac{\partial}{\partial y}+\hat{z}\frac{\partial}{\partial z}\right)\times\left(\hat{x}\hat{x}G_{xx}+\hat{y}\hat{y}G_{yy}+\hat{z}\hat{z}G_{zz}\right) \tag{2.263}$$

$$\vec{\nabla}\times\bar{\bar{G}}=\left(\hat{z}\hat{y}\frac{\partial G_{yy}}{\partial x}-\hat{y}\hat{z}\frac{\partial G_{zz}}{\partial x}\right)+\left(\hat{x}\hat{z}\frac{\partial G_{zz}}{\partial y}-\hat{z}\hat{x}\frac{\partial G_{xx}}{\partial y}\right)+\left(\hat{y}\hat{x}\frac{\partial G_{xx}}{\partial z}-\hat{x}\hat{y}\frac{\partial G_{yy}}{\partial z}\right) \tag{2.264}$$

At the wall of the cavity, x = -l and $\hat{n}=\hat{x}$,

$$\hat{n}\times\left(\vec{\nabla}\times\bar{\bar{G}}\right)=\hat{x}\times\left(\vec{\nabla}\times\bar{\bar{G}}\right)=-\hat{y}\hat{y}\frac{\partial G_{yy}}{\partial x}-\hat{z}\hat{z}\frac{\partial G_{zz}}{\partial x}+\hat{y}\hat{x}\frac{\partial G_{xx}}{\partial y}+\hat{z}\hat{x}\frac{\partial G_{xx}}{\partial z} \tag{2.265}$$

Since $\hat{n}\times\left(\nabla\times\bar{\bar{G}}\right)\Big|_{x=-l}=0$

$$\Rightarrow \frac{\partial G_{yy}}{\partial x}\Big|_{x=-l}=0,\ \frac{\partial G_{zz}}{\partial x}\Big|_{x=-l}=0,\ \frac{\partial G_{xx}}{\partial y}\Big|_{x=-l}=0,\ \frac{\partial G_{xx}}{\partial z}\Big|_{x=-l}=0 \tag{2.266}$$

Using (2.265) and (2.266) $\quad G_{xx}\Big|_{x=-l}=0$ (2.267)

Similarly, at the walls of the cavity $y=\pm w,\ G_{yy}=0$ and at $z=\pm t,\ G_{zz}=0$ and

$$\nabla\times\tilde{G}^{cty}=0$$

$$\Rightarrow\nabla\times\left(\hat{x}\hat{x}\ G_{xx}+\hat{y}\hat{y}\ G_{yy}+\hat{z}\hat{z}\ G_{zz}\right)$$
$$\Rightarrow\left(\nabla\times\hat{x}G_{xx}\right)\hat{x}+\left(\nabla\times\hat{y}G_{yy}\right)\hat{y}+\left(\nabla\times\hat{z}G_{zz}\right)\hat{z}$$
$$\Rightarrow\hat{y}\hat{x}\frac{\partial G_{xx}}{\partial z}-\hat{z}\hat{x}\frac{\partial G_{xx}}{\partial y}-\hat{x}\hat{y}\frac{\partial G_{yy}}{\partial z}+\hat{z}\hat{y}\frac{\partial G_{yy}}{\partial x}+\hat{x}\hat{z}\frac{\partial G_{zz}}{\partial y}-\hat{y}\hat{z}\frac{\partial G_{zz}}{\partial x}=0 \tag{2.268}$$

For evaluating G_{xx}, consider the boundary conditions

at $x = \pm l$, $$G_{xx} = 0 \tag{2.269}$$

at xz plane $$\nabla \times \tilde{G}^{cty} = 0 \quad \Rightarrow \quad \hat{z}\hat{x}\frac{\partial G_{xx}}{\partial y} = 0 \tag{2.270}$$

at $y = \pm w$, $$\frac{\partial G_{xx}}{\partial y} = 0 \tag{2.271}$$

Similarly in the xy plane,

$$\nabla \times \tilde{G}^{cty} = 0 \quad \Rightarrow \hat{y}\hat{x}\frac{\partial G_{xx}}{\partial z} = 0 \text{ or } \frac{\partial G_{xx}}{\partial z} = 0 \tag{2.272}$$

Expressing G_{xx} as the product of the function of three separate variables,

$$G_{xx} = g_{xx}(x)\, g_{xy}(y)\, g_{xz}(z) \tag{2.273}$$

There are two ways for expressing the solution of the individual function. One is the closed from solution and other is the series expansion in terms of its eigen-functions. Expressing $g_{xx}(x)$ and $g_{xy}(y)$ in terms of series expansion, G_{xx} can be written as:

$$\begin{aligned} G_{xx} = \sum_{m=0}^{\infty}\sum_{n=0}^{\infty} g_{xz}(z)\left[A\sin\left\{\frac{m\pi}{2l}(x+l)\right\} + B\cos\left\{\frac{m\pi}{2l}(x+l)\right\}\right] \\ \times\left[C\sin\left\{\frac{n\pi}{2w}(y+w)\right\} + D\cos\left\{\frac{n\pi}{2w}(y+w)\right\}\right] \end{aligned} \tag{2.274}$$

Employing the boundary conditions $G_{xx} = 0$ at $x = \pm l$ & $\frac{\partial G_{xx}}{\partial x} = 0$ at $y = \pm w$ in equation (2.274)

$$G_{xx}=\sum_{m=1}^{\infty}\sum_{n=0}^{\infty}g_{xx}(z)\sin\left\{\frac{m\pi}{2l}(x+l)\right\}\cos\left\{\frac{n\pi}{2w}(y+w)\right\} \tag{2.275}$$

Using the Helmholtz equation for the Green's function results in

$$\nabla^2 G_{xx}+k^2 G_{xx}=-\delta(x-x')\delta(y-y')\delta(z-z')$$

$$\Rightarrow\left(\frac{\partial^2}{\partial x^2}+\frac{\partial^2}{\partial y^2}+\frac{\partial^2}{\partial z^2}\right)G_{xx}=-\delta(x-x')\delta(y-y')\delta(z-z')-k^2G_{xx}$$

$$\Rightarrow\sum_{m=1}^{\infty}\sum_{n=0}^{\infty}\left\{-\left(\frac{m\pi}{2l}\right)^2-\left(\frac{n\pi}{2w}\right)^2+\frac{\partial^2}{\partial z^2}+k^2\right\}g_{xz}(z)\sin\left\{\frac{m\pi}{2l}(x+l)\right\}\cos\left\{\frac{n\pi}{2w}(y+w)\right\}$$
$$=-\delta(x-x')\delta(y-y')\delta(z-z')$$

$$\Rightarrow\sum_{m=1}^{\infty}\sum_{n=0}^{\infty}\left\{\frac{\partial^2}{\partial z^2}+\Gamma_{mn}^2\right\}g_{xz}(z)\sin\left\{\frac{m\pi}{2l}(x+1)\right\}\cos\left\{\frac{n\pi}{2w}(y+w)\right\}$$
$$=-\delta(x-x')\delta(y-y')\delta(z-z') \tag{2.276}$$

Where

$$\Gamma_{mn}=\sqrt{k^2-\left(\frac{m\pi}{2l}\right)^2-\left(\frac{n\pi}{2w}\right)^2} \tag{2.277}$$

$g_{xx}(z)$ can be evaluated using the orthogonal property of sine and cosine functions. Multiplying both sides of (2.276) with $\sin\left\{\frac{m'\pi}{2l}(x+l)\right\}$ and $\cos\left\{\frac{n'\pi}{2w}(y+w)\right\}$ and integrating over the entire transverse aperture gives:

$$\sum_{m=1}^{\infty}\sum_{n=0}^{\infty}\left\{\frac{\partial^2}{\partial z^2}+\Gamma_{mn}^2\right\}g_{xz}(z)\int_{-l}^{l}\sin\left\{\frac{m\pi}{2l}(x+l)\right\}\sin\left\{\frac{m'\pi}{2l}(x+l)\right\}dx\int_{-w}^{w}\cos\left\{\frac{n'\pi}{2w}(y+w)\right\}$$
$$\times\cos\left\{\frac{n'\pi}{2w}(y+w)\right\}dy=-\delta(z-z')\sin\left\{\frac{m'\pi}{2l}(x'+l)\right\}\cos\left\{\frac{n'\pi}{2w}(y'+w)\right\} \tag{2.278}$$

Equation (2.278) can be simplified using the orthogonal properties of sine and cosine terms given by (2.279) and (2.280).

$$\int_{-l}^{+l} \sin\left\{\frac{m\pi}{2l}(x+l)\right\}\sin\left\{\frac{m'\pi}{2l}(x+l)\right\}dx = \begin{cases} 0 & \text{for } m \neq m' \\ 0 & \text{for } m = m' = 0 \\ l & \text{for } m = m' \neq 0 \end{cases} \tag{2.279}$$

$$\int_{-w}^{w} \cos\left\{\frac{n\pi}{2w}(y+w)\right\}\cos\left\{\frac{n'\pi}{2w}(y+w)\right\}dy = \begin{cases} 0 & \text{for } n \neq n' \\ 2w & \text{for } n = n' = 0 \\ w & \text{for } n = n' \neq 0 \end{cases} \tag{2.280}$$

Applying (2.279) and (2.280) in (2.278) gives

$$\left\{\frac{\partial^2}{\partial z^2} + \Gamma_{mn}^2\right\} g_{xx}(z) = -\frac{\varepsilon_m \varepsilon_n}{4lw}\sin\left\{\frac{m\pi}{2l}(x'+l)\right\}\cos\left\{\frac{n\pi}{2w}(y'+w)\right\}\delta(z-z') \tag{2.281}$$

The above equation is solved using closed form method. For solving, (2.281) is broken into two parts around the source point, at $z = z'$. Since the right hand side contains a delta function, the equation becomes zero at all points, except at $z = z'$. Hence,

$$\left[\frac{\partial^2}{\partial z^2} + \Gamma_{mn}^2\right] g_{xx}^{I}(z) = 0 \text{ at } z < z' \tag{2.282}$$

$$\left[\frac{\partial^2}{\partial z^2} + \Gamma_{mn}^2\right] g_{xx}^{II}(z) = 0 \text{ at } z > z' \tag{2.283}$$

Solving (2.282) and (2.283) gives

$$g_{xx}^{I}(z) = A\,\sin\left\{\Gamma_{mn}(z+t)\right\} + B\cos\left\{\Gamma_{mn}(z+t)\right\} \tag{2.284}$$

$$g_{xx}^{II}(z) = C\,\sin\left\{\Gamma_{mn}(z-t)\right\} + D\cos\left\{\Gamma_{mn}(z-t)\right\} \tag{2.285}$$

By (2.273), $\frac{\partial g_{xx}(z)}{\partial z}=0$ at $z=-t$, hence $A = 0$. Similarly $\frac{\partial g_{xx}(z)}{\partial z} = 0$ at $z = t$, hence $C = 0$. Therefore (2.284) and (2.285) become:

$$g_{xx}^{I}(z)=B\cos\left\{\Gamma_{mn}(z+t)\right\} \tag{2.286}$$

$$g_{xx}^{II}(z)=D\cos\left\{\Gamma_{mn}(z-t)\right\} \tag{2.287}$$

Applying the continuity condition of g_{xx} at $z=z'$ gives:

$$D=B\frac{\cos\left\{\Gamma_{mn}(z'+t)\right\}}{\cos\left\{\Gamma_{mn}(z'-t)\right\}} \tag{2.288}$$

Substituting (2.288) in (2.287)

$$g_{xx}^{II}(z)=B\frac{\cos\left\{\Gamma_{mn}(z'+t)\right\}}{\cos\left\{\Gamma_{mn}(z'-t)\right\}}\cos\left\{\Gamma_{mn}(z-t)\right\} \tag{2.289}$$

Applying the discontinuity condition of $\frac{\partial g_{xx}}{\partial z}$ at $z=z'$,

$$\left.\frac{\partial g_{xx}^{II}(z)}{\partial z}\right|_{z=z'} - \left.\frac{\partial g_{xx}^{I}(z)}{\partial z}\right|_{z=z'} = -\frac{\varepsilon_m\varepsilon_n}{4lw}\sin\left\{\frac{m\pi}{2l}(x'+l)\right\}\cos\left\{\frac{n\pi}{2w}(y'+w)\right\} \tag{2.290}$$

Taking the derivative of (2.289) and comparing with (2.290)

$$B=-\frac{\varepsilon_m\varepsilon_n}{4lw}\sin\left\{\frac{m\pi}{2l}(x'+l)\right\}\cos\left\{\frac{n\pi}{2w}(y'+w)\right\}\frac{\cos\left\{\Gamma_{mn}(z'-t)\right\}}{\Gamma_{mn}\sin\left\{2\Gamma_{mn}t\right\}} \tag{2.291}$$

Substituting the value of B in (2.286)

$$g_{xx}^{I}(z) = -\frac{\varepsilon_m \varepsilon_n}{4lw}\sin\left\{\frac{m\pi}{2l}(x'+l)\right\}\cos\left\{\frac{n\pi}{2w}(y'+w)\right\} \times \frac{\cos\{\Gamma_{mn}(z'-t)\}\cos\{\Gamma_{mn}(t+z)\}}{\Gamma_{mn}\sin\{2\Gamma_{mn}t\}} \tag{2.292}$$

Substituting for B in (2.289)

$$g_{xx}^{II}(z) = -\frac{\varepsilon_m \varepsilon_n}{4lw}\sin\left\{\frac{m\pi}{2l}(x'+l)\right\}\cos\left\{\frac{n\pi}{2w}(y'+w)\right\} \times \frac{\cos\{\Gamma_{mn}(z-t)\}\cos\{\Gamma_{mn}(t+z')\}}{\Gamma_{mn}\sin\{2\Gamma_{mn}t\}} \tag{2.293}$$

Substituting (2.292) and (2.293) along with the expression of $g_{xx}(x)$ and $g_{xx}(y)$, G_{xx} (2.273) can be written as:

$$G_{xx} = \sum_{m=1}^{\infty}\sum_{n=0}^{\infty}\frac{\varepsilon_m \varepsilon_n}{4lw}\sin\left\{\frac{m\pi}{2l}(x+l)\right\}\sin\left\{\frac{m\pi}{2l}(x'+l)\right\}\cos\left\{\frac{n\pi}{2w}(y+w)\right\}\cos\left\{\frac{n\pi}{2w}(y'+w)\right\} \times \frac{-1}{\Gamma_{mn}\sin\{2\Gamma_{mn}t\}}\begin{cases}\cos\{\Gamma_{mn}(z-t)\}\cos\{\Gamma_{mn}(z'+t)\} & z > z' \\ \cos\{\Gamma_{mn}(z'-t)\}\cos\{\Gamma_{mn}(z+t)\} & z < z'\end{cases} \tag{2.294}$$

Similarly, for evaluating G_{yy}, the following boundary conditions are used. At

$$x = \pm l, \quad \frac{\partial G_{yy}}{\partial x} = 0 \tag{2.295a}$$

$$y = \pm w, \quad G_{yy} = 0 \tag{2.295b}$$

$$z = \pm t, \quad \frac{\partial G_{yy}}{\partial z} = 0 \tag{2.295c}$$

Proceeding in the similar fashion for evaluating G_{xx}, the term G_{yy} can be written as

$$G_{yy}=\sum_{m=0}^{\infty}\sum_{n=1}^{\infty}\frac{\varepsilon_m\varepsilon_n}{4lw}\cos\left\{\frac{m\pi}{2l}(x+l)\right\}\cos\left\{\frac{m\pi}{2l}(x'+l)\right\}\sin\left\{\frac{n\pi}{2w}(y+w)\right\}\sin\left\{\frac{n\pi}{2w}(y''+w)\right\}$$
$$\frac{-1}{\Gamma_{mn}\sin\{2\Gamma_{mn}t\}}\begin{cases}\cos\{\Gamma_{mn}(z-t)\}\cos\{\Gamma_{mn}(z'+t)\} & z>z'\\ \cos\{\Gamma_{mn}(z'-t)\}\cos\{\Gamma_{mn}(z+t)\} & z<z'\end{cases} \quad (2.296)$$

For the evaluation of G_{zz}, the following boundary conditions are used. At

$$x=\pm l,\ \frac{\partial G_{zz}}{\partial x}=0 \quad (2.297a)$$

$$y=\pm w,\ \frac{\partial G_{zz}}{\partial y}=0 \quad (2.297b)$$

$$z=\pm t,\ G_{zz}=0 \quad (2.297c)$$

Using these boundary conditions, G_{zz} can be obtained as:

$$G_{zz}=\sum_{m=0}^{\infty}\sum_{n=1}^{\infty}\frac{\varepsilon_m\varepsilon_n}{4lw}\cos\left\{\frac{m\pi}{2l}(x+l)\right\}\cos\left\{\frac{m\pi}{2l}(x'+l)\right\}\cos\left\{\frac{n\pi}{2w}(y+w)\right\}$$
$$\times\cos\left\{\frac{n\pi}{2w}(y'+w)\right\}\frac{-1}{\Gamma_{mn}\sin\{2\Gamma_{mn}t\}}\begin{cases}\sin\{\Gamma_{mn}(z-t)\}\sin\{\Gamma_{mn}(z'+t)\} & z>z'\\ \sin\{\Gamma_{mn}(z'-t)\}\sin\{\Gamma_{mn}(z+t)\} & z<z'\end{cases} \quad (2.298)$$

The Dyadic Green's function of the electric vector potential of a rectangular cavity can be expressed using (2.294), (2.296) and (2.298). With the cavity Green's function of electric vector potential being determined, the next step is to derive the expressions for the scattered magnetic fields inside the rectangular cavity due to magnetic currents. The scattered magnetic field can be determined in terms of the electric vector potential using (2.197) and is given as follows:

$$\vec{H}=\frac{j}{\omega\mu}\left[\nabla\times\vec{E}+\vec{M}\right]=\frac{j}{\omega\mu}\left[-\nabla\times\nabla\times\vec{F}+\vec{M}\right] \quad (2.299)$$

Using (2.206) and (2.210) in (2.299) and simplifying,

$$\vec{H} = -j\omega\varepsilon\left[\bar{\bar{I}} + \frac{\nabla\nabla}{k^2}\right]\vec{F} \tag{2.300}$$

Expanding $\vec{H}$ into its components:

$$H = -j\omega\varepsilon\begin{bmatrix}\left[F_x + \frac{1}{k^2}\frac{\partial}{\partial x}\left\{\frac{\partial F_x}{\partial x} + \frac{\partial F_y}{\partial y} + \frac{\partial F_z}{\partial z}\right\}\right]\hat{u}_x \\ +\left[F_y + \frac{1}{k^2}\frac{\partial}{\partial y}\left\{\frac{\partial F_x}{\partial x} + \frac{\partial F_y}{\partial y} + \frac{\partial F_z}{\partial z}\right\}\right]\hat{u}_y \\ +\left[F_z + \frac{1}{k^2}\frac{\partial}{\partial z}\left\{\frac{\partial F_x}{\partial x} + \frac{\partial F_y}{\partial y} + \frac{\partial F_z}{\partial z}\right\}\right]\hat{u}_z\end{bmatrix} \tag{2.301}$$

With no F_z component present, the like terms on both sides gives:

$$H_x^{cav} = -j\omega\varepsilon\left[\left\{1 + \frac{1}{k^2}\frac{\partial^2}{\partial x^2}\right\}F_x + \frac{1}{k^2}\frac{\partial^2 F_y}{\partial x\partial y}\right] = H_x^{cav}\left(M_x\right) + H_x^{cav}\left(M_y\right) \tag{2.302a}$$

$$H_y^{cav} = -j\omega\varepsilon\left[\frac{1}{k^2}\frac{\partial^2 F_x}{\partial y\partial x} + \left\{1 + \frac{1}{k^2}\frac{\partial^2}{\partial y^2}\right\}F_y\right] = H_y^{cav}\left(M_x\right) + H_y^{cav}\left(M_y\right) \tag{2.302b}$$

$$H_z^{cav} = -\frac{j\omega\varepsilon}{k^2}\left[\frac{\partial^2 F_x}{\partial z\partial x} + \frac{\partial^2 F_y}{\partial z\partial y}\right] = H_z^{cav}\left(M_x\right) + H_z^{cav}\left(M_y\right) \tag{2.302c}$$

Being established the relationship between the scattered magnetic fields and the electric vector potentials; the next step is to determine the electric vector potentials from cavity Green's functions and the unknown magnetic currents.

$$F_x = \iint_{Aperture} G_{xx} M_x ds' \text{ where } M_x = \hat{u}_y E_y \times \hat{u}_z = \hat{u}_x E_y \tag{2.303a}$$

$$F_y = \iint_{Aperture} G_{yy} M_y ds' \text{ where } \mathrm{M_y} = \hat{u}_x E_x \times \hat{u}_z = -\hat{u}_y E_x \tag{2.303b}$$

Substituting for G_{xx} and M_x in (2.303a)

$$F_x = \sum_{p=1}^{M} E_{yp}^{i} \sum_{m=1}^{\infty}\sum_{n=0}^{\infty} \frac{\varepsilon_m \varepsilon_n}{4lw} \sin\left\{\frac{m\pi}{2l}(x+l)\right\} \cos\left\{\frac{n\pi}{2w}(y+w)\right\} \int_{x_{wi}-L_i}^{x_{wi}+L_i} \sin\left\{\frac{m\pi}{2l}(x'+l)\right\}$$
$$\times \sin\left\{\frac{p\pi}{2L}(x'-x_{wi}+L_i)\right\} dx_0 \int_{y_{wi}-W_i}^{y_{wi}+W_i} \cos\left\{\frac{n\pi}{2w}(y'+w)\right\} dy_0$$
$$\times \frac{-1}{\Gamma_{mn}\sin\{2\Gamma_{mn}t\}} \begin{cases} \cos\{\Gamma_{mn}(z-t)\}\cos\{\Gamma_{mn}(z'+t)\} & z > z' \\ \cos\{\Gamma_{mn}(z'-t)\}\cos\{\Gamma_{mn}(z+t)\} & z < z' \end{cases}$$

$$F_x = \sum_{p=1}^{M} E_{yp}^{i} \sum_{m=1}^{\infty}\sum_{n=0}^{\infty} \frac{\varepsilon_m \varepsilon_n L_i W_i}{2lw} \sin\left\{\frac{m\pi}{2l}(x+l)\right\} \cos\left\{\frac{n\pi}{2w}(y+w)\right\} \cos\left\{\frac{n\pi}{2w}(y_{wi}+w)\right\}$$
$$\times \sin c\left\{\frac{n\pi}{2w}W_i\right\} F_x(p) \frac{(-1)}{\Gamma_{mn}\sin\{2\Gamma_{mn}t\}} \begin{cases} \cos\{\Gamma_{mn}(z-t)\}\cos\{\Gamma_{mn}(z_0+t)\} & z>z_0 \\ \cos\{\Gamma_{mn}(z_0-t)\}\cos\{\Gamma_{mn}(z+t)\} & z<z_0 \end{cases} \quad (2.304)$$

Similarly

$$F_y = \sum_{p=1}^{M} E_{xp}^{i} \sum_{m=0}^{\infty}\sum_{n=1}^{\infty} \frac{\varepsilon_m \varepsilon_n}{4lw} \cos\left\{\frac{m\pi}{2l}(x+l)\right\} \sin\left\{\frac{n\pi}{2w}(y+w)\right\} \times$$
$$\int_{x_{wi}-L_i}^{x_{wi}+L_i} \cos\left\{\frac{m\pi}{2l}(x'+l)\right\} dx' \int_{y_{wi}-W_i}^{y_{wi}+W_i} \cos\left\{\frac{n\pi}{2w}(y'+w)\right\} \sin\left\{\frac{p\pi}{2W_i}(y'-y_{wi}+W_i)\right\} dy'$$
$$\times \frac{-1}{\Gamma_{mn}\sin\{2\Gamma_{mn}t\}} \begin{cases} \cos\{\Gamma_{mn}(z-t)\}\cos\{\Gamma_{mn}(z'+t)\} & z > z' \\ \cos\{\Gamma_{mn}(z'-t)\}\cos\{\Gamma_{mn}(z+t)\} & z < z' \end{cases}$$

On simplifying F_y becomes

$$F_y = \sum_{p=1}^{M} E_{xp}^{i} \sum_{m=0}^{\infty}\sum_{n=1}^{\infty} \frac{\varepsilon_m \varepsilon_n L_i W_i}{2lw} \cos\left\{\frac{m\pi}{2l}(x+l)\right\} \sin\left\{\frac{n\pi}{2w}(y+w)\right\} \cos\left\{\frac{m\pi}{2l}(x_{wi}+l)\right\}$$
$$\times \sin c\left\{\frac{m\pi}{2l}L_i\right\} F_y(p) \frac{(-1)}{\Gamma_{mn}\sin\{2\Gamma_{mn}t\}} \begin{cases} \cos\{\Gamma_{mn}(z-t)\}\cos\{\Gamma_{mn}(z_0+t)\} & z>z_0 \\ \cos\{\Gamma_{mn}(z_0-t)\}\cos\{\Gamma_{mn}(z+t)\} & z<z_0 \end{cases} \quad (2.305)$$

$F_x(p)$ and $F_y(p)$ are given in (2.249) and (2.250) respectively. Transverse components of the scattered magnetic fields inside the cavity can be computed using (2.302a) and (2.302b).

$$H_x^{cav}\left(M_x^i\right)=-\frac{j\omega\varepsilon}{k^2}\sum_{p=1}^{M}E_{yp}^i\sum_{m=1}^{\infty}\sum_{n=0}^{\infty}\frac{\varepsilon_m\varepsilon_n L_i W_i}{2lw}\left\{k^2-\left(\frac{m\pi}{2l}\right)^2\right\}\sin\left\{\frac{m\pi}{2l}(x+l)\right\}$$
$$\times\cos\left\{\frac{n\pi}{2w}(y+w)\right\}\cos\left\{\frac{n\pi}{2w}(y_w+w)\right\}\sin c\left\{\frac{n\pi}{2w}W_i\right\}F_x(p)$$
$$\times\frac{(-1)}{\Gamma_{mn}\sin\{2\Gamma_{mn}t\}}\begin{cases}\cos\{\Gamma_{mn}(z-t)\}\cos\{\Gamma_{mn}(z_0+t)\} & z>z_0\\ \cos\{\Gamma_{mn}(z_0-t)\}\cos\{\Gamma_{mn}(z+t)\} & z<z_0\end{cases} \tag{2.306}$$

$$H_x^{cav}\left(M_y^i\right)=\frac{j\omega\varepsilon}{k^2}\sum_{p=1}^{M}E_{xp}^i\sum_{m=0}^{\infty}\sum_{n=1}^{\infty}\frac{\varepsilon_m\varepsilon_n L_i W_i}{2lw}\frac{m\pi}{2l}\frac{n\pi}{2w}\sin\left\{\frac{m\pi}{2l}(x+l)\right\}$$
$$\times\cos\left\{\frac{n\pi}{2w}(y+w)\right\}\cos\left\{\frac{m\pi}{2l}(x_w+l)\right\}\sin c\left\{\frac{m\pi}{2l}L_i\right\}F_y(p)$$
$$\times\frac{(-1)}{\Gamma_{mn}\sin\{2\Gamma_{mn}t\}}\begin{cases}\cos\{\Gamma_{mn}(z-t)\}\cos\{\Gamma_{mn}(z_0+t)\} & z>z_0\\ \cos\{\Gamma_{mn}(z_0-t)\}\cos\{\Gamma_{mn}(z+t)\} & z<z_0\end{cases} \tag{2.307}$$

$$H_y^{cav}\left(M_x^i\right)=\frac{j\omega\varepsilon}{k^2}\sum_{p=1}^{M}E_{yp}^i\sum_{m=1}^{\infty}\sum_{n=0}^{\infty}\frac{\varepsilon_m\varepsilon_n L_i W_i}{2lw}\frac{m\pi}{2l}\frac{n\pi}{2w}\cos\left\{\frac{m\pi}{2l}(x+l)\right\}$$
$$\times\sin\left\{\frac{n\pi}{2w}(y+w)\right\}\cos\left\{\frac{n\pi}{2w}(y_w+w)\right\}\sin c\left\{\frac{n\pi}{2w}W_i\right\}F_x(p)\times$$
$$\times\frac{(-1)}{\Gamma_{mn}\sin\{2\Gamma_{mn}t\}}\begin{cases}\cos\{\Gamma_{mn}(z-t)\}\cos\{\Gamma_{mn}(z_0+t)\} & z>z_0\\ \cos\{\Gamma_{mn}(z_0-t)\}\cos\{\Gamma_{mn}(z+t)\} & z<z_0\end{cases} \tag{2.308}$$

$$H_y^{cav}\left(M_y^i\right)=-\frac{j\omega\varepsilon}{k^2}\sum_{p=1}^{M}E_{xp}^i\sum_{m=0}^{\infty}\sum_{n=1}^{\infty}\frac{\varepsilon_m\varepsilon_n L_i W_i}{2lw}\left\{k^2-\left(\frac{n\pi}{2w}\right)^2\right\}\cos\left\{\frac{m\pi}{2l}(x+l)\right\}$$
$$\times\sin\left\{\frac{n\pi}{2w}(y+w)\right\}\cos\left\{\frac{m\pi}{2l}(x_w+l)\right\}\sin c\left\{\frac{m\pi}{2w}L_i\right\}F_y(p)$$
$$\times\frac{(-1)}{\Gamma_{mn}\sin\{2\Gamma_{mn}t\}}\begin{cases}\cos\{\Gamma_{mn}(z-t)\}\cos\{\Gamma_{mn}(z_0+t)\} & z>z_0\\ \cos\{\Gamma_{mn}(z_0-t)\}\cos\{\Gamma_{mn}(z+t)\} & z<z_0\end{cases} \tag{2.309}$$

2.7 Analysis of waveguide shorted end slot coupled HDRA

The waveguide shorted end slot coupled HDRA can be analyzed by solving (2.1) and (2.2). For solving matrix equations, scattered magnetic field inside the waveguide, slot and HDRA are required. Expressions for the field components are derived in the previous sections. To solve the matrix equations, Galerkin's procedure of MoM is used and the final expressions for elements of the matrix are as follows.

$$\left\langle H_x^{inc}, e_q^1(x)\right\rangle = -2W_i L_i Y_0 \left[\sin\left\{\frac{\pi x_w}{2a}+\frac{q\pi}{2}\right\}\operatorname{sinc}\left\{\frac{\pi L}{2a}+\frac{q\pi}{2}\right\} - \sin\left\{\frac{\pi x_w}{2a}-\frac{q\pi}{2}\right\}\operatorname{sinc}\left\{\frac{\pi L}{2a}-\frac{q\pi}{2}\right\}\right] \tag{2.310}$$

$$\left\langle \left[H_x^{WG}\left(M_x^i\right)\right], e_q^i(x)\right\rangle = -W_i^2 L_i^2 \sum_{p=1}^{M} E_{yp}^i \sum_{m}^{\infty}\sum_{n}^{\infty} \frac{ab}{(mb)^2+(na)^2}\left[\frac{m^2}{a}\varepsilon_m\varepsilon_n Y_{mn}^e + \frac{4n}{b^2}Y_{mn}^m\right] \times\cos^2\left\{\frac{n\pi}{2b}(y_w+b)\right\}\operatorname{sinc}^2\left\{\frac{n\pi}{2b}W_1\right\}F_x(p)F_x(q) \tag{2.311}$$

$$\left\langle H_x^{cav}\left(M_x^s\right), e_q^o(x)\right\rangle = -\frac{j\omega\varepsilon}{k^2}\frac{L_s W_s L_o W_o}{L_s W_s}\sum_{p=1}^{M} E_{yp}^i \sum_{m=1}^{\infty}\sum_{n=0}^{\infty}\varepsilon_m\varepsilon_n\left\{k^2-\left(\frac{m\pi}{2L_s}\right)^2\right\} \times\cos\left\{\frac{n\pi}{2W_s}(y_{ws}+W_s)\right\}\operatorname{sin}c\left\{\frac{n\pi}{2W_s}W_s\right\}\cos\left\{\frac{n\pi}{2W_s}(y_{wo}+W_s)\right\}\operatorname{sin}c\left\{\frac{n\pi}{2W_s}W_o\right\} \times\frac{\{-F_{xs}(p)F_{xo}(q)\}}{\Gamma_{mn}\sin\{2\Gamma_{mn}t\}}\begin{cases}\cos\{\Gamma_{mn}(z-t)\}\cos\{\Gamma_{mn}(z_0+t)\} & z>z_0\\ \cos\{\Gamma_{mn}(z_0-t)\}\cos\{\Gamma_{mn}(z+t)\} & z<z_0\end{cases} \tag{2.312}$$

$$\left\langle \left[H_x^{DRA}(\bar{M}_x^2)\right], e_q^2(x)\right\rangle = \left\langle \left[G_{spec}\right], e_q^2(x)\right\rangle + \iint_{slot}\iint_{slot} G_{HS} e_p^2(x') e_q^2(x)\, ds' ds \tag{2.313}$$

In the present problem of waveguide shorted end slot coupled HDRA, $L_s = L_o = L$ and $W_s = W_o = W$. The second part of the integration in (2.313) is directly computed by quad integral in the program. The first part of (2.313) is simplified as:

$$\left\langle \left[G_{spec} \right], e_q^2(x) \right\rangle = -\frac{4W^2L^2}{\pi^2 k\eta} \int_{-\infty}^{\infty}\int_{-\infty}^{\infty} \frac{k^2 - k_x^2}{\left(k^2 - k_x^2 - k_y^2\right)^{1/2}} \mathrm{sinc}^2\left(k_y W\right) \frac{\begin{Bmatrix} \sin^2(k_x L) & \text{p,q both even} \\ \cos^2(k_x L) & \text{p,q both odd} \\ 0 & \text{otherwise} \end{Bmatrix}}{\frac{p\pi}{2}\left\{1-\left(\frac{2Lk_x}{p\pi}\right)^2\right\}\frac{q\pi}{2}\left\{1-\left(\frac{2Lk_x}{q\pi}\right)^2\right\}} dk_x dk_y \tag{2.314}$$

To carry out the integral in the spectral domain, certain substitutions are made to obtain the real and imaginary parts of the integral. The real part is obtained by evaluating the integral given by (2.314) for $k_x^2 + k_y^2 \le k^2$, and the imaginary part by evaluating the integral for $k_x^2 + k_y^2 \ge k^2$. These two regions correspond to visible region (radiation field) and invisible region (evanescent field) respectively.

In the visible region, $k_x^2 + k_y^2 \le k^2$

$$k_x = k\sin\theta\cos\phi \tag{2.315a}$$

$$k_y = k\sin\theta\sin\phi \tag{2.315b}$$

$$dk_x dk_y = k^2 \sin\theta\cos\theta d\theta d\phi \tag{2.315c}$$

In the invisible region, $k_x^2 + k_y^2 \ge k^2$

$$k_x = k\cosh\theta\cos\phi \tag{2.316a}$$

$$k_y = k\cosh\theta\sin\phi \tag{2.316b}$$

$$dk_x dk_y = k^2 \sinh\theta\cosh\theta d\theta d\phi \tag{2.316c}$$

After making the substitution using the above equations, the modified expression of equation (2.314) is

$$\left\langle \left[G_{spc} \right], e_q^2(x) \right\rangle \Big|_{visible\ region} = -\frac{16W^2L^2}{\lambda^2\eta} \int_{\theta=0}^{\pi/2} \int_{\phi=0}^{2\pi} \left(1 - \sin^2\theta\cos^2\phi\right) sinc^2\left(Wk\sin\theta\sin\phi\right) \frac{\begin{Bmatrix} \sin^2\left(Lk\sin\theta\cos\phi\right) & for\ p,\ q\ both\ even \\ \cos^2\left(Lk\sin\theta\cos\phi\right) & for\ p,\ q\ both\ odd \\ 0 & otherwise \end{Bmatrix}}{\frac{p\pi}{2}\frac{q\pi}{2}\left\{1-\left(\frac{2Lk\sin\theta\cos\phi}{p\pi}\right)^2\right\}\left\{1-\left(\frac{2Lk\sin\theta\cos\phi}{q\pi}\right)^2\right\}} \sin\theta d\theta d\phi \tag{2.317}$$

$$\left\langle \left[G_{spc} \right], e_q^2(x) \right\rangle \Big|_{invisible\ region} = -j\frac{16W^2L^2}{\lambda^2\eta} \int_{\theta=0}^{\infty} \int_{\phi=0}^{2\pi} \left(1 - \cosh^2\theta\cos^2\phi\right) sinc^2\left(Wk\cosh\theta\sin\phi\right) \frac{\begin{Bmatrix} \sin^2\left(Lk\cosh\theta\cos\phi\right) & for\ p,\ q\ both\ even \\ \cos^2\left(Lk\cosh\theta\cos\phi\right) & for\ p,\ q\ both\ odd \\ 0 & otherwise \end{Bmatrix}}{\frac{p\pi}{2}\frac{q\pi}{2}\left\{1-\left(\frac{2Lk\cosh\theta\cos\phi}{p\pi}\right)^2\right\}\left\{1-\left(\frac{2Lk\cosh\theta\cos\phi}{q\pi}\right)^2\right\}} \cosh\theta d\theta d\phi \tag{2.318}$$

2.7.1 Evaluation of Reflection Coefficient

To determine the reflection coefficient, we decouple the sources, one at $-\infty$ in the feed waveguide and the other at the window. The incident electric field due to TE_{10} excitation at the z = 0 plane is:

$$E_y^{inc} = \cos\left(\frac{\pi x}{2a}\right) \tag{2.319}$$

When the window aperture is shorted, the electric field is the field reflected by the electric short circuit and is given by,

$$E_y^{ref} = -\cos\left(\frac{\pi x}{2a}\right) \tag{2.320}$$

When the generator in the feed waveguide is removed and replaced by a perfect match, the electric field for the dominant TE_{10} mode scattered by the window into the waveguide is derived from (2.253) by substituting $m = 1$ and $n = 0$, at the $z = 0$ plane as:

$$E_y^1 = \sum_{p=1}^{M} E_{yp}^1 \frac{WL}{ab}\left[\cos\left\{\frac{\pi}{2}\left(-\frac{x_w}{a}+p-1\right)\right\}\operatorname{sinc}\left\{\frac{\pi L}{2}\left(\frac{p}{L_1}-\frac{1}{a}\right)\right\}\right.$$
$$\left.-\cos\left\{\frac{\pi}{2}\left(\frac{x_w}{a}+p+1\right)\right\}\operatorname{sinc}\left\{\frac{\pi L}{2}\left(\frac{p}{L}+\frac{1}{a}\right)\right\}\right]\cos\left(\frac{\pi x}{2a}\right) \tag{2.321}$$

Reflection coefficient Γ can be expressed as:

$$\Gamma = \frac{E_y^1 + E_y^{ref}}{E_y^{inc}} = -1 + \frac{WL}{ab}\sum_{p=1}^{M} E_{yp}^1\left[\cos\left\{\frac{\pi}{2}\left(-\frac{x_w}{a}+p-1\right)\right\}\operatorname{sinc}\left\{\frac{\pi L}{2}\left(\frac{p}{L}-\frac{1}{a}\right)\right\}\right.$$
$$\left.-\cos\left\{\frac{\pi}{2}\left(\frac{x_w}{a}+p+1\right)\right\}\operatorname{sinc}\left\{\frac{\pi L_i}{2}\left(\frac{p}{L}+\frac{1}{a}\right)\right\}\right] \tag{2.322}$$

The slot loaded HDRA can be characterized as a shunt load to the feed waveguide. The normalized admittance and impedance are given by the following relations:

$$Y = \frac{1-\Gamma}{1+\Gamma} \tag{2.323}$$

$$Z = \frac{1+\Gamma}{1-\Gamma} \tag{2.324}$$

The coupled power can be computed using

$$Pc / Pin = 1 - |\Gamma|^2 \tag{2.325}$$

2.7.2 Computed Results

To analyze the waveguide shorted end slot coupled HDRA using the developed theory, an in-house MATLAB code is written with radius and permittivity of the

HDRA, dimension of the slot and cross sectional dimension of the waveguide as variables. WR90 waveguide with cross sectional dimension 22.86 mm x 10.16 mm is used for exciting the DRA in X band. Hemispherical DRA of radius a_{dr} = 7.5 mm with dielectric constant ε_r = 9.8 is used. DRA is excited in TM_{101} mode with resonant frequency 8.735 GHz. Once the resonant frequency of the HDRA is fixed, dimension of the slot plays an important role in determining the resonant frequency. Optimum value of slot dimension is 9.5 mm × 1.0 mm × 1.3 mm and the slot is kept at the center of the ground plane (x_w = y_w = 0 mm). The admittance and reflection characteristics of waveguide shorted end slot coupled HDRA by running the developed MATLAB code with optimized parameters are shown in Fig.2.7 and 2.8 respectively. The admittance plot reveals that the susceptance is always inductive, and it never touches the zero value for the entire frequency band. Due to this inductive susceptance, reflection coefficient is found to be very high. Therefore coupling enhancement techniques are to be developed, which is the major objective of this thesis.

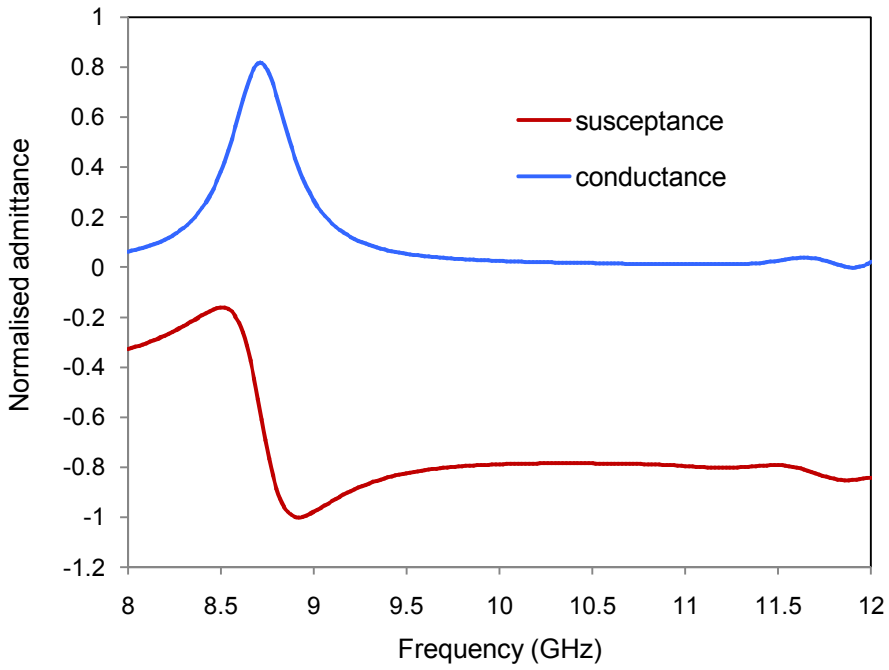

Fig. 2.7 Normalized input admittance of waveguide shorted end slot coupled HDRA with slot length $2L$ = 9.5 mm, slot width $2W$ = 1.0 mm, slot thickness $2t$ = 1.3 mm, $x_w = y_w$ = 0 mm, a_{dr} = 7.5 mm and ε_r = 9.8.

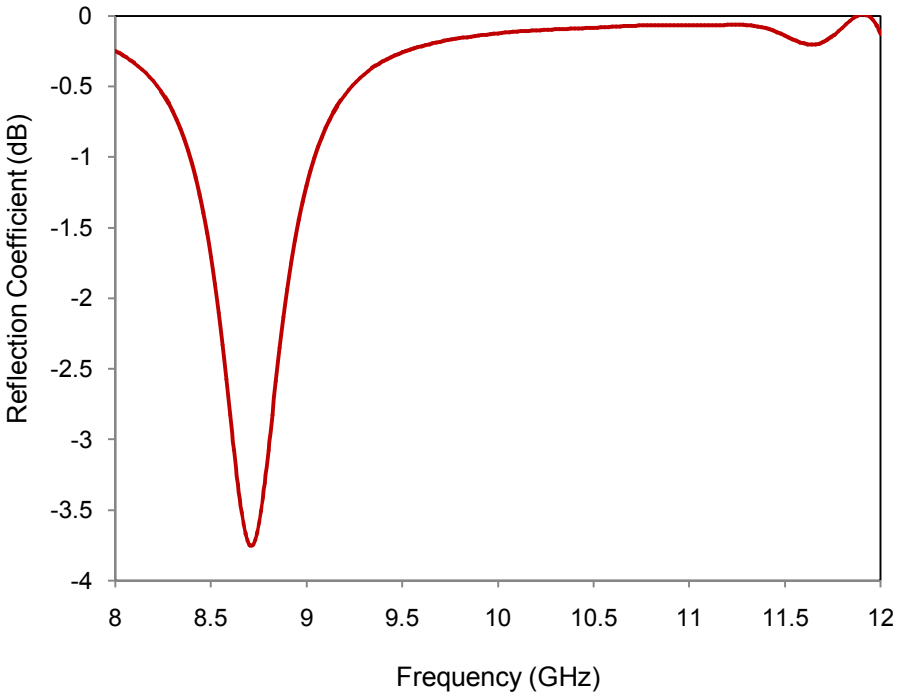

Fig. 2.8 Reflection characteristics of waveguide shorted end slot coupled HDRA with slot length $2L$ = 9.5 mm, slot width $2W$ = 1.0 mm, slot thickness $2t$ = 1.3 mm, $x_w = y_w$ = 0 mm, a_{dr} = 7.5 mm and $\varepsilon_r = 9.8$.

2.8 Inference

A waveguide shorted end slot coupled HDRA has been studied theoretically using method of moments. In order to perform the theoretical analysis using MoM, the problem is formulated by applying magnetic field boundary conditions at various apertures. The problem is represented by two equations, which involves scattered magnetic fields inside the waveguide, slot and HDRA. Expressions for scattered magnetic fields inside the waveguide, rectangular cavity (slot), and HDRA are derived in this chapter. These expressions are general and can be used for solving problems, which involves waveguide, slot and HDRA. The derived expressions are used for solving the boundary condition equations. An in house MATLAB code is developed to implement the theoretical analysis. On executing the MATLAB code, reflection and admittance characteristics are studied. From the reflection characteristics, it is evident

that the waveguide shorted end slot coupled HDRA gives only poor coupling, a maximum of 37% only. This poor coupling is due to the inductive susceptance offered by the DRA loaded slot. If the inductive susceptance can be neutralized by its capacitive counterpart, coupling could be improved. Chapter 3 gives the detailed theory and experimental results for the developed coupling enhancement technique. The expressions for the scattered magnetic fields inside the waveguide, rectangular cavity and HDRA derived in this chapter are used for the theoretical analysis of the developed coupling enhancement technique, which is discussed in chapter 3.

Chapter 3

Theoretical Analysis and Experiments of Double Step Junction Coupled Waveguide fed Hemispherical DRA

Theoretical analysis of double step junction coupled rectangular waveguide fed hemispherical dielectric resonator antenna (HDRA) using method of moments (MoM) and its experiments are presented in this chapter. The steps inserted between the rectangular waveguide and the slotted thick ground plane provide coupling enhancement. DRA is placed at the center of the ground plane. The proposed technique can implement single, dual and wide band operations. The slot kept at the centre of the ground plane provides single resonance operation. Dual and wide band operations can be obtained by giving an offset to the slot along its length, while keeping the DRA at the centre of the ground plane. Theoretical analysis is performed by solving coupled integral equations obtained by imposing magnetic field boundary conditions at various apertures using MoM. The DRA, steps and the slot are analyzed using Green's function. For waveguide, modal analysis is performed. In order to determine the effects of various design parameters, parametric study has been carried out using the developed MATLAB code. Measurements were carried out to verify the theory and reasonable agreement is obtained between them. Excellent agreement is obtained between the computed result using the developed theory and the simulation result using Ansoft HFSS. Maximum gain of the antenna is 5.7 dBi at 9.09 GHz. Radiation patterns with low cross-polarization signals in the direction of maximum radiation are obtained. The proposed coupling enhancement technique guarantees very good coupling.

3.1 Introduction

Over the last three decades, significant research has been made in various aspects of dielectric resonator antenna technology. These investigations have shown dielectric resonator antenna to be a versatile and efficient radiator, which make it an attractive alternative to traditional low gain antennas. In addition to the absence of conductor loss, DRAs offer many attractive features like small size, light weight, high power handling capability, wide bandwidth, and ease of excitation [106]. Though DRAs can be fabricated with different shapes, hemispherical dielectric resonator antenna (HDRA) is used in this work due to its simple interface with free space. Also closed form solution exists for hemispheres, which makes analytical solution easy to obtain. Different feeding mechanisms can be used with DRAs such as coaxial probe [24], [43], direct microstrip line [44-47], aperture coupled microstrip [48-52], conformal strip [53-55], and coplanar waveguide [56-59]. The main drawback of these excitation techniques is that the feed line losses become significant at high frequencies. On the other hand, metallic waveguide does not suffer from feed line losses. This is due to the metallic walls of the waveguide that provide excellent shielding between the interior and exterior regions, avoiding radiation loss even in the millimetre wave band.

DRA can be excited by slots cut at the broad wall, narrow wall or at the shorted end of the waveguide. This thesis concentrates only on waveguide shorted end slot coupled DRA. In the literature, very few studies have been reported on DRA placed at the shorted end, narrow wall and broad wall of the waveguide. Though a high permittivity DRA can be efficiently excited by an empty waveguide [70], coupling is very poor with DRA of low dielectric constants, which is illustrated in chapter 2. The reason for poor coupling of waveguide shorted end slot coupled DRA is the inductive susceptance offered by the DRA loaded slot. A second dielectric resonator placed inside the waveguide close to the slot in the ground plane provides increased coupling [73]. This technique of coupling enhancement requires a second dielectric resonator to increase the coupling that increases the cost of the system, and keeping the dielectric resonator inside the waveguide seems to be very difficult. Coupling enhancement can also be achieved by using a capacitive waveguide junction, inserted between the rectangular waveguide and ground plane [74]. But the narrow wall dimension of the

capacitive waveguide junction is very small that makes fabrication difficult at high frequencies, especially at millimetre wave frequencies. Also analytical solution is difficult, since the DRA used is rectangular in shape. Full wave analysis is not possible due to the edge shaped boundaries of the rectangular DRA that act as secondary sources. Another technique for coupling enhancement using multilayer DRA is proposed in [75]. Though this technique does not require extra matching elements, fabrication of multilayer DRA is very difficult.

To solve the coupling problem of waveguide shorted end slot coupled DRA (direct coupled DRA); two steps are inserted between the rectangular waveguide and the slotted ground plane. The steps are symmetrical with respect to the x and y axes. Steps provide the capacitive susceptance, required to neutralize the inductive susceptance of DRA loaded slot of direct coupled waveguide fed HDRA. The proposed coupling enhancement technique is easy to realize and provides flexibility in frequency tuning by varying various design parameters. Complexity and cost of the proposed technique are very less when compared with other coupling enhancement techniques reported in the literature. Theoretical analysis of the proposed double step junction coupled waveguide fed HDRA is carried out using Method of Moments (MoM). In order to perform MoM analysis, the problem is formulated by writing integral equations corresponding to the problem. By applying the continuity condition of the tangential components of the magnetic field at the interfacing apertures, expanding the unknown magnetic current densities in terms of entire domain sinusoidal basis functions and applying Galerkin's specialization of MoM, the problem can be represented using simultaneous linear equations. The linear equations are converted into matrix form and solved to get the unknown magnetic currents at various apertures. The problem consists of waveguide, steps, slot and HDRA. Steps and the slot can be considered as rectangular cavities and the magnetic field scattered inside the cavity region due to the magnetic current source is determined by using the cavity Green's function of the electric vector potential discussed in chapter 2. The magnetic fields inside the feed waveguide are determined using modal vectors and modal functions. The field coupled to the HDRA can be computed efficiently by using the particular and homogeneous parts of the Green's function. The

expressions for the scattered magnetic fields required for solving the double step junction coupled waveguide fed HDRA are derived in chapter 2.

3.2 Formulation of the problem

Coupling enhancement of waveguide shorted end slot coupled HDRA is achieved by inserting steps between the rectangular waveguide and the ground plane. The antenna configuration is shown in Fig. 3.1, where a hemispherical DRA of radius a_{dr} with dielectric constant ε_r is excited by a narrow slot of length *2L3* and width *2W3* located at

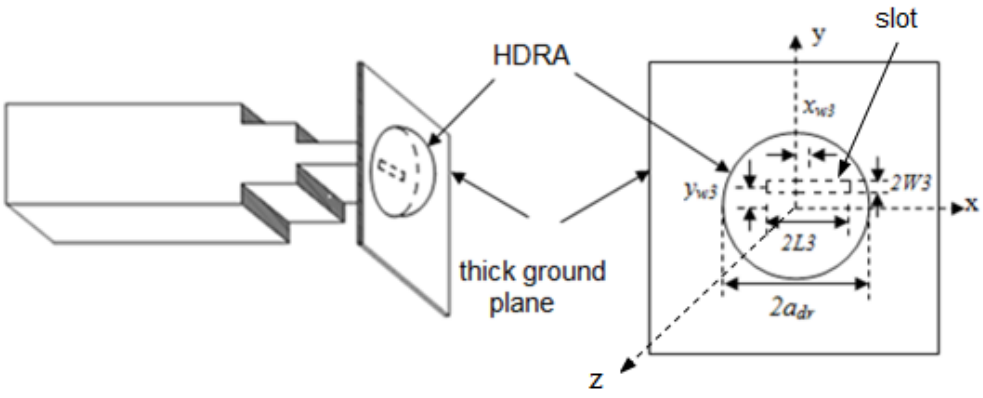

(a) (b)

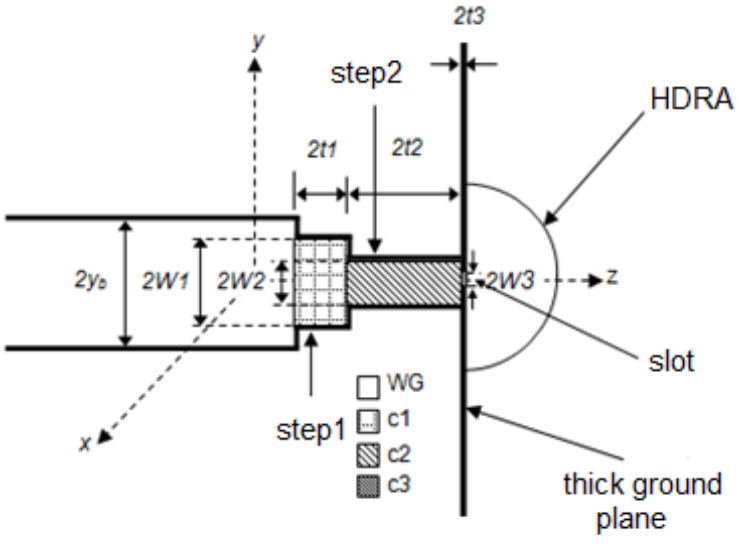

(c)

Fig. 3.1 Configuration of the double step junction coupled waveguide fed HDRA: (a) three dimensional view (b) top view (c) longitudinal cross section

a displacement x_{w3} and y_{w3} along the x and y direction respectively on the ground plane with thickness *2t3*. Width of the slot is narrow to eliminate any possible cross polarization. Due to narrow slot assumption, variation of the slot magnetic current only along the length of the slot is considered in the analysis. Two steps with thickness *2t1*, *2t2* and width *W1*, *W2* (measured with respect to y axis) are inserted above and below the *y* axis between the waveguide with cross section *2a x 2b* and the ground plane. The DRA is always kept at the centre of the ground plane. For single resonance operation, the slot is kept at the centre of the ground plane. Dual and wide band operations are achieved by placing the slot off-centered.

In the following formulations, the fields are assumed to have a time dependence of $e^{j\omega t}$, which is suppressed throughout. Invoking surface equivalence principle, the slot can be closed by a perfect electric conductor, which divides the problem into two: the slotted stair shaped waveguide and the DRA placed above the ground plane. Applying magnetic field boundary conditions at various apertures, the magnetic field *H(M)* can be expressed as:

At aperture 1 (between waveguide, WG and first step, c1)

$$-H_x^{WG}(\vec{M}_x^1)-H_x^{c1}(\vec{M}_x^1)+H_x^{WG}(\vec{M}_y^1)+H_x^{c1}(\vec{M}_y^1)+H_x^{c1}(\vec{M}_x^2)-H_x^{c1}(\vec{M}_y^2)=-2\,\mathrm{H}_x^{inc} \tag{3.1}$$

$$-H_y^{WG}(\vec{M}_x^1)-H_y^{c1}(\vec{M}_x^1)+H_y^{WG}(\vec{M}_y^1)+H_y^{c1}(\vec{M}_y^1)+H_y^{c1}(\vec{M}_x^2)-H_y^{c1}(\vec{M}_y^2)=0 \tag{3.2}$$

At aperture 2 (between first step, c1 and second step, c2)

$$H_x^{c1}(\vec{M}_x^1)-H_x^{c1}(\vec{M}_y^1)-H_x^{c1}(\vec{M}_x^2)-H_x^{c2}(\vec{M}_x^2)+H_x^{c1}(\vec{M}_y^2)+H_x^{c2}(\vec{M}_y^2)+H_x^{c2}(\vec{M}_x^3)=0 \tag{3.3}$$

$$H_y^{c1}(\vec{M}_x^1)-H_y^{c1}(\vec{M}_y^1)-H_y^{c1}(\vec{M}_x^2)-H_y^{c2}(\vec{M}_x^2)+H_y^{c1}(\vec{M}_y^2)+H_y^{c2}(\vec{M}_y^2)+H_y^{c2}(\vec{M}_x^3)=0 \tag{3.4}$$

At aperture 3 (between second step, c2 and slot, c3)

$$H_x^{c2}(\vec{M}_x^2)-H_x^{c2}(\vec{M}_y^2)-H_x^{c2}(\vec{M}_x^3)-H_x^{c3}(\vec{M}_x^3)+H_x^{c3}(\vec{M}_x^4)=0 \tag{3.5}$$

At aperture 4 (between slot, c3 and DRA)

$$H_x^{c3}(\vec{M}_x^3)-H_x^{c3}(\vec{M}_x^4)-H_x^{DRA}(\vec{M}_x^4)=0 \tag{3.6}$$

where $H^{\alpha}_{x,y}(\vec{M}^{i}_{x,y})$ (i = 1, 2, 3, 4 and α = WG, c1, c2, c3, DRA) is the magnetic field due to the magnetic current at aperture i. If E^{i}_{p} is the unknown coefficient of the electric field expansion at aperture i, the magnetic currents are assumed to be of the form:

$$\vec{M}^{i}_{x,y}(x,y) = \sum_{p=1}^{M} E^{i}_{yp,xp} e^{i}_{p}(y/x) \tag{3.7}$$

where $e^{i}_{p}(x/y)$ (p = 1, 2, 3, ..., M) is defined by

$$e^{j}_{p}(x) = \begin{cases} \sin\left[\dfrac{p\pi}{2L_i}(x - x_{wi} + L_i)\right] & x_{wi} - L_i \le x \le x_{wi} + L_i \\ & y_{wi} - W_i \le y \le y_{wi} + W_i \\ 0 \quad , & \text{elsewhere} \end{cases} \tag{3.8}$$

$$e^{j}_{p}(y) = \begin{cases} \sin\left[\dfrac{p\pi}{2W_i}(y - y_{wi} + W_i)\right] & x_{wi} - L_i \le x \le x_{wi} + L_i \\ & y_{wi} - W_i \le y \le y_{wi} + W_i \\ 0 \quad , & \text{elsewhere} \end{cases} \tag{3.9}$$

Where L_i and W_i denote the length and width of the aperture, i. Since each component of the field is described by M basis functions, 6M unknowns are to be determined from the boundary conditions. Galerkin's specialization of MoM [42] is used to obtain 6M equations from the boundary conditions. The testing functions are same as the basis functions and are given by

$$e^{i}_{q}(x) = \begin{cases} \sin\left[\dfrac{q\pi}{2L_i}(x - x_{wi} + L_i)\right], & x_{wi} - L_i \le x \le x_{wi} + L_i \\ & y_{wi} - W_i \le y \le y_{wi} + W_i \\ 0, & \text{elsewhere} \end{cases} \tag{3.10}$$

$$e^{i}_{q}(y) = \begin{cases} \sin\left[\dfrac{q\pi}{2W_i}(y - y_{wi} + W_i)\right], & x_{wi} - L_i \le x \le x_{wi} + L_i \\ & y_{wi} - W_i \le y \le y_{wi} + W_i \\ 0, & \text{elsewhere} \end{cases} \tag{3.11}$$

Applying Galerkin's procedure of MoM, (3.1) to (3.6) become:

$$\begin{aligned} &-\left\langle\left[H^{WG}_{x}(\bar{M}^{1}_{x}) + H^{c1}_{x}(\bar{M}^{1}_{x})\right], e^{1}_{q}(x)\right\rangle + \left\langle\left[H^{WG}_{x}(\bar{M}^{1}_{y}) + H^{c1}_{x}(\bar{M}^{1}_{y})\right], e^{1}_{q}(x)\right\rangle \\ &\quad + \left\langle\left[H^{c1}_{x}(\bar{M}^{2}_{x})\right], e^{1}_{q}(x)\right\rangle - \left\langle\left[H^{c1}_{x}(\bar{M}^{2}_{y})\right], e^{1}_{q}(x)\right\rangle = -\left\langle 2H^{inc}_{x}, e^{1}_{q}(x)\right\rangle \end{aligned} \tag{3.12}$$

$$-\left\langle\left[H_y^{WG}(\bar{M}_x^1)+H_y^{c1}(\bar{M}_x^1)\right],e_q^1(y)\right\rangle+\left\langle\left[H_y^{WG}(\bar{M}_y^1)+H_y^{c1}(\bar{M}_y^1)\right],e_q^1(y)\right\rangle$$
$$+\left\langle\left[H_y^{c1}(\bar{M}_x^2)\right],e_q^1(y)\right\rangle-\left\langle\left[H_y^{c1}(\bar{M}_y^2)\right],e_q^1(y)\right\rangle=0 \quad (3.13)$$

$$\left\langle H_x^{c1}(\bar{M}_x^1),e_q^2(x)\right\rangle-\left\langle H_x^{c1}(\bar{M}_y^1),e_q^2(x)\right\rangle-\left\langle\left[H_x^{c1}(\bar{M}_x^2)+H_x^{c2}(\bar{M}_x^2)\right],e_q^2(x)\right\rangle$$
$$+\left\langle\left[H_x^{c1}(\bar{M}_y^2)+H_x^{c2}(\bar{M}_y^2)\right],e_q^2(x)\right\rangle+\left\langle H_x^{c2}(\bar{M}_x^3),e_q^2(x)\right\rangle=0 \quad (3.14)$$

$$\left\langle H_y^{c1}(\bar{M}_x^1),e_q^2(y)\right\rangle-\left\langle H_y^{c1}(\bar{M}_y^1),e_q^2(y)\right\rangle-\left\langle\left[H_y^{c1}(\bar{M}_x^2)+H_y^{c2}(\bar{M}_x^2)\right],e_q^2(y)\right\rangle$$
$$+\left\langle\left[H_y^{c1}(\bar{M}_y^2)+H_y^{c2}(\bar{M}_y^2)\right],e_q^2(y)\right\rangle+\left\langle H_y^{c2}(\bar{M}_x^3),e_q^2(y)\right\rangle=0 \quad (3.15)$$

$$\left\langle H_x^{c2}(\bar{M}_x^2),e_q^3(x)\right\rangle-\left\langle H_x^{c2}(\bar{M}_y^2),e_q^3(x)\right\rangle-\left\langle\left[H_x^{c2}(\bar{M}_x^3)+H_x^{c3}(\bar{M}_x^3)\right],e_q^3(x)\right\rangle$$
$$+\left\langle H_x^{c3}(\bar{M}_x^4),e_q^3(x)\right\rangle=0 \quad (3.16)$$

$$\left\langle H_x^{c3}(\bar{M}_x^3),e_q^4(x)\right\rangle-\left\langle\left[H_x^{c3}(\bar{M}_x^4)+H_x^{DRA}(\bar{M}_x^4)\right],e_q^4(x)\right\rangle=0 \quad (3.17)$$

Equations (3.12) to (3.17) can be written in matrix form as:

$$\begin{Bmatrix}[Y_{11}] & [Y_{12}] & [Y_{13}] & [Y_{14}] & [Y_{15}] & [Y_{16}]\\ [Y_{21}] & [Y_{22}] & [Y_{23}] & [Y_{24}] & [Y_{25}] & [Y_{26}]\\ [Y_{31}] & [Y_{32}] & [Y_{33}] & [Y_{34}] & [Y_{35}] & [Y_{36}]\\ [Y_{41}] & [Y_{42}] & [Y_{43}] & [Y_{44}] & [Y_{45}] & [Y_{46}]\\ [Y_{51}] & [Y_{52}] & [Y_{53}] & [Y_{54}] & [Y_{55}] & [Y_{56}]\\ [Y_{61}] & [Y_{62}] & [Y_{63}] & [Y_{64}] & [Y_{65}] & [Y_{66}]\end{Bmatrix}\begin{Bmatrix}[E_{py}^1]\\ [E_{px}^1]\\ [E_{py}^2]\\ [E_{px}^2]\\ [E_{py}^3]\\ [E_{py}^4]\end{Bmatrix}=\begin{Bmatrix}\left[2\left\langle H_x^{inc},e_q^1(x)\right\rangle\right]\\ [0]\\ [0]\\ [0]\\ [0]\\ [0]\end{Bmatrix} \quad (3.18)$$

3.3 Evaluation of Matrix Elements

The equations (3.12) to (3.17) are described in matrix form as given in (3.18). The elements of the matrix are the inner product of scattered field and the testing function. The expressions for the scattered magnetic field inside the waveguide, rectangular cavity and HDRA derived in chapter 2 are used to find out the matrix elements. The final expressions for the different components of the matrix elements are given below.

$$\left\langle H_x^{inc}, e_q^i(x)\right\rangle = -2W_iL_iY_0\left[\sin\left\{\frac{\pi x_{wi}}{2a}+\frac{q\pi}{2}\right\}\operatorname{sinc}\left\{\frac{\pi L_i}{2a}+\frac{q\pi}{2}\right\} - \sin\left\{\frac{\pi x_{wi}}{2a}-\frac{q\pi}{2}\right\}\operatorname{sinc}\left\{\frac{\pi L_i}{2a}-\frac{q\pi}{2}\right\}\right] \tag{3.19}$$

$$\left\langle\left[H_x^{WG}\left(M_x^i\right)\right], e_q^i(x)\right\rangle = -W_i^2L_i^2\sum_{p=1}^{M}E_{yp}^i\sum_m^{\infty}\sum_n^{\infty}\frac{ab}{(mb)^2+(na)^2}\left[\frac{m^2}{a^2}\varepsilon_m\varepsilon_nY_{mn}^e+\frac{4n}{b^2}Y_{mn}^m\right] \times\cos^2\left\{\frac{n\pi}{2b}(y_{wi}+b)\right\}\operatorname{sinc}^2\left\{\frac{n\pi}{2b}W_i\right\}F_x(p)F_x(q) \tag{3.20}$$

$$\left\langle\left[H_x^{WG}\left(M_y^i\right)\right], e_q^i(x)\right\rangle = W_i^2L_i^2\sum_{p=1}^{M}E_{yp}^i\sum_m^{\infty}\sum_n^{\infty}\frac{mn}{(mb)^2+(na)^2}\left[\varepsilon_m\varepsilon_nY_{mn}^e-4Y_{mn}^m\right]\cos\frac{m\pi}{2a}(x_{wi}+a) \times\cos\left\{\frac{n\pi}{2b}(y_{wi}+b)\right\}\operatorname{sinc}\left\{\frac{m\pi}{2a}L_i\right\}\operatorname{sinc}\left\{\frac{n\pi}{2b}W_i\right\}F_y(p)F_x(q) \tag{3.21}$$

$$\left\langle\left[H_y^{WG}\left(M_x^i\right)\right], e_q^j(y)\right\rangle = -W_i^2L_i^2\sum_{p=1}^{M}E_{xp}^i\sum_m^{\infty}\sum_n^{\infty}\frac{mn}{(mb)^2+(na)^2}\left[4Y_{mn}^m-\varepsilon_m\varepsilon_nY_{mn}^e\right]\cos\frac{m\pi}{2a}(x_{wi}+a) \times\cos\left\{\frac{n\pi}{2b}(y_{wi}+b)\right\}\operatorname{sinc}\left\{\frac{m\pi}{2a}L_i\right\}\operatorname{sinc}\left\{\frac{n\pi}{2b}W_i\right\}F_x(p)F_y(q) \tag{3.22}$$

$$\left\langle\left[H_y^{WG}\left(M_y^i\right)\right], e_q^i(y)\right\rangle = W_i^2L_i^2\sum_{p=1}^{M}E_{xp}^i\sum_m^{\infty}\sum_n^{\infty}\frac{ab}{(mb)^2+(na)^2}\left[\frac{n^2}{b^2}\varepsilon_m\varepsilon_nY_{mn}^e+\frac{4m^2}{a^2}Y_{mn}^m\right] \times\cos^2\left\{\frac{m\pi}{2a}(x_{wi}+a)\right\}\operatorname{sinc}^2\left\{\frac{m\pi}{2a}L_i\right\}F_y(p)F_y(q) \tag{3.23}$$

$$\left\langle H_x^{cav}\left(M_x^s\right), e_q^o(x)\right\rangle = -\frac{j\omega\varepsilon}{k^2}\frac{L_sW_sL_oW_o}{L_sW_s}\sum_{p=1}^{M}E_{yp}^i\sum_{m=1}^{\infty}\sum_{n=0}^{\infty}\varepsilon_m\varepsilon_n\left\{k^2-\left(\frac{m\pi}{2L_s}\right)^2\right\} \times\cos\left\{\frac{n\pi}{2W_s}(y_{ws}+W_s)\right\}\operatorname{sinc}\left\{\frac{n\pi}{2W_s}W_s\right\}\cos\left\{\frac{n\pi}{2W_s}(y_{wo}+W_s)\right\}\operatorname{sinc}\left\{\frac{n\pi}{2W_s}W_o\right\} \times\frac{\{-F_{xs}(p)F_{xo}(q)\}}{\Gamma_{mn}\sin\{2\Gamma_{mn}t\}}\begin{cases}\cos\{\Gamma_{mn}(z-t)\}\cos\{\Gamma_{mn}(z_0+t)\} & z>z_0\\ \cos\{\Gamma_{mn}(z_0-t)\}\cos\{\Gamma_{mn}(z+t)\} & z<z_0\end{cases} \tag{3.24}$$

$$\left\langle H_y^{cav}\left(M_x^s\right), e_q^o(y)\right\rangle = \frac{j\omega\varepsilon}{k^2}\frac{L_sW_sL_oW_o}{L_sW_s}\sum_{p=1}^{M}E_{xp}^o\sum_{m=1}^{\infty}\sum_{n=0}^{\infty}\varepsilon_m\varepsilon_n\frac{m\pi}{2L_s}\frac{n\pi}{2W_s}\times$$
$$\times\cos\left\{\frac{m\pi}{2L_s}\left(x_{wo}+L_s\right)\right\}\operatorname{sinc}\left\{\frac{m\pi}{2L_1}L_o\right\}\cos\left\{\frac{n\pi}{2W_s}\left(y_{ws}+W_s\right)\right\}\operatorname{sinc}\left\{\frac{n\pi}{2W_s}W_s\right\}$$
$$\times\frac{\left\{-F_{xs}(p)F_{yo}(q)\right\}}{\Gamma_{mn}\sin\left\{2\Gamma_{mn}t\right\}}\begin{cases}\cos\left\{\Gamma_{mn}(z-t)\right\}\cos\left\{\Gamma_{mn}(z_0+t)\right\} & z>z_0\\ \cos\left\{\Gamma_{mn}(z_0-t)\right\}\cos\left\{\Gamma_{mn}(z+t)\right\} & z<z_0\end{cases} \tag{3.25}$$

$$\left\langle H_x^{cav}\left(M_y^s\right), e_q^o(x)\right\rangle = -\frac{j\omega\varepsilon}{k^2}\frac{L_sW_sL_oW_o}{L_sW_s}\sum_{p=1}^{M}E_{yp}^i\sum_{m=0}^{\infty}\sum_{n=1}^{\infty}\varepsilon_m\varepsilon_n\frac{m\pi}{2L_s}\frac{n\pi}{2W_s}$$
$$\times\cos\left\{\frac{m\pi}{2L_s}\left(x_{ws}+L_s\right)\right\}\operatorname{sinc}\left\{\frac{m\pi}{2L_s}L_s\right\}\cos\left\{\frac{n\pi}{2b_j}\left(y_{wo}+W_s\right)\right\}\operatorname{sinc}\left\{\frac{n\pi}{2W_s}W_o\right\}$$
$$\times\frac{\left\{-F_{ys}(p)F_{xo}(q)\right\}}{\Gamma_{mn}\sin\left\{2\Gamma_{mn}t\right\}}\begin{cases}\cos\left\{\Gamma_{mn}(z-t)\right\}\cos\left\{\Gamma_{mn}(z_0+t)\right\} & z>z_0\\ \cos\left\{\Gamma_{mn}(z_0-t)\right\}\cos\left\{\Gamma_{mn}(z+t)\right\} & z<z_0\end{cases} \tag{3.26}$$

$$\left\langle H_y^{cav}\left(M_y^s\right), e_q^o(y)\right\rangle = \frac{j\omega\varepsilon}{k^2}\frac{L_sW_sL_oW_o}{a_jb_j}\sum_{p=1}^{M}E_{xp}^i\sum_{m=0}^{\infty}\sum_{n=1}^{\infty}\varepsilon_m\varepsilon_n\left\{k^2-\left(\frac{n\pi}{2W_s}\right)^2\right\}$$
$$\times\cos\left\{\frac{m\pi}{2L_s}\left(x_{ws}+L_s\right)\right\}\operatorname{sinc}\left\{\frac{m\pi}{2L_s}L_s\right\}\cos\left\{\frac{m\pi}{2L_s}\left(x_{wo}+L_s\right)\right\}\operatorname{sinc}\left\{\frac{m\pi}{2L_s}L_o\right\}$$
$$\times\frac{\left\{-F_{ys}(p)F_{yo}(q)\right\}}{\Gamma_{mn}\sin\left\{2\Gamma_{mn}t\right\}}\begin{cases}\cos\left\{\Gamma_{mn}(z-t)\right\}\cos\left\{\Gamma_{mn}(z_0+t)\right\} & z>z_0\\ \cos\left\{\Gamma_{mn}(z_0-t)\right\}\cos\left\{\Gamma_{mn}(z+t)\right\} & z<z_0\end{cases} \tag{3.27}$$

$$\left\langle H_x^{DRA}\left(\bar{M}_x^4\right), e_q^4(x)\right\rangle = \left\langle\left[G_{spc}\right], e_q^4(x)\right\rangle + \iint_{slot}\iint_{slot}G_{HS}e_p^4(x')e_q^4(x)\,ds'ds \tag{3.28}$$

The second part of (3.28) is computed directly by quad integral in program. First part is given by

$$\left\langle\left[G_{spc}\right], e_q(x)\right\rangle = -\frac{4W_3^2L_3^2}{\pi^2k\eta}\int_{-\infty}^{\infty}\int_{-\infty}^{\infty}\frac{k^2-k_x^2}{\left(k^2-k_x^2-k_y^2\right)^{1/2}}\operatorname{sinc}^2\left(k_yW_3\right)$$
$$\frac{\begin{cases}\sin^2\left(k_xL_3\right) & \text{p,q both even}\\ \cos^2\left(k_xL_3\right) & \text{p,q both odd}\\ 0 & \text{otherwise}\end{cases}}{\frac{p\pi}{2}\left\{1-\left(\frac{2L_3k_x}{p\pi}\right)^2\right\}\frac{q\pi}{2}\left\{1-\left(\frac{2L_3k_x}{q\pi}\right)^2\right\}}dk_xdk_y \tag{3.29}$$

3.4 Computation of Reflection Coefficient

Once the unknown coefficients are determined, reflection coefficient can be found out by decoupling the sources, one at -∞ in the feed waveguide and the other at aperture1. The incident electric field due to TE_{10} excitation at z = 0 plane is:

$$E_y^{inc} = \cos\left(\frac{\pi x}{2a}\right) \tag{3.30}$$

When the window aperture is shorted, electric field is the field reflected by the electric short circuit. The reflected electric field is given by

$$E_y^{ref} = -\cos\left(\frac{\pi x}{2a}\right) \tag{3.31}$$

When the generator in the feed waveguide is removed and replaced by a perfect match, the electric field for the dominant TE_{10} mode scattered by the window into the waveguide is,

$$E_y^1 = \sum_{p=1}^{M} E_{yp}^1 \frac{W_1 L_1}{ab}\left[\cos\left\{\frac{\pi}{2}\left(-\frac{x_{w1}}{a}+p-1\right)\right\}\operatorname{sinc}\left\{\frac{\pi L_1}{2}\left(\frac{p}{L_1}-\frac{1}{a}\right)\right\}\right.$$
$$\left.-\cos\left\{\frac{\pi}{2}\left(\frac{x_{w1}}{a}+p+1\right)\right\}\operatorname{sinc}\left\{\frac{\pi L_1}{2}\left(\frac{p}{L_1}+\frac{1}{a}\right)\right\}\right]\cos\left(\frac{\pi x}{2a}\right) \tag{3.32}$$

Reflection coefficient Γ can then be expressed as:

$$\Gamma = \frac{E_y^1 + E_y^{ref}}{E_y^{inc}} \tag{3.33}$$

Substituting the expressions for E_y^1 , E_y^{ref} and E_y^{inc} in (3.33) and simplifying

$$\Gamma = -1 + \frac{W_1 L_1}{ab}\sum_{p=1}^{M} E_{yp}^1\left[\cos\left\{\frac{\pi}{2}\left(-\frac{x_{w1}}{a}+p-1\right)\right\}\operatorname{sinc}\left\{\frac{\pi L_1}{2}\left(\frac{p}{L_1}-\frac{1}{a}\right)\right\}\right.$$
$$\left.-\cos\left\{\frac{\pi}{2}\left(\frac{x_{w1}}{a}+p+1\right)\right\}\operatorname{sinc}\left\{\frac{\pi L_1}{2}\left(\frac{p}{L_1}+\frac{1}{a}\right)\right\}\right] \tag{3.34}$$

3.5 Simulated and Measured Results

The analysis presented in the preceding section is used to compute the input impedance and reflection coefficient of the double step junction coupled waveguide fed hemispherical DRA. A general MATLAB code has been written with frequency, dimension of the steps, slot, radius and dielectric constant of the HDRA as variables. Many design parameters are involved in the problem under consideration. To achieve optimum performance, a thorough parametric study has been conducted using the developed MATLAB code. The double step junction coupled waveguide fed HDRA consists of two resonant structures: DRA and the slot. For single resonance operation, dimension of the slot is tuned to resonate the double step junction coupled waveguide fed HDRA at the resonant frequency of HDRA.

Hemispherical DRA of ε_r = 9.8, a_{dr} = 7.5 mm and WR-90 waveguide are used in the proposed design. DRA is excited in TM_{101} mode, with resonant frequency 8.735 GHz [24]. The poor performance of direct coupled waveguide fed DRA is due to the inductive susceptance offered by the DRA loaded slot. If the inductive susceptance is neutralised by its capacitive counterpart, coupling could be improved. Steps in the proposed design provide the capacitive susceptance required to neutralise the inductive susceptance of waveguide shorted end slot coupled DRA. Figure 3.2 shows the normalised admittance plot of the double step junction coupled waveguide fed HDRA with parameters: *2t1* = 4.0 mm, *2t2* = 8.0 mm, *2t3* = 1.3 mm, *2W1* = 6.5 mm, *2W2* = 3.4 mm, *2W3* = 1.0 mm, *2L3* = 9.5 mm and $x_{w3} = y_{w3} = 0$ mm. From the plot it is clear that the susceptance at resonant frequency is zero. Convergence check for the moment method solution is shown in Fig. 3.3. It is found that the results with number of basis function, M = 1 is very close to those using larger M. Computation time increases as the number of basis function increases. Therefore, in order to save the computation time, M = 1 is used in all the computations.

3.5.1 Parametric study and discussion

Many design parameters are involved in the problem under consideration. A thorough parametric study has been conducted to find out the effect of various design parameters on resonant frequency and matching. The proposed structure consists of two

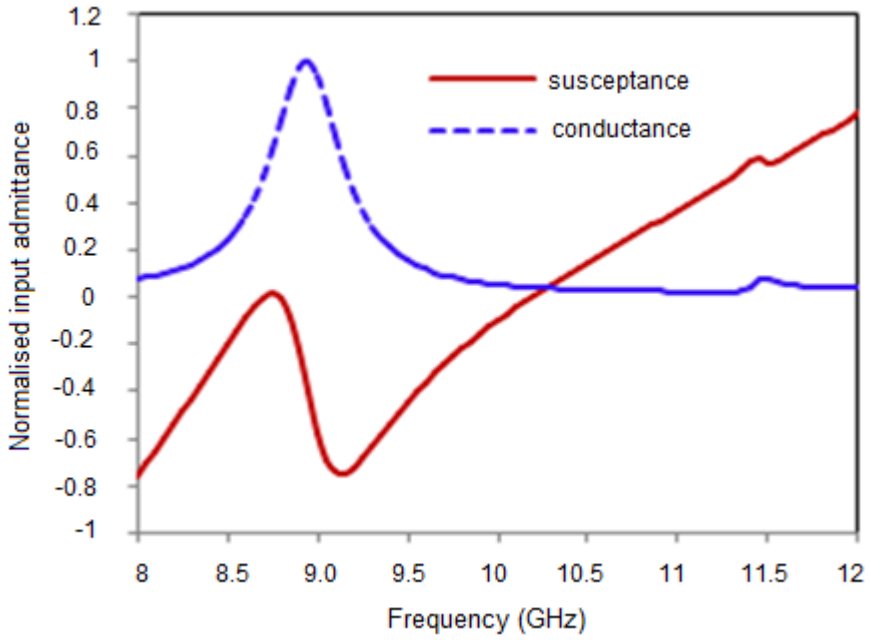

Fig. 3.2 Normalised input admittance of the double step junction coupled waveguide fed HDRA with *2t1* = 4.0 mm, *2t2* = 8.0 mm, *2t3* = 1.3 mm, *2W1* = 6.5 mm, *2W2* = 3.4 mm, *2W3* = 1.0 mm, *2L3* = 9.5 mm, and x_{w3}= y_{w3}= 0 mm.

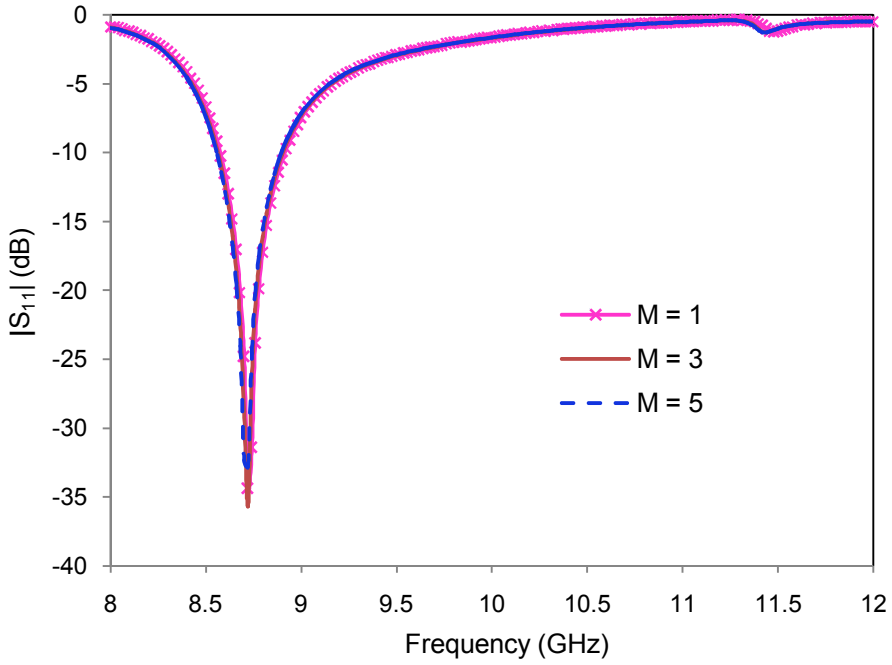

Fig. 3.3 Computed reflection coefficient of the double step junction coupled waveguide fed HDRA as a function of the number of basis functions *M* with *2t1* = 4.0 mm, *2t2* = 8.0 mm, *2t3* = 1.3 mm, *2W1* = 6.5 mm, *2W2* = 3.4 mm, *2W3* = 1.0 mm, *2L3* = 9.5 mm, and x_{w3}= y_{w3}= 0 mm.

resonant structures: slot and HDRA. The resonant frequency of the two structures can be adjusted to implement single, dual and wide band operations. DRA of dielectric constant, ε_r = 9.8, and radius, a_{dr} = 7.5 mm is used in this design. DRA is excited in TM_{101} mode, with resonant frequency 8.735 GHz. Once the dimension and resonant frequency of the DRA are fixed, dimension of the slot is adjusted to resonate the entire structure at the resonant frequency of the HDRA to obtain single band operation. In order to resonate the DRA in X band WR90 waveguide is used.

3.5.1.1 Effect of Slot Dimension

The length, width and thickness of the slot play an important role in determining the resonant frequency and matching. Effect of slot thickness on reflection coefficient can be explained by considering the thick wall of the ground plane as a secondary waveguide with relatively small cross sectional dimension. Figure 3.4 shows the variation in reflection coefficient as the slot thickness 2*t3* is varied from 1.0 mm to 1.6 mm in steps of 0.3 mm. From the plot it is evident that the resonant frequency increases with increase in the value of slot thickness. Matching increases as the slot thickness increases from 1.0 mm to 1.3 mm and decreases as the slot thickness increases to 1.6 mm. Optimum value of slot thickness is 1.3 mm, which corresponds to the resonant frequency of the DRA along with maximum matching.

The resonant frequency and matching are also affected by slot length. Since the effective permittivity seen by the slot is not well defined, resonant frequency is not known exactly. As the resonant length of the slot is not well defined, tuning of the slot length is required to determine its resonant length. Figure 3.5 exhibits the effect of slot length on reflection coefficient. Increase in slot length leads to stronger capacitive loading and causes the resonant frequency to decrease. The resonant frequency corresponding to the DRA resonance, along with maximum matching is obtained for slot length, *2L3* = 9.5 mm. The resonant frequency as well as matching can be tuned by adjusting the slot width. Increase in slot width *2W3* causes the resonant frequency to decrease and matching to increase as shown in Fig. 3.6. But the slot width cannot be increased above 1.0 mm due to narrow slot approximation. Also increase in slot width will increase the cross polarization.

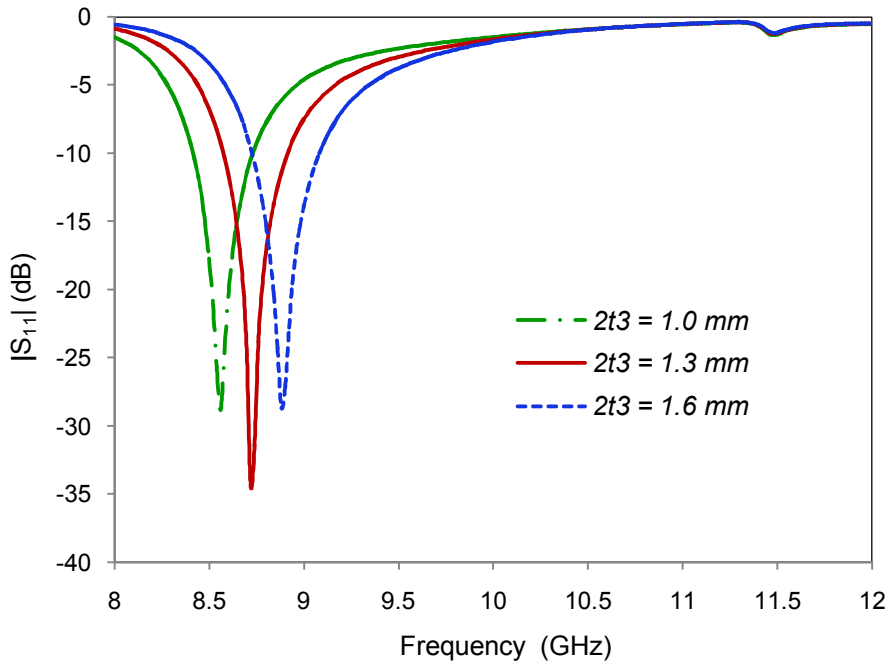

Fig. 3.4 Computed reflection coefficient of the double step junction coupled waveguide fed HDRA as a function of slot thickness *2t3* with *2t1* = 4.0 mm, *2t2* = 8.0 mm, *2W1* = 6.5 mm, *2W2* = 3.4 mm, *2W3* = 1.0 mm, *2L3* = 9.5 mm and $x_{w3} = y_{w3} = 0$ mm.

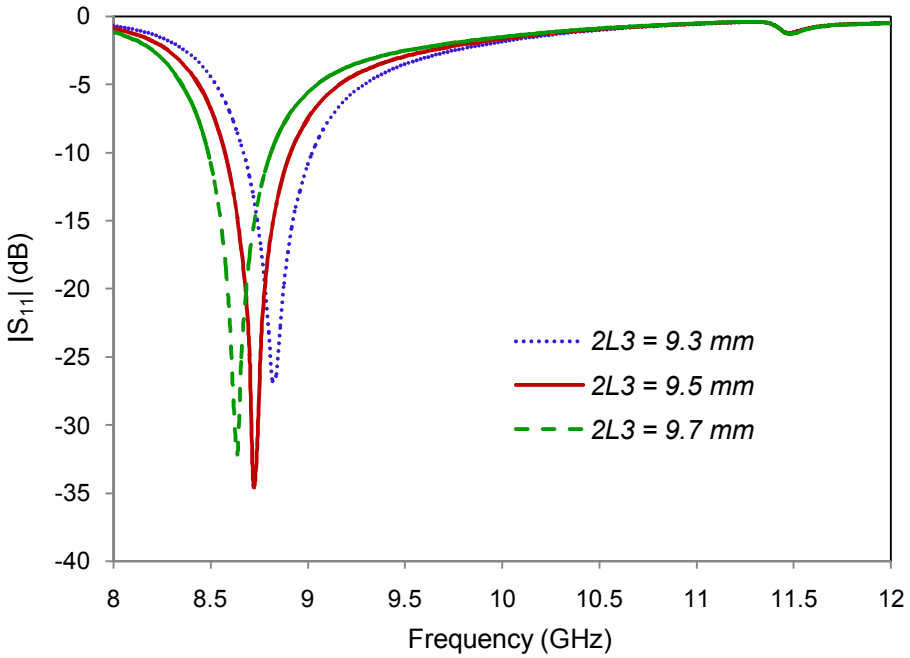

Fig. 3.5 Computed reflection coefficient of the double step junction coupled waveguide fed HDRA as a function of slot length *2L3* with *2t1* = 4.0 mm, *2t2* = 8.0 mm, *2t3* = 1.3 mm, *2W1* = 6.5 mm, *2W2* = 3.4 mm, *2W3* = 1.0 mm, and $x_{w3} = y_{w3} = 0$ mm.

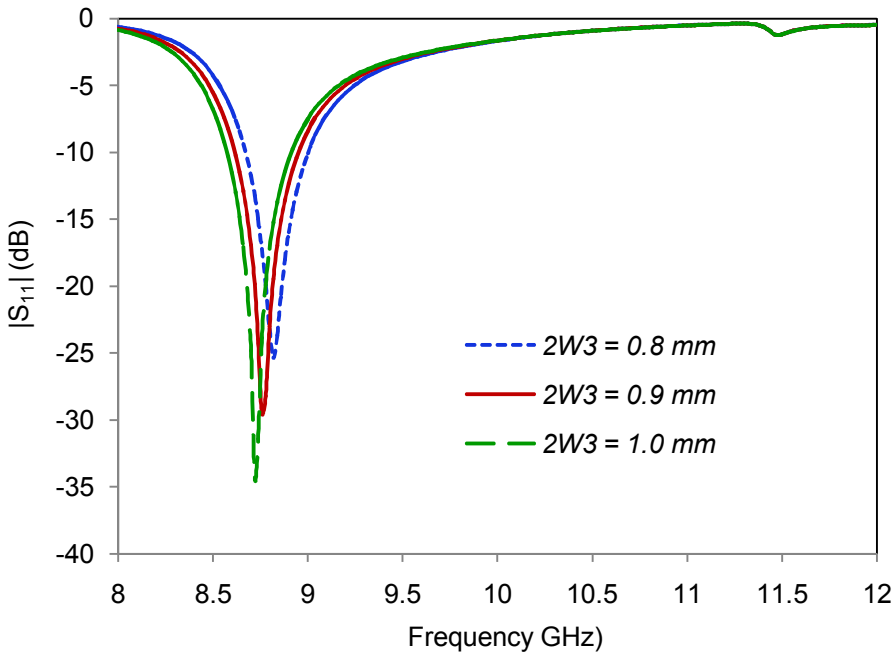

Fig. 3.6 Computed reflection coefficient of the double step junction coupled waveguide fed HDRA as a function of slot width *2W3* with *2t1* = 4.0 mm, *2t2* = 8.0 mm, *2t3* = 1.3 mm, *2W1* = 6.5 mm, *2W2* = 3.4 mm, *2L3* = 9.5 mm and $x_{w3} = y_{w3} = 0$ mm.

3.5.1.2 Effect of Slot Position

The proposed double step junction coupled waveguide fed HDRA consists of two resonators: slot (feeding structure) and DRA. Each of the resonators in the hybrid structure can be designed to radiate in its own separate band. Single band operation can be achieved by merging the resonant frequencies of the DRA and slot. If the two bands are separated, but close to each other, hybrid resonator can offer broadband operation. The resonant frequency of the slot and DRA can be separated by giving an offset to the slot along its length (x direction). The slot offset causes the DRA to operate in higher order modes, which causes the resonant frequency of the DRA to increase slightly.

3.5.1.2.1 Wide Band Operation

The development of modern communication applications demands antennas that provide wide bandwidth with reduced size [107]. The need for increased information transfer also demands increased bandwidth without sacrificing performance. For antennas with regular geometries, certain portion from the dielectric resonator structure

is removed to obtain broad-banding [108]. Another approach is to modify the geometry so as to obtain various shapes, such as a tetrahedron and triangular [109], truncated tetrahedron [110], split cylinder [111], conical DRA [112], pentagon shaped DRA [113], dumb-bell shaped DRA [114] and P shaped DRA [115]. These approaches have the advantage of keeping the DRA in a single volume, thereby maintaining compact size. However modified geometries have more design parameters that increases the design difficulty. Also due to the hardness of the DRA materials, re-shaping the geometry is very difficult. Poly DRAs (combination of multiple units consisting of same or different dielectric materials) can increase the bandwidth [116], [117]. But the design is not compact and not feasible for microwave integrated circuits. Dielectric resonator partially coated with metal on its surface can provide wideband operation [118]. However, covering the DRA with metal increases the fabrication complexity. Parasitic DRAs can be used to provide wide bandwidth [119]. DRAs with modified microstrip line can achieve wide band operation [120], [121].

In this work hybrid DRA method is used. Each of the resonators (DRA and slot) in the hybrid structure is designed to radiate in its own separate band. If the two bands are close to each other, hybrid resonator can offer broadband operation. The resonant frequencies of the slot and DRA can be separated by giving an offset to the slot along its length (x direction). The slot offset causes the DRA to operate in higher order modes, which causes the resonant frequency of the DRA to increase slightly. A thorough parametric study has been conducted to optimize the various parameters. Figure 3.7 shows the simulated reflection coefficient for wideband operation.

3.5.1.2.2 Dual Band Operation

Multiple frequency operation is highly desirable in modern wireless communication systems. If a single DRA can support multiple frequency bands, multiple single frequency antennas are not needed. Dual resonance can be achieved by using defected ground or combining multiple DRAs [122], [123]. Dual band operation can also be achieved by using special shaped DRAs [99], [124]. In [125], dual band operation is achieved by using a diamond shaped slot. Higher order modes of the DRA can be used for implementing dual band operation [126]. A compact dual band DRA using a parasitic

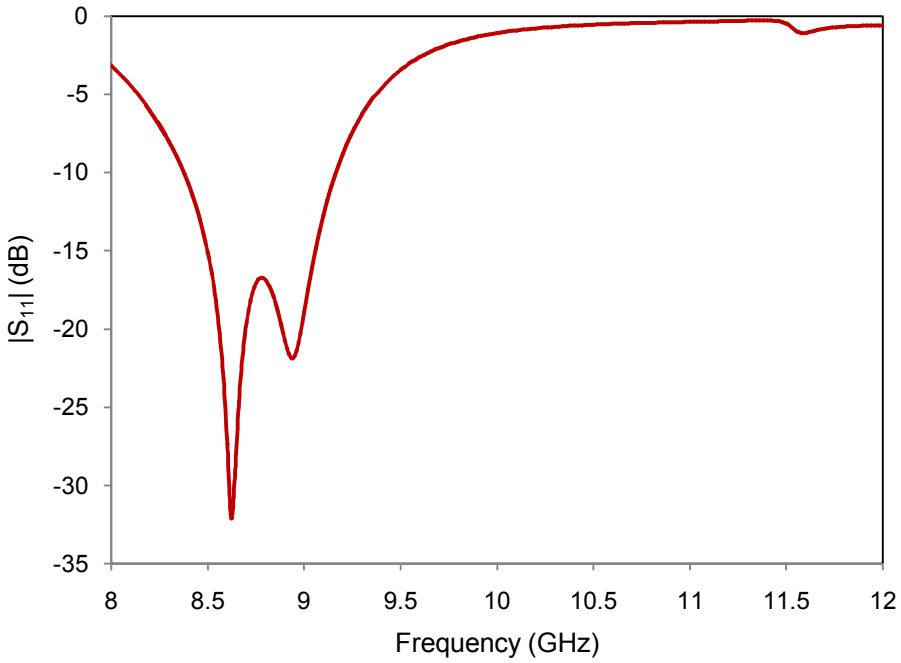

Fig. 3.7 Computed reflection coefficient of double step junction coupled waveguide fed HDRA for wideband operation with *2t1* = 7.0 mm, *2t2* = 10.0 mm, *2t3* = 1.3 mm, *2W1* = 6.3 mm, *2W2* = 3.0 mm, *2W3* = 1.0 mm, *2L3* = 10.0 mm, x_{w3} = 0.6 mm, and y_{w3} = 0 mm.

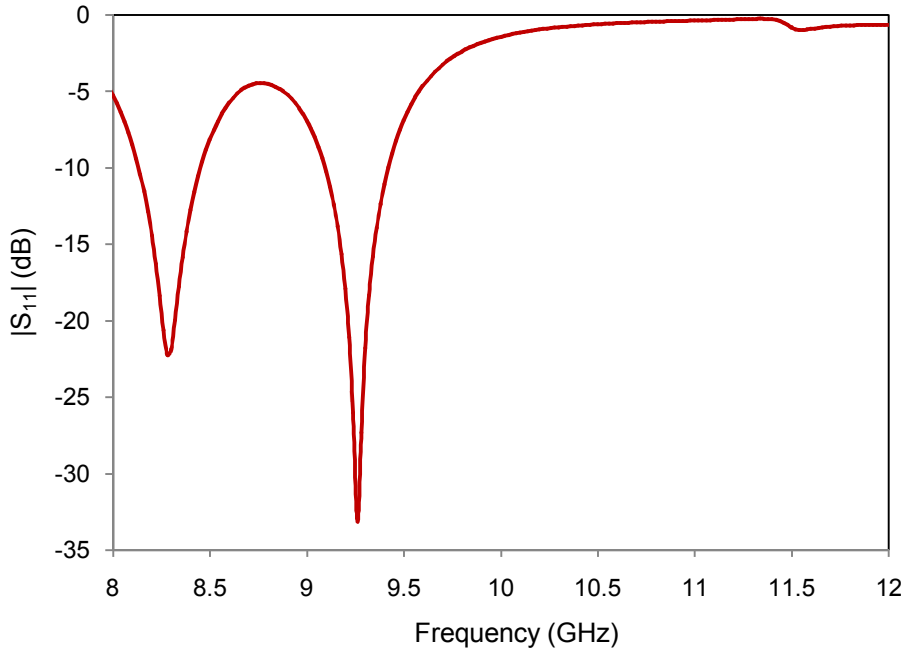

Fig. 3.8 Computed reflection coefficient for dual band operation of double step junction coupled waveguide fed HDRA with *2t1* = 7.0 mm, *2t2* = 10.0 mm, *2t3* = 1.3 mm, *2W1* = 6.3 mm, *2W2* = 3.0 mm, *2W3* = 1.0 mm, *2L3* = 10.0 mm, x_{w3} = 1.4 mm, and y_{w3} = 0 mm.

C slot fed by a microstrip is proposed in [127]. Splitting a rectilinear DR and carving notches off the DR provide dual band operation [128]. The main drawback of these designs is the increased fabrication complexity. In this thesis dual resonance is implemented without using any additional structures. Keeping the DRA at the centre of the ground plane and moving the slot away from the centre along *x* direction can excite DRA in higher order modes. It is observed that when the offset is increased to 1.4 mm, keeping the other parameters same as that used for implementing wideband operation, two separate bands resonating at 8.32 GHz and 9.28 GHz are obtained. Simulated S_{11} for dual band operation is shown in Fig. 3.8.

3.5.1.3 Effect of Step Dimension

The coupling enhancement achieved in double step junction coupled waveguide fed HDRA is due to the waveguide steps inserted between the rectangular waveguide and the ground plane. The length of the steps is same as the broad wall dimension of the waveguide. Waveguide steps reduce only the narrow wall dimension of the rectangular waveguide, keeping the broad wall dimension intact. Reducing the narrow wall dimension of the waveguide introduces a capacitive susceptance [66] that neutralises the

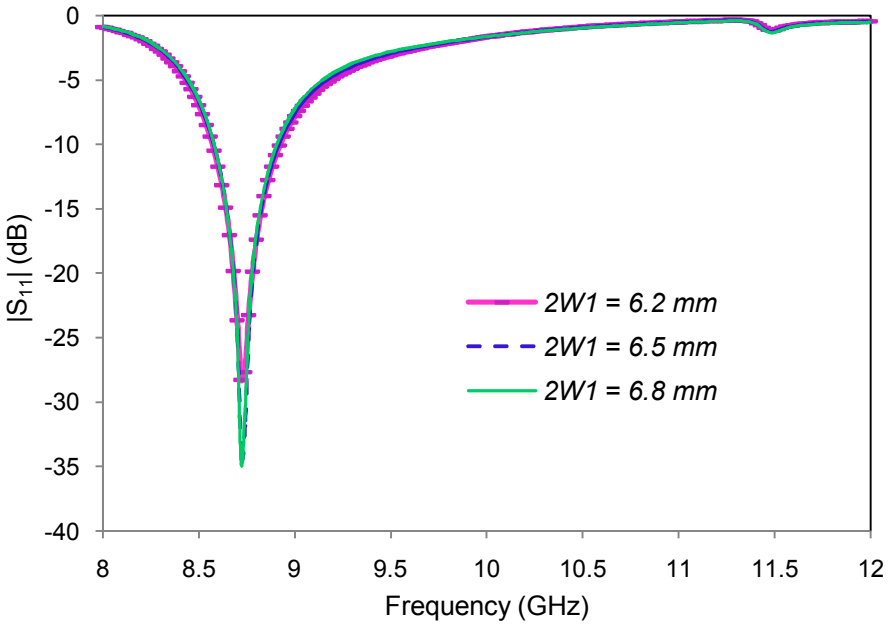

Fig. 3.9 Computed reflection coefficient of the double step junction coupled waveguide fed HDRA as a function of step1 width *2W1* with *2t1* = 4.0 mm, *2t2* = 8.0 mm, *2t3* = 1.3 mm, *2W2* = 3.4 mm, *2W3* = 1.0 mm, *2L3* = 9.5 mm and $x_{w3} = y_{w3} = 0$ mm.

inductive susceptance present in waveguide shorted end slot coupled (direct coupled) HDRA. Figure 3.9 shows the variation in reflection coefficient as a function of the width of the first step *2W1*. The resonant frequency is almost same, as the width of the step1, *2W1* increases from 6.2 mm to 6.8 mm. Matching increases as *2W1* increases from 6.2 mm to 6.5 mm and remains the same for *2W1* = 6.8 mm. The effect of the thickness of step1 *2t1* on reflection coefficient is shown in Fig. 3.10. Resonant frequency is almost same for different values of step1 thickness. As the thickness of step1, *2t1* increases from 3.5 mm to 4.0 mm, matching increases and then matching decreases, when the thickness is increased to 4.5 mm.

The effect of width and thickness of step2 on reflection coefficient is shown in Fig. 3.11 and 3.12 respectively. Resonant frequency increases slightly with increase in the width of step2, *2W2*. Maximum matching at the resonant frequency of the DRA is obtained for step2 width, *2W2* = 3.4 mm. The thickness of step2 does not change the resonant frequency, but it affects matching greatly. Maximum value of matching is obtained for step2 thickness, *2t2* = 8.0 mm.

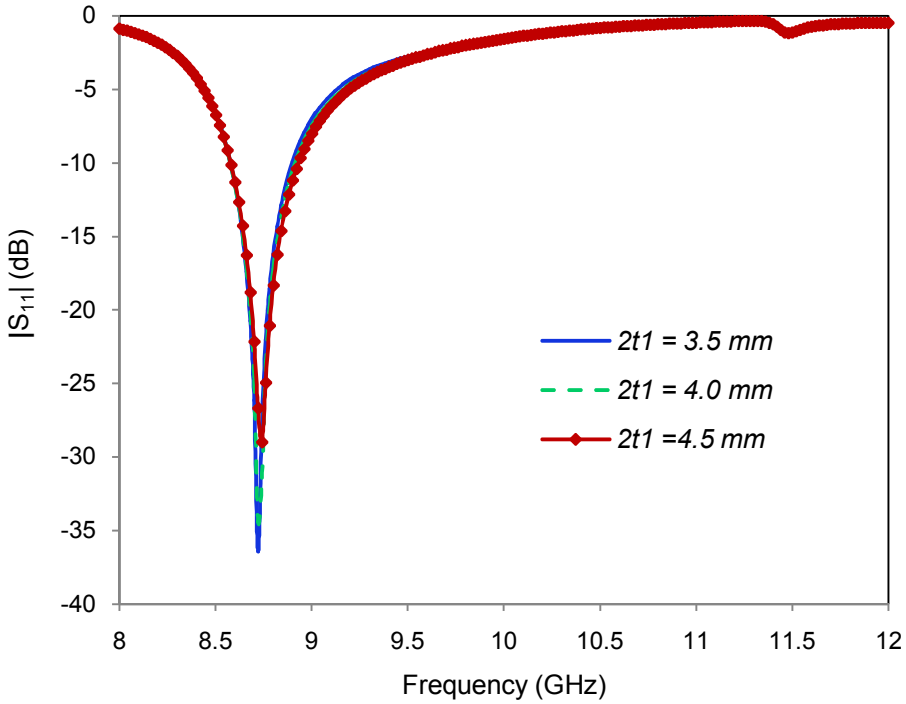

Fig. 3.10 Computed reflection coefficient of the double step junction coupled waveguide fed HDRA as a function of step1 thickness *2t1* with *2t2* = 8.0 mm, *2t3* = 1.3 mm, *2W1* = 6.5 mm, *2W2* = 3.4 mm, *2W3* = 1.0 mm, *2L3* = 9.5 mm and $x_{w3} = y_{w3} = 0$ mm.

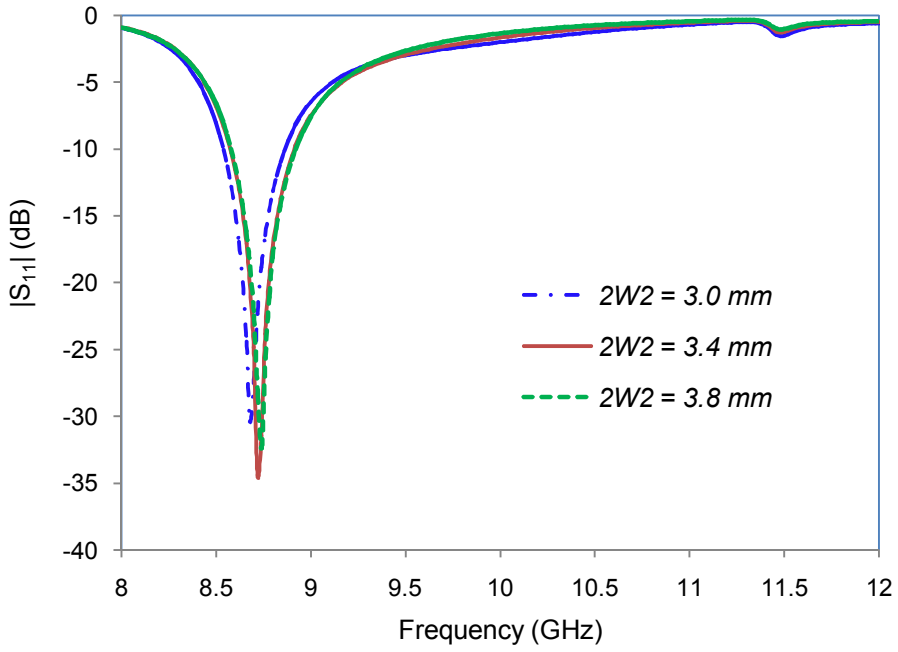

Fig. 3.11 Computed reflection coefficient of the double step junction coupled waveguide fed HDRA as a function of step2 width *2W2* with *2t1* = 4.0 mm, *2t2* = 8.0 mm, *2t3* = 1.3 mm, *2W1* = 6.5 mm, *2W3* = 1.0 mm, *2L3* = 9.5 mm and $x_{w3} = y_{w3} = 0$ mm.

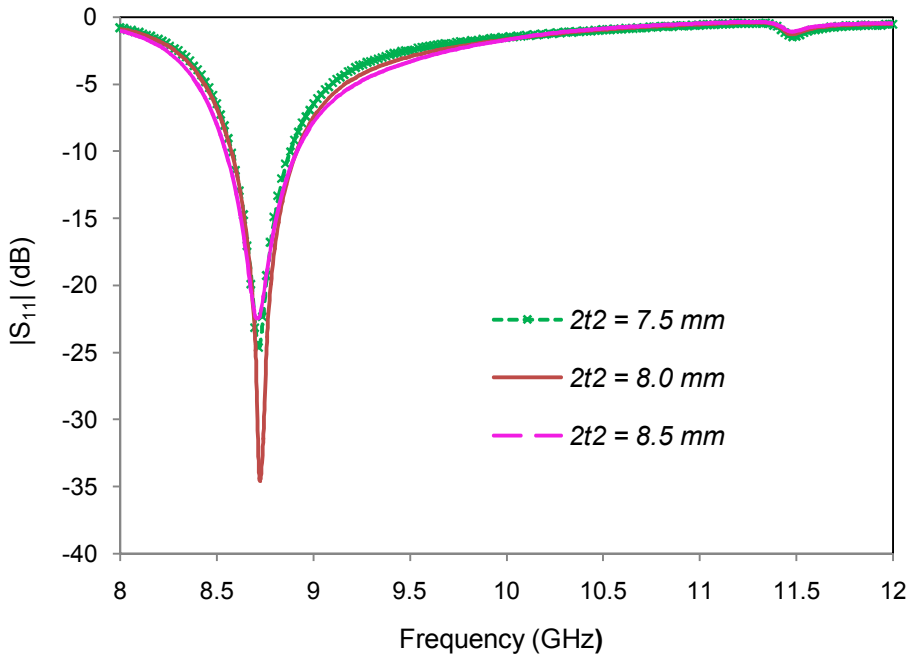

Fig. 3.12 Computed reflection coefficient of the double step junction coupled waveguide fed HDRA as a function of step2 thickness *2t2* with *2t1* = 4.0 mm, *2t3* = 1.3 mm, *2W1* = 6.5 mm, *2W2* = 3.4 mm, *2W3* = 1.0 mm, *2L3* = 9.5 mm and $x_{w3} = y_{w3} = 0$ mm.

3.5.1.4 Effect of Ground plane Dimension

In theoretical formulation, dimension of the ground plane is assumed to extend to infinity along its length and width. However, in practical situations, the dimension of the ground plane is to be fixed. The effect of the square ground plane dimension, *gd* on reflection coefficient and radiation pattern are studied using Ansoft HFSS. Fig. 3.13 shows the variation in reflection coefficient when the size of the ground plane is varied from 50 mm to 150 mm in steps of 50 mm. Resonant frequency decreases as the dimension of the ground plane increases. Resonant frequency corresponding to DRA resonance occurs for *gd* = 100 mm. Matching increases as *gd* increases from 50 mm to 100 mm and decreases as *gd* increases to 150 mm. Therefore optimum value of the ground plane dimension is *gd* = 100 mm when considering the reflection coefficient. The backward radiation is very much influenced by the dimension of the ground plane. The back radiation decreases as the dimension *gd* of the ground plane increases, which is evident from Fig. 3.14. But increasing the size of the ground plane increases the overall dimension of the structure. Therefore, size of the ground plane is selected as 100 mm x 100 mm as a compromise between the size of the structure and performance. Simulated three dimensional radiation pattern with optimized parameters is shown in Fig. 3.15.

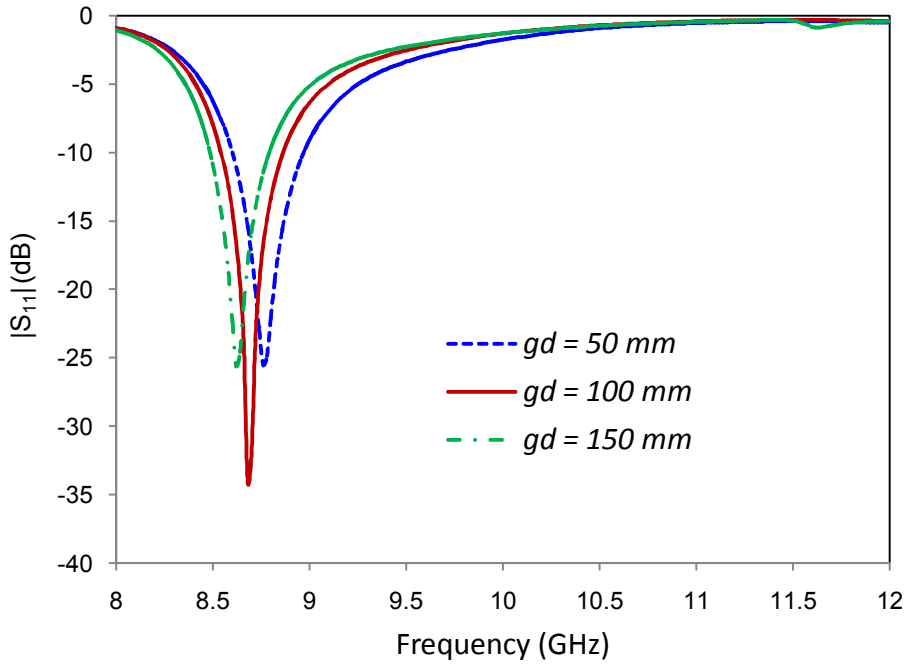

Fig. 3.13 Computed reflection coefficient of double step junction coupled waveguide fed HDRA as a function of ground plane dimension *gd* with *2t1* = 4.0 mm, *2t2* = 8.0 mm, *2t3* = 1.3 mm, *2W1* = 6.5 mm, *2W2* = 3.4 mm, *2W3* = 1.0 mm *2L3* = 9.5 mm and $x_{w3} = y_{w3} = 0$ mm.

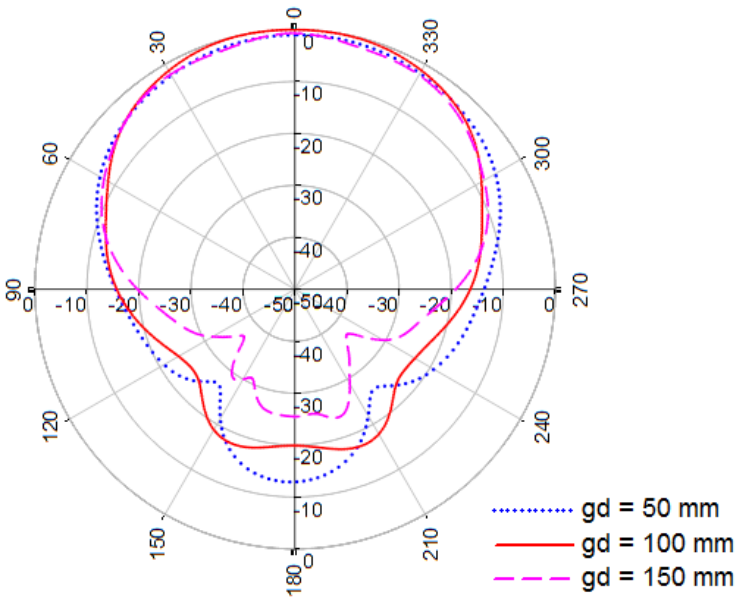

Fig. 3.14 Simulated radiation pattern of double step junction coupled waveguide fed HDRA as a function of the ground plane dimension *gd* with *2t1* = 4.0 mm, *2t2* = 8.0 mm, *2t3* = 1.3 mm, *2W1* = 6.5 mm, *2W2* = 3.4 mm, *2W3* = 1.0 mm *2L3* = 9.5 mm and $x_{w3} = y_{w3} = 0$ mm.

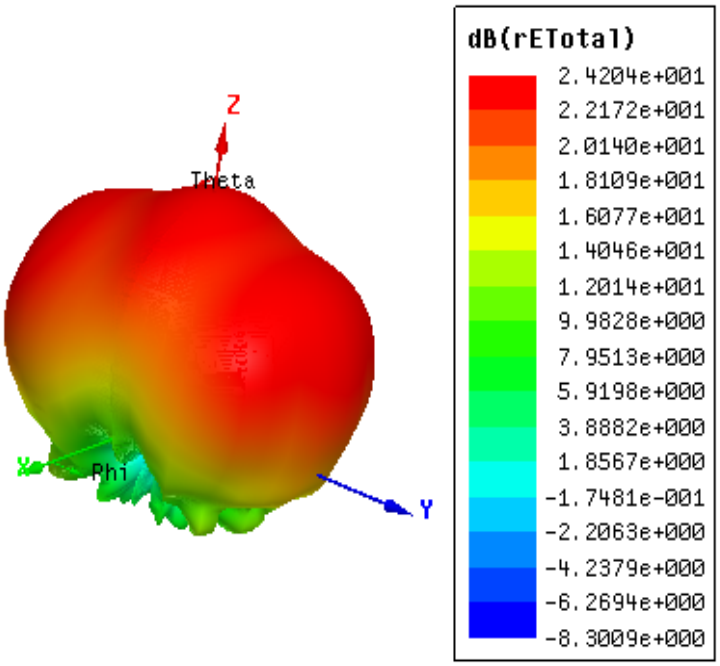

Fig. 3.15 Simulated three dimensional radiation pattern of the double step junction coupled waveguide fed HDRA with *2t1* = 4.0 mm, *2t2* = 8.0 mm, *2t3* = 1.3 mm, *2W1* = 6.5 mm, *2W2* = 3.4 mm, *2W3* = 1.0 mm *2L3* = 9.5 mm and $x_{w3} = y_{w3} = 0$ mm.

3.6 Measurement Results and Discussion

A prototype of the double step junction coupled waveguide fed hemispherical DRA for single band operation is fabricated with optimized parameters. Various parameters of the fabricated structure are: *2t1* = 4.0 mm, *2t2* = 8.0 mm, *2t3* = 1.3 mm, *2W1* = 6.5 mm, *2W2* = 3.4 mm, *2W3* = 1.0 mm, *2L3* = 9.5 mm, $x_{w3} = y_{w3} = 0$ mm, a_{dr} = 7.5 mm and $\varepsilon_r = 9.8$. Dimension of the ground plane is 100 mm x 100 mm x 1.3 mm and length of the rectangular waveguide is 60 mm. Photograph of the fabricated structure is shown in Fig. 3.16. The measurements were carried out using R&S ZVL 13 Vector Network Analyser. Fig. 3.17 shows the comparison between computed, measured and simulated reflection coefficients. The simulations were carried out using Ansoft HFSS. Excellent agreement is observed between analytical result and simulation result using HFSS. The measured resonant frequency is 9.2 GHz with a 10 dB bandwidth of 7.4%, extending from 9.07 GHz to 9.75 GHz. The measured resonance shows a 465 MHz upward shift along with reduced matching when compared with the computed reflection coefficient. This is due to the very small surface roughness of the DRA and ground plane that leads to uneven air gaps between the ground plane and DRA. The air gap between

Fig. 3.16 Photograph of the fabricated double step junction coupled waveguide fed HDRA with *2t1* = 4.0 mm, *2t2* = 8.0 mm, *2t3* = 1.3 mm, *2W1* = 6.5 mm, *2W2* = 3.4 mm, *2W3* = 1.0 mm, *2L3* = 9.5 mm, $x_{w3} = y_{w3} = 0$ mm, $a_{dr} = 7.5$ mm, and $\varepsilon_r = 9.8$.

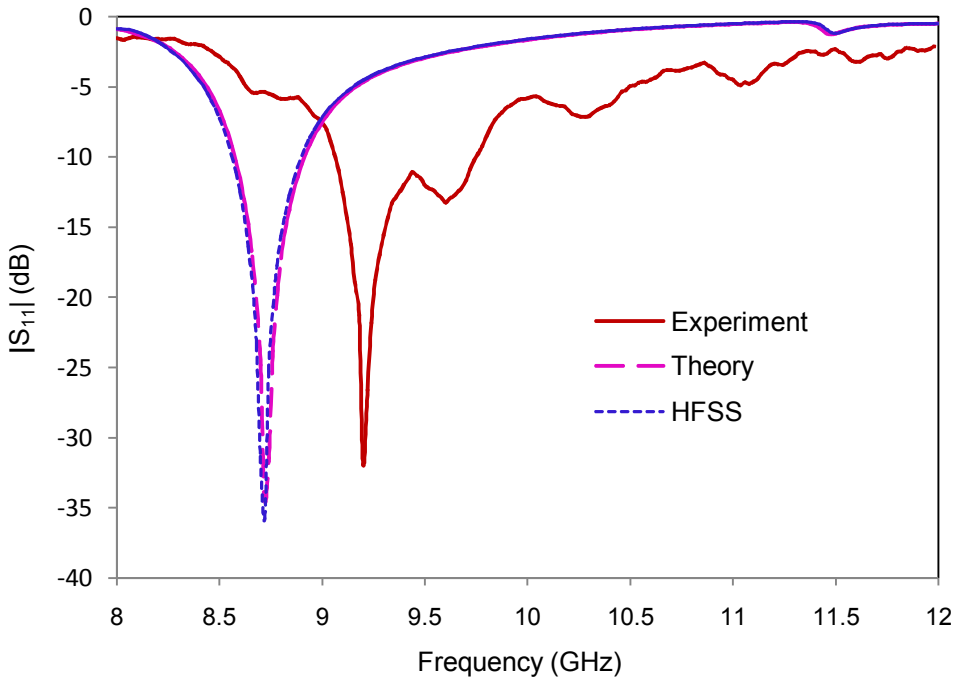

Fig. 3.17 Calculated, simulated and measured reflection coefficient of double step junction coupled waveguide fed HDRA with *2t1* = 4.0 mm, *2t2* = 8.0 mm, *2t3* = 1.3 mm, *2W1* = 6.5 mm, *2W2* = 3.4 mm, *2W3* = 1.0 mm, *2L3* = 9.5 mm, $x_{w3} = y_{w3} = 0$ mm, $a_{dr} = 7.5$ mm, and $\varepsilon_r = 9.8$.

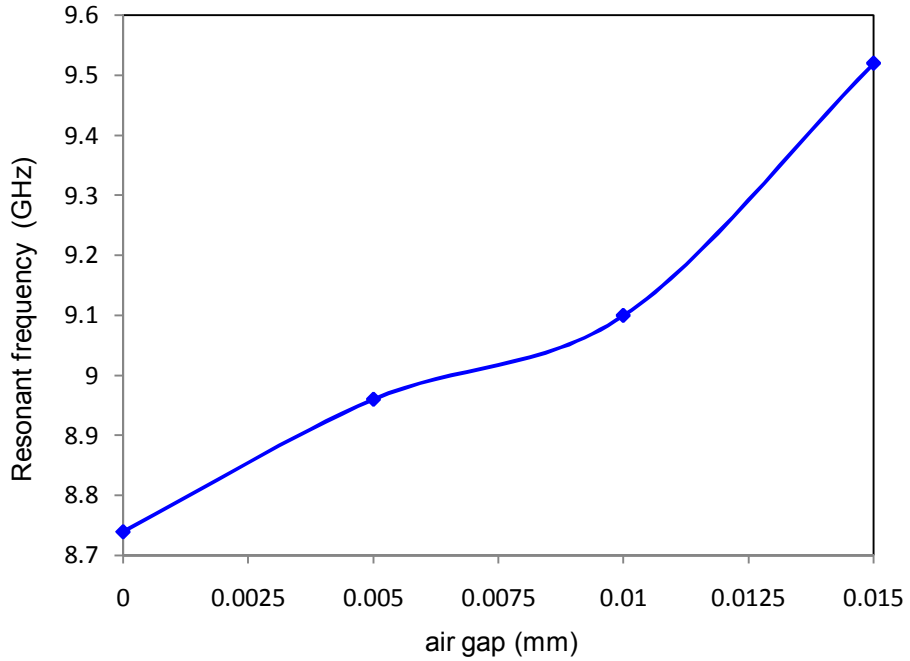

Fig. 3.18 Simulated resonant frequency versus air gap of the double step junction coupled waveguide fed HDRA with optimized parameters.

the ground plane and DRA lowers the equivalent permittivity of the DRA, which leads to the increase in resonant frequency [129-131]. Simulated result of resonant frequency versus air gap of the structure with optimized parameters is shown in Fig. 3.18. Resonant frequency is 9.2 GHz for a very small air gap of 0.0113 mm.

The shift in resonant frequency can be reduced by making the ground plane and bottom surface of the DRA flat and smooth by using better fabrication techniques. The measured and simulated radiation patterns of the fabricated structure as a function of elevation angle, θ at 9.2 GHz and 9.5 GHz are shown in Fig. 3.19. It is observed that symmetrical broadside radiation patterns with low levels of cross polarisation are obtained in both the planes. The increased cross polarization levels in measured results when compared with the simulated results are due to the limited measurement facility available in our laboratory. Also the air gap present between the ground plane and DRA increases cross-polarisation. Figure 3.20 shows the simulated radiation patterns with air gap (0.0113 mm) and without air gap. The measured gain versus frequency is shown in

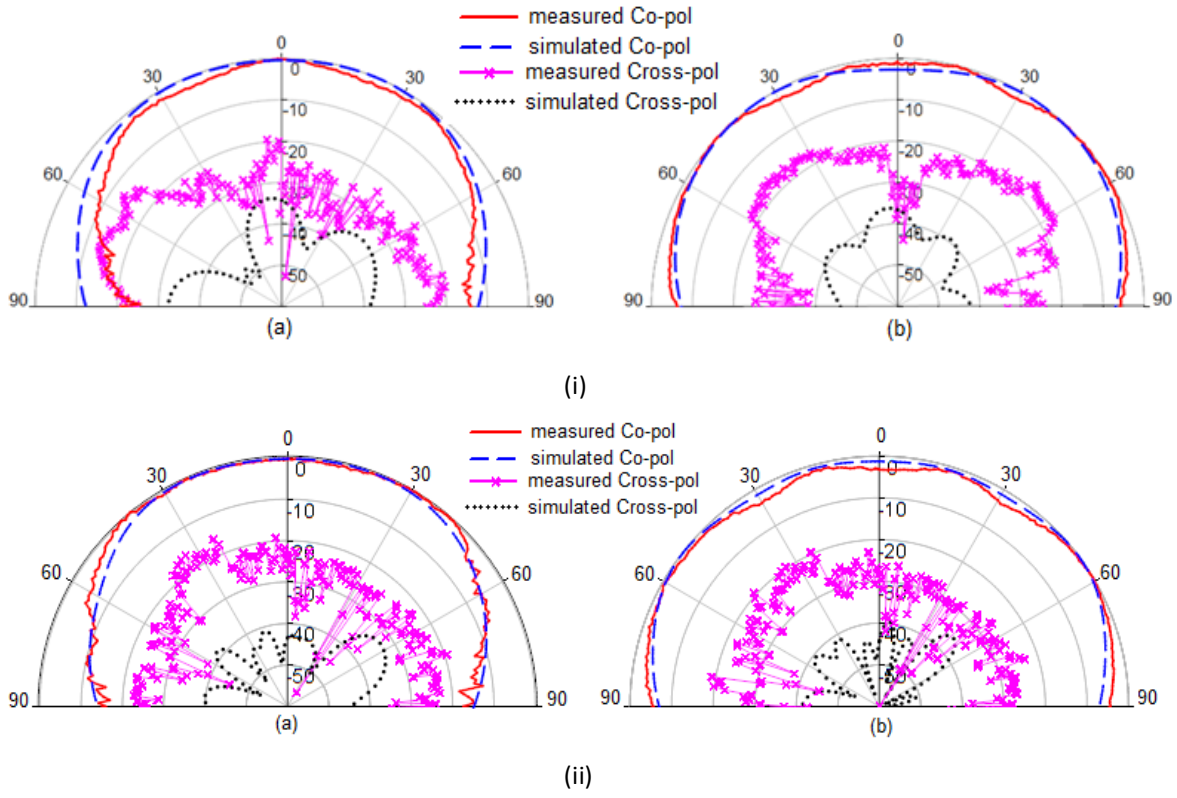

Fig. 3.19 Measured and simulated radiation pattern of double step junction coupled waveguide fed HDRA: (i) at 9.2 GHz (ii) at 9.5 GHz a) in xz plane b) in yz plane.

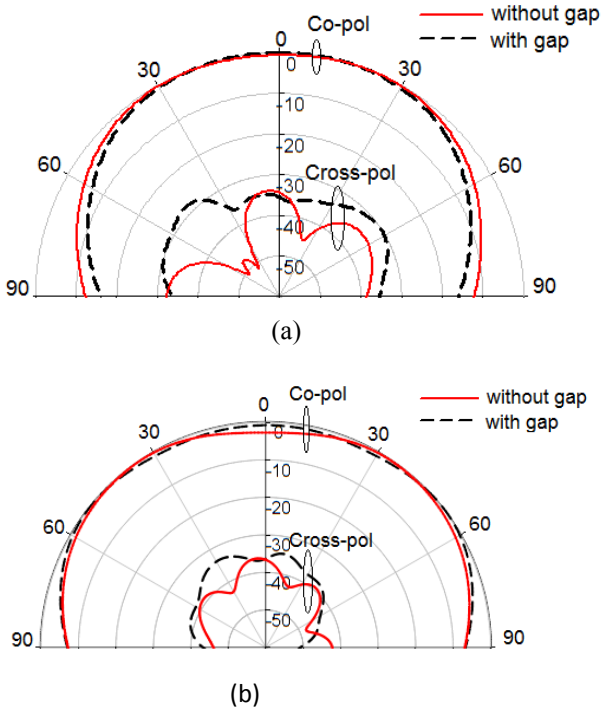

Fig. 3.20 Simulated radiation patterns with air gap (0.0113 mm) and without air gap:(a) In xz plane and (b) In yz plane.

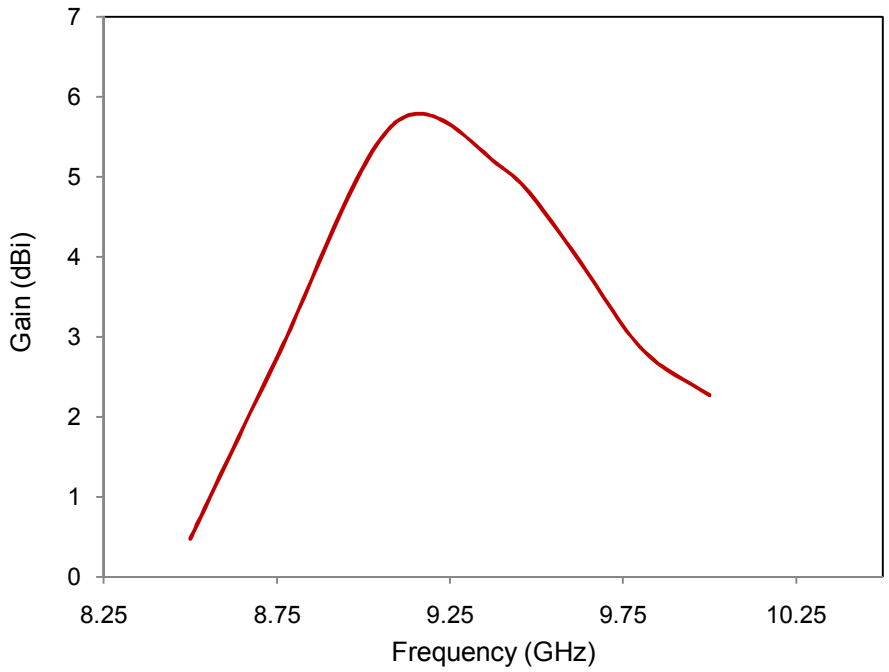

Fig. 3.21 Measured gain of the double step junction coupled waveguide fed HDRA.

Fig. 3.21. The structure has a high gain of 5.7 dBi at 9.09 GHz with a 3 dB gain bandwidth of 11.08%.

This work is published in IET Microwaves Antennas and Propagation, Vol. 10, 2016.

3.7 Inference

A novel technique for the coupling enhancement of waveguide shorted end slot coupled hemispherical DRA is presented in this paper. Two steps are inserted between the rectangular waveguide and ground plane to improve coupling. Steps provide the capacitive susceptance required to neutralize the inductive susceptance present in direct coupled waveguide fed DRA. Theoretical analysis of the proposed technique has been performed using method of moments. Entire domain sinusoidal function is selected as the basis function for analysis. Since closed form analytical solution is used, efficiency is very high. In order to enhance the efficiency of computation, Green's function of the HDRA is expressed as the sum of particular and homogeneous solutions. This allows the slowly convergent particular solution to be expressed using spectral domain approach to enhance the speed of computation. Scattered magnetic field inside the waveguide is determined using modal analysis. Slot and steps are considered as rectangular cavity to perform the theoretical analysis. Scattered magnetic field inside the rectangular cavity is derived using Green's function.

In order to study the effect of various design parameters on reflection coefficient, a thorough parametric study has been conducted using the developed MATLAB code. The double step junction coupled waveguide fed HDRA consists of two resonant structures: slot and HDRA. Therefore, once the dimension and dielectric constant of the HDRA is fixed, resonant frequency is mainly affected by the slot dimension. Dimension of the step affects only the matching, keeping the resonant frequency almost constant. Increasing the size of the ground plane reduces back radiation. However, the size of the ground plane cannot be increased too much, since it will increase the overall size of the structure. Dual and wide band operations can be implemented using the same structure with the slot kept off-centred. A prototype of the double step junction coupled waveguide fed HDRA is fabricated for implementing single band operation. Measurements were taken using R&S ZVL 13 Vector Network Analyser. Reasonable

agreement is obtained between the computed and measured results. The upward shift in resonant frequency is due to the air gap present between the ground plane and DRA. This can be avoided by making the ground plane and the bottom surface of the DRA perfectly flat and smooth by using better fabrication techniques. Symmetrical broadside radiation patterns with low levels of cross polarisation are obtained in both the planes. The proposed antenna has a high gain of 5.7 dBi at 9.09 GHz with a 3 dB gain bandwidth of 11.08%. The proposed technique and the developed code can be utilised for millimetre wave applications.

Chapter 4

Rectangular Waveguide Fed Hemispherical DRA Using Tapered Waveguide Section

Rectangular waveguide is tapered at the end for the coupling enhancement of waveguide fed hemispherical dielectric resonator antenna (HDRA). Tapered section of the waveguide introduced at the end of the rectangular waveguide acts as an impedance transformer that enhances the coupling from waveguide to DRA. Waveguide with tapered section at the end is terminated by a thick square ground plane and a rectangular slot is cut at the centre of the ground plane for exciting the DRA. The effects of different antenna parameters on reflection coefficient are studied using the simulation software, Ansoft HFSS. The experimental results are in reasonable agreement with the simulated results. The measured resonant frequency of the proposed rectangular waveguide fed HDRA using tapered waveguide section is 10.78 GHz with a 10 dB bandwidth of 4.5%. Maximum gain of the proposed antenna is 5.5 dBi at 10.85 GHz. Very good coupling is obtained with the proposed rectangular waveguide fed HDRA using tapered waveguide section.

4.1 Introduction

The main objective of the thesis is to develop different coupling enhancement techniques for waveguide shorted end slot coupled DRA. The poor coupling of waveguide shorted end slot coupled DRA is due to the inductive susceptance offered by the DRA loaded slot. If the inductive susceptance is neutralised by its capacitive counterpart, coupling could be improved. The coupling enhancement technique discussed in chapter 3 achieved capacitive susceptance by introducing two waveguide steps with reduced narrow wall dimension in between the rectangular waveguide and the thick ground. The DRA is placed above the ground on which a slot is cut for exciting the DRA. Instead of using steps, capacitive susceptance can also be introduced by reducing the narrow wall dimension of the waveguide gradually, which looks like a tapered section placed in between the rectangular waveguide and the ground. The two parameters which determine the narrow wall dimension at the end of the tapered section are the length and angle of tapering. Therefore, the length and angle of tapering play an important role in matching. A thorough parametric study has been conducted to find out optimum value of the length and angle of tapering. The tapered waveguide fed HDRA consists of two resonant structures: HDRA and slot. Once the dimension and dielectric constant of the HDRA is fixed, resonant frequency is mainly affected by the dimension of the slot. Length, width and thickness of the slot are adjusted to resonate the entire structure at the resonant frequency of the HDRA. The resonant frequency and matching are also influenced by the length and angle of tapering. In order to determine the effects of various design parameters on resonant frequency and matching, a thorough parametric study has been conducted using the simulation software, Ansoft HFSS. The proposed coupling enhancement technique is validated in X band.

The waveguide shorted end slot excited HDRA gives poor coupling due to the inductive susceptance offered by the DRA loaded slot [71]. Coupling could be improved, if the inductive susceptance is neutralised by its capacitive counterpart. In direct coupled waveguide fed HDRA, there is an abrupt change in the narrow wall dimension of the waveguide to the slot width. Tapered section of the waveguide incorporated between the rectangular waveguide and the ground plane, causes the

narrow wall dimension of the waveguide to reduce gradually, before it makes contact with the ground plane. The gradual reduction in the narrow wall dimension of the waveguide provides very good impedance matching. The tapered section of the proposed structure also acts as a capacitive junction [66] that provides the capacitive susceptance required to neutralize the inductive susceptance present in direct coupled waveguide fed HDRA.

4.2 Configuration of Rectangular Waveguide fed HDRA using Tapered Waveguide Section

Configuration of the proposed structure is shown in Fig. 4.1. The structure consists of a rectangular waveguide, tapered section, slotted thick ground and hemispherical DRA. For exciting the DRA in X-band, WR90 rectangular waveguide is used. The rectangular waveguide is tapered at the end with length and angle of tapering

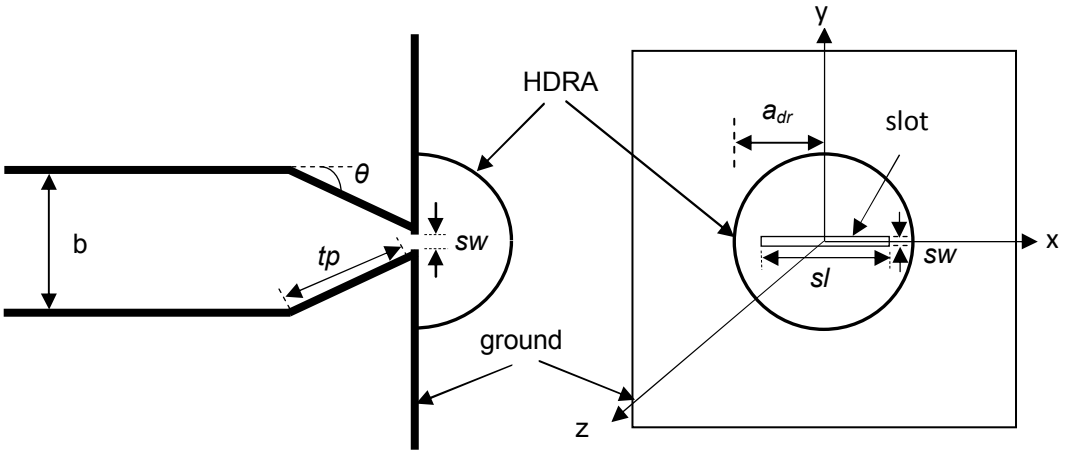

Fig. 4.1 Configuration of the rectangular waveguide fed HDRA using tapered waveguide section.

denoted by *tp,* and θ respectively. Tapering reduces only the narrow wall dimension of the waveguide, keeping the broad wall dimension intact, which provides the required capacitive susceptance. The tapered waveguide is terminated by a thick square ground plane. A rectangular slot of dimension *sl* x *sw* is cut at the centre of the thick ground plane, and HDRA is placed symmetrically above the slot. Tapering introduced at the end of the rectangular waveguide minimizes the reflections due to discontinuity

between the waveguide and the ground plane, which is present in direct coupled waveguide fed HDRA.

4.3 Simulation Results and Discussion

Many parameters are involved in the design of the proposed rectangular waveguide fed HDRA using tapered waveguide section. A thorough parametric study has been conducted using the simulation software, Ansoft HFSS to find out the optimum value of the parameters those lead to good coupling at the resonant frequency of HDRA. Resonant frequency of the hemispherical DRA is determined by its radius and dielectric constant of the material used. Hemispherical DRA of radius 6.27 mm with dielectric constant 9.8 is used in the proposed design. The resonant frequency of the HDRA is fixed at 10.49 GHz. WR90 waveguide is used for exciting the DRA in X-band and dimension of the ground plane is 100 mm x 100 mm x 1.3 mm. Increasing the length and width of the ground plane will reduce back radiation. But this will increase the overall size of the structure. Therefore size of the ground plane is selected as a compromise between the performance and size.

4.3.1 Effect of Slot Dimension

As the slot itself acts as a resonant structure, dimension of the slot affects the resonant frequency of the proposed rectangular waveguide fed HDRA using tapered waveguide section. Since the effective permittivity seen by the slot is not exactly defined, resonant length of the slot is not well defined. Therefore tuning of the slot length is required to determine its resonant length. The effect of varying the slot length on reflection coefficient is depicted in Fig. 4.2. Resonant frequency decreases with increase in slot length. As the slot length *sl* increases from 8.8 mm to 9.2 mm, in steps of 0.2 mm, resonant frequency decreases from 10.74 GHz to 10.34 GHz. Increase in slot length also leads to slight decrease in matching. The resonant frequency that corresponds to the DRA resonance along with good matching is obtained for slot length $sl = 9.0$ mm.

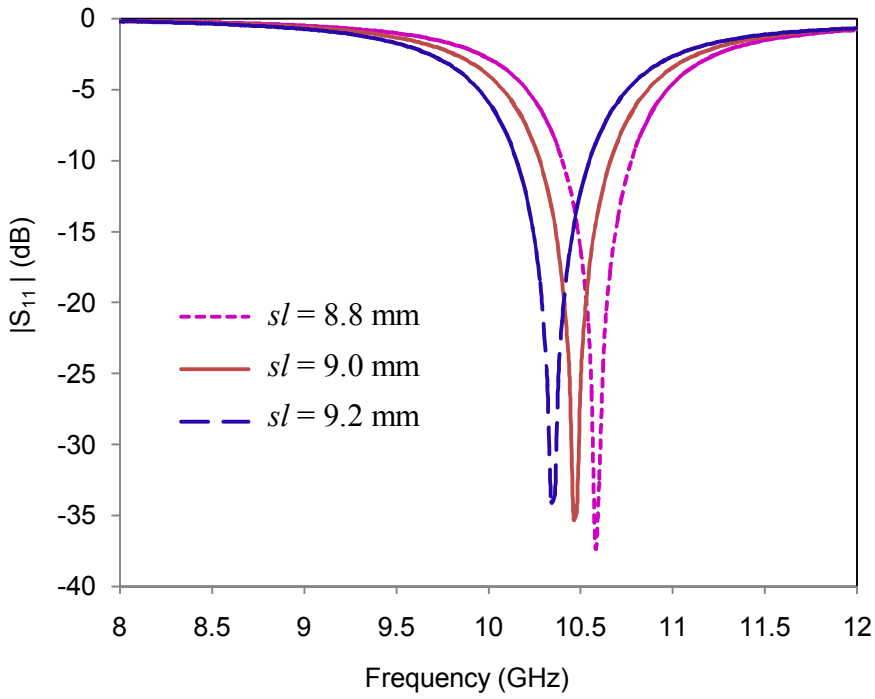

Fig. 4.2 Effect of slot length *sl* on reflection coefficient with *sw* = 0.7 mm, *tp* = 21.0 mm and $\theta = 13^{\circ}$.

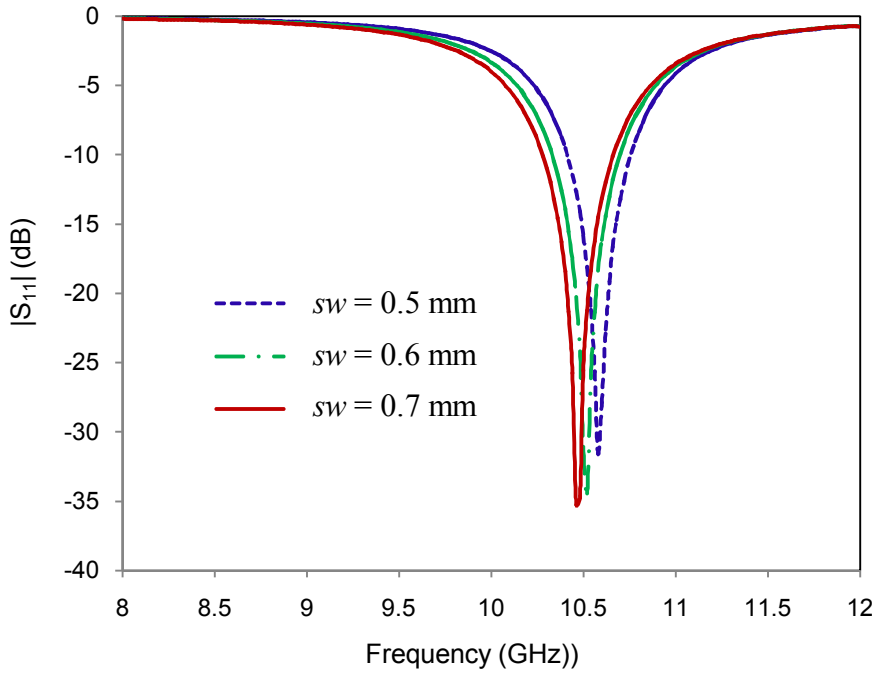

Fig. 4.3 Effect of slot width *sw* on reflection coefficient with *sl* = 9.0 mm, *tp* = 21.0 mm and $\theta = 13^{\circ}$.

The effect of variation in reflection coefficient as the slot width *sw* is varied from 0.5 mm to 0.7 mm is shown in Fig. 4.3. Resonant frequency decreases with increase in slot width like the slot length. A slight increase in matching is also observed with increase in slot width. Resonant frequency corresponding to the DRA resonance along with maximum matching is obtained for *sw* = 0.7 mm. The effect of slot length and slot width can be explained by considering the slot as a seconadary waveguide with very small dimension. As the cross sectional dimension of the waveguide decreses, cut off frequency increases.

4.3.2 Effect of the Dimension of Tapered Section

Capacitive susceptance is introduced in the proposed structure by introducing the tapered waveguide section between the rectangular waveguide and the ground. Therefore, dimension of the tapered section plays an important role in matching. Figure 4.4 illustrates the variation in reflection coefficient as a function of the length of tapering *tp*. Increase in *tp* from 20.0 mm to 21.0 mm enhances the matching along with a slight upward shift in resonant frequency.

The effect of angle of tapering on reflection coefficient is shown in Fig. 4.5. A slight increase in resonant frequency is observed when the angle of tapering θ increases from 12.0° to 13.0°. Increase in θ also causes the matching to increase as illustrated in Fig 4.5. However, the length and angle of tapering cannot be increased above a certain value, since it will reduce the width of the slot and tend to merge the broad walls of the tapered section. As the length and angle of tapering increases, the resonant frequency increases. Length of tapering *tp* = 21.0 mm, and angle of tapering, θ = 13°, provide maximum matching at the resonant frequency of the HDRA.

4.3.3 Effect of Radius and Dielectric Constant of HDRA

Resonant frequency of the HDRA is determined by its radius and dielectric constant. Resonant frequency is inversely proportional to the square root of the dielectric constant [10]. Reflection coefficient of the rectangular waveguide fed HDRA with tapered waveguide section as a function of the dielectric constant ε_r is shown in Fig. 4.6. Resonant frequency decreases as the dielectric constant of the HDRA

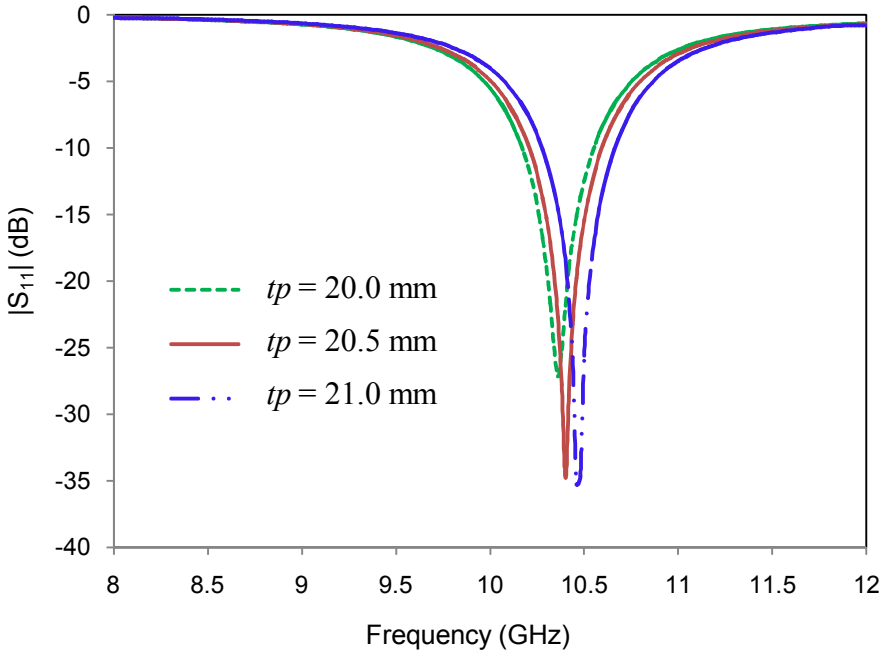

Fig. 4.4 Effect of the length of tapering *tp* on reflection coefficient with *sl* = 9.0 mm, *sw* = 0.7 mm and $\theta = 13^{\circ}$.

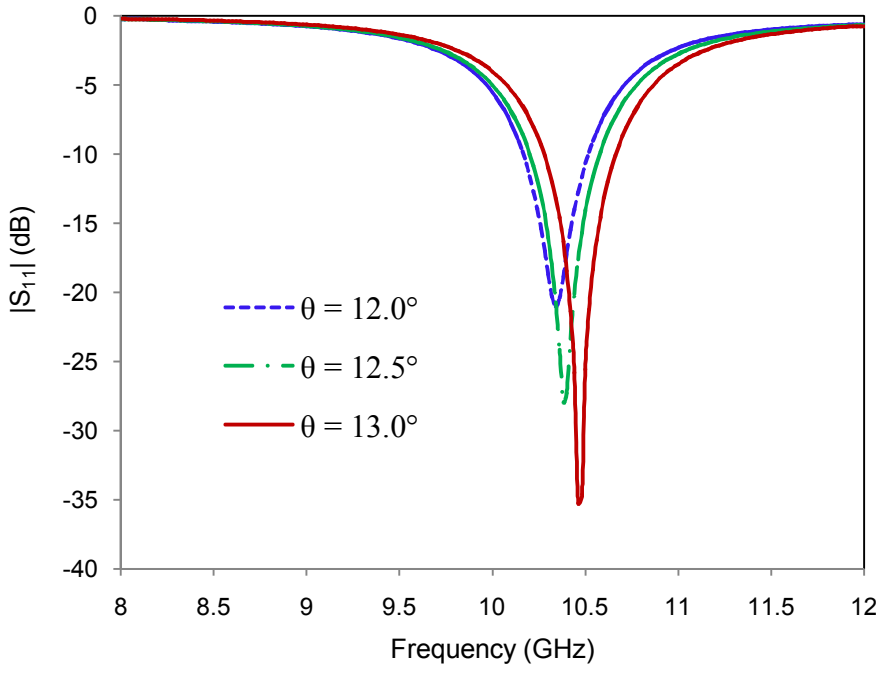

Fig. 4.5 Effect of the angle of tapering θ on reflection coefficient with *sl* = 9.0 mm, *sw* = 0.7 mm and *tp* = 21.0 mm.

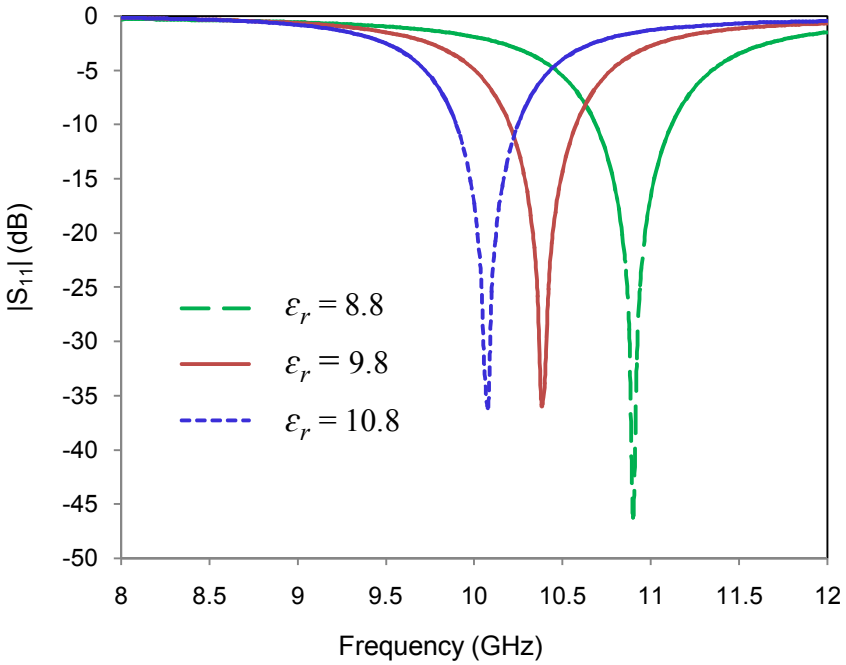

Fig. 4.6 Effect of dielectric constant ε_r of the HDRA on reflection coefficient with a_{dr} = 6.27 mm, sl = 9.0 mm, sw = 0.7 mm, tp = 21.0 mm and θ = 13°.

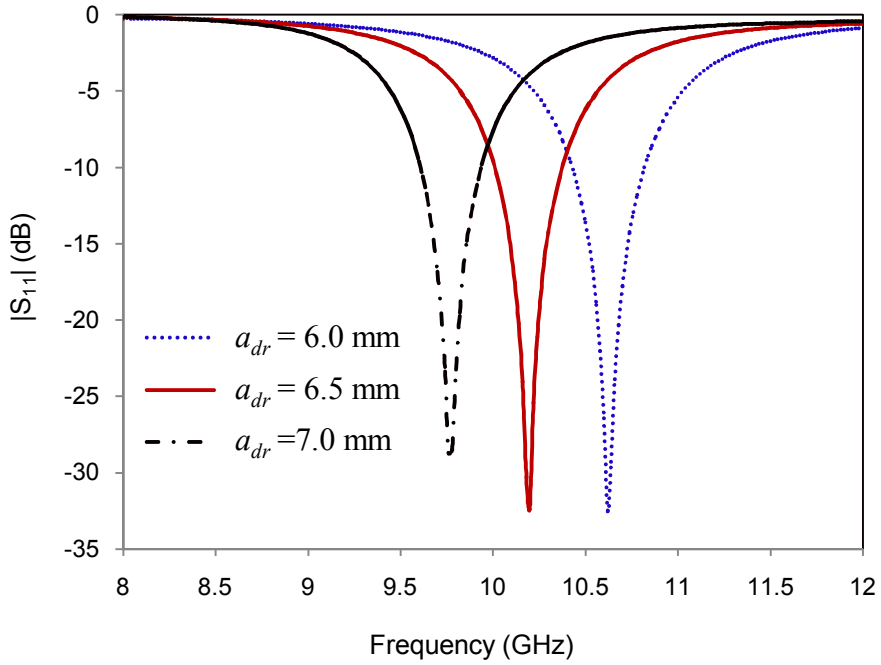

Fig. 4.7 Effect of the radius a_{dr} of HDRA on reflection coefficient with ε_r = 9.8, sl = 9.0 mm, sw = 0.7 mm, tp = 21.0 mm and θ = 13°.

increases. A slight increase in the bandwidth is also observed with decrease in dielectric constant of the DRA. As ε_r increases from 8.8 to 10.8, resonant frequency decreases from 10.9 GHz to 10.08 GHz. Dimension of the DRA also plays an important role in determining the resonant frequency. The effect of radius a_{dr} of HDRA on reflection coefficient is shown in Fig. 4.7. From the figure it is evident that the resonant frequency is inversely related to the radius of the hemispherical DRA. Resonant frequency decreases from 10.62 GHz to 9.8 GHz as radius of the HDRA increases from 6.0 mm to 7.0 mm.

4.3.4 Simulated Radiation Pattern

In the field of antenna design, the term radiation pattern refers to the directional (angular) dependence of the strength of the radio waves from the antenna or other source. The far field radiation pattern may be represented graphically as a plot of one of the related variables: the field strength at a constant radius, the power per unit solid angle and the directive gain. Figure 4.8 shows the simulated three dimensional radiation pattern of the proposed antenna using optimized parameters.

4.4 Measured Results

A prototype of the tapered waveguide fed HDRA with optimized parameters is fabricated and measured. WR-90 waveguide is used for fabrication. Photograph of the fabricated rectangular waveguide fed HDRA using tapered waveguide section is shown in Fig. 4.9. Measured and simulated reflection coefficients are compared in Fig. 4.10. The measured resonant frequency is 10.78 GHz, which shows an upward shift of 290 MHz when compared with the simulated resonant frequency. The upward shift in resonant frequency is mainly due to the fabrication problem. As the bottom surface of the DRA and ground plane are not perfectly flat and smooth, there exist uneven air gaps between the ground plane and DRA. The practical situation can be realised in simulations by introducing uniform air gap g between the ground plane and HDRA. Figure 4.11 illustrates the variation in reflection coefficient as a function of the air gap, g that exists between the DRA and ground plane. The thin air gap introduced between

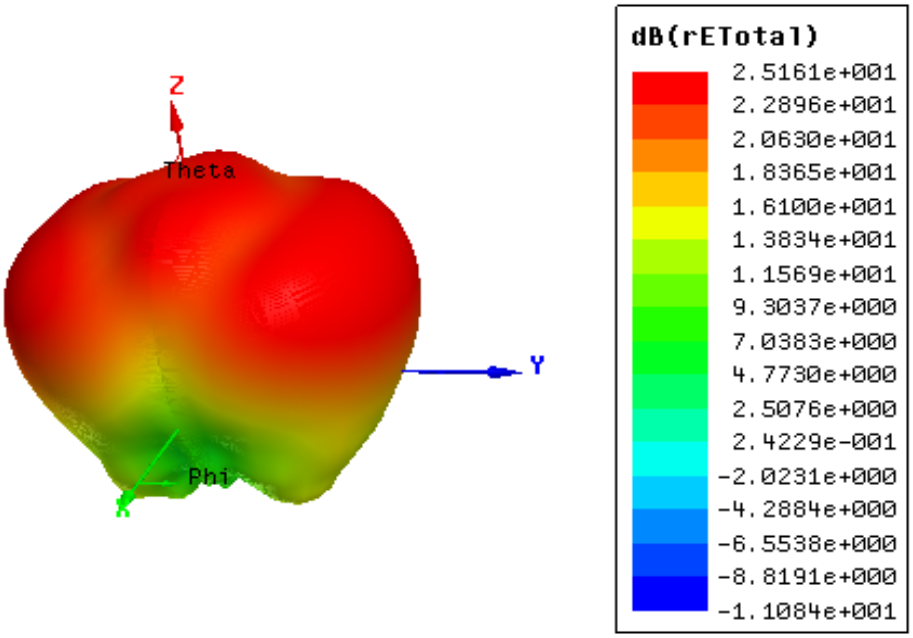

Fig. 4.8 Simulated three dimensional radiation pattern of the rectangular waveguide fed HDRA with tapered section using optimized parameters.

Fig. 4.9 Photograph of the rectangular waveguide fed HDRA using tapered waveguide section with sl = 9.0 mm, sw = 0.7 mm, tp = 21.0 mm, θ = 13°, a_{dr} = 6.27 mm and ε_r = 9.8.

the ground plane and DRA slightly lowers the equivalent permittivity of the DRA. As a result the air gap causes the resonant frequency to shift upwards and reduces the coupling. From Fig. 4.11, it is clear that a very small air gap of 0.01 mm causes the resonant frequency to increase by 270 MHz. The air gap and hence the shift in resonant frequency can be minimized by making the ground plane and bottom surface of the DRA perfectly flat and smooth by using better fabrication techniques. The measured 10 dB bandwidth is 4.5% extending from 10.54 GHz to 11.03 GHz. Figure 4.12 shows the simulated and measured normalized radiation patterns at 10.78 GHz in the xz and yz planes as a function of the elevation angle, θ. Symmetrical broadside radiation patterns with low cross polarization levels are maintained in both the planes at resonant frequency. The measured gain of the antenna as a function of frequency is shown in Fig. 4.13. The gain varies from 4 dBi to 5.5 dBi as the frequency varies from 10.1 GHz to 11.04 GHz. The gain of the proposed antenna is much higher than that of a conventional half wavelength dipole antenna.

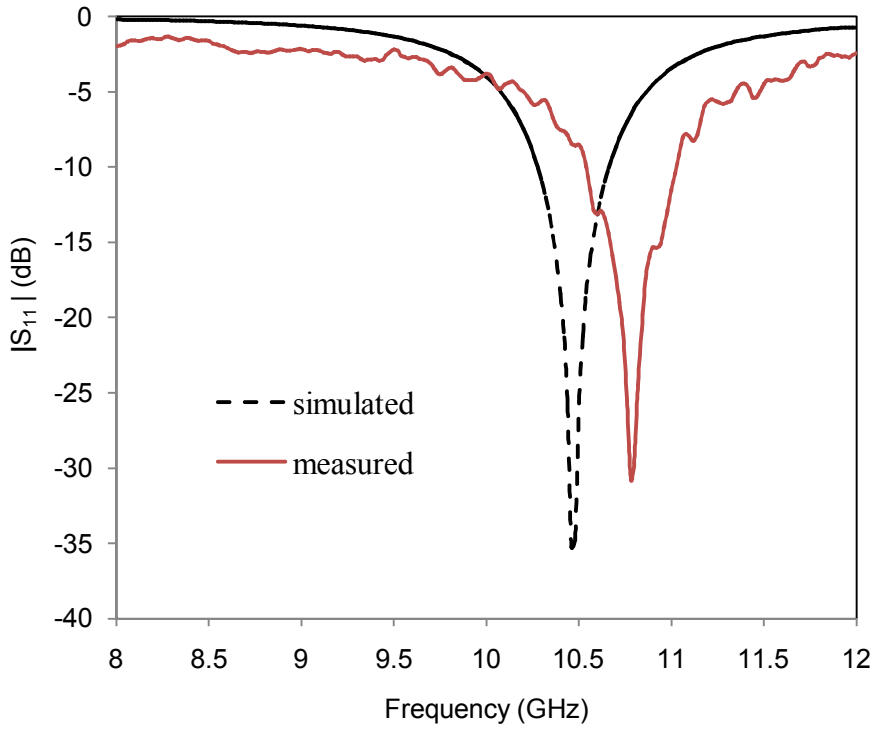

Fig. 4.10 Measured and simulated reflection coefficients of the rectangular waveguide fed HDRA using tapered waveguide section.

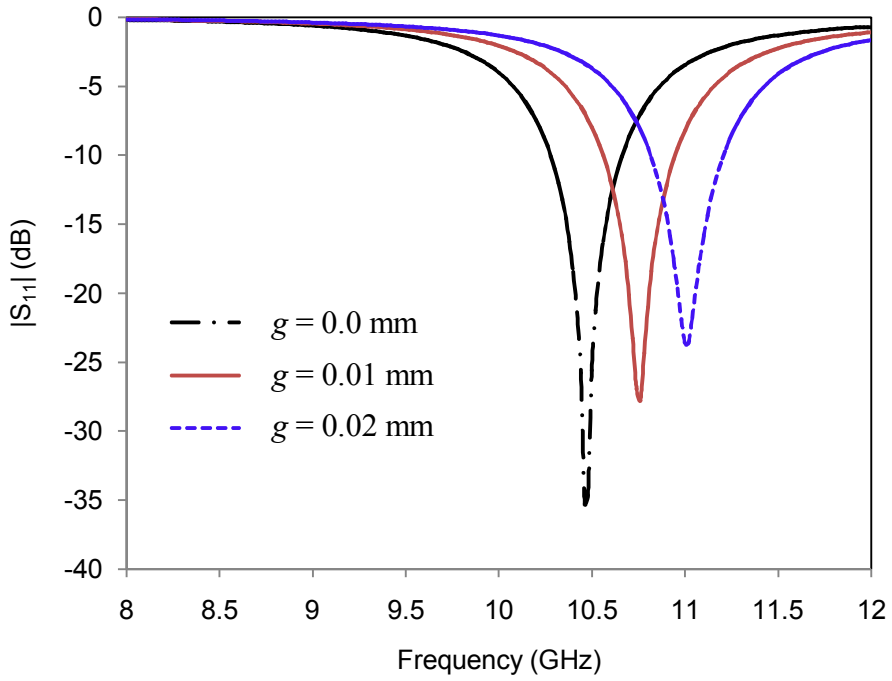

Fig. 4.11 Effect of the air gap *g* on reflection coefficient with *sl* = 9.0 mm, *sw* = 0.7 mm, *tp* = 21.0 mm, and θ = 13°.

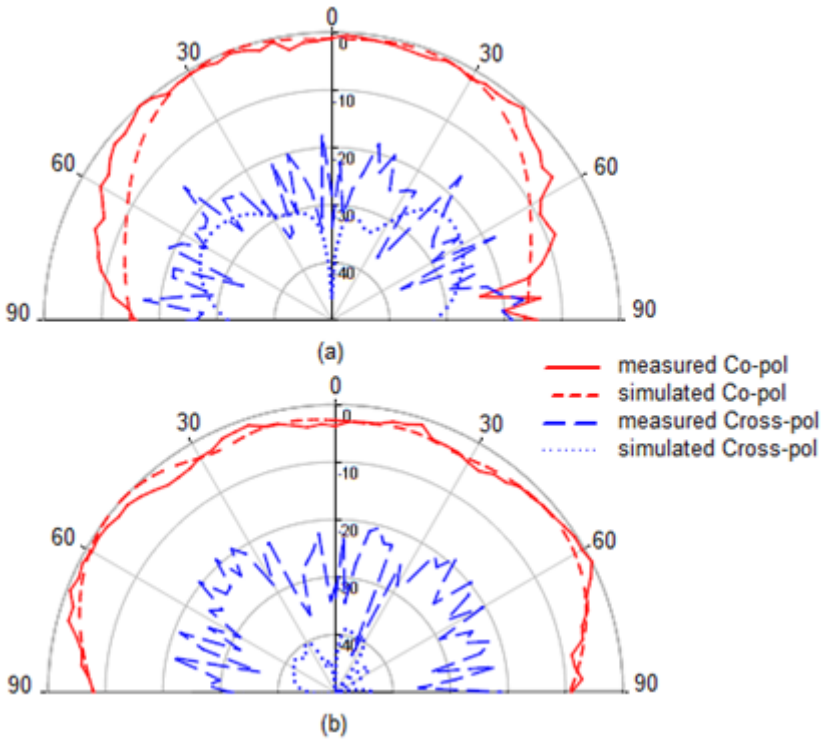

Fig. 4.12 Measured and simulated radiation patterns of the rectangular waveguide fed HDRA using tapered waveguide section at 10.78 GHz: a) in xz plane b) in yz plane.

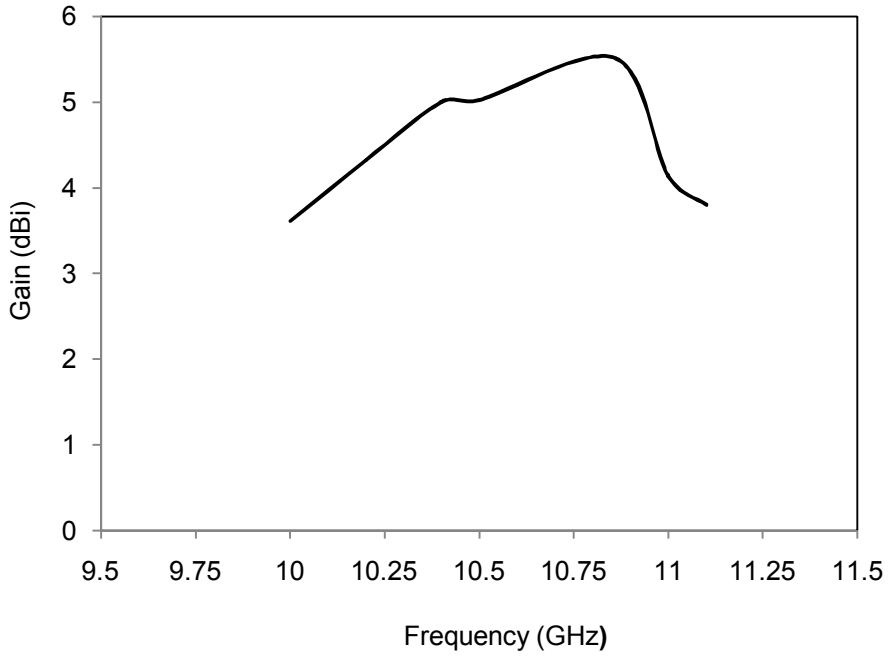

Fig. 4.13 Measured gain of the rectangular waveguide fed HDRA using tapered waveguide section.

This work is published in Microwave and Optical Technology Letters, September 2015.

4.5 Inference

Coupling enhancement of direct coupled waveguide fed HDRA by inserting a tapered section of the waveguide between the rectangular waveguide and the thick ground is discussed in this chapter. Inserting the tapered section of the waveguide ensures very good coupling. Tapered section can be considered as a combination of large number of steps with very small changes in the narrow wall dimension of the rectangular waveguide. Tapered section provides the capacitive susceptance required to neutralise the inductive susceptance of waveguide shorted end slot coupled HDRA. A thorough parametric study has been conducted to analyze the effect of various design parameters on resonant frequency and matching. Since the slot itself acts as a radiator, dimension of the slot plays an important role in determining the resonant frequency. The improved matching is due to the tapered section, the length and angle of tapering play an important role in matching, while it affects the resonant frequency slightly. A prototype of the rectangular waveguide fed HDRA using tapered waveguide section is

fabricated and the reflection and radiation characteristics are measured. Fabrication of the rectangular waveguide fed HDRA with tapered section is easier compared to double step junction coupled waveguide fed HDRA.

Measured resonant frequency shows an upward shift of 290 MHz, when compared with the simulated resonant frequency. The shift in resonant frequency is mainly due to the air gap that exists between the ground plane and DRA. The air gap and hence the shift in resonant frequency can be avoided by making the ground plane and bottom surface of the DRA perfectly flat and smooth by using better fabrication techniques. The proposed structure has a maximum gain of 5.5 dBi. Broadside radiation patterns with low cross-polarization levels in the direction of maximum radiation are obtained. The co-polarized signals are at least 20 dB stronger than the cross-polarized signals in the direction of maximum radiation. The coupling enhancement technique using tapered waveguide section can be extended for DRAs of other shapes too.

Chapter 5

Coupling Enhancement of Stair Shaped Waveguide fed Hemispherical DRA

Coupling enhancement of rectangular waveguide fed hemispherical dielectric resonator antenna (HDRA) using stair shaped waveguide is presented in this chapter. Two steps are introduced at the end of the rectangular waveguide, which give stair shaped appearance to the waveguide. The stair shaped waveguide is terminated by a slotted thick ground plane and DRA is placed directly above the slot. The steps act as an impedance matching device that enhances the coupling from waveguide to DRA. The proposed coupling enhancement technique guarantees very good coupling. The antenna has a high gain of 7.2 dBi at 9.35 GHz and broadside radiation patterns with low levels of cross polarization are obtained. In addition to single band operation, simulation studies of dual and wide band operations of the proposed technique are also presented.

5.1 Introduction

Coupling enhancement of direct coupled waveguide fed HDRA by inserting double step junction between the rectangular waveguide and ground is presented in chapter 3. In double step junction coupled waveguide fed HDRA, two steps are inserted above and below the y axis between waveguide and ground plane. Alternatively, we can say that the steps are symmetrical with respect to the x and y coordinate axes. The purpose of the steps is to provide the capacitive susceptane required to neutralize the inductive susceptance of waveguide shorted end slot coupled HDRA. Reduction in narrow wall dimension of the waveguide without changing the broad wall dimension introduces capacitive susceptance [66]. The narrow wall dimension of the waveguide reduced in two steps non-symmetrically gives the waveguide a stair shaped appearance. The total number of steps in the stair shaped waveguide fed HDRA is two, whereas that of the double step junction coupled waveguide fed HDRA is four. The reduced number of steps makes the stair shaped waveguide fed HDRA less complex compared to the double step junction coupled waveguide fed HDRA. Also the narrow wall dimension of the steps in the proposed stair shaped waveguide fed HDRA is greater than that of the double step junction coupled waveguide fed HDRA. Increase in the narrow wall dimension of the steps makes fabrication easier at millimeter wave frequencies compared to double step junction coupled waveguide fed HDRA. Feasibility of the proposed technique is implemented in X band and the technique can also be implemented in high frequency applications by proper scaling. In addition to single band operation, dual and wide band operations of the proposed technique are suggested. The proposed technique can also be extended to DRAs of other shapes like cylindrical, rectangular, conical etc.

5.2 Configuration of the Stair Shaped Waveguide fed HDRA

Configuration of the proposed stair shaped waveguide fed HDRA is shown in Fig. 5.1. The structure consists of a rectangular waveguide with its narrow wall dimension at the shorted end is reduced in two steps, which gives the waveguide a stair shaped appearance. Thickness and width of the first and second steps are denoted by t_1, w_1 and t_2, w_2 respectively. Steps are introduced in such a way that, it changes only the

narrow wall dimension of the waveguide, keeping the broad wall dimension intact. The stair shaped waveguide is terminated by a square ground plane of thickness *st* on which a rectangular slot of dimension *sl* x *sw* is cut at the centre with an offset, x_w along the *x* direction and HDRA is placed at the centre of the ground plane. Ground plane is placed above the step2 in such a way that slot is at the top and center of step2 along the y direction.

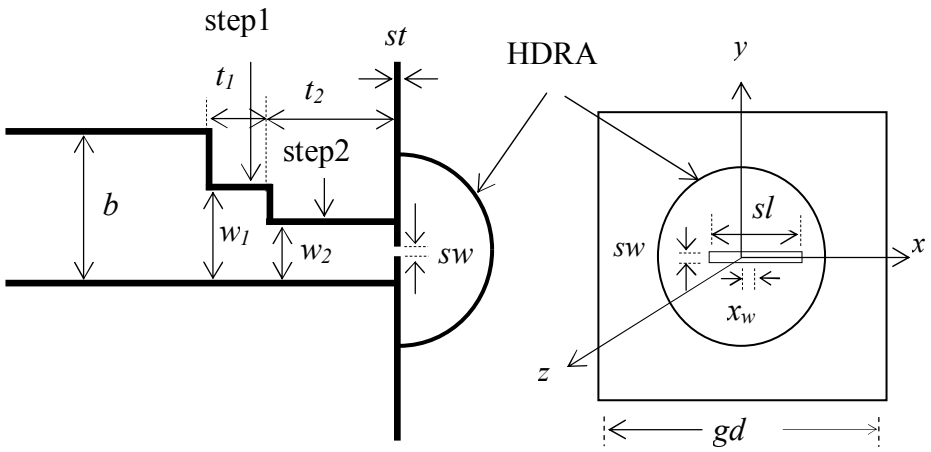

Fig. 5.1 Configuration of the stair shaped waveguide fed HDRA.

5.3 Simulation Results and Discussion

Resonant frequency of a hemispherical DRA is determined by its radius and dielectric constant. Hemispherical DRA of radius 7.5 mm with dielectric constant 9.8 is used in the design of the stair shaped waveguide fed HDRA. DRA is excited in TM_{101} mode, with resonant frequency 8.735 GHz [24]. A rectangular slot is made in the thick ground plane for exciting the DRA. The stair shaped waveguide fed HDRA consists of two resonant structures: the slot and the HDRA. Therefore, in order to resonate the entire structure at 8.735 GHz, parameters of the feeding structure are to be tuned. The length, width and thickness of the slot play a major role in determining the resonant frequency and matching of the proposed stair shaped waveguide fed HDRA. Steps provide the capacitive susceptance [66] required to neutralize the inductive susceptance present in waveguide shorted end slot coupled hemispherical DRA. Therefore dimension of the steps plays an important role in matching, while it alters the resonant

frequency slightly. Susceptance of the proposed structure is zero and conductance is maximum at resonant frequency as illustrated in Fig. 5.2 that ensures good matching.

The resonant frequency and matching of the proposed stair shaped waveguide fed HDRA are influenced by different design parameters. Therefore a thorough parametric study has been conducted using Ansoft HFSS to find out the effect of various design parameters on resonant frequency and matching. Resonant frequency is mainly influenced by the dimension of the slot for a particular DRA with fixed resonant frequency. Figure 5.3 shows the variation in resonant frequency and matching, when the slot length *sl* is varied from 9.9 mm to 10.3 mm in steps of 0.2 mm. From the plot it is clear that the resonant frequency decreases with increase in slot length. Resonant frequency corresponding to the DRA resonance along with maximum matching is obtained for *sl* = 10.1 mm.

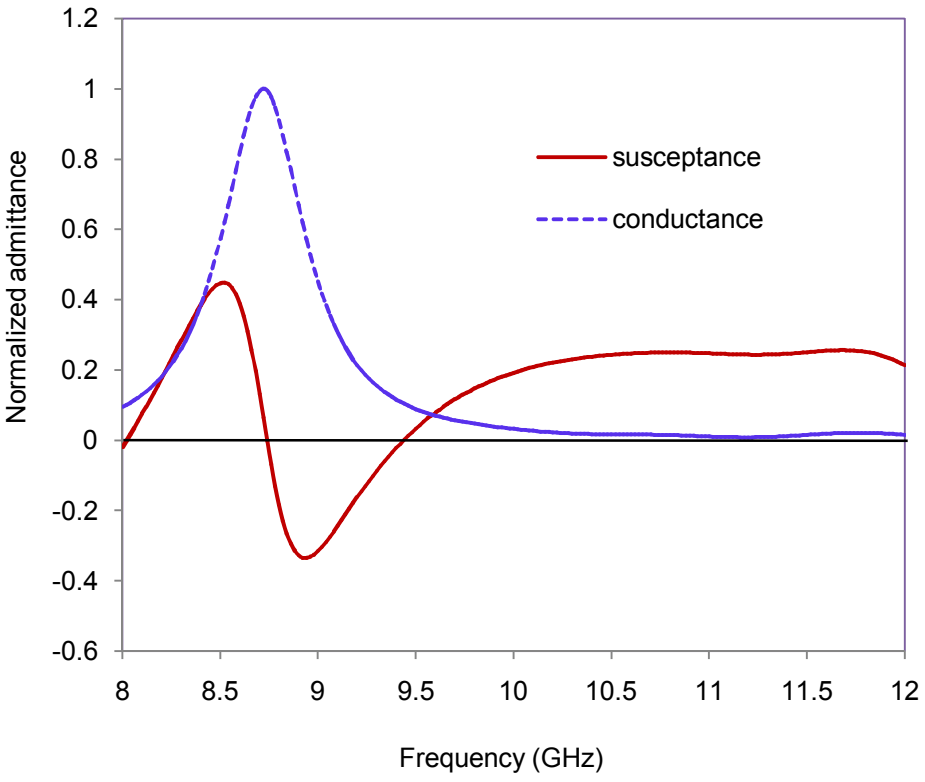

Fig. 5.2 Normalized input admittance of the stair shaped waveguide fed HDRA with *sl* =10.1 mm, *sw* = 0.8 mm, *st* = 1.3 mm, x_w = 0 mm, w_1 = 7.0 mm, t_1 = 5.5 mm, w_2 = 4.3 mm and t_2 = 9.2 mm.

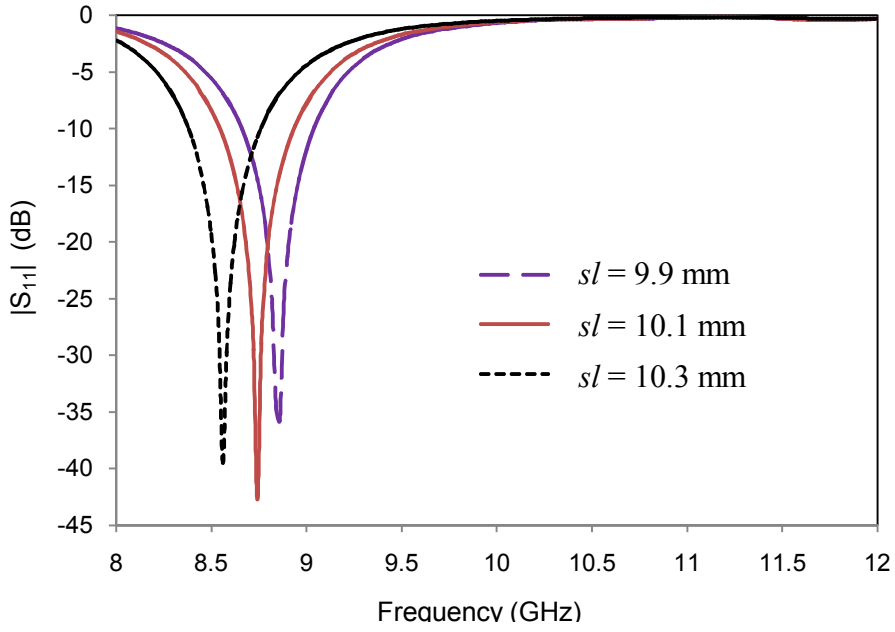

Fig. 5.3 Simulated reflection coefficient as a function of slot length *sl* with *st* = 1.3 mm, *sw* = 0.8 mm, x_w = 0 mm, w_1 = 7.0 mm, t_1 = 5.5 mm, w_2 = 4.3 mm and t_2 = 9.2 mm.

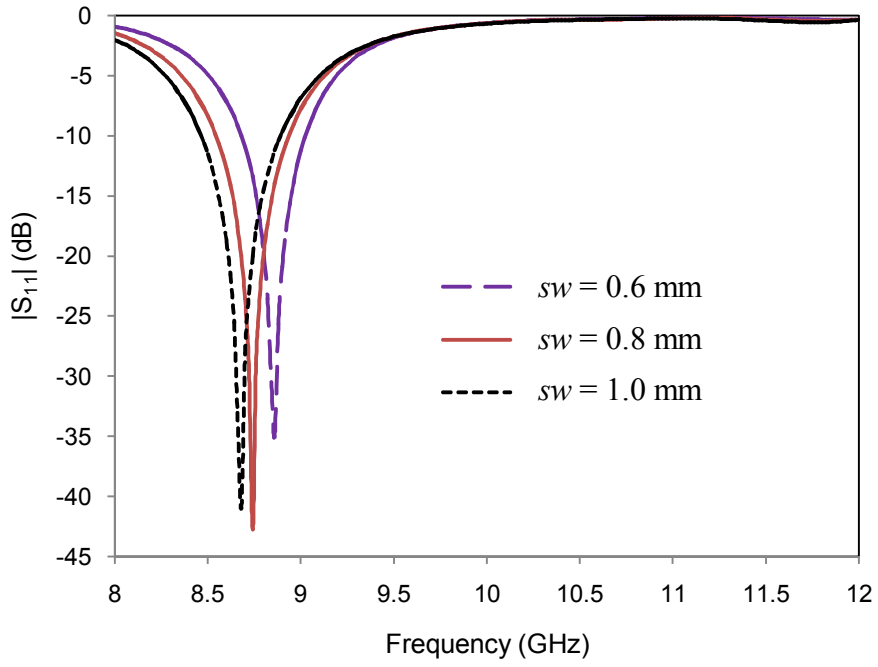

Fig. 5.4 Simulated reflection coefficient as a function of slot width *sw* with *sl* =10.1 mm, *st* = 1.3 mm, x_w = 0 mm, w_1 = 7.0 mm, t_1 = 5.5 mm, w_2 = 4.3 mm and t_2 = 9.2 mm.

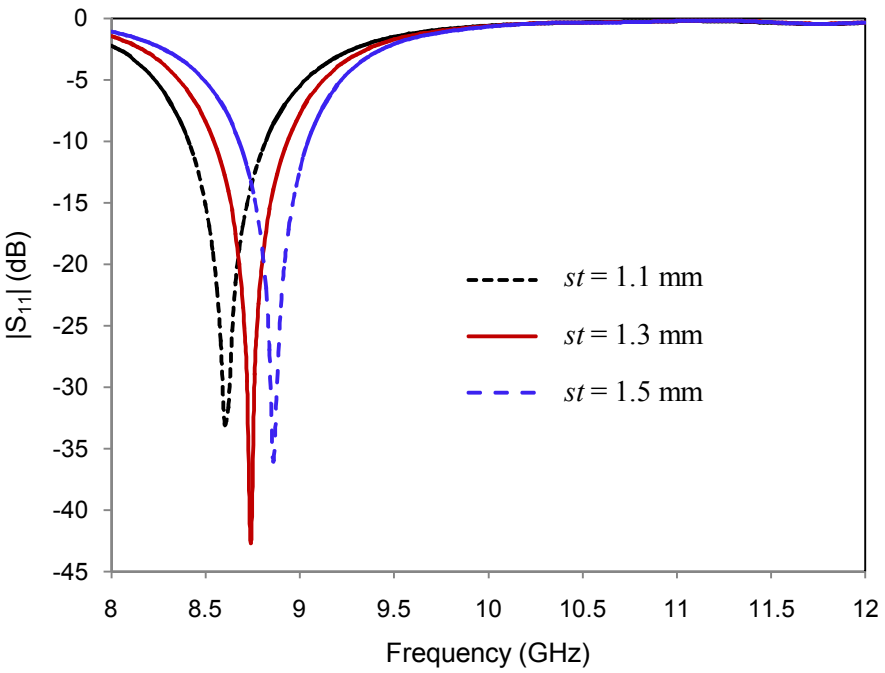

Fig. 5.5 Simulated reflection coefficient as a function of slot thickness *st* with x_w = 0 mm, *sl* = 10.1 mm, *sw* = 0.8 mm, w_1 = 7.0 mm, t_1=5.5 mm, w_2 = 4.3 mm and t_2 = 9.2 mm.

The effect of variation in slot width on reflection coefficient is shown in Fig. 5.4. Resonant frequency decreases with increase in slot width like the slot length, but the effect of slot width on resonant frequency is less compared to slot length. Slot width *sw* = 0.8 mm corresponds to DRA resonance along with maximum matching. The effect of slot length and slot width on resonant frequency can be explained by considering the slot as a secondary waveguide of very small dimension. Cut off frequency is inversely proportional to the cross sectional dimension of the rectangular waveguide. Therefore resonant frequency decreases with increase in slot length and slot width.

Effect of slot thickness on reflection coefficient is shown in Fig. 5.5. The effect of slot thickness *st* can be explained by considering the slot in the thick ground plane as a secondary waveguide with relatively small cross sectional dimension. The resonant frequency increases from 8.62 GHz to 8.86 GHz as the thickness *st* increases from 1.1 mm to 1.5 mm, which is due to the fact that high frequencies have lesser attenuation in

the secondary waveguide [35]. The resonance close to the DRA resonance occurs for slot thickness *st* = 1.3 mm along with maximum coupling.

Dimension of the steps affects matching very much, though it alters the resonant frequency slightly. Variation in w_1 alters the resonant frequency slightly as illustrated in Fig. 5.6. Increase in w_1 from 6.0 mm to 7.0 mm increases the matching and increase in w_1 again to 8.0 mm decreases the matching. The resonant frequency corresponding to DRA resonance along with maximum matching is obtained for w_1 = 7.0 mm. The effect of step1 thickness t_1 on reflection coefficient is shown in Fig. 5.7. Resonant frequency is almost the same for different values of t_1 as indicated in the figure. The optimum value of t_1 for maximum coupling is 5.5 mm.

The effect of varying the step2 width w_2 on reflection coefficient is shown in Fig. 5.8. Resonant frequency is almost same for different values of step2 width w_2. Optimum value of step2 width is w_2 = 4.3 mm, for which maximum matching is obtained. Figure 5.9 shows the effect of the thickness of step2 on reflection coefficient. There is a slight increase in resonant frequency as step2 thickness t_2 increases from 8.8 mm to 9.6 mm. Resonant frequency corresponding to the resonant frequency of the DRA (8.735 GHz) along with maximum matching is obtained for step2 thickness t_2 = 9.2 mm.

In the field of antenna design, the term radiation pattern refers to the directional dependence of the strength of the radio waves from the antenna or other source. The far field radiation pattern may be represented graphically as a plot of one of the related variables: the field strength at a constant radius, the power per unit solid angle and the directive gain. The rear directed radiation from the antenna can introduce difficulties in packaging, or cause coupling to components or other antennas mounted behind. The backward radiation is very much influenced by the dimension of the ground plane. The effect of ground plane dimension on backward radiation is shown in Fig. 5.10. Backward radiation decreases as the size of the square ground plane increases from 50 mm to 150 mm. But the size of the ground plane cannot be increased too much, since it will increase the overall size of the structure. As a compromise between the size and performance, dimension of the ground plane *gd* is selected as 100 mm. The three dimensional radiation pattern of the antenna is simulated using Ansoft HFSS and the

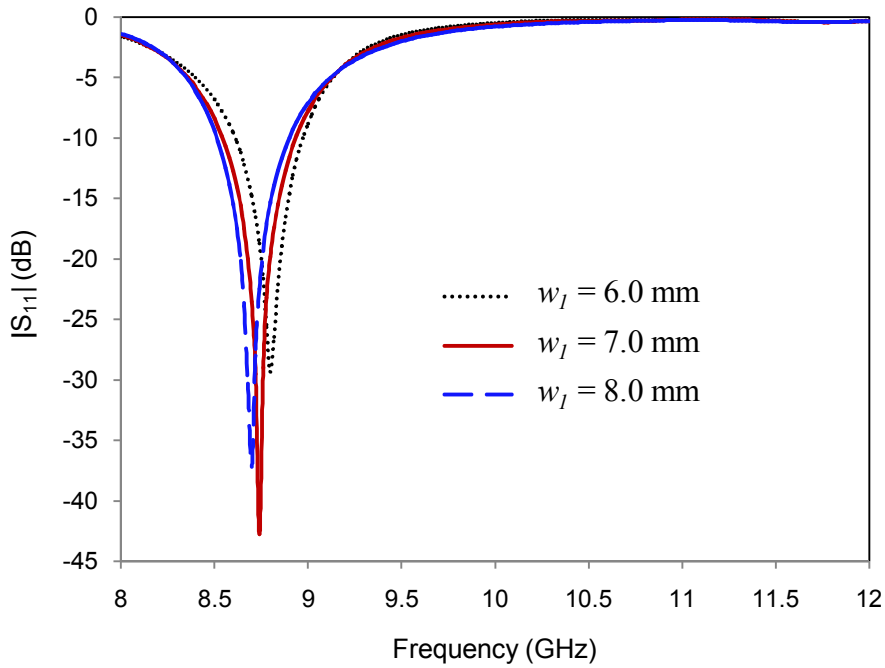

Fig. 5.6 Simulated reflection coefficient as a function of step1 width, w_1 with st = 1.3 mm, sl =10.1 mm, sw = 0.8 mm, x_w = 0 mm, t_1 = 5.5 mm, t_2 = 9.2 mm and w_2 = 4.3 mm.

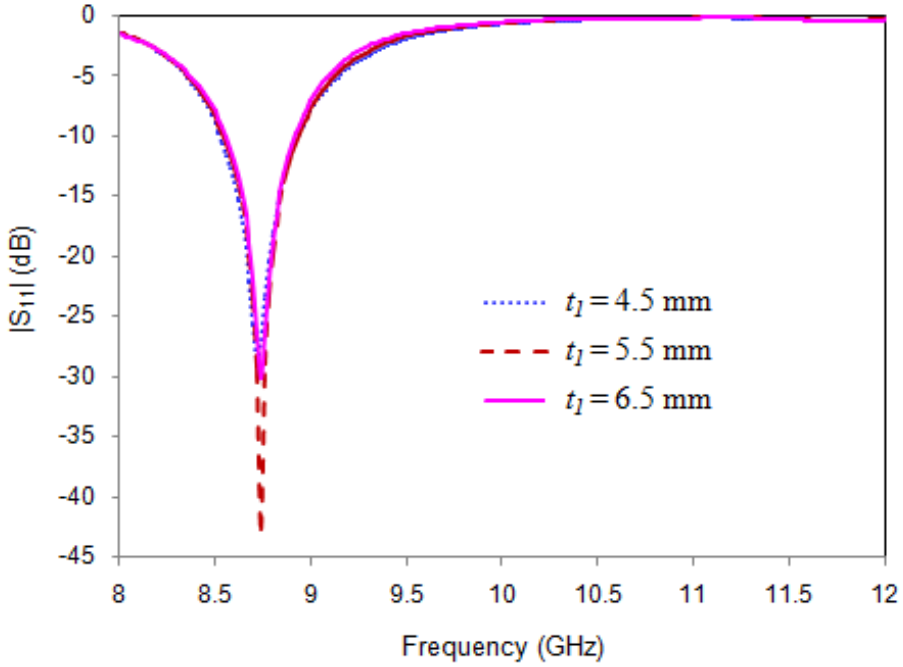

Fig. 5.7 Effect of variation in step1 thickness t_1 on reflection coefficient with x_w = 0 mm, sl = 10.1 mm, sw = 0.8 mm, st = 1.3 mm, w_1 = 7.0 mm, w_2 = 4.3 mm and t_2 = 9.2 mm.

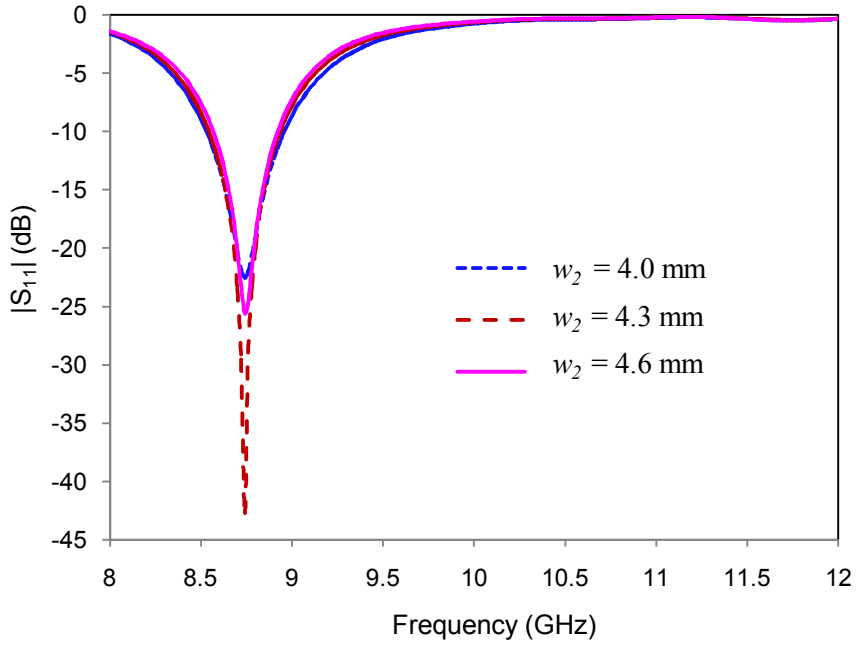

Fig. 5.8 Simulated reflection coefficient as a function of step2 width w_2 with sl =10.1 mm, sw = 0.8 mm, st = 1.3 mm, x_w = 0 mm, w_1 = 7.0 mm, t_1 = 5.5 mm and t_2 = 9.2 mm.

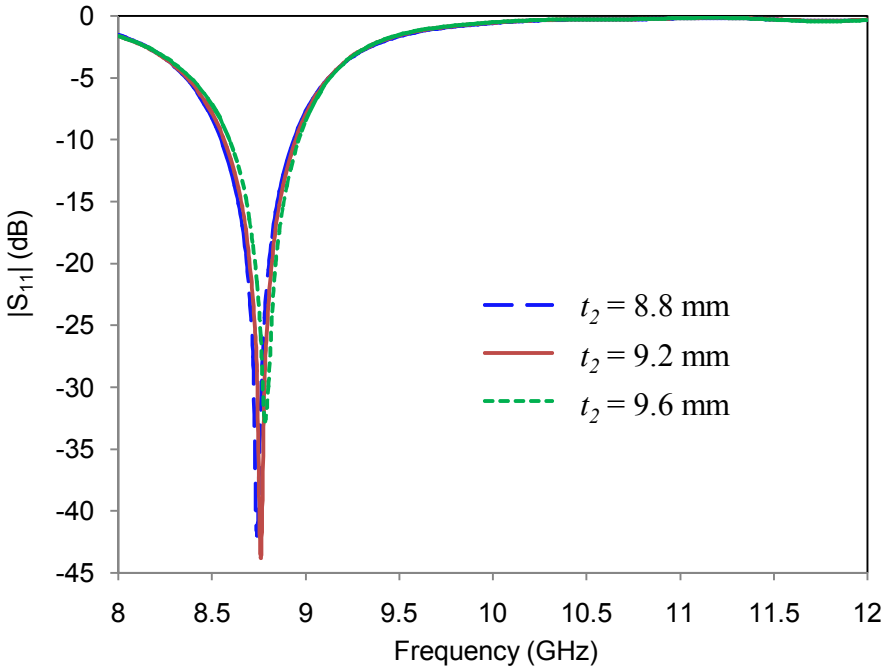

Fig. 5.9 Simulated reflection coefficient as a function of step2 thickness t_2 with sl =10.1 mm, sw = 0.8 mm, st = 1.3 mm, x_w = 0 mm, w_1 = 7.0 mm, t_1 = 5.5 mm and w_2 = 4.3 mm.

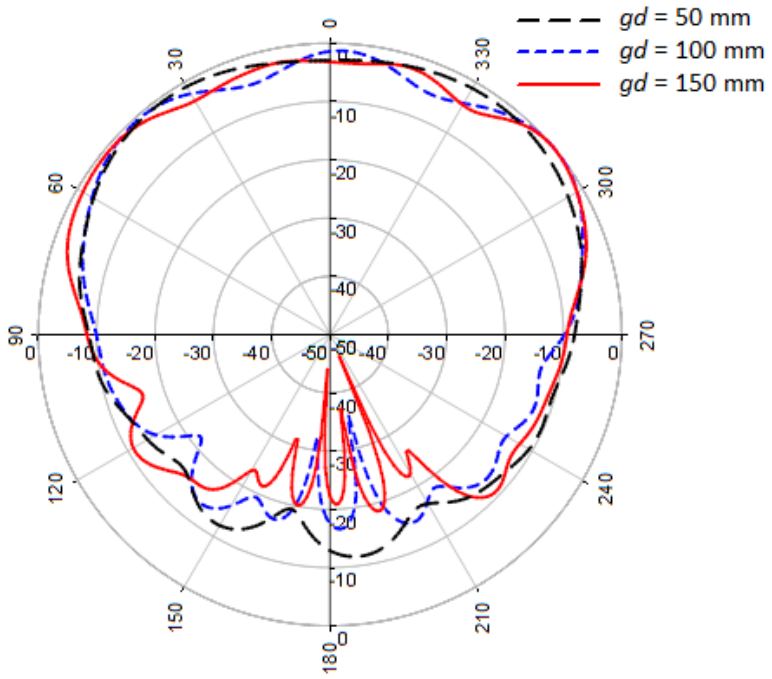

Fig. 5.10. Effect of ground plane dimension, *gd* on backward radiation with *sl* = 10.1 mm, *sw* = 0.8 mm, *st* = 1.3 mm, x_w = 0 mm, w_1 = 7.0 mm, w_2 = 4.3 mm, t_1 = 5.5 mm and t_2 = 9.2 mm.

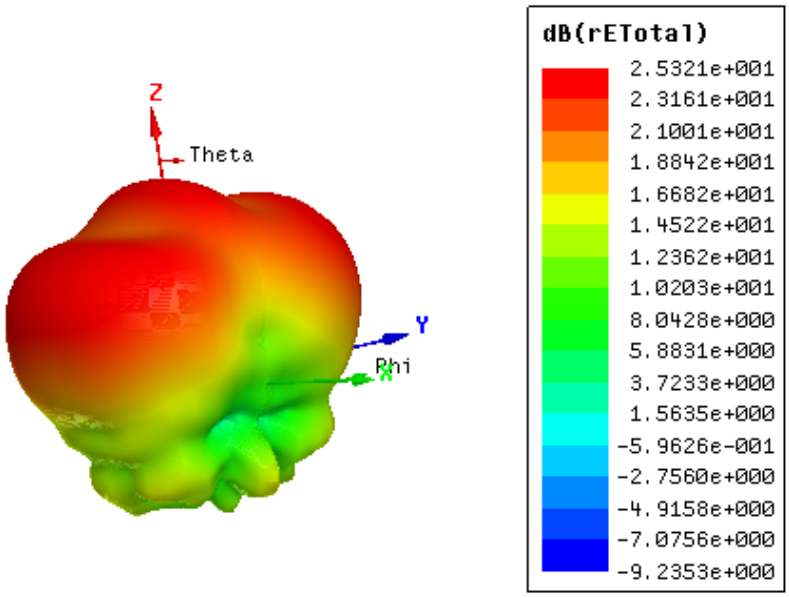

Fig. 5.11 Simulated three dimensional radiation pattern of the stair shaped waveguide fed HDRA at 8.74 GHz with *sl* =10.1 mm, *sw* = 0.8 mm, *st* = 1.3 mm, x_w = 0 mm,w_1 = 7.0 mm, t_1 = 5.5 mm, w_2 = 4.3 mm and t_2 = 9.2 mm.

three dimensional radiation pattern of the stair shaped waveguide fed HDRA with optimized parameters is shown in Fig. 5.11.

5.4 Dual and Wide band Operations of Stair Shaped Waveguide fed HDRA

Resonance of the proposed structure is due to both slot and HDRA. For single resonance operation, resonances of the slot and HDRA are to be merged. The slot is located at the centre of the ground plane or $x_w = 0$ for single resonance operation. Multiple frequency operation is highly desirable in modern wireless communication systems. If a single DRA can support multiple frequency bands, multiple single frequency antennas are not needed. Dual resonance can be achieved by using defected ground, DRAs of special shapes and stacked DRAs [122-125].

In this dissertation, dual resonance is implemented without using any additional structures. The resonant frequency and matching can be controlled by giving an offset to the slot along its length. Keeping the DRA at the centre of the ground plane and moving the slot away from the centre along its length can excite DRA in higher order modes. It is observed that when the offset is increased, a second resonance at lower frequency starts appearing, which finally leads to dual band operation for offset, x_w = 1.5 mm. For dual band operation, values of other parameters are: w_1 = 6.5 mm, w_2 = 2.8 mm, t_1 = 6.5 mm, t_2 = 9.5 mm, sl = 10.0 mm, sw = 0.7 mm and st = 1.3 mm. Simulated reflection coefficient for dual band operation is shown in Fig. 5.12. The resonant frequency corresponding to the first and second bands are: 8.32 GHz and 9.28 GHz with 10 dB bandwidths of 4.33% and 4.31% respectively. Figure 5.13(a) and 5.13(b) represent the radiation patterns at 8.32 GHz and 9.28 GHz respectively. The co-polarized signals are at least 20 dB stronger than the cross-polarized signals in the direction of maximum radiation.

Single resonance operation of stair shaped waveguide fed HDRA provides only a narrow bandwidth of 4.63%. Bandwidth can be improved by using stacked DRAs [82-86]. But this will increase the cost of the system due to the additional DRA required. DRAs with special shapes can be used to increase bandwidth [108-110]. In stair shaped waveguide fed HDRA; wide band operation is achieved by making the

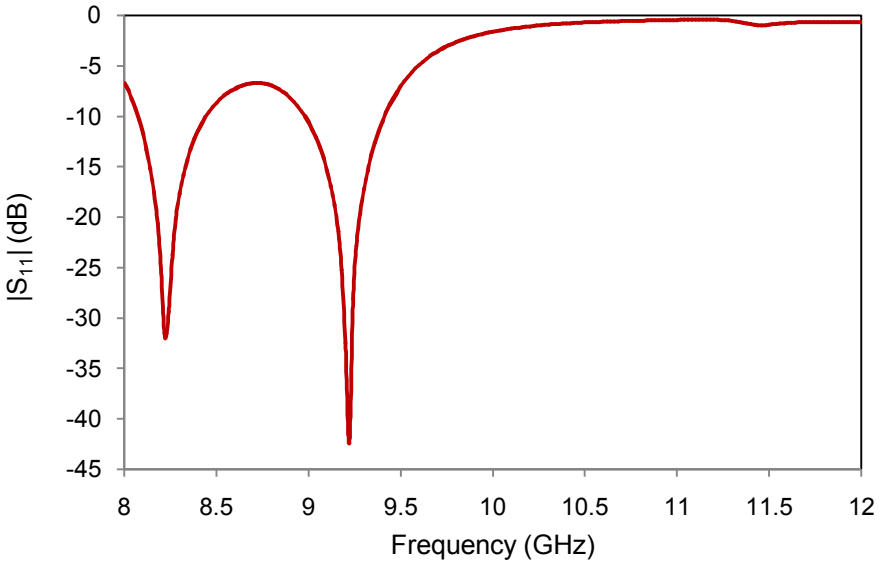

Fig. 5.12 Simulated reflection coefficient of stair shaped waveguide fed HDRA for dual band operation with sl = 10.0 mm, sw = 0.7 mm, st =1.3 mm, t_1 = 6.5 mm, t_2 = 9.5 mm, w_1 = 6.5 mm, w_2 = 2.8 mm and x_w = 1.5 mm.

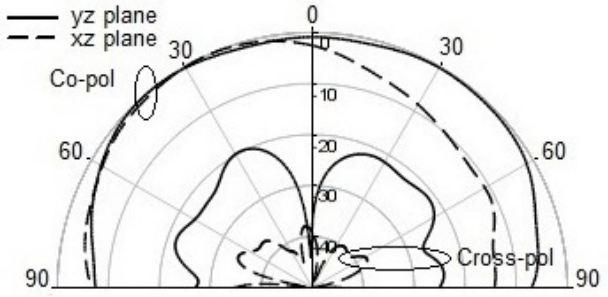

(a)

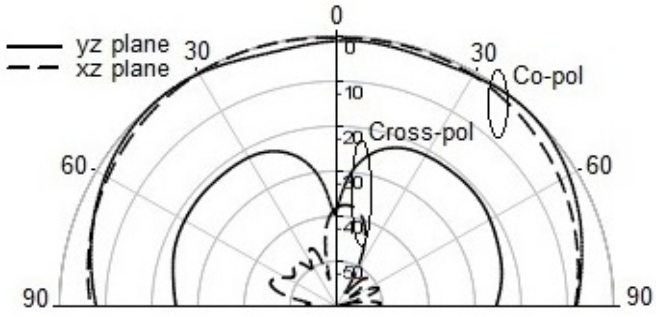

(b)

Fig. 5.13 Simulated radiation pattern of stair shaped waveguide fed HDRA for dual band operation with parameters same as in Fig. 5.12: (a) at 8.32 GHz (b) at 9.28 GHz.

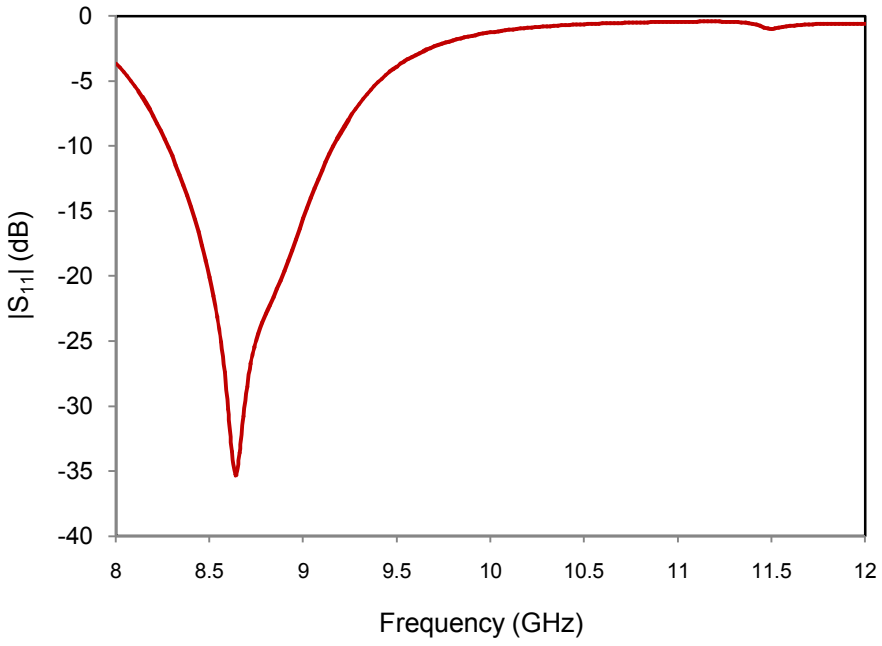

(a)

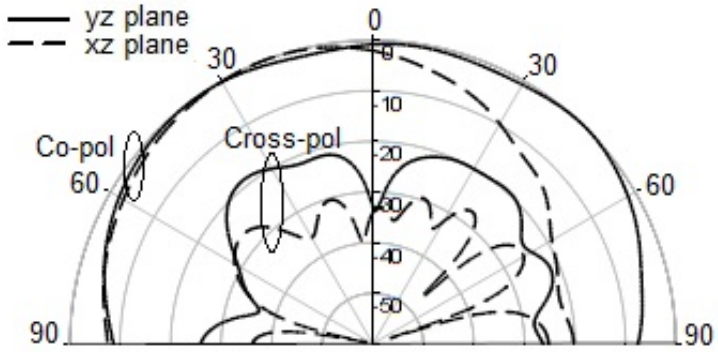

(b)

Fig. 5.14 Simulated results of wide band operation with sl = 10.0 mm, sw = 0.7 mm, st =1.3 mm, t_1 = 6.5 mm, t_2 = 9.5 mm, w_1 = 6.5 mm, w_2 = 2.8 mm, and x_w = 0.7 mm: (a) reflection coefficient (b) radiation pattern at 8.5 GHz.

resonance of the slot and DRA to occur separately. If the resonant frequency of the slot and DRA are adjusted in such a way that they are separated and close to each other wide band operation can be obtained. This can be done by reducing the slot offset x_w = 0.7 mm while keeping all other parameters same as in the dual band operation.

Simulated reflection coefficient of wideband operation is shown in Fig. 5.14(a). The 10 dB bandwidth obtained is 9.93%, which is more than twice that obtained in single resonance operation. Fig. 5.14(b) shows the radiation pattern in both the planes at 8.5 GHz. The co-polarized signals are much stronger than the cross-polarized signals in the direction of maximum radiation.

5.5. Measured Results

A prototype of the stair shaped waveguide fed HDRA for single band operation is fabricated using the optimized parameters. The optimized parameters are: sl = 10.1 mm, sw = 0.8 mm, st = 1.3 mm, x_w = 0.0 mm, w_1 = 7.0 mm, t_1 = 5.5 mm, w_2 = 4.3 mm, and t_2 = 9.2 mm. Width of the steps in stair shaped waveguide fed HDRA is much greater than the steps used in the double step junction coupled waveguide fed HDRA that makes fabrication easier at millimeter wave frequencies. Photograph of the prototype of the fabricated stair shaped waveguide fed HDRA is shown in Fig. 5.15. As the bottom surface of the DRA and ground plane are not perfectly flat and smooth, the fabricated structure shows uneven air gaps between the ground plane and DRA. Therefore the structure is again simulated by introducing very small values of air gap between the ground plane and DRA. The air gap causes the equivalent permittivity of the DRA to decrease, which causes the resonant frequency to increase and the matching to decrease as illustrated in Fig. 5.16.

Reflection coefficient, radiation pattern and gain of the stair shaped waveguide fed HDRA are measured using R&S ZVL 13 Vector Network analyzer. Figure 5.17 shows the comparison between the measured and simulated reflection coefficients (air gap g = 0.02 mm). The measured resonant frequency is 9.37 GHz, with a 10 dB bandwidth of 5.76%. The measured resonant frequency shows an upward shift of 635 MHz, when compared with the simulated resonant frequency (without air gap). The shift in resonant frequency is due to the air gap present between the ground plane and DRA, which can be reduced by making the ground plane and bottom surface of the DRA perfectly flat and smooth by using efficient fabrication techniques.

Fig. 5.15 Photograph of the fabricated stair shaped waveguide fed DRA with sl = 10.1 mm, sw = 0.8 mm, st =1.3 mm, x_w = 0.0 mm, w_1 = 7.0 mm, t_1 = 5.5 mm, w_2 = 4.3 mm and t_2 = 9.2 mm.

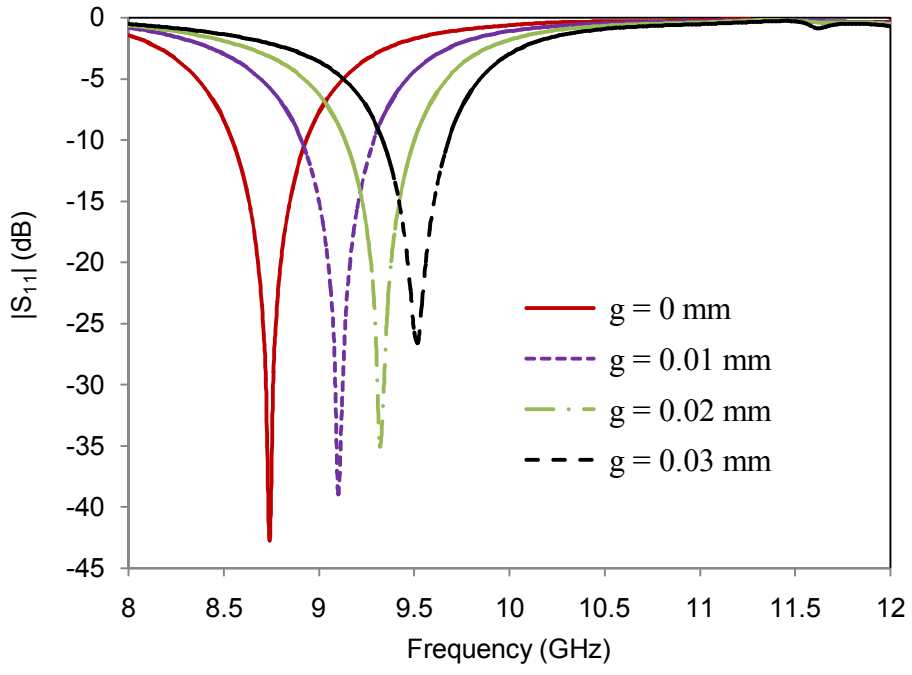

Fig. 5.16 Effect of air gap, g between the ground plane and DRA on reflection coefficient with sl = 10.1 mm, sw = 0.8 mm, st =1.3 mm, x_w = 0.0 mm, w_1 = 7.0 mm, t_1 = 5.5 mm, w_2 = 4.3 mm and t_2 = 9.2 mm.

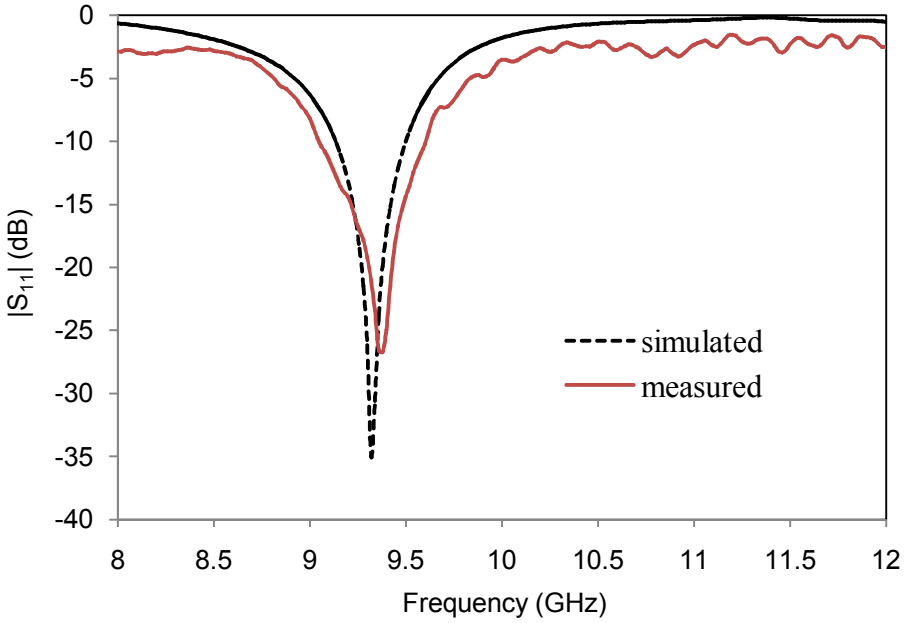

Fig. 5.17 Measured and simulated reflection coefficients of stair shaped waveguide fed HDRA.

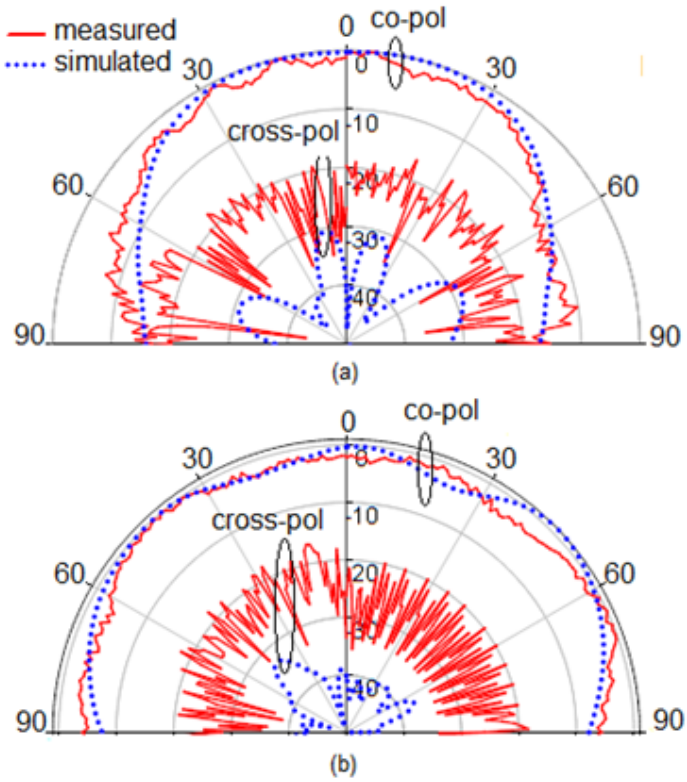

Fig. 5.18 Measured and simulated radiation patterns of the stair shaped waveguide fed HDRA at 9.38 GHz: (a) in xz plane and (b) in yz plane.

Figure 5.18 illustrates the comparison between the measured and simulated radiation patterns in xz and yz planes at 9.38 GHz as a function of the elevation angle, θ. Low cross-polarization levels are obtained, since the slot is centered under the DRA, which would mitigate the excitation of higher order modes that contribute to cross-pol levels [132]. The co-polarization signals are symmetrical with respect to the z axis and the cross-polarized signals are at least 20 dB below the corresponding co-polarized signals in the broadside direction. The measured and simulated radiation patterns have the same characteristics over the operating frequency band. Gain of the antenna is measured using gain comparison method and the measured gain for a frequency range from 8.5 GHz to 10.5 GHz is shown in Fig. 5.19. The antenna has a high gain of 7.2 dBi at 9.35 GHz with a 3 dB gain bandwidth of 17%. The measured gain is more than 5 dBi for the entire 10 dB impedance bandwidth.

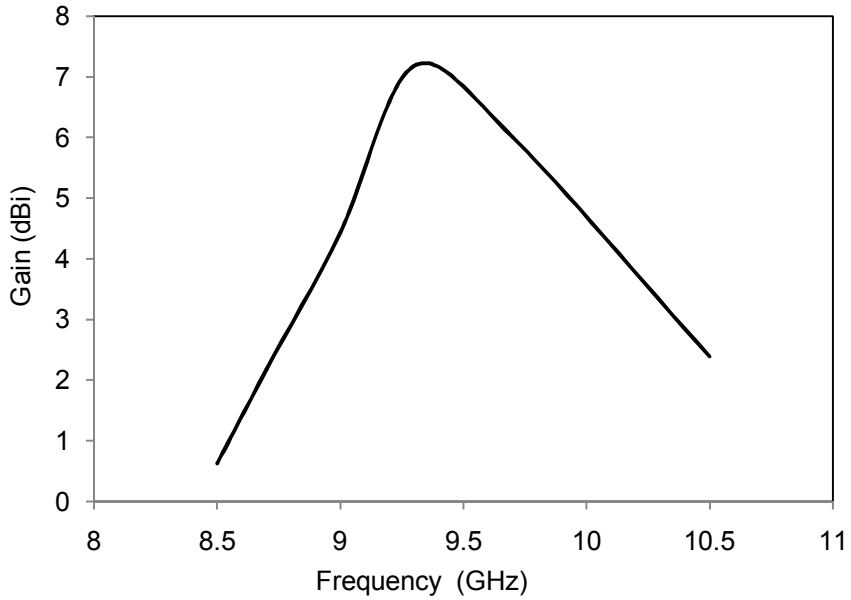

Fig. 5.19 Measured gain of the stair shaped waveguide fed HDRA

This work is published in International Journal of Scientific Progress and Research

5.6. Inference

The poor coupling of waveguide shorted end slot coupled HDRA is due to the inductive susceptance offered by the DRA loaded slot. If the inductive suseptance is overcome by its capacitive counterpart, coupling could be improved. Reducing the

narrow wall dimension of the waveguide without changing the broad wall dimension introduces capacitive susceptance. The capacitive susceptance introduced by the steps neutralizes the inductive susceptance of waveguide shorted end slot coupled HDRA and provides increased coupling. The double step junction coupled waveguide fed HDRA discussed in chapter 3 provides very good coupling. But the structure is somewhat complex since it requires two steps with different narrow wall dimension above and below the y axis. Thus the total number of steps in the double step junction coupled waveguide fed HDRA is four. But the total number of steps in the stair shaped waveguide fed HDRA is only two. The steps with reduced narrow wall dimension give the waveguide a stair shaped appearance. The reduced number of steps makes fabrication easier compared to the double step junction coupled waveguide fed HDRA. Another advantage of the stair shaped waveguide fed HDRA is that the narrow wall dimension of the second step is 4.3 mm, which is 0.9 mm higher than that used in the double step junction coupled waveguide fed HDRA. In order to study the effect of various design parameters on antenna design, a thorough parametric study has been conducted using Ansoft HFSS.

The proposed stair shaped waveguide fed HDRA is fabricated with the optimum parameters and measurements were taken using R&S ZVL 13 vector network analyzer. The measured resonant frequency shows an upward shift in resonant frequency and reduction in matching, which is mainly due to the air gap present between the ground plane and DRA. The air gap and hence the shift in resonant frequency can be reduced by making the ground plane and bottom surface of the DRA perfectly flat and smooth by using efficient fabrication techniques. Radiation patterns with very low levels of cross polarization are obtained in both the planes. The proposed antenna has a high gain of 7.2 dBi at 9.3 GHz, which is much higher than that of a dipole antenna. Dual and wideband operations of the proposed method are also suggested. An offset is applied to the slot to implement dual and wide band operations. The proposed coupling enhancement technique ensures very good coupling with reduced fabrication complexity.

Chapter 6

Coupling Enhancement of Waveguide Shorted End Slot Coupled Cylindrical DRA

Coupling enhancement techniques developed for rectangular waveguide fed hemispherical DRA can also be applied to DRAs of other shapes. Double step junction and tapered section coupled waveguide fed cylindrical dielectric resonator antenna (CDRA) is studied in this chapter. Reflection coefficient, radiation pattern and gain of the antennas are measured. Double step junction coupled waveguide fed cylindrical DRA gives a maximum gain of 8.83 dBi. The measured 10 dB bandwidth is 6.1% extending from 9.22 GHz to 9.8 GHz. Measured resonant frequency of the rectangular waveguide fed cylindrical DRA using tapered waveguide section is 9.46 GHz with 10 dB bandwidth 6.34%. The antenna achieves a maximum gain of 6 dBi at 9.3 GHz with a 3 dB gain bandwidth of 14%.

6.1 Introduction

Theoretical and experimental study of double step junction coupled waveguide fed hemispherical dielectric resonator antenna is conducted in chapter 3. The double step junction coupled waveguide fed HDRA can be applied to DRAs of other shapes like rectangular, cylindrical, conical etc. Cylindrical dielectric resonator antennas (CDRA) are easy to fabricate, but they have edge shaped boundaries, which makes analytical solution difficult to obtain. The experimental verification of double step junction coupled rectangular waveguide fed CDRA and tapered waveguide fed CDRA is performed in this chapter. Since the effect of the different parameters on the performance of the antenna is already studied in previous chapters, it is not repeated here. However the effect of the dimension of the cylindrical DRA on reflection coefficient is studied in this chapter.

6.2 Cylindrical DRA

Dielectric resonators of any shape can be used for antenna design, though rectangular, cylindrical, and hemispherical are predominant. The design parameters such as permittivity, resonant frequency, input impedance, coupling mechanisms and radiation patterns vary for different shapes and hence the analytical model for analyzing each geometrical configuration is different. Simplified analysis and mechanical fabrication play an important role in selecting the shape of DRAs. Since hemispherical DRA has zero degree of design freedom, bandwidth remains fixed and is difficult to optimize for particular requirements. While cylindrical DRA has one degree of freedom and different values of radius-height pairs give different values of bandwidth, and directivity. The edge shaped boundaries of the cylindrical DRA makes rigorous analysis difficult. However, approximate methods can be used for the analysis of cylindrical DRAs. These include magnetic wall, dielectric waveguide wall, variational, mixed model, and effective dielectric constants [133], [134]. The rigorous methods reported are mode matching method, finite element method, finite difference time domain method, perturbational-asymptotic series techniques, and methods based on surface or volume integral equations [135-137]. These rigorous techniques provide accurate description of the electromagnetic field in and around the resonator and also

permit taking into account the influence of the surrounding structure more accurately. The TM_{110} mode resonant frequency of CDRA can be calculated using [138]:

$$f_r = \frac{c}{2\pi a\sqrt{\varepsilon_r}}\left[1.71+2\left(\frac{a}{2h}\right)+0.1578\left(\frac{a}{2h}\right)^2\right]$$

where c is the speed of light in vacuum and a, h represent the radius and height respectively of the CDRA.

6.3 Double Step Junction Coupled Waveguide fed CDRA

Configuration of the double step junction coupled waveguide fed cylindrical DRA is shown in Fig. 6.1. The structure consists of a rectangular waveguide with two steps at the end, which is terminated in a slotted thick ground plane and cylindrical DRA is placed above the slot on the ground plane. *2t1*, *2w1* represent the thickness and width of step1 and *2t2*, *2w2* represent the thickness and width of step2. Length, width and thickness of the slot are denoted by *2L3*, *2w3*, *2t3* respectively. The steps reduce only the narrow wall dimension of the waveguide keeping the broad wall dimension intact and thus provide the required capacitive susceptance.

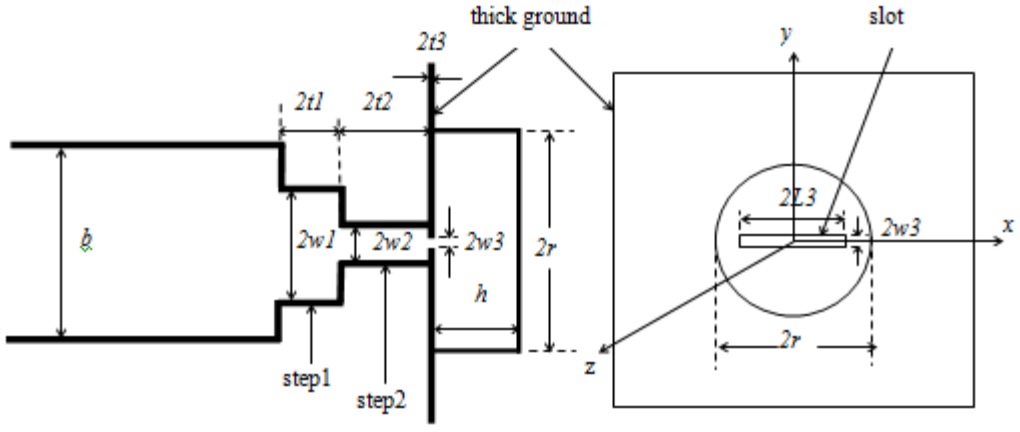

Fig. 6.1 Configuration of the double step junction coupled waveguide fed CDRA

The optimum parameters obtained for double step junction coupled waveguide fed HDRA is used for experimentation with cylindrical DRA. Cylindrical DRA with radius, r = 7.0 mm, height, h = 5.0 mm and dielectric constant, ε_r = 9.8 is used in the

design of double step junction coupled rectangular waveguide fed cylindrical DRA. The dimension of the slot is: *2L3* = 9.5 mm, *2w3* = 1.0 mm, and *2t3* = 1.3 mm. Dimensions of the steps are: *2t1* = 4.0 mm, *2w1* = 6.5 mm, *2t2* = 8.0 mm and *2w2* = 3.4 mm. Comparison between the normalized admittance plot of waveguide shorted end slot coupled (direct coupled) cylindrical DRA and double step junction coupled waveguide fed cylindrical DRA is shown in Fig. 6.2. Dimension of the slot in the direct coupled waveguide fed cylindrical DRA is same as that used in the double step junction coupled waveguide fed CDRA. Susceptance of the direct coupled waveguide fed cylindrical DRA is inductive over the entire operating frequency range. The normalized susceptance at resonant frequency is zero for the double step junction coupled waveguide fed CDRA. This is due to the steps that provide the required capacitive susceptance. The normalized conductance is maximum at resonant frequency.

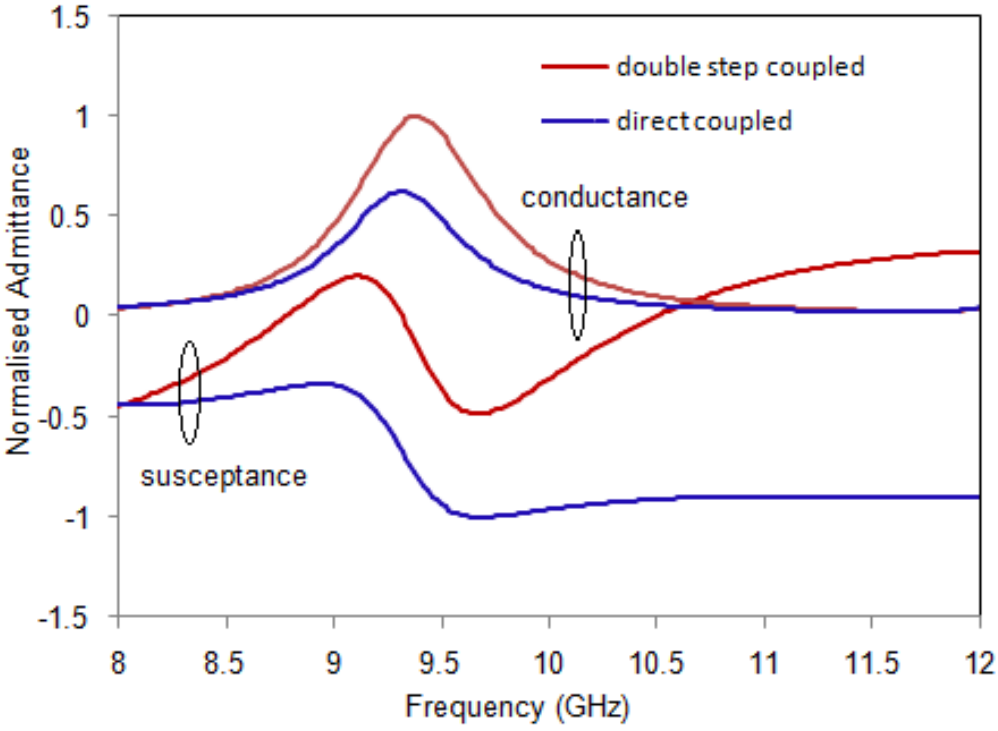

Fig. 6.2 Comparison between the normalized conductance/susceptance of direct coupled and double step junction coupled waveguide fed CDRA

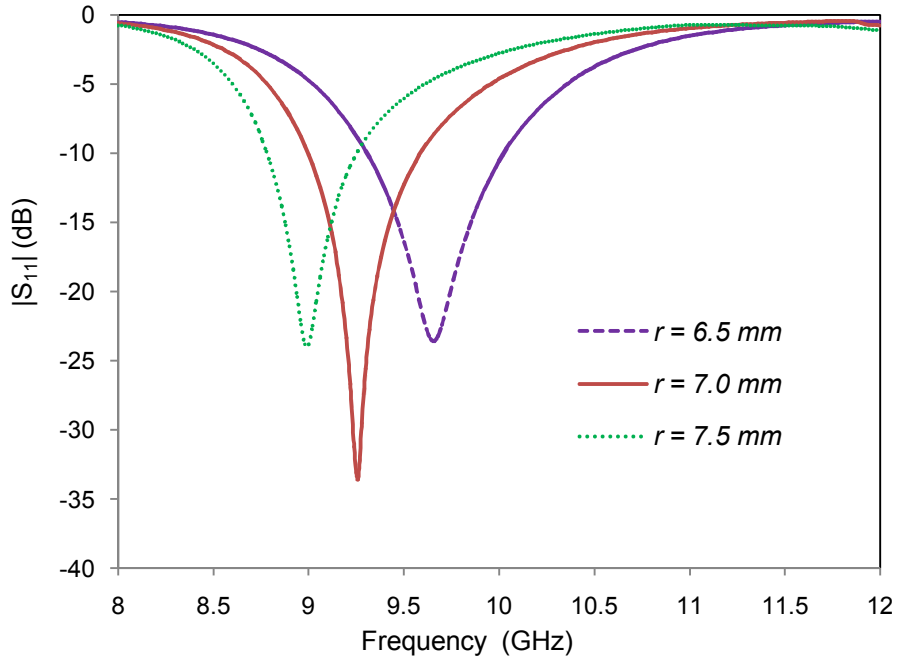

Fig. 6.3 Reflection coefficient of double step junction coupled waveguide fed CDRA as a function of radius *r* of CDRA with *h* = 5.0 mm, *2t1* = 4.0 mm, *2w1* = 6.5 mm, *2t2* = 8.0 mm, *2w2* = 3.4 mm, *2t3* = 1.3 mm, *2w3* = *1.0* mm and *2L3* = 9.5 mm.

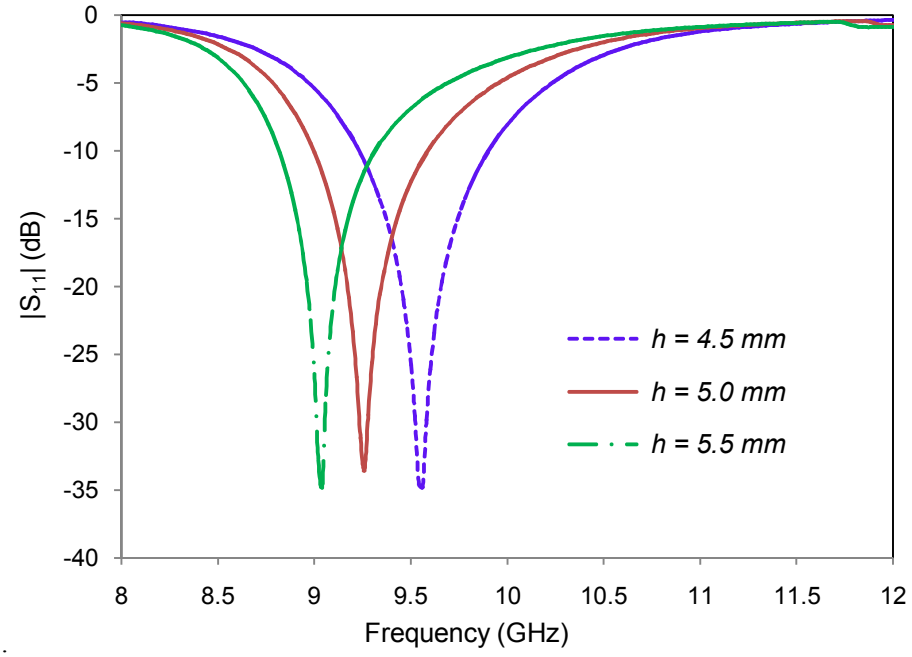

Fig. 6.4 Reflection coefficient of double step junction coupled waveguide fed CDRA as a function of height *h* of CDRA with the optimized parameters of the feeding structure.

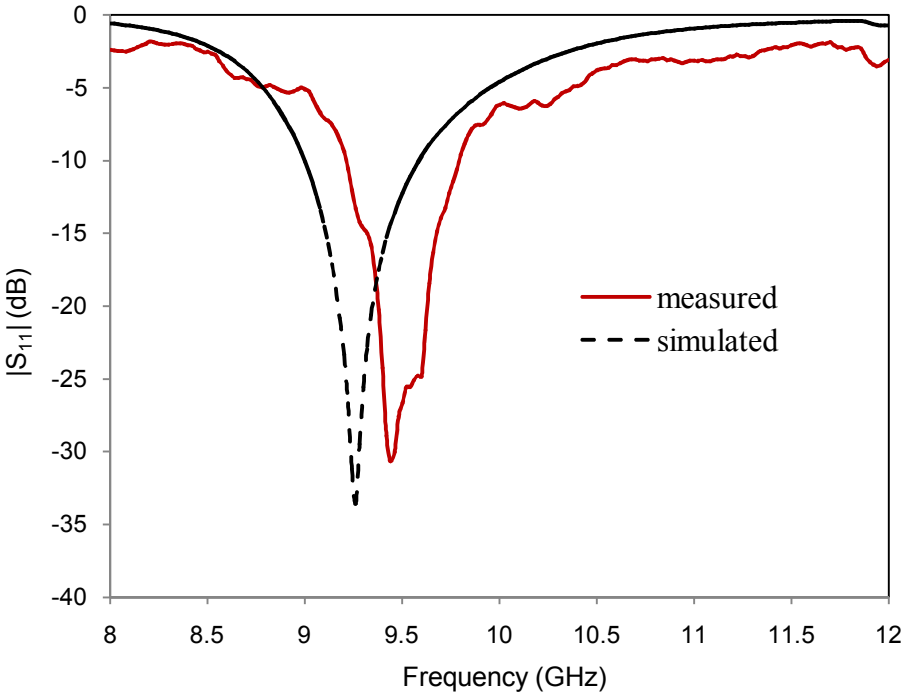

Fig. 6.5 Reflection coefficient of double step junction coupled waveguide fed CDRA with r = 7.0 mm, h = 5.0 mm, *2t1* = 4.0 mm, *2w1* = 6.5 mm, *2t2* = 8.0 mm, *2w2* = 3.4 mm, *2t3* = 1.3 mm, *2w3 = 1.0* mm and *2L3* = 9.5 mm.

The effect of radius r and height h of CDRA on reflection coefficient is shown in Fig. 6.3 and 6.4 respectively. The resonant frequency decreases with increase in the dimension of CDRA. Reflection characteristics of double step junction coupled waveguide fed CDRA is shown in Fig. 6.5. The measured resonant frequency is 9.44 GHz, which shows a small shift of 180 MHz when compared with the simulated resonant frequency (9.26 GHz). The shift in resonant frequency is mainly due to the air gap present between the ground plane and CDRA. Measured 10 dB bandwidth is 6.1% extending from 9.22 GHz to 9.8 GHz. Gain of the double step junction coupled waveguide fed CDRA is measured and is shown in Fig. 6.6. Gain of the double step junction coupled waveguide fed cylindrical DRA is 8.83 dBi, which is much higher than the gain of the dipole antenna.

Radiation pattern in E and H planes at 9.44 GHz is measured and compared with the simulated radiation pattern. Figures 6.7 and 6.8 represent the radiation patterns at 9.44 GHz in E plane and H plane respectively. Good agreement is observed between

the measured and simulated co-polarization signals. The measured cross-polarization signals are at least 20 dB below the corresponding co-polarization signals.

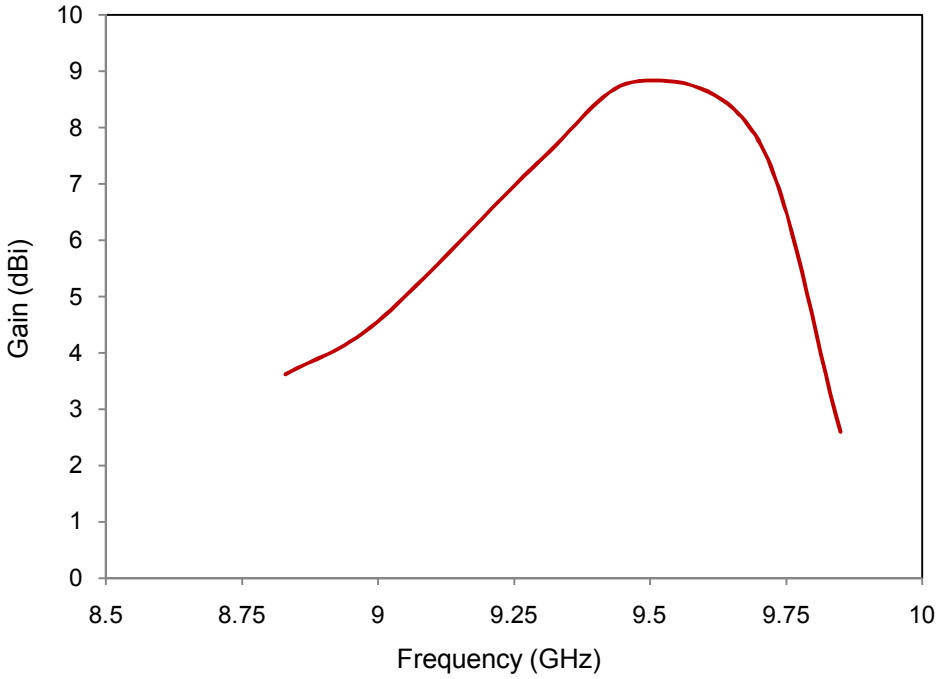

Fig. 6.6 Measured gain of the double step junction coupled waveguide fed cylindrical DRA with r = 7.0 mm, h = 5.0 mm, $2t1$ = 4.0 mm, $2w1$ = 6.5 mm, $2t2$ = 8.0 mm, $2w2$ = 3.4 mm, $2t3$ = 1.3 mm, $2w3$ = 1.0 mm and $2L3$ = 9.5 mm.

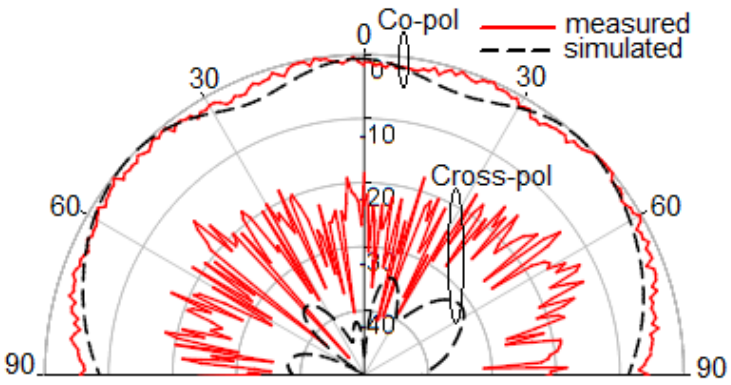

Fig. 6.7 E plane radiation pattern of double step junction coupled waveguide fed CDRA at 9.44 GHz with r = 7.0 mm, h = 5.0 mm, $2t1$ = 4.0 mm, $2w1$ = 6.5 mm, $2t2$ = 8.0 mm, $2w2$ = 3.4 mm, $2t3$ = 1.3 mm, $2w3$ = 1.0 mm and $2L3$ = 9.5 mm.

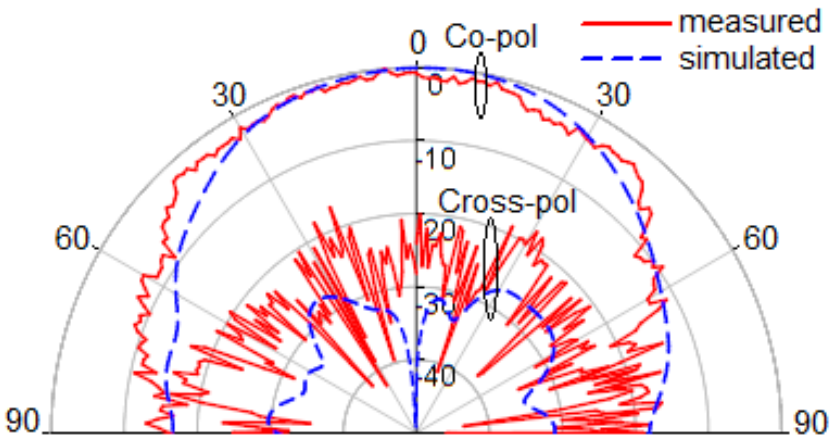

Fig. 6.8 H Plane radiation pattern of double step junction coupled waveguide fed CDRA at 9.44 GHz with r = 7.0 mm, h = 5.0 mm, $2t1$ = 4.0 mm, $2w1$ = 6.5 mm, $2t2$ = 8.0 mm, $2w2$ = 3.4 mm, $2t3$ = 1.3 mm, $2w3$ = 1.0 mm and $2L3$ = 9.5 mm.

6.4 Waveguide fed Cylindrical DRA with Tapered Section

A tapered section of the waveguide with tapering only along the narrow wall is connected in between the rectangular waveguide and ground plane to introduce capacitive susceptance. Configuration of the proposed tapered waveguide fed cylindrical DRA is shown in Fig. 6.9. A tapered section of the waveguide with length of tapering, tp and angle of tapering, θ is connected at the end of the rectangular

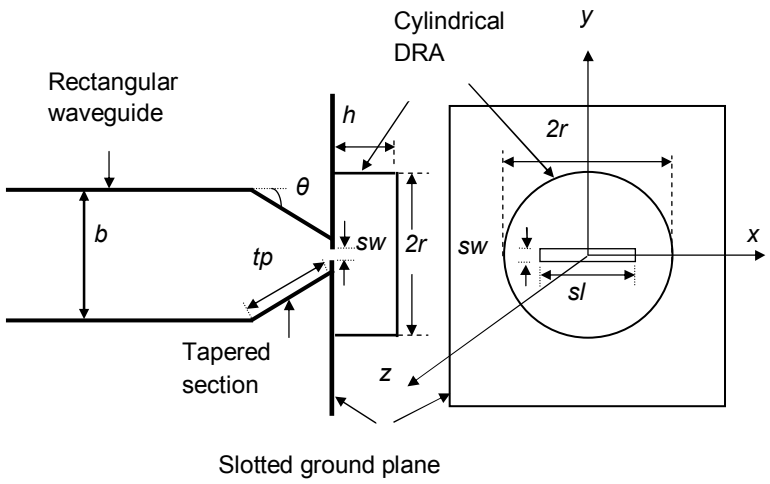

Fig. 6.9. Configuration of waveguide fed CDRA with tapered waveguide section.

waveguide and it is terminated in a thick square ground plane of dimension 100 mm x 100 mm x 1.3 mm. A rectangular slot with length *sl* and width *sw* is cut at the center of the ground plane, which is used to couple electromagnetic energy from waveguide to DRA. The CDRA is placed at the center of the ground plane above the slot. Narrow wall dimension of the waveguide is denoted by *b, r* and *h* respectively represent the radius and height of the cylindrical DRA. Optimum value of the parameters obtained for rectangular waveguide fed hemispherical DRA (radius 7.5 mm) with tapered section is used for the experimentation of rectangular waveguide fed CDRA with tapered section. Optimum value of various parameters is: tp = 22.2 mm, $\theta = 12^0$, sl = 10.5 mm, and sw = 0.7 mm. Cylindrical DRA of r = 7.0 mm, h = 5.0 mm and dielectric constant ε_r = 9.8 is used. Figure 6.10 shows the normalized input admittance plot of the tapered waveguide fed CDRA. The normalized susceptance at resonance is close to zero value and the normalized conductance is maximum at resonance as illustrated in Fig. 6.10. The measured reflection coefficient along with simulated reflection coefficient is shown in Fig. 6.11.

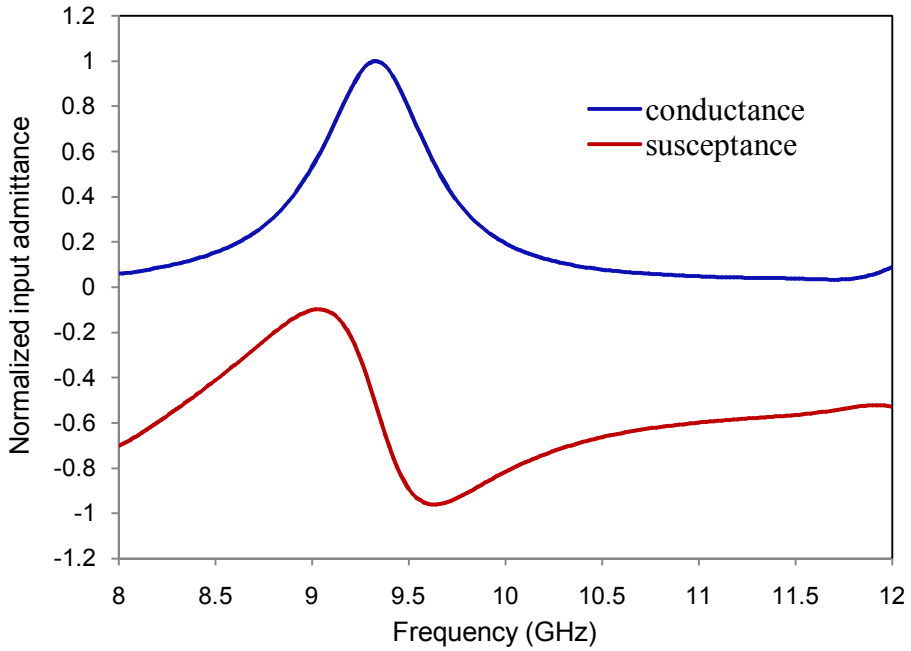

Fig. 6.10 Normalized input admittance of the tapered section coupled rectangular waveguide fed CDRA with tp = 22.2 mm, $\theta = 12^0$, sl = 10.5 mm, sw = 0.7 mm, r = 7.0 mm and h = 5.0 mm.

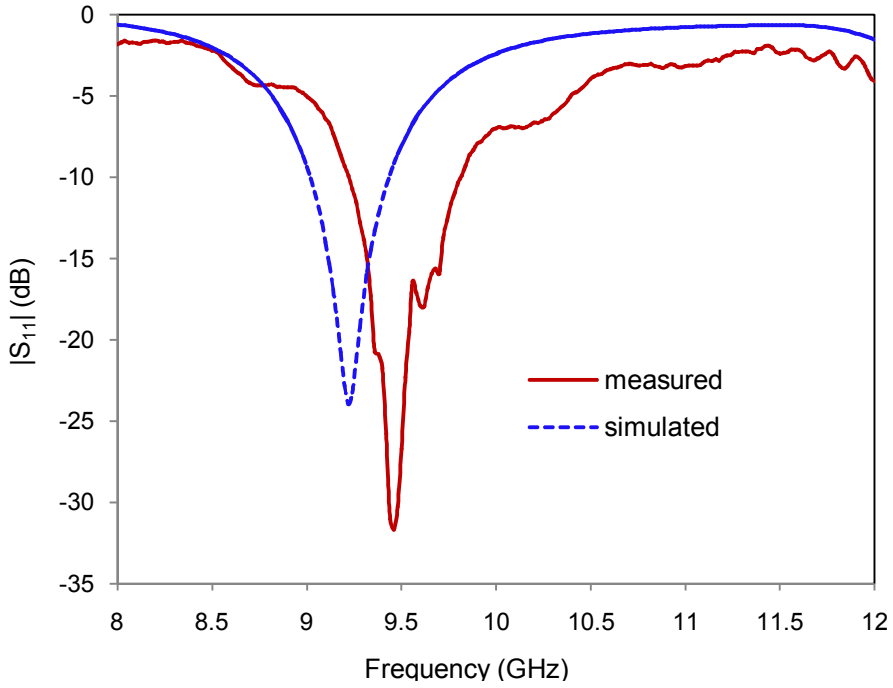

Fig. 6.11 Reflection coefficient of the tapered section coupled rectangular waveguide fed CDRA with *tp* = 22.2 mm, $\theta = 12^0$, *sl* = 10.5 mm, *sw* = 0.7 mm, *r* = 7.0 mm and *h* = 5.0 mm.

Very good matching is obtained for rectangular waveguide fed CDRA with tapered section. The measured resonant frequency is 9.46 GHz with a 10 dB bandwidth of 6.34%. The measured resonant frequency shows a small shift of 340 MHz when compared with the simulated resonant frequency. The main reason for the upward shift in resonant frequency is due to the air gap present between the ground plane and DRA. The air gap and hence the shift in resonant frequency can be avoided by making the ground plane and base of the cylindrical DRA perfectly flat and smooth using better fabrication techniques. Figure 6.12 illustrates the measured gain of the tapered section coupled rectangular waveguide fed CDRA. The antenna achieves a maximum gain of 6 dBi at 9.3 GHz with a 3 dB gain bandwidth of 14%. Comparison between the measured and simulated radiation patterns at 9.48 GHz are shown in Fig. 6.13 and Fig. 6.14. Both the E and H plane patterns are symmetrical about the broadside direction. The 3 dB beamwidths of the E and H plane patterns are 138° and 90° respectively. The cross-

polarized signals are at least 20 dB below the corresponding co-polarized signals in the broadside direction.

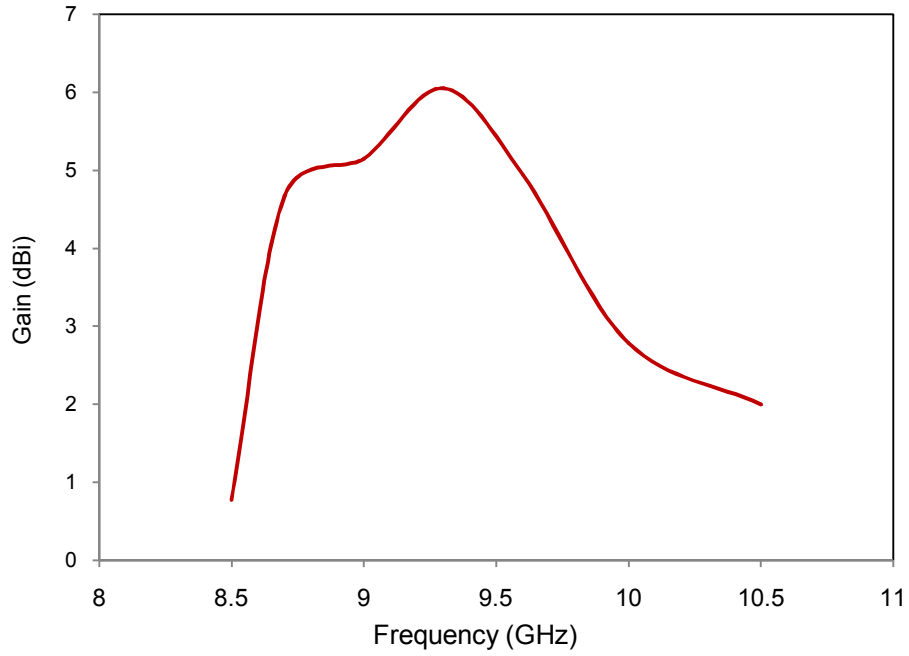

Fig. 6.12 Measured gain of the tapered section coupled rectangular waveguide fed CDRA with *tp* = 22.2 mm, $\theta = 12^0$, *sl* = 10.5 mm, *sw* = 0.7 mm, *r* = 7.0 mm and *h* = 5.0 mm.

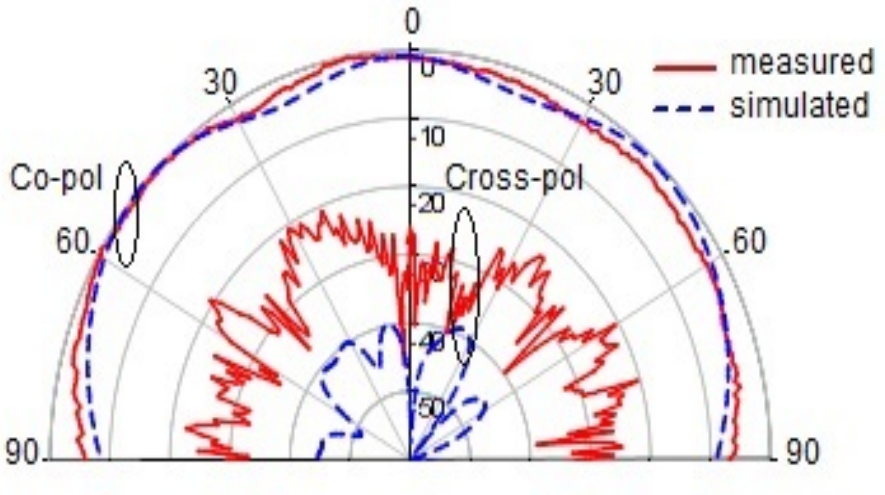

Fig.6.13 Radiation pattern of the waveguide fed CDRA at 9.48 GHz in the E Plane with *tp* = 22.2 mm, $\theta = 12^0$, *sl* = 10.5 mm, *sw* = 0.7 mm, *r* = 7.0 mm and *h* = 5.0 mm.

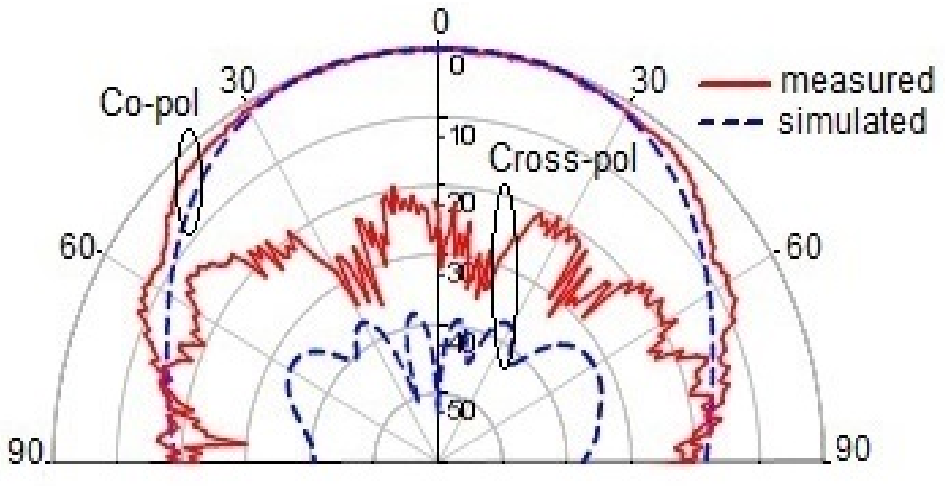

Fig. 6.14 Radiation pattern of the waveguide fed CDRA at 9.48 GHz in the H Plane with tp = 22.2 mm, θ = 12^0, sl = 10.5 mm, sw = 0.7 mm, r = 7.0 mm and h = 5.0 mm.

6.5. Inference

Coupling enhancement of waveguide-fed cylindrical DRA using tapered section and double step junction is demonstrated in this chapter. Cylindrical DRA with radius 7.0 mm and height 5.0 mm is used. The dielectric constant of the CDRA used is 9.8. The rectangular waveguide with tapered waveguide section and double step junction fabricated for exciting the HDRA are also used for exciting the CDRA. The simulation studies of the antennas are done using Ansoft HFSS. Very good matching is obtained for both the antennas. Reasonable agreement between the experimental results and simulation results are obtained. The double step junction coupled waveguide fed CDRA gives a maximum gain of 8.83 dBi. The measured 10 dB bandwidth is 6.1% for double step junction coupled rectangular waveguide fed cylindrical DRA and 6.34% for tapered section coupled rectangular waveguide fed cylindrical DRA. The small discrepancy observed in the measured results when compared with the simulated results is due to the air gap present between the CDRA and ground plane. The shift in resonant frequency is very less for the double step junction coupled rectangular waveguide fed cylindrical DRA when compared with the double step junction coupled rectangular waveguide fed HDRA. This is due to the fact that the fabrication of cylindrical DRA is

easier compared to HDRA that makes the bottom surface of the CDRA more smooth and flat. Radiation patterns with low cross polarization levels are obtained for both the coupling enhancement techniques. The coupling enhancement techniques applied to cylindrical DRA provides very good matching. Therefore we can conclude that the proposed coupling enhancement techniques in this thesis can be extended for DRAs of other shapes like rectangular, conical etc.

Chapter 7

Conclusion and Future Perspectives

This chapter highlights the conclusions drawn from the theoretical and experimental investigations of the various coupling enhancement techniques of rectangular waveguide fed dielectric resonator antenna. Some of the future directions in this area are also discussed in this chapter. The results presented in the thesis have been published by the author in different international journals and conferences.

7.1 Thesis Summary and Conclusion

The main objective of the thesis is the analysis and experiments on coupling enhancement of rectangular waveguide fed dielectric resonator antenna. Three different types of coupling enhancement techniques are developed for hemispherical dielectric resonator antenna. Theoretical analysis of one of the coupling enhancement techniques (double step junction coupled rectangular waveguide fed HDRA) is also carried out. Validity of the developed coupling enhancement techniques is also verified for cylindrical DRA. Findings of the research works described in this thesis along with future works are summarized in the following sections.

A broad literature review regarding the development of dielectric resonator antenna and the different methods for exciting the DRA are discussed in chapter 1. Since the thesis concentrates on coupling enhancement of rectangular waveguide fed DRAs, a thorough literature review on the coupling enhancement techniques of waveguide fed DRA especially at the shorted end of the waveguide are discussed in the first chapter. The motivation behind the present work, regarding the coupling enhancement technique of waveguide shorted end slot coupled DRA persistent towards the current technological developments is explained in detail in chapter 1.

Theoretical analysis of waveguide shorted end slot coupled HDRA is carried out in chapter 2. Waveguide shorted end slot coupled HDRA consists of three sections: waveguide, rectangular cavity and HDRA. Scattered magnetic field inside the waveguide, rectangular cavity and HDRA are derived in this chapter. The derived equations are used to solve the integral equations corresponding to the problem. A general MATLAB code is written to perform the analysis of waveguide shorted end slot coupled HDRA. The developed code is executed to study the reflection and admittance characteristics. It is found that maximum coupling achieved by the waveguide shorted end slot coupled HDRA is only 37%. Poor coupling is due to the inductive susceptance of waveguide shorted end slot coupled HDRA. Therefore different coupling enhancement techniques are to be developed, which are discussed in chapter 3, 4 and 5.

7.1.1 Analysis and Experiments on Double Step Junction Coupled Waveguide fed HDRA

Coupling enhancement of waveguide shorted end slot coupled HDRA is obtained by introducing capacitive susceptance to neutralize the inductive susceptance of waveguide shorted end slot coupled HDRA. Capacitive susceptance can be introduced by reducing the narrow wall dimension of the rectangular waveguide in different ways. In double step junction coupled waveguide fed HDRA, capacitive susceptance is introduced by inserting steps with reduced narrow wall dimension between the rectangular waveguide and the ground plane. The steps with reduced narrow wall dimension provide very good coupling from waveguide to HDRA. MoM is used for the analysis of double step junction coupled rectangular waveguide fed HDRA. The expressions for the scattered magnetic fields derived in chapter 2 are used for solving the integral equations corresponding to the double step junction coupled waveguide fed HDRA. An in house MATLAB code is developed to implement the theoretical study. A thorough parametric study has been conducted using the developed MATLAB code to find out the optimum value of various parameters. In order to validate the theory, the proposed structure is fabricated with optimized parameters and measured the reflection and radiation characteristics. Reasonable agreement is obtained between the measured result and the results using the developed theory. The results are reported in publication no. 1 and 7.

7.1.2 Coupling Enhancement of Rectangular Waveguide fed HDRA using Tapered Waveguide Section

Coupling enhancement of rectangular waveguide fed HDRA with tapered waveguide section is discussed in chapter 4. The tapered section introduced between the rectangular waveguide and the ground plane reduces the narrow wall dimension of the rectangular waveguide and provides increased coupling from rectangular waveguide to HDRA. Multi-cavity modeling technique used for the analysis of double step junction coupled waveguide fed HDRA cannot be used here. Since the tapered section is continuous, multi-cavity modeling is not possible. Therefore only

experiments are performed to validate the simulation using HFSS. The results of this work are reported in publication no. 2 and 8.

7.1.3 Coupling Enhancement of Stair Shaped Waveguide fed HDRA

Coupling enhancement of rectangular waveguide fed HDRA using stair shaped waveguide is presented in chapter 5. Two steps introduced at the end of the rectangular waveguide give the waveguide a stair shaped appearance. The total number of steps in this case is only two; while the number of steps in double step junction coupled waveguide fed HDRA is four. Also width of the steps in this case is higher compared to the double step junction coupled waveguide fed HDRA. The reduced number of steps along with increased width makes fabrication less complex. The fabricated antenna has a high gain of 7.2 dBi along with very good coupling. Partial results of this work are published in publication no. 6.

7.1.4 Coupling Enhancement of Waveguide fed Cylindrical DRA

The developed coupling enhancement techniques are applicable to DRAs of any shape. Two of the proposed coupling enhancement techniques are experimentally verified for cylindrical DRA. Chapter 6 describes the double step junction coupled waveguide fed cylindrical DRA and tapered section coupled waveguide fed cylindrical DRA. High gain and excellent matching are obtained for cylindrical DRA too. Therefore we can conclude that the proposed coupling enhancement techniques are suitable for DRAs of any shape.

7.2 Scope for Future Work

Three different coupling enhancement techniques are proposed in this thesis. In addition to experiments, MoM analysis of the double step junction coupled waveguide fed hemispherical HDRA has also been carried out. MoM analysis of the other two techniques can be carried out as future work. For MoM analysis entire domain basis function is used in this thesis. Complexity of analysis can be reduced by using sub domain basis functions like pulse and polynomial, which can be tried in future. All the developed coupling enhancement techniques provide linear polarization. Circular

polarization of waveguide fed DRAs can be carried out in the future. In this thesis coupling enhancement of only waveguide shorted end slot coupled DRA is carried out. Coupling enhancement of waveguide broad wall and narrow wall excited DRAs can be conducted in future.

References

[1] R. D. Richtmyer, "Dielectric Resonators", *Journal of Applied Physics*, vol. 10, pp. 391-398, June 1939.

[2] D. Kajfez and P. Guillon, "Dielectric Resonators", Artech House, Dedham, MA, 1986.

[3] M. W. Pospieszalski, "Cylindrical dielectric resonators and their applications in TEM line microwave circuits" , *IEEE Trans. Microwave Theory Tech*., vol. 27, pp. 233-238, March 1979.

[4] M. Gastine, L. Courtois and J. J. Dormann, "Electromagnetic resonances of free dielectric spheres", *IEEE Trans. Microwave Theory Tech*., vol. 15, pp. 694-700, Dec. 1967.

[5] O. Sager and F. Tisi, "On eigen modes and forced resonance-modes of dielectric spheres", *Proc. IEEE*, vol. 56, pp. 1593-1594, Sept. 1968.

[6] J. Van Bladel, "On the resonances of dielectric resonator of very high permittivity", IEEE *Trans. Microwave Theory Tech,* vol. 23, pp.199-208, Feb. 1975.

[7] J. Van Bladel, "The excitation of dielectric resonators of very high permittivity", *IEEE Trans. Microwave Theory Tech*., vol. 23, pp. 208-217, Feb. 1975.

[8] M. T. Birand and R. V. Gelsthorpe, "Experimental millimetric array using dielectric radiators fed by means of dielectric waveguide", *Electron. Lett*., vol. 17, pp. 633-635, Sept. 1981.

[9] S. A. Long, M. W. McAllister and L. C. Shen, "The resonant cylindrical dielectric cavity antenna," *IEEE Trans. Antennas Propag*., vol. 31**,** pp. 406-412, 1983.

[10] R. K. Mongia and P. Bhartia, "Dielectric resonator antennas—A review and general design relations for resonant frequency and bandwidth", *International Journal of Microwave and Millimeter-Wave Engineering*, vol. 4, pp. 230–247, July 1994.

[11] K. W. Leung, K. M. Chow and K. M. Luk, "Low-profile high-permittivity dielectric resonator antenna excited by a disk-loaded coaxial aperture", IEEE *Antennas Wireless Propag. Lett*., vol. 2, 2003.

[12] A. A. Kishk, "Dielectric resonator antenna, a candidate for radar applications", Proceedings of *IEEE radar Conference*, pp. 258-264, 2003.

[13] T. Elkarkraoui1, G.Y. Delisle, N. Hakem and Y. Coulibaly, "High gain cross DRA antenna array for underground communications", *IEEE Antennas and Propagation Society International Symposium* APSURSI 2014, pp. 1942-1943, 2014.

[14] A. Elboushi and A.R. Sebak, "High Gain Hybrid DRA / Horn Antenna for MMW Applications", *IEEE Antennas and Propag. Society International Symposium* APSURSI 2014, pp. 1968-1969, 2014.

[15] Y. Wang, T. A. Denidni, Q. Zeng, and G. Wei, "A wideband high-gain stacked cylindrical dielectric resonator antenna", *Progress In Electromagnetics Research Letters*, vol. 43, 155–163, 2013.

[16] J. Carr, "Practical Antenna Handbook", McGraw-Hill, New York.

[17] A. Okaya, and L. F. Barash, "The Dielectric Microwave Resonator", *Proceedings of IRE*, vol. 50, pp. 2081-2092, October 1962.

[18] A. Petosa and A. Ittipiboon, "Dielectric Resonator Antennas: A historical review and the current state of the art", *IEEE Antennas and Propag. Magazine*, vol. 52, No. 5, October 2010.

[19] H. Wong, K. M. Luk, Chi Hou Chan, Q.Xue, K. K. So and H. W. Lai, "Small antennas in wireless Communications", *Proceedings of IEEE*, vol. 100, pp. 2109-2121, July 2012.

[20] Q. Lai, G. Almpanis, C. Fumeaux, H. Benedickter and R. Vahldieck, "Comparison of the radiation efficiency for the dielectric resonator antenna and the microstrip antenna at Ka band", *IEEE Trans. Antennas Propag.*, Vol. 56, pp. 3589-3592, 2008.

[21] R. K. Mongia, A. Ittipiboon, and M. Cuhaci, "Measurement of radiation efficiency of dielectric resonator antennas", *IEEE Microwave Guided Wave Lett*., vol. 4, pp. 80–82, Mar. 1994.

[22] A. M. Faiz, "Dielectric Resonator antennas for satellite and body area network applications", Ph.D Dissertation, Paris-EST University, 2012.

[23] K. W. Leung, W. C. Wong, K. M. Luk and E. K. N. Yung, "Annular slot coupled dielectric resonator antenna", *Electron. Lett.*, vol.34, pp. 1275-1277, 1998.

[24] K. W. Leung, K. M. Luk, K. Y. A. Lai and D. Lin, "Theory and experiment of a coaxial probe fed hemispherical dielectric resonator antenna", IEEE *Trans. Antennas Propag.*, vol. 41, pp. 1390-1398, 1993.

[25] M. W. McAllister, S. A. Long and G. L. Conway, "Rectangular dielectric resonator antenna", *Electron. Lett*., vol. 19, pp. 218-219, 1983.

[26] A. Ittipiboon, R. K. Mongia, Y. M. M. Antar, P. Bhartia and M. Cuhaci, "Aperture fed rectangular and triangular dielectric resonators for use as magnetic dipole antennas", *Electron. Lett*., vol. 29, pp. 2001-2002, Nov. 1993.

[27] A. A. Kishk, Y. Lin and A. W. Glisson, "Conical dielectric resonator antennas for wide band applications", IEEE *Trans. Antennas Propag.*, vol. 50, pp. 469-474, 2002.

[28] K. W. Leung, K. M. Luk and E. K. N. Yung, "Spherical cap dielectric resonator antenna using aperture coupling", *Electron. Lett.*, vol. 30, pp. 1366-1367, 1994.

[29] A. Tadjalli, A. R. Sebak, and T. A. Denidni, "Response frequencies and far field patterns of elliptical dielectric resonator antenna: analytical approach", Progress in Electromagnetic Research, vol. 64, pp. 81-98, 2006.

[30] V. Hamsakutty, A. V. Praveen Kumar, J. Yohannan and K. T. Mathew, "Hexagonal dielectric resonator antenna for 2.4 GHz WLAN applications", *Microwave and Opt. Technol. letters*, vol. 49. pp. 162-164, January 2007.

[31] T. Elkarkraoui1, G. Y. Delisle, N. Hakem and Y. Coulibaly, "DRA antenna with a superstrate at millimeter-wave" *IEEE International Symposium on Antennas and propagation & USNC/URSI National Radio Science Meeting*, pp. 2079-2080, 2015.

[32] R. K. Mongia, A. Ittipiboon, P. Bhartia and M. Cuhaci, "Electric monopole antenna using a dielectric ring resonator", *Electron Lett.*, vol. 29, pp. 1530-1531, Aug 1993.

[33] D. Guha and Y. M. M. Antar, "New half hemispherical dielectric antenna for broadband monopole type radiation", IEEE *Trans. Antennas Propag.*, vol. 54, pp. 3621-3628, 2006.

[34] A. Okaya, and L. F. Barash, "The dielectric microwave resonator," Proc. IRE, Vol. 50, No. 10, 2081–2092, 1962.

[35] I. A. Eshrah, A. A. Kishk, A. B. Yakovlev and A. W. Glisson, "Theory and implementation of dielectric resonator antenna excited by a waveguide slot", IEEE *Trans. Antennas Propag.,* vol. 53, pp. 483-494, 2005.

[36] Y. Zhang, A. A. Kishk, A. B. Yakovlev and A. W. Glisson, "FDTD analysis of dielectric resonator antenna arrays for waveguide based spatial power combining", *Antennas and Propagation Society International Symposium*, vol. 4B, pp. 230-233, 2005.

[37] K. M. Luk, K. W. Leung and S. M. Shum, "Numerical study of dielectric resonator antenna", Advances *in Microstrip and Printed Antennas*, John Wiley, pp. 553-592, 1997.

[38] S. M. Shum and K. M. Luk, "FDTD analysis of probe-fed cylindrical dielectric resonator antenna", *IEEE Trans. Antennas Propag.*, vol. 46, pp. 325-333, 1998.

[39] R. K. Mongia and A. Ittipiboon, "Theoretical and experimental investigations on rectangular dielectric resonator antennas", IEEE Trans. Antennas Propag., vol. 45, pp. 1348–1356, 1997.

[40] Y. M. M. Antar, "New direction in antenna research using dielectrics", in Proc. *Radio Science Conf.*, pp. 1–13, URSI Conf., 2003.

[41] K. W. Lueng, K. M. Luk, K. Y. A. Lai and D. Lin, "Input impedance of hemispherical dielectric resonator antenna", *Electron. Lett.*, vol.27, pp. 2259-2260, 1991.

[42] R. F. Harrington, "Field Computation by Moment Methods", *Wiley IEEE Press* Publishing Company, USA.

[43] G. P. Junker, A. A. Kishk and A. W. Glisson, "Input impedance of dielectric resonator antennas excited by a coaxial probe", IEEE *Trans. Antennas Propag.*, vol. 42, pp. 960-966, 1994.

[44] R. A. Kranenburg and S. A. Long, "Microstrip transmission line excitation of dielectric resonator antennas", *Electron. Lett.*, vol.24, pp. 1156-1157, 1988.

[45] K. W. Leung, K. Y. Chow, K. M. Luk and E. K. N. Yung, "Low profile circular disk DR antenna of very high permittivity excited by a microstrip line", *Electron. Lett.*, vol.33, pp. 1004-1005, 1997.

[46] M. Saeed and R. Yadla, "Microstrip-fed low profile and compact dielectric resonator antennas", *Progress in Electromagnetics Research*, vol. 56, 151–162, 2006.

[47] Y. Coulibaly, T. A. Denidni and H. Boutayeb, "Broadband microstrip-fed dielectric resonator antenna for X-Band applications", IEEE *Antennas and Wireless Propag. Lett.*, vol. 7, pp. 341-345, 2008.

[48] G. P. Junker, A. A. Kishk, and A. W. Glisson, "Input impedance of aperture coupled dielectric resonator antennas", *IEEE Trans. Antennas and Propag.*, vol. 44, pp. 600-607, May 1996.

[49] G. P. Junker, A. A. Kishk, D. Kajfez, A. W. Glisson and J. Guo, "Input impedance of microstrip-slot-coupled dielectric resonator antennas mounted on thin dielectric layers", *International Journal of Mocrowave and Millimeter-wave Computer-Aided Engineering*, vol. 6, pp. 174-182, 1996.

[50] J. T. H. St. Martin, Y. M. M. Antar, A. A. Kishk and A. Ittipiboon, "Dielectric resonator antenna using aperture coupling", *Electron. Lett.*, Vol.26, pp. 2015-2016, 1990.

[51] K. W. Lueng, K. M. Luk, K. Y. A. Lai and D. Lin., "Theory and experiment of an aperture-coupled hemispherical dielectric resonator antenna", IEEE *Trans. Antennas Propag.*, vol. 43, , pp. 1192–1198, Nov. 1995.

[52] R. Chair, A. A. Kishk and K. F. Lee, "Wideband simple cylindrical dielectric resonator antennas", IEEE *Microw. Wireless Component Lett.*, vol. 15, pp. 241-243, 2005.

[53] K. W. Leung, "Conformal strip excitation of dielectric resonator antenna", *IEEE Trans. Antennas Propag.*, vol. 48, pp. 961-967, 2000.

[54] Imran Khan, R. Kumari and S. K. Behera "A notched chamfered rectangular dielectric resonator antenna array for wireless applications", *Proceedings of International Conference on Automation, Computing, Communication, Control and Compressed Sensing (iMac4s)*, pp. 326-329, 2013.

[55] K. W. Leung, W.C. Wong, K. M. Luk and E. K. N. Yung, "Circular polarized dielectric resonator antenna excited by dual conformal strips", *Electron. Lett.*, vol. 36, pp. 484-486, 2000.

[56] R. A. Kranenburg, S. A. Long, and J. T. Williams, "Coplanar waveguide excitation of dielectric resonator antennas", *IEEE Trans. Antennas Propag.*, vol. 39, pp. 119-122, 1991.

[57] M. S. Al Salameh, Y. M. M. Antar and Guy Seguin, "Coplanar-waveguide fed slot coupled rectangular dielectric resonator antenna", *IEEE Trans. Antennas Propag.*, vol. 50, pp. 1415-1419, 2002.

[58] Q. Rao, T. A. Dendini, A. R. Sebak and R. H. Johnston, "On improving impedance matching of a CPW fed low permittivity dielectric resonator antenna", *Progress In Electromagnetics Research,* vol. 53, 21–29, 2006.

[59] J. Y. Wu, C. Y. Huang and K. L. Wong, "Low-profile, very-high permittivity dielectric resonator antenna excited by a co-planar waveguide", Microw. and Opt. Technol. Lett., vol. 22, pp. 96-97, July 1999.

[60] I. A. Eshrah, A. A. Kishk, A.B. Yakovlev and A. W. Glisson, "Equivalent circuit model of a waveguide probe with application to DRA excitation", *IEEE Trans. Antennas Propag.,* vol. 54, pp. 1433-1441, 2006.

[61] Y. Zhang, Y., A. A. Kishk, A. B. Yakovlev and A. W. Glisson, "Analysis of wideband dielectric resonator antenna arrays for waveguide based spatial power combining", *IEEE Trans. Microw. Theory Tech.,* vol. 55, pp. 1332-1340, 2007.

[62] G. P. Junker, A. A. Kishk, A. W. Glisson, and D. Kajfez, "Effect of an air gap around the coaxial probe exciting a cylindrical dielectric resonator antenna", *Electron. Lett.*, vol. 30, pp. 177-178, 1994.

[63] G. Drossos, Z. Wu and L. E. Davis, "Circular polarized cylindrical dielectric resonator antenna", *Electron. Lett.*, vol. 32, pp. 281-283, 1996.

[64] D. M. Pozar, "A reciprocity method of analysis for printed slot and slot-coupled microstrip antennas", *IEEE Trans. Antennas Propag.,* vol. 34, pp. 1439-1446, Dec. 1986.

[65] K. M. Luk and K. W. Leung, "Dielectric Resonator Antennas", Research Studies Press, Baldock, England.

[66] R. F. Harrington, "Time harmonic electromagnetic fields", McGraw-Hill Book Company, New York, 1961.

[67] R. E. Collin, "Field theory of guided waves", IEEE Press, 1991.

[68] L. Lewin, "Advanced theory of waveguide", Ilife 1951.

[69] D. M. Pozar, "Microwave engineering", John Wiley & Sons , 1988.

[70] K. W. Leung, H. Y. Lo, K. K. So and K. M. Luk, "High-permittivity dielectric resonator antenna excited by a rectangular waveguide", *Microw. Opt. Tech. Lett.,* vol. 34, pp.157-158, 2002.

[71] P. Abdulla, A. B. Kakade, Y. K. Singh and A. Chakrabarthy, "Analysis of dielectric resonator antenna excited by a slot at the waveguide shorted end", *Microw. Opt. Tech. Lett.,* vol. 50**,** pp. 1356-1359, 2008.

[72] I. A. Eshrah, A. A. Kishk, A. B. Yakovlev, and A. W. Glisson, "Excitation of dielectric resonator antennas by a waveguide probe: modelling technique and wideband design", *IEEE Trans. Antennas Propag.,* vol. 53, pp. 1028-1037, 2005.

[73] K. W. Leung and K. K. So, "Rectangular waveguide excitation of dielectric resonator antenna", *IEEE Trans. Antennas Propag.,* vol. 51, pp. 2477-2481, 2003.

[74] P. Abdulla, Y. K. Singh, and A. Chakrabarthy, "Coupling enhancement of waveguide-fed dielectric resonator antenna", *Microw. Opt. Tech. Lett.,* vol. 53, pp. 769-770, 2011.

[75] A. B. Kakade and B. Ghosh, "Analysis of the rectangular waveguide slot coupled multilayer hemispherical dielectric resonator antenna", *IET Microw. Antennas Propag*., vol. 6, pp. 338-347, 2012.

[76] J. A. Stratton, "Electromagnetic Theory," McGraw Hill Publication, New York, 1941.

[77] C. T. Tai, and Rozenfeld, "Different representation of dyadic Green's function for rectangular cavity", IEEE *Trans. Microw. Theory Tech.,* vol. 24, pp. 597-601, Sept. 1976.

[78] Y. Rahmat Samii, "On the question of computation of the dyadic Green's function at the source region in waveguides and cavities", *IEEE Trans. Microw. Theory Tech.*, vol. 23, pp. 762-765, Sept. 1975.

[79] D. I. Wu. and C. D. Chang. "A hybrid representation of the Green's function in an overmode rectangular cavity", *IEEE Trans. Microw. Theory Tech.,* vol. 36, pp. 597-601, Sept. 1988.

[80] C. A. Balanis, "Advanced Engineering Electromagnetics", *John-Wiley Sons*, 1989.

[81] R. Kumari, K. Parmar and S. K. Behera, "Conformal patch fed stacked triangular dielectric resonator antenna for WLAN Applications", *International Conference on Emerging Trends in Robotics and Communication Technologies* (INTERACT 2010), pp. 104-107, 2010.

[82] Q. Rao, T. A. Denidni and A. R. Sebak, "Broadband compact stacked T-Shaped DRA with equilateral-triangle cross sections", *IEEE Microwave Wireless Component Letters*, vol. 16, pp.7-9, 2006.

[83] M. AI Sharkawy, A. Z. Elsherbeni, and C. E. Smith, "Stacked elliptical dielectric resonator antennas for wideband applications", *International Symposium on Antennas and Propag.*, vol. 2, pp. 1371-1374, 2004.

[84] A. Motevasselian, "Bandwidth enhancement of helix excited cylindrical dielectric resonator antennas by means of stacking", *Proceedings of Antennas and Propagation Conference*, pp. 1-3, 2012.

[85] R. Ghosal and B. Gupta, "Design of reconfigurable band notched ultra wide band (UWB) stacked DRA using metamaterial structure", *IEEE International Conference on Computing and Communication*, IEMCON 2015, pp. 1-4, 2015.

[86] K. M. Luk, K. W. Leung and K. W. Chow, "Bandwidth and gain enhancement of a dielectric resonator with the use of a stacking element", *Microw. Opt. Tech. Lett*., pp. 215-217, 1997.

[87] T. A. Denidni and Z. Weng, "Rectangular dielectric resonator antenna for ultra wideband applications", *Electron. Lett.*, vol. 45, pp. 1210-1212, 2009.

[88] A. A. Kishk, R. Chair and K. F. Lee, "Broadband dielectric resonator antennas excited by L-shaped probe", *IEEE Trans. Antennas Propag.,* vol. 44, pp. 2182 – 2189, 2006.

[89] S. K. Dash, S. Sahu, D. Behera and N. D. Manish, "Concentric three-layer cylindrical DRA for UWB applications", *International Conference on Communications and Signal Processing* (ICCSP 2015), pp. 676-679, 2015.

[90] J. M. Lee, S. J. Kim, G. Kwon, C. M. Song, Y. Yang, K. Y. Lee and K. C. Hwang, "Circularly polarized semi-eccentric annular dielectric resonator antenna for X-Band applications", *IEEE Antennas Wireless propag. Lett.*, vol. 14, pp. 1810-1813, 2015.

[91] X. S. Fang, Ka Ki Ng and K. W. Leung, "On a wideband circularly polarized dielectric resonator antenna using a higher-order mode", *IEEE International Conference on Computational Electromagnetics*, pp. 230-231, 2015.

[92] R. Kumar and R. K. Chaudhary, "A wideband circularly polarized cubic dielectric resonator antenna excited with modified microstrip feed", *IEEE Antennas Wireless propag. Letters*, vol. 15, pp.1285-1288, 2016.

[93] P. Patel, B. Mukherjee and J. Mukherjee, "A compact wideband rectangular dielectric resonator antenna using perforations and edge grounding", *IEEE Antennas Wireless propag. Lett.*, vol. 14, 2015.

[94] M. Zou, J. Pan and Z. Nie, "A wideband circularly polarized rectangular dielectric resonator antenna excited by an Archimedean spiral slot", *IEEE Antennas Wireless propag. Lett.*, vol. 14, 2015.

[95] K. P. Esselle and T. S. Bird, "A hybrid-resonator antenna: experimental results", *IEEE Trans. Antennas Propag.,* vol. 53, pp. 870-871, 2005.

[96] Y. Coulibaly, T. A. Denidni, and L. Talbi, "Wideband impedance bandwidth hybrid dielectric resonator antenna for X-band applications", *IEEE Antennas and Propagation Society International Symposium*, pp. 2429–2432, 2006.

[97] R. Kumari, K. Parmar and S. K. Behera, "A dual band triangular shaped DRA array for WLAN/WiMAX applications", *Proceedings of IEEE India Conference* (INDICON*)* pp.1–4, 2011.

[98] Ac HrafJaouj al, N. Aknin and A. EI Moussaoui, "Dual-band rectangular dielectric resonator antenna for ISM and 4 GHz bands applications", *IEEE Mediterranian Microwave Symposium*, pp. 1-3, 2009.

[99] K. J. Babu and K. R. Krishna, "A novel Swastika shaped dielectric resonator antenna for MIMO Systems," *IEEE International Microwave and RF Conference* (IMaRC), pp. 170-173, 2014.

[100] H. M. Chen, Y. K. Wang, Y. F. Lin, S. C. Lin and S. C. Pan, "A compact dual-band dielectric resonator antenna using a parasitic slot", *IEEE Antennas Wireless propag. Lett.*, vol. 8, pp. 173-176, 2009.

[101] Y. F. Lin, H. M. Chen, and Chia-Ho Lin, "Compact dual-band hybrid dielectric resonator antenna with radiating slot", *IEEE Antennas Wireless Propag. Lett.*, vol. 8, 2009.

[102] Matrix Laboratory (MATLAB), version 12, Mathworks, Massachusetts, U.S.A.

[103] Ansoft High Frequency Structure Simulator (HFSS), version 12, Ansoft Corporation, Pittsburgh, USA.

[104] CST (Computer Simulation Technology) Mirowave Studio, 2012, Germany.

[105] S. Paramesha, and A. Chakrabarthy, "Moment method analysis of rectangular waveguide as near field measuring probe", *Microw. Opt. Technol. Lett*., vol. 48, pp. 1802-1805, 2006.

[106] K. M. Luk, and K. W. Leung, "Dielectric Resonator Antenna", R. S. Press, London, UK, 2003.

[107] D. Soren, R. Ghatak, R. K. Mishra and D. R. Poddar, "Dielectric Resonator antennas: Design and Advances", *Progress in Electromagnetics Research*, vol. 60, pp. 195-313, 2014.

[108] T. H. Chang, and J. F. Kiang, "Broadband dielectric resonator antenna with a tunnel", *IEEE Antennas and Wireless Propag. Lett*., vol. 7, pp. 275-278, 2008.

[109] A. A. Kishk, "Tetrahedron and triangular dielectric resonator with wideband performance", *IEEE AP-S Int. Symp. Dig*., vol. 4, pp. 462-465, June 2002.

[110] A. A. Kishk, "Wide-band truncated tetrahedron dielectric resonator antenna excited by a coaxial probe", *IEEE Trans. Antennas Propag*., vol. 51, pp. 2913-2917, 2003.

[111] A. A. Kishk, A.W. Glisson, and G. P. Junker, "Bandwidth enhancement for a split cylindrical dielectric resonator antennas", *Progress in Electromagnetics Research*, vol. 33, pp. 97-118, 2001.

[112] A. A. Kishk and A.W. Glisson, "Conical dielectric resonator antennas for wide-band applications", *IEEE Trans. Antennas Propag.,* vol. 50, pp. 469-474, April 2002.

[113] S. K. Sharma and M. K. Brar, "Aperture-coupled pentagon shape dielectric resonator antennas providing wideband and multiband performance", *Microw. Opt. Technol. Lett*., vol. 55, pp. 395-400, Feb. 2013.

[114] R. K. Chaudhary, K. V. Srivastava, and A. Biswas, "A broadband dumbbell-shaped dielectric resonator antenna", *Microw. Opt. Technol. Lett.,* vol. 56, pp. 2944-2947, 2014.

[115] M. Khalily, K. A. Rahim, A. A. Kishk and S. Danesh, "Wideband P-shaped dielectric resonator antenna", *Radioengineering*, vol.22, no.1, pp. 281-285, 2013.

[116] W. Huang and A. A. Kishk, "Compact wideband multi-layer cylindrical dielectric resonator antennas", *IET Microwaves Antennas Propag*., vol. 1, pp. 998-1005, Oct. 2007.

[117] A. G. Walsh, S. Christopher, D. Young and S. A. Long, "An investigation of stacked and embedded cylindrical dielectric resonator antennas", *IEEE Antennas and Wireless Propag. Lett*., vol. 5, pp. 130-133, 2006.

[118] T. H. Chang and J. F. Kiang, "Broadband dielectric resonator antenna with metal coating", *IEEE Trans. Antennas Propag.,* vol. 55, pp. 1254-1259, May 2007.

[119] R. N. Simons and R. Q. Lee, "Effect of parasitic dielectric resonators on CPW / aperture-coupled dielectric resonator antennas", *IEEE Proc.-H,* vol. 140, pp. 336-338, 1993.

[120] P. V. Bijumon, S. K. Menon, M. N. Suma, M. T. Sebastian and P. Mohanan, "Broadband cylindrical dielectric resonator antenna excited by modified microstrip line", *Electron Lett*., vol. 41, pp. 385-387, March 2005.

[121] A. Rashidian, M. T. Aligodarz, L. Shafai, and D. M. Klymyshyn, "On the matching of microstrip-fed dielectric resonator antenna," *IEEE Trans. Antennas Propag.,* vol. 61, pp. 5291-5296, Oct 2013.

[122] K. S. Ryu and A. A. Kishk, "Dual band dielectric resonator antenna mounted on a defected ground plane", Proceedings *of IEEE Symposium on Antennas and Propagation* (APSURSI 2011), pp. 2589–2592, 2011.

[123] A. A. Kishk, B. Ahn and D. Kajfez, "Broadband stacked dielectric resonator antennas", *Electron Lett*., vol. 25, pp. 1232-1233, 1989.

[124] M. Khalily, M. K. A. Rahim, N. A. Murad, N. A. Samsuri and A. A. Kishk, "Rectangular ring shaped dielectric resonator antenna for dual and wideband frequency", *Microw. and Opt. Technol. Lett*., vol. 55, pp. 1077-1081, Aug. 2012.

[125] C. P. Mahesh and P. M. Hadalgi, "Proximity coupled equilateral triangular microstrip antenna with diamond shape slot for dual band operation", *International Journal of Advanced Research in Electrical, Electronics and Instrumentation Engineering,* vol. 3, pp. 133115-13119, Nov. 2014.

[126] H. S. Ngan, X. S. Fang and K. W. Leung, "Design of dual band circularly polarized dielectric resonator antenna using a higher-order mode", *IEEE-APS Tropical Conference on Antennas and Propagation in Wireless Communications*, pp. 424-427, Sept. 2012.

[127] H. M. Chen, Y. K. Wang, Y. F. Lin, S. C. Lin and S. C. Pan, "A compact dual-band DRA using a parasitic slot", *IEEE Antennas and Wireless Propag. Lett*., vol. 8, pp. 173-174, 2009.

[128] T. H. Chang and J. F. Kiang, "Dual band split dielectric resonator antenna", *IEEE Trans. Antennas Propag.,* vol. 55, pp. 1254-1259, Nov. 2007.

[129] G.P. Junker, A. A. Kishk, A. W. Glisson and D. Kajfez, "Effect of air gap on cylindrical dielectric resonator antenna operating in TM_{01} mode", *Electron. Lett.,* vol. 30, pp. 97-98,1994.

[130] G. P. Junker, A. A. Kishk, A. W. Glisson and D. Kajfez, "Effect of fabrication imperfections for ground plane backed dielectric resonator antennas", *IEEE antennas and Propag. Magazine*, vol. 37, pp. 40-47, Feb. 1995.

[131] G. Drossos, Z. Wu, and L. E. Davis, "The air gap effect on a microstrip coupled cylindrical dielctric resonator antenna", *Microw. and Opt. Technol. Lett*., vol. 20, pp. 36-40, 1999.

[132] A. Beurkle, K. Sarabandi and H. Mosallaei, "Compact slot and dielectric resonator antenna with dual-resonance, broadband characteristics", IEEE *Trans. Antennas and Propag.*, vol. 53, no. 3, pp.1020–1027. 2005.

[133] D. Maystre, P. Vincent and J. C. Mage, "Theoretical and experimental study of the resonant frequency of cylindrical dielectric resonator", *IEEE Trans. Microw. Theory Tech*., vol. 31, pp. 846-848, 1983.

[134] R. K. Mongia and B. Bhat, "Accurate resonant frequencies of cylindrical dielectric resonator using a simple analytical technique", *Electron. Lett*., vol. 21, pp. 479-480, 1985.

[135] P. Kooi, M. S. Leong, and A. L. S. Prakash, "Finite element analysis of the shielded cylindrical dielectric resonator", *Proceedings of IEE H. Microwaves*, vol. 132, pp. 7-16, 1985.

[136] M. Jaworski and M. W. Pospieszalski, "An accurate solution of the cylindrical dielectric resonator problem", *IEEE Trans. Microwave Theory Tech*., vol. 27, pp. 639-643,1979.

[137] A. W. Glisson, D. Kajfez and J. James, "Evaluation of modes in dielectric resonators using a surface integral equation formulation", *IEEE MTT-S International Microw. Symp. Digest*, vol. 31, pp. 1023-1029, 1983.

[138] A. A. kishk, A. Ittipiboon, Y. M. M. Antar and M. Cuhaci, "Slot excitation of the dielectric disk radiator", *IEEE Trans. Antennas and Propag.*, vol. 43, no. 3, pp.198-201, 1995.

Appendix A

Vector Analysis

A.1 Rectangular/spherical transformation

In this appendix vector transformations from rectangular to spherical and vice versa are discussed. The rectangular and spherical coordinates are related by

$$x = r\sin\theta\cos\phi \tag{A.1}$$

$$y = r\sin\theta\sin\phi \tag{A.2}$$

$$x = r\cos\theta \tag{A.3}$$

Rectangular to spherical transformation can be done using

$$\begin{bmatrix} A_r \\ A_\theta \\ A_\phi \end{bmatrix} = \begin{bmatrix} \sin\theta\cos\phi & \sin\theta\sin\phi & \cos\theta \\ \cos\theta\cos\phi & \cos\theta\sin\phi & -\sin\theta \\ -\sin\phi & \cos\phi & 0 \end{bmatrix} \begin{bmatrix} A_x \\ A_y \\ A_z \end{bmatrix} \tag{A.4}$$

The transformation matrix (A.4) is orthonormal and its inverse transform, spherical to rectangular can be written as:

$$\begin{bmatrix} A_x \\ A_y \\ A_z \end{bmatrix} = \begin{bmatrix} \sin\theta\cos\phi & \cos\theta\cos\phi & -\sin\phi \\ \sin\theta\sin\phi & \cos\theta\sin\phi & \cos\phi \\ \cos\theta & -\sin\theta & 0 \end{bmatrix} \begin{bmatrix} A_r \\ A_\theta \\ A_\phi \end{bmatrix} \tag{A.5}$$

A.2 Vector differential operators in spherical coordinates

The differential operators of a scalar ($\nabla\psi$), divergence of a vector (∇.A), curl of a vector (∇ X A), Laplacian of a scalar ($\nabla^2\psi$) and Laplacian of a vector (∇^2A) frequently encountered in the thesis are given below.

$$\nabla\psi = \hat{a}_r\frac{\partial\psi}{\partial r} + \hat{a}_\theta\frac{1}{r}\frac{\partial\psi}{\partial\theta} + \hat{a}_\phi\frac{1}{r\sin\theta}\frac{\partial\psi}{\partial\phi} \tag{A.6}$$

$$\nabla.A = \frac{1}{r^2}\frac{\partial}{\partial r}(r^2 A_r) + \frac{1}{r\sin\theta}\frac{\partial}{\partial\theta}(\sin\theta A_\theta) + \frac{1}{r\sin\theta}\frac{\partial A_\phi}{\partial\phi} \quad \text{(A.7)}$$

$$\nabla \text{ X } A = \frac{\hat{a}_r}{r\sin\theta}\left[\frac{\partial}{\partial\theta}(A_\phi\sin\theta) - \frac{\partial A_\theta}{\partial\phi}\right] + \frac{\hat{a}_\theta}{r}\left[\frac{1}{\sin\theta}\frac{\partial A_r}{\partial\phi} - \frac{\partial}{\partial r}(rA_\phi)\right] + \frac{\hat{a}_\phi}{r}\left[\frac{\partial}{\partial r}(rA_\theta) - \frac{\partial A_r}{\partial\theta}\right] \quad \text{(A.8)}$$

$$\nabla^2\psi = \frac{1}{r^2}\frac{\partial}{\partial r}\left(r^2\frac{\partial\psi}{\partial r}\right) + \frac{1}{r^2\sin\theta}\frac{\partial}{\partial\theta}\left(\sin\theta\frac{\partial\psi}{\partial\theta}\right) + \frac{1}{r^2\sin^2\theta}\frac{\partial^2\psi}{\partial\phi^2} \quad \text{(A.9)}$$

$$\nabla^2 A = \nabla(\nabla.A) - \nabla \text{ X } \nabla \text{ X A} \quad \text{(A.10)}$$

APPENDIX B

BESSEL FUNCTIONS

Bessel's equation can be written as

$$x^2 \frac{d^2y}{dx^2} + x\frac{dy}{dx} + (x^2 - p^2)y = 0 \tag{B.1}$$

Using the method of Frobenius, the solutions can be written as

$$J_v(x) = \sum_{m=0}^{\infty} \frac{(-1)^m (x)^{2m+v}}{m!(m-v)!2^{2m+v}}$$

$$J_{-v}(x) = \sum_{m=0}^{\infty} \frac{(-1)^m (x)^{2m-v}}{m!(m-v)!2^{2m-v}} \tag{B.2}$$

As long as v is not an integer, (B.2) and (B.3) are two independent solutions to Bessel's equation. However, when v = n is an integer,

$$J_{-n}(x) = (-1)^m J_n(x) \tag{B.3}$$

and (B.2) are no longer two independent solutions. In this case a second solution may be obtained by a limiting procedure and is defined as

$$N_v(x) = \frac{J_v(x)\cos v\pi - J_{-v}(x)}{\sin v\pi} \tag{B.4}$$

where, for integral $v = n$,

$$N_n(x) = \lim_{v \to n} N_v(x) \tag{B.5}$$

This limit exists and establishes a second solution to Bessel's equation of integral order. $J_v(x)$ is called Bessel functions of the first kind of order v, and $N_v(x)$ is called Bessel functions of second kind of order v. In many applications, Bessel functions of small and large arguments are required. Using asymptotic methods, it can be shown that

$$J_0(x) \underset{x \to 0}{\to} 1 \tag{B.6}$$

$$N_0(x) \underset{x\to 0}{\rightarrow} \frac{2}{\pi}\log\frac{\gamma x}{2} \tag{B.7}$$

and, for $v > 0$,

$$J_v(x) \underset{x\to 0}{\rightarrow} \frac{1}{v!}\left(\frac{x}{2}\right)^v \tag{B.8}$$

$$N_v(x) \underset{x\to 0}{\rightarrow} \frac{(v-1)!}{\pi}\left(\frac{2}{x}\right)^v \tag{B.9}$$

For the expression of wave phenomena, it is convenient to define linear combinations of Bessel's function

$$H_v^{(1)}(x) = J_v(x) + jN_v(x) \tag{B.10}$$

$$H_v^{(2)}(x) = J_v(x) - jN_v(x) \tag{B.10}$$

where $H_v^{(1)}(x)$ is the Hankel function of first kind of order *v* and $H_v^{(2)}(x)$ is the Hankel function of second kind of order *v*. Bessel functions represent standing waves and Hankel functions represent travelling waves.

APPENDIX C

Legendre Functions

The associated legendre equation is

$$\left(1-x^2\right)\frac{d^2y}{dx^2}-2u\frac{dy}{dx}+\left[n(n+1)-\frac{m^2}{1-x^2}\right]y=0 \tag{C.1}$$

where the indices *m* and *n* represent the degree and order respectively. Solution of (C.1) for nonnegative integer values of *m* and *n* takes the form

$$y(x)=A_1P_n^m(x)+B_1Q_n^m(x) \tag{C.2}$$

where $P_n^m(x)$ and $Q_n^m(x)$ are the associated Legendre function of the first and second kind respectively. The associated Legendre differential equation is often written in a form obtained by setting $x = cos\theta$. A study of the solutions to associated Legendre equation shows that all solutions have singularities at $\theta = 0$ or $\theta = \pi$ except $P_n^m(\cos\theta)$ with *n* an integer. Some of the identities of associated Legendre functions are:

$$P_{-n}^m(x)=P_{n-1}^m(x) \tag{C.3}$$

$$P_n^{-m}(x)=(-1)^m\frac{(n-m)!}{(n+m)!}P_n^m(x) \tag{C.4}$$

$$\int_{-1}^{+1}P_k^mP_n^m\,dx=\frac{2(n+m)!}{(2n+1)(n-m)!}\delta_{kn} \tag{C.5}$$

where δ_{kn} is the Kronecker delta function.

The first few associated Legendre functions are:

$$P_0^0(x)=1$$

$$P_1^0(x)=x$$

$$P_2^0(x) = \frac{1}{2}(3x^2 - 1)$$

$$P_3^0(x) = \frac{1}{2}(5x^2 - 3x)$$

$$P_0^1(x) = 0$$

$$P_0^2(x) = 0$$

$$P_1^2(x) = 0$$

$$P_2^2(x) = 3(1 - x^2)$$

$$P_3^1(x) = -\frac{3}{2}(5x^2 - 1)(1 - x^2)^{1/2}$$

$$P_3^2(x) = 15x(1 - x^2)$$

APPENDIX D

Mathematical Identities

$$\int_0^{\pi}\left[\frac{d\left(P_n^m(\cos\theta)\right)}{d\theta}\frac{d\left(P_l^m(\cos\theta)\right)}{d\theta}+\frac{m^2}{\sin^2\theta}P_n^m(\cos\theta)P_l^m(\cos\theta)\right]\sin\theta d\theta$$
$$=\begin{cases}\dfrac{2}{2n+1}\dfrac{(n-m)}{(n+m)}n(n+1) & , \quad \text{for } n=l\\ 0 & , \quad \text{for } n\neq l\end{cases} \tag{D.1}$$

$$\int_0^{\pi}\left[\frac{d\left(P_r^m(\cos\theta)\right)}{d\theta}P_n^m(\cos\theta)+\frac{d\left(P_n^m(\cos\theta)\right)}{d\theta}P_r^m(\cos\theta)\right]\mathrm{d}\theta=0 \tag{D.2}$$

$$\int_0^{\pi}\frac{P_n^m(\cos\theta)P_n^r(\cos\theta)}{\sin\theta}d\theta=\begin{cases}\dfrac{1}{m}\dfrac{(n+m)!}{(n-m)!}\delta_{mr}\end{cases} \tag{D.3}$$

$$\int_0^{\pi}P_n^m(\cos\theta)P_r^m(\cos\theta)\sin\theta d\theta=\frac{2}{(2n+1)}\frac{(n+m)!}{(n-m)!}\delta_{nr} \tag{D.4}$$

where δ_{nr} is the Kronecker delta function and is defined as

$$\delta_{nr}=\begin{cases}1 & \text{n = r}\\ 0 & \text{otherwise}\end{cases} \tag{D.5}$$

$$\int_0^{2\pi}e^{jm\phi}e^{-jn\phi}d\phi=\begin{cases}2\pi & \text{for } n=m\\ 0 & \text{for } n\neq m\end{cases} \tag{D.6}$$

$$\hat{J}_n\left(kr'\right)\hat{H}_n^{(2)\prime}\left(kr'\right)-\hat{J}_n'\left(kr'\right)\hat{H}_n^{(2)}\left(kr'\right)=-j \tag{D.7}$$

Publications

i. Related to the work reported in the thesis

1. **P. M. Jasmine**, P. Abdulla and P. M. Raphika, "Analysis and experiment of stair-shaped waveguide-fed dielectric resonator antenna", *IET Microwaves Antennas and Propagation*, Vol. 10, No. 4, pp. 453-458, 2016.

2. **P. M. Jasmine,** P. Abdulla and P. M. Raphika, "Rectangular waveguide fed DRA using tapered waveguide section", *Microwave and Optical Technology Letters*. Vol. 57, No. 9, pp. 2025-2028, 2015.

3. **P. M. Jasmine,** P. Abdulla and P. M. Raphika, "Coupling Enhancement of fed Waveguide fed HDRA using Steps", *International Journal of Scientific Progress and Research*", Vol. 25, No.2, pp. 78-80, July 2016.

4. **P. M. Jasmine,** P. Abdulla and P. M. Raphika, "Tapered Waveguide Fed Cylindrical Dielectric Resonator Antenna" accepted for publication in *Loughborough Antennas and Propagation Symposium*, LAPC 2016.

5. **P. M. Jasmine,** P. Abdulla and P.M. Raphika, "Double step junction coupled waveguide fed dielectric resonator antenna", IEEE *International Conference on Advances in computing and Communications*, (ICACC 2015), Kochi, pp. 297-300, 3-5 September 2015.

6. **P. M. Jasmine**, P. Abdulla and P.M. Raphika, "Theoretical analysis of double step junction coupled waveguide fed DRA", *Proceedings of International Symposium on Antennas & Propagation*, (APSYM 2014), Kochi, pp. 287-290, December 17-19, 2014.

7. **P. M. Jasmine**, P. Abdulla and P.M. Raphika, "Coupling enhancement of waveguide fed dielectric resonator antenna using tapered section of waveguide", *Procedia Computer Science,* Vol. 46, pp. 1278-1284, ICICT Kochi, 3-5 December 2014.

8. **P. M. Jasmine**, P. Abdulla and P.M. Raphika, "A novel technique of coupling enhancement of waveguide fed dielectric resonator antenna", *Spectrum, UGC Sponsored National Conference*, Govt. College, *Chittoor, Palakkad,* 29-31 October, 2014.

9. **P. M. Jasmine**, P.M. Raphika and P. Abdulla, "MoM analysis of waveguide fed dielectric resonator antenna", *UGC Sponsored National Seminar, Sree Ayyappa College, Eramallikkara*, Alappuzha, 20-21 December 2013.

ii. Related to other works

1. A. R. Anu, P. Abdulla, **P. M. Jasmine** and P. M. Raphika, "Semicircular Aperture Coupled Hemispherical Dielectric Resonator Antenna", *International Journal of Advances in Microwave Technology*, Vol.1, No.2, pp. 53-57, 2016.

2. P. M. Raphika, P. Abdulla and **P. M Jasmine,** "Compact wide stopband lowpass filter with high suppression using corrugated transmission line", *IOP Conference Series Materials Science and Engineering*. Vol. 120, No.1, 2016.

3. P. M. Raphika, P. Abdulla and **P. M Jasmine,** "Planar elliptic function lowpass filter with sharp roll-off and wide stopband", *Microwave and Optical Technology Letters*. Vol. 58, No. 1, pp. 133-136, 2016.

4. P. M. Raphika, P. Abdulla and **P. M Jasmine**, "Compact lowpass filter with sharp roll-off using funnel patch resonator", *Microwave and Optical Technology Letters*. Vol. 56, No. 4, pp. 2534-2536, 2014.

5. P. Abdulla, **P. M**. **Jasmine** and P. M. Raphika, "Waveguide-fed cylindrical DRA: Wide-band design", *IEEE International Symposium on Antennas and Propagation, Kaohsiung, Taiwan (ISAP 2014*), pp. 241-242, 2-5 December 2014.

6. P. M. Raphika, P. Abdulla and **P. M Jasmine,** "Compact microstrip elliptic function lowpass filter with sharp roll-off and wide stopband by cascading multiple patch resonators", Proceedings of *IEEE International Microwave & RF Conference (IMaRC 2014)*, Bangalore, pp. 316-319, 15-17 December 2014.

7. P. M. Raphika, P. Abdulla and **P. M Jasmine**, "Planar lowpass filter with sharp roll- off using patch resonators on high impedance microstrip line", *IEEE RADIO 2015,* Mauritius, pp. 1-2, 21-24 September 2015.

8. P. M. Raphika, P. Abdulla and **P. M Jasmine**, "Compact planar lowpass filter with sharp roll-off and wide stopband using multiple patch Resonators", Proceedings of *International Symposium on Antennas & Propagation (APSYM 2014),* Kochi, pp. 347-350, 17-19 December, 2014.

9. P. M. Raphika, P. Abdulla and **P. M Jasmine.,** "Compact microstrip lowpass filter with sharp roll-off and wide stopband by cascading multiple resonators", *Asia Pacific Microwave Conference, (APMC 2014)*, Sendai, Japan, pp. 1229-1231, 4-7 November 2014.

10. P. S. Arya, P. Abdulla, **P. M. Jasmine** and Divya Mohan, "Semicircular slot coupled hemispherical dielectric resonator antenna", *UGC Sponsored National*

Conference on Recent Advances in Microwave Communication, *MES College, Marampally*, 11-12 August 2015.

11. P. M. Raphika, Abdulla P. and **P. M. Jasmine,** "Review of compact planar lowpass filter with sharp roll-off using patch resonators", *Spectrum, UGC Sponsored National Conference*, *Govt. College, Chittoor, Palakkad,* 29-31 October 2014.

Cochin University of Science and Technology, Kochi – 22, India.